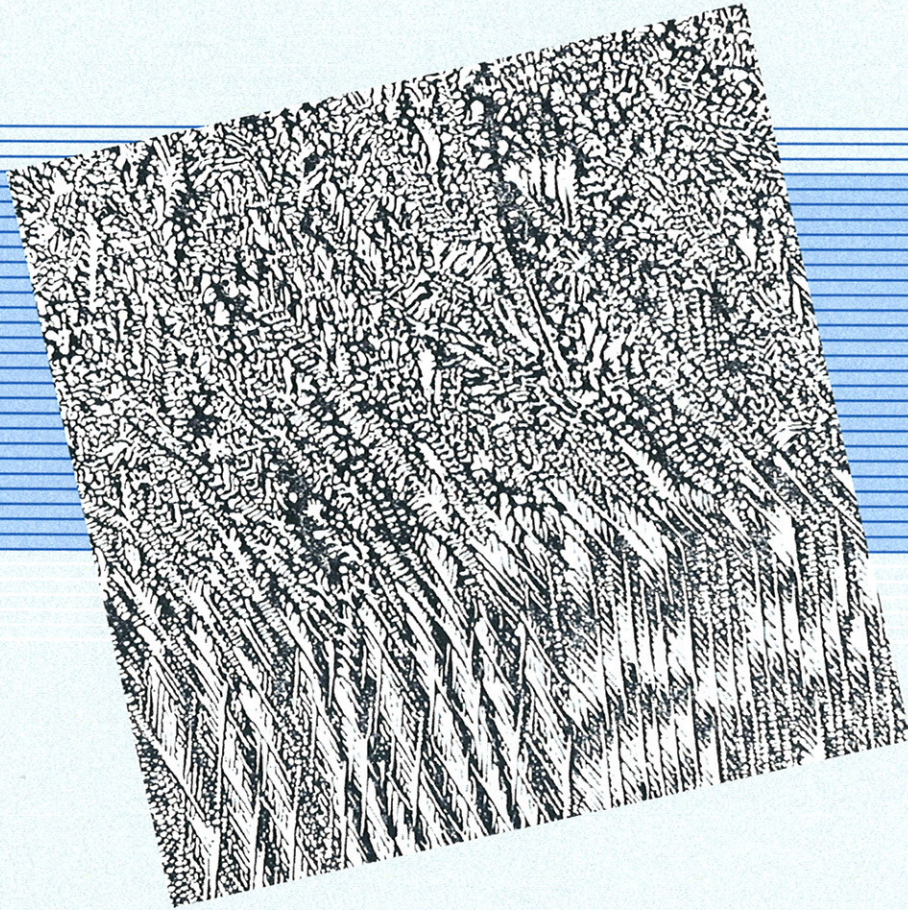


FZR-457



Wissenschaftlich - Technische Berichte
FZR-457 2006 · ISSN 1437-322X

Annual Report 2005

Institute of Safety Research



Forschungszentrum
Rossendorf

Wissenschaftlich-Technische Berichte
FZR-457
2006

Annual Report 2005

Institute of Safety Research

Editors:
Prof. Dr. Frank-Peter Weiss
Prof. Dr. Udo Rindelhardt



**Forschungszentrum
Rossendorf**

Cover Pictures:

The micrograph shows the transition from a parallel to an inclined growth of columnar dendrites in a Sn-15wt.% Pb alloy. The morphology transition is caused by the initiation of convection in the liquid phase driven by a rotating magnetic field (see contribution page 53ff).

Forschungszentrum Rossendorf e.V.
Institut für Sicherheitsforschung

Postfach 51 01 19
D-01314 Dresden
Bundesrepublik Deutschland

Direktor	Prof. Frank-Peter Weiß
Telefon	+ 49 (3 51) 2 60 34 80
Telefax	+ 49 (3 51) 2 60 34 40
E-Mail	f.p.weiss@fz-rossendorf.de
WWW	http://www.fz-rossendorf.de/FWS

CONTENTS

Preface

Selected reports

Ch. Vallee, Th. Höhne, T. Sühnel Experiments and CFD simulation of stratified horizontal two-phase flow	3
H. Hristov, S. Boden, G. Hessel, H. Kryk, H.-M. Prasser, W. Schmitt CFD simulations of single and two-phase mixing processes in stirred tank reactors	10
Th. Höhne, S. Kliem, U. Rohde, F.-P. Weiss Bouyancy driven mixing studies of natural circulation flows at the ROCOM facility using the ANSYS CFX code	16
H.-M. Prasser, T. Frank, M. Beyer, H. Carl, S. Al-Issa, H. Pietruske, P. Schütz Gas-liquid flow around an obstacle in a vertical pipe - experiment and CFD simulation	24
E. Krepper, A. Grahn, S. Alt, W. Kästner, A. Kratzsch, A. Seeliger Numerical investigations for insulation particle transport phenomena in water flow	31
A. Bieberle, U. Hampel, D. Hoppe, E. Schleicher, H.-M. Prasser, T. Sühnel, C. Zippe First results with the new high-resolution gamma ray tomograph	41
E. Schleicher, M. J. da Silva, U. Hampel New developments in fast needle probe sensors for multiphase flow measurements	45
S. Eckert, B. Willers Solidification of Sn-Pb alloys with magnetic field control of the melt flow	53
F. Stefani, G. Gerbeth, U. Günther A simple model of earth's magnetic field reversals	59
P. Petkov and S. Mittag Evaluation of homogenisation error in two-group nodal diffusion calculation for VVER-1000 core	65
U. Rohde, U. Grundmann, Y. Kozmenkov, V. Pivovarov, Yu. Matveev Core design and transient analyses for weapons Plutonium burning in VVER-1000 type reactors	69

M. Abendroth, H.-G. Willschütz, E. Altstadt	
Modelling of in-vessel retention after relocation of corium into the lower plenum: Evaluation of the thermoshock stresses due to outside vessel cooling	77
F. Bergner, A. Ulbricht	
Thermal dissolution kinetics of irradiation induced clusters in RPV steels	82
R. KÜchler, K. Noack	
The solution behaviour of Pyrite in four columns of different porous sand material	87
Summaries of research activities	95
Accident analysis of nuclear reactors	96
Materials and components safety	99
Particle and radiation transport	101
Pulsed photo-neutron-source at the radiation source ELBE	103
Safety and efficiency of chemical processes	104
Liquid metal magnetohydrodynamics	106
Thermal fluid dynamics of multiphase systems	108
TOPFLOW thermohydraulic test facility	111
Publications	113
Publications in journals	114
Conference contributions and other oral presentations	120
Contributions to proceedings and other collected editions	135
FZR reports and other reports	146
Patents	148
PhD and diploma theses	149
Awards	150
Guests	151
Meetings and workshops	155
Seminars of the Institute	156
Lecture courses	158
Departments of the Institute	159
Personnel	160

Preface

The Institute of Safety Research (ISR) is one of the six Research Institutes of Forschungszentrum Rossendorf e.V. (FZR e.V.) which is a member institution of the Wissenschaftsgemeinschaft Gottfried Wilhelm Leibniz (Leibniz Association).

Together with the Institute of Radiochemistry, ISR constitutes the research programme „Safety and Environment“ which is one from three scientific programmes of FZR. In the framework of this research programme, the institute is responsible for the two sub-programmes “Plant and Reactor Safety” and “Thermal Fluid Dynamics”, respectively (see Table 1). We also provide minor contributions to the sub-programme “Radio-Ecology”. Moreover, with the development of a pulsed photo-neutron source at the radiation source ELBE (**E**lectron linear accelerator for **b**eams of high brilliance and low **e**mittance), we are involved in a networking project carried out by the FZR Institute of Nuclear and Hadron Physics, the Physics Department of TU Dresden, and ISR.

The research of ISR aims at assessing and enhancing the safety of technical plants and at improving the environmental sustainability of the processes involved. The applications are as well related to nuclear plants of present and future designs as to installations of process industries.

To achieve the goals mentioned, the institute does research in thermal fluid dynamics including magneto-hydrodynamics (MHD) and in materials sciences as related to ageing materials and components. The thermal fluid dynamics research work is essentially based on the experiments performed at the **T**ransient **T**wo-**P**hase **F**low Test Facility, TOPFLOW. TOPFLOW is one of the large research and user facilities of FZR and represents the reference thermal hydraulic experiment of the so called “German CFD (Computational Fluid Dynamics) Initiative”.

Our work is financed through the basic funding of FZR as well as by external funds from public and private research grants, and from contracts with the industry. 41 % (3.005 k€) of our total budget could be acquired from such external funds, in 2005, with 19 % from research grants of the Federal Government and the Free State of Saxony. 10 % of the funding originated from Deutsche Forschungsgemeinschaft, 5 % from the EU and 7 % from research contracts mainly with the industry (see Fig.1). The deployment of the total budget on the different projects and the user facility TOPFLOW (see Table 1) is illustrated in Fig.2.

Sub-programme	Project/User facility
Plant and reactor safety	Accident analysis of nuclear reactors
	Safety of materials and components
	Particle and radiation transport
	Safety and efficiency of chemical processes
Thermal fluid dynamics	Magneto-hydrodynamics
	Thermal fluid dynamics of multi-phase flows
Radio-ecology	Simulation of the migration of radio-nuclides
User facility TOPFLOW	Transient two-phase flow test facility
Networking research activity	Design and construction of a pulsed photo-neutron source at ELBE

Table 1. Research projects and user facility of the Institute of Safety Research, 2005

Together with the Dresden Technical University and with the Zittau University of Applied Sciences, the ISR represents the East German Centre of Competence in Nuclear Technology (Kompetenzzentrum Ost) being a member of the German Alliance for Competence in Nuclear Technology (Kompetenzverbund Kerntechnik). As such, the ISR also takes care to keep and promote the expertise in nuclear engineering. For that end, a strategic partnership was established between Kompetenzzentrum Ost and Vattenfall Europe Nuclear Energy (VENE). VENE sponsors the education of three PhD students in nuclear technology, one in each of the participating institutions.

Beyond this, ISR in general cares for the next generation of young scientists by, e.g., supervising PhD and Diploma students. The quality of the education at ISR is underlined by the prizes awarded to our PhD students. Jiří Krepel received the Young Authors award at the conference Nuclear Energy for New Europe (Bled, Slovenia) for his work on the simulation of Molten Salt Reactors. H.-G. Willschütz was awarded the “Förderpreis 2005 der Friedrich-und-Elisabeth-Boysen-Stiftung“ for his PhD thesis „Thermo-mechanical modelling of the reactor pressure vessel during the late phase of a core melt accident“.

In 2005, we were involved in several Integrated Projects and Networks of Excellence of EU FP6 like in PERFECT (Prediction of Irradiation Damage Effects in Reactor Components), SARNET (Severe Accident Research Network), EUROTRANS (European Research Project on the Transmutation of High Level Nuclear Waste in an Accelerator Driven System), and NURESIM (Nuclear Reactor Simulation). This strengthens the position of ISR as one of the major players in European nuclear safety research. In particular it is noteworthy that our reactor dynamics code DYN3D has been decided to become part of the European software platform for reactor simulation, NURESIM.

Amongst others, the ISR develops advanced calculation models for the behaviour of the nuclear reactor pressure vessel (RPV) during severe core melt accidents in PWR with the corium being relocated to the lower plenum. It is the aim of these calculations to obtain information about the time and the mode of the potential RPV failure and to derive severe accident mitigation measures suited to retain the melt in the vessel. The model considers the thermal fluid dynamics in the melt pool as well as the thermo-mechanical behaviour of the RPV wall, in particular mechanical creeping up to pressure vessel failure.

Post-test calculations of the FOREVER experiments performed at KTH Stockholm proved that as well the failure mode as the time of failure can be predicted in reasonable agreement with the experiment. Like in the experiment, the calculated creeping crack starts from the RPV outer surface near the melt pool upper level and grows into the wall.

From the numerical analyses, two patents were derived for passive in vessel melt retention: (1) the so called creep stool reduces the mechanical load to highly damaged (by creeping) RPV zones by supporting the centre of the lower calotte, that is slowly moving down, with pillars. (2) The second device allows for passive external flooding of the reactor pit. The heat removal from the melt increased in this way reduces the thermal load to the RPV wall. Calculations on prototypical medium size PWRs have shown that the combined application of both measures enables in vessel core melt retention.

The efficiency of bubble columns that are widely used for heterogeneous chemical reactions in process industry strongly depends on the structure of the two-phase flow. For years the change has been studied from the wanted homogeneous bubble flow to the unwanted heterogeneous flow. Many mechanisms and criteria have been proposed for that flow structure change. However, their validity was limited and the results were partly in contradiction to the experiments. These contradictions could be resolved by considering that

the lift force that acts on a bubble strongly depends on its size. The lift force coefficient is positive for small bubbles (diameter < 5.8mm in air-water mixture), while it is negative for bigger bubbles. By means of linear stability analysis, criteria were obtained for the prediction of the local stability in a two-phase flow in dependence on the bubble size spectrum. Small bubbles stabilise the flow and large bubbles will amplify local disturbances. Since the stability analysis has been published, two international groups (University of Montreal and TU Delft) could experimentally validate our new stability criteria.

The new high resolution gamma tomography system has been put into operation for flow visualization. It was developed to study multi-phase flow phenomena in fuel elements, in hydrodynamic machinery, and in chemical reactors.

The tomography system consists from a high resolution detector array including the electronic equipment, and the gamma radiation source (Co-60 or Cs-137). The detector is based on the advanced scintillator avalanche photo-diodes technology and a special electronics for data acquisition. In this kind of tomography, either the object to be studied is rotated or the radiation source and the detector rotate around the subject. The described system marks the front end in the spatial resolution of heavy construction components which are hardly accessible to tomographic imaging due to their strong shielding effects.

End of July 2005, the system has been used for steam content measurements in BWR fuel elements at the KATHY test facility of AREVA in Erlangen for the first time. The related project that is supported by AREVA strives for the non-invasive measurement of the local steam content distribution near the so called boiling crisis. The results gained mean a decisive break through in the diagnostics of the local boiling crisis and offer a unique basis for the validation of CFD models used for fuel element optimisation.

ISR's engagement in thermal fluid dynamics is completed by research in magneto-hydrodynamics (MHD). In general, the target of MHD is to investigate the interactions of magnetic fields with electrically conducting fluids. The particular aim is to influence the flow of liquid metals in metallurgy or, e.g., of liquid semi-conductors in crystal growth by "tailored" external magnetic fields to optimise the processes involved regarding product quality and energetic efficiency. Most of our scientific activities in this field are part of the Collaborative Research Centre 609 (Sonderforschungsbereich SFB 609) "Electromagnetic flow control in metallurgy, crystal growth, and electrochemistry" funded by Deutsche Forschungsgemeinschaft. SFB 609 has been running since 2002. ISR coordinates 5 from 17 sub-projects of the SFB and further participates in 4 other sub-projects. The SFB receives a total annual funding of about 1.8 M€ for all the 17 projects. Today, Rossendorf and Dresden clearly belong to the worldwide leading places in MHD research. Invitations to joint R&D programmes with Chinese and Japanese teams underline this recognition.

One topic of the MHD project is dedicated to the so called dynamo effect in electrically conducting fluids which plays a key role in the explanation of the magnetic field of the earth and of its properties. It is known from paleomagnetic measurements that the orientation of the earth's magnetic field changes irregularly. The rate of change varies between 0 and 4-5 events in one million years. The pole changes are characterised by three features: (1) the process of pole changing is asymmetric. First, the existing field slowly decays but then the new field with opposite orientation quickly emerges. (2) There is a significant correlation between the mean field intensity and the length of the time intervals between the pole changes. (3) The distribution of the magnetic dipole moments exhibits two maxima.

To explain these peculiarities, a theoretical model was developed for a mean field dynamo. The helical turbulence is an essential parameter of the spherical dynamo model. It has been known from earlier work (Stefani, Gerbeth: Phys. Rev. E67 (2003), 027302) that such a

dynamo can oscillate in a narrow range, a so called corridor, of that turbulence parameter. Now, it could be shown that the above mentioned peculiarities can consistently be explained by the behaviour of the dynamo at the edge of that turbulence corridor (Stefani, Gerbeth: Phys. Rev. Lett. 94 (2005), 184506).

In materials safety research ISR is focussed on irradiation induced ageing phenomena of reactor pressure vessel materials. This topic is of special importance to the Soviet type VVER reactors. Improved insight in irradiation induced ageing is expected from the post-service investigations of specimens that were taken from unit 1 of the decommissioned Greifswald reactors end of 2005. Further specimens will be taken from the other units in the coming years. With our recently licensed hot cell laboratory for the machining of standard specimens from large size materials pieces, we are well prepared for the testing programme that has attracted international attention.

During the reporting period, the ISR organised important meetings and workshops with international participation. In particular, one should mention the international Workshop on “Multi-Phase Flow: Simulation, Experiment and Application” which was commonly hosted by ISR and ANSYS/CFX[®] and which continues the series of meetings on that topic in Rossendorf. One should further mention the “International Conference on Fundamental and Applied MHD” commonly organised by the University of Latvia, LEGI Grenoble, and the ISR. Moreover, the second “Sino-German Workshop on Electromagnetic Processing of Materials” was held in Dresden. The latter was sponsored by the National Nature Science Foundation of China and Deutsche Forschungsgemeinschaft, respectively.

Meetings like these underline the international scientific reputation of the Institute of Safety Research.

I would like to thank all staff members of the institute for their excellent work and for making the year 2005 a successful one. In particular, I direct my congratulations to H.-M. Prasser who was awarded the FZR Forschungspreis 2005 for his experimental work on CFD validation.

F.-P. Weiß

Rossendorf, 7 May 2006

Fig. 1: Funding sources 2005

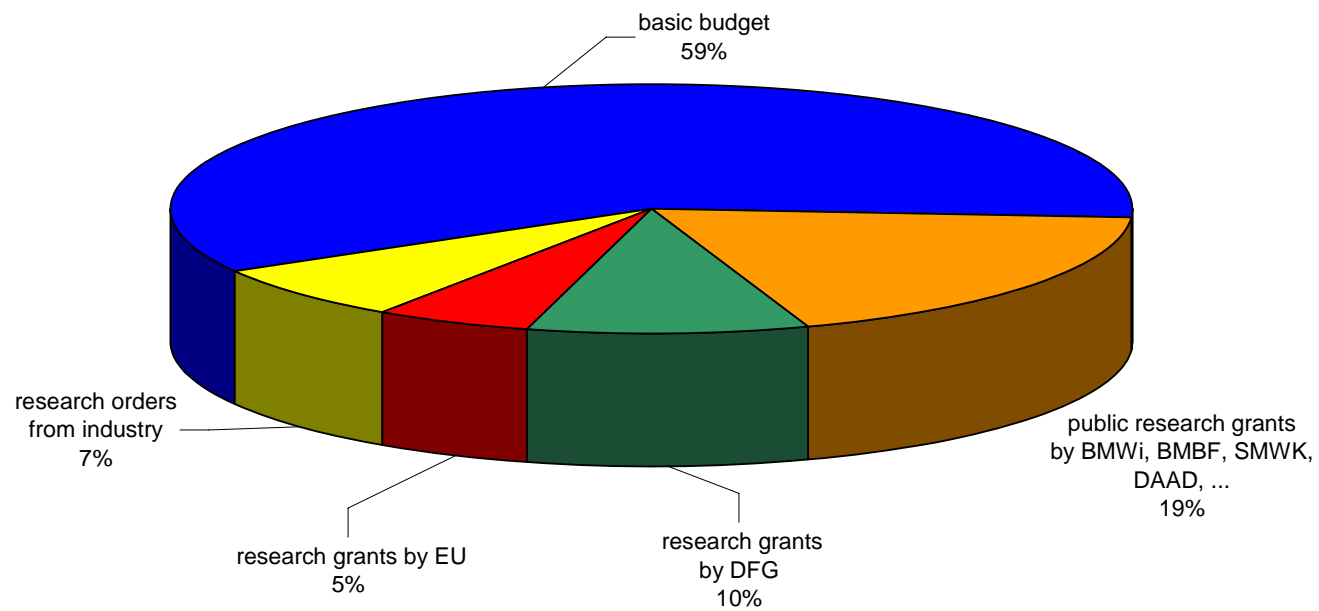
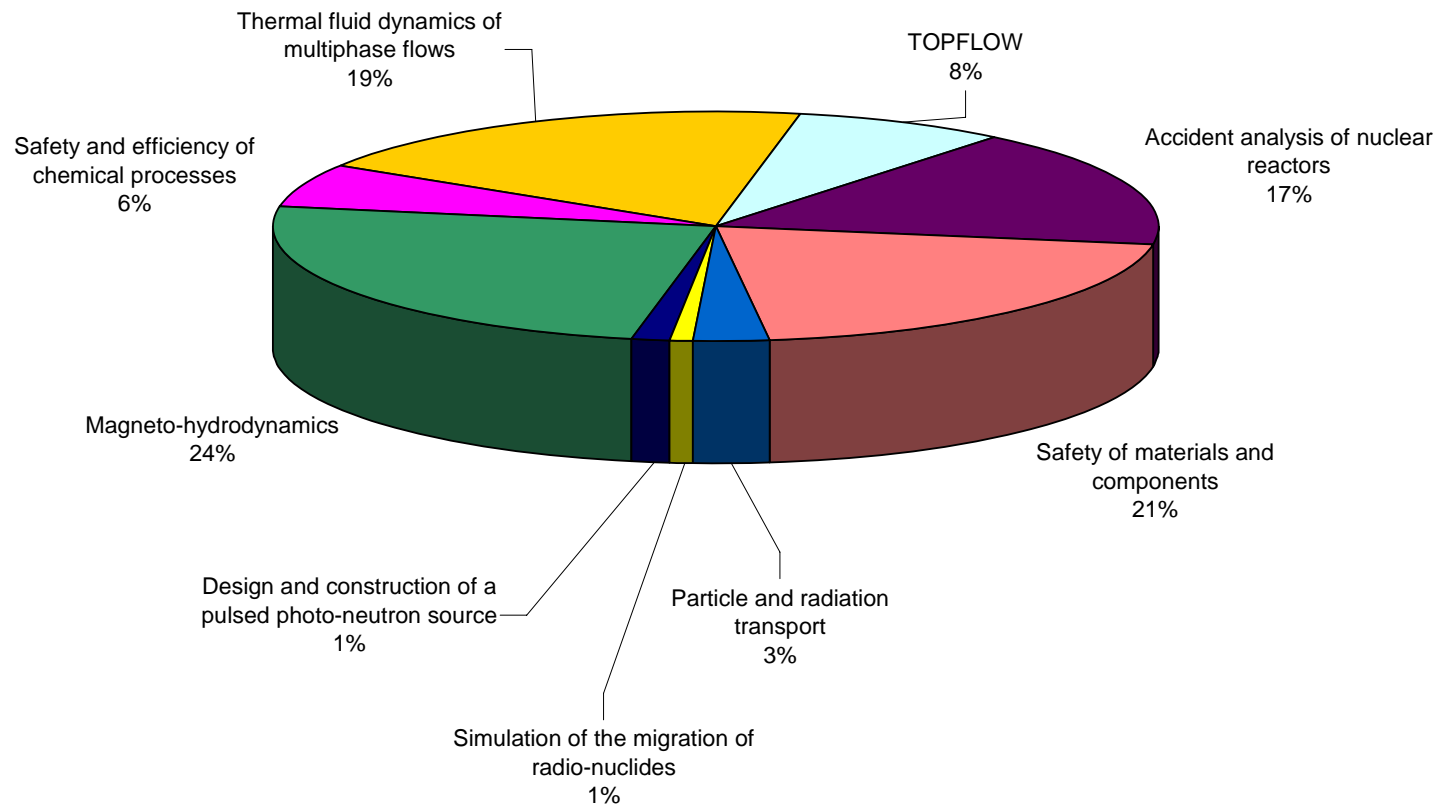


Fig. 2: Deployment of funding on the projects and user facilities 2005



Selected reports

EXPERIMENTS AND CFD SIMULATION OF STRATIFIED HORIZONTAL TWO-PHASE FLOW

Christophe Vallée, Thomas Höhne and Tobias Sühnel

1. Introduction

Slug flow as a multiphase flow regime can occur in the cold legs of pressurized water reactors, for instance after a small break Loss of Coolant Accident (SB-LOCA). Slug flow is usually characterized by an acceleration of the gaseous phase and by the transition of fast liquid slugs, which entrain a significant amount of the liquid with high kinetic energy. For the experimental investigation of air/water flows, a horizontal channel with rectangular cross-section was built at Forschungszentrum Rossendorf. Experimental data were used to check the feasibility to predict the slugging phenomenon with the existing multiphase flow models available in CFX-5.

2. The horizontal air-water flow duct

Experiments were carried out at a horizontal duct mounted between two separators (Fig. 1). The two-meter long acrylic glass test section has a rectangular cross-section (height x width: 250 x 50 mm²). A jet pump is driving the water flow, while air is being injected at the top of one of the separators. Both co-current and counter-current tests were performed.

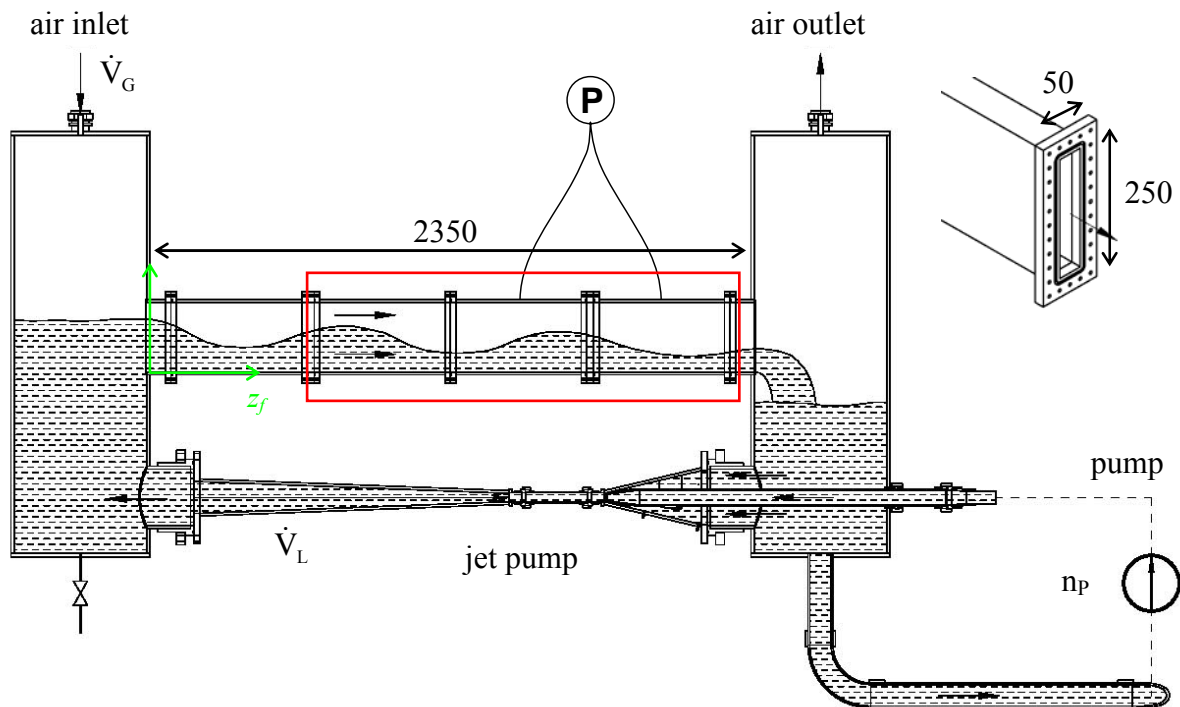


Fig. 1: Schematic view of the horizontal air-water flow duct and modelled part (in red)

The rectangular cross-section was chosen for its optimal optical access in order to observe the flow structure from the side of the duct. A high-speed video camera as well as a PIV-system were used for this purpose. For dynamic pressure measurements, piezoelectric transducers with a rise time of 2 μ s were mounted on top of the duct and were synchronised with the high-speed video camera. The dynamic liquid level measurement as well as the analysis of the slug

propagation were achieved by processing the high-speed camera image sequences, both with a time resolution of 100 Hz.

In the following, a selected co-current test run is analysed. It was carried out at a superficial water velocity of $v_L = 0.69$ m/s and a superficial air velocity of $v_G = 2.2$ m/s. The pressure was at an ambient level and the water temperature $16,5^\circ\text{C}$. Under these conditions, a slug flow is generated.

3. CFD model of the duct

The CFD calculation was performed using the software package CFX-5.7 (CFX, 2004). For free surface simulations, the inhomogeneous multiphase model recommended by Frank (2003) was used, where the gaseous and liquid phases can be partially mixed in certain areas of the flow domain. In this case, the local phase demixing after gas entrainment is controlled by buoyancy and interphase drag and is not hindered by the phase interface separating the two fluids. A further decision has to be made regarding the applied fluid morphology and interphase drag law for the multiphase flow. The total drag force D is most conveniently expressed in terms of the dimensionless drag coefficient C_D ,

$$D = \frac{1}{2} \cdot \rho_{LG} \cdot (U_L - U_G)^2 \cdot A \cdot C_D \quad (1)$$

where ρ is the fluid density, $(U_L - U_G)$ is the relative speed and A is the projected area of the interphase in flow direction. In (1), L describes the liquid phase and G the gaseous phase.

The fluid-dependent shear stress transport (SST) turbulence models were selected for each phase. Damping of turbulent diffusion at the interface was not considered. The k - ω based SST model accounts for the transport of the turbulent shear stress and gives highly accurate predictions of the onset and the amount of flow separation. The SST model combines the advantages of the Wilcox and of the k - ε model.

To take buoyancy effects into account, a buoyancy production term was applied in the turbulence model and was included in the k - and ω -equations for additional turbulence production and dissipation. If the full buoyancy model is being used, the buoyancy production term P is modelled as:

$$P = - \frac{\mu_t}{\rho \cdot Pr_t} \cdot \vec{g} \cdot \nabla \rho \quad (2)$$

where ρ is the density of the fluid, Pr_t the turbulent Prandtl number, μ_t the turbulent viscosity and \vec{g} the gravity vector.

4. Geometry, grid generation and boundary conditions

Due to very high numerical efforts of transient slug flow simulations, the modelling of the complete test facility is not feasible. In order to keep the computational time within acceptable limits, only the horizontal test section with its rectangular cross-section was modelled. The model dimensions are: length x height x width = $2000 \times 250 \times 50$ mm³. The grid was created with CFX-MESHBUILD and transferred to CFX-5 PRE. It consists of 4×10^5 hexahedral elements, which reduces the computational time and improves the quality of the mesh compared to tetrahedrons.

At the inlet of the channel, air and water velocities are set to constant values over the part of the inlet cross-section that is occupied by each phase. In accordance to the initial water level,

the inlet velocities were set to values that correspond to the gas and liquid flow rates measured during the experiment. These velocities were kept constant in time. The level at the inlet was varied according to the time history of the liquid level measured by the high-speed camera at $z_f = 0.75$ m (Fig. 2). The outlet boundary condition has been applied to the cross section at the other end of the horizontal channel and was pressure controlled. The walls of the channel were set as hydraulically smooth walls with a non-slip boundary condition applied to both gaseous and liquid phases.

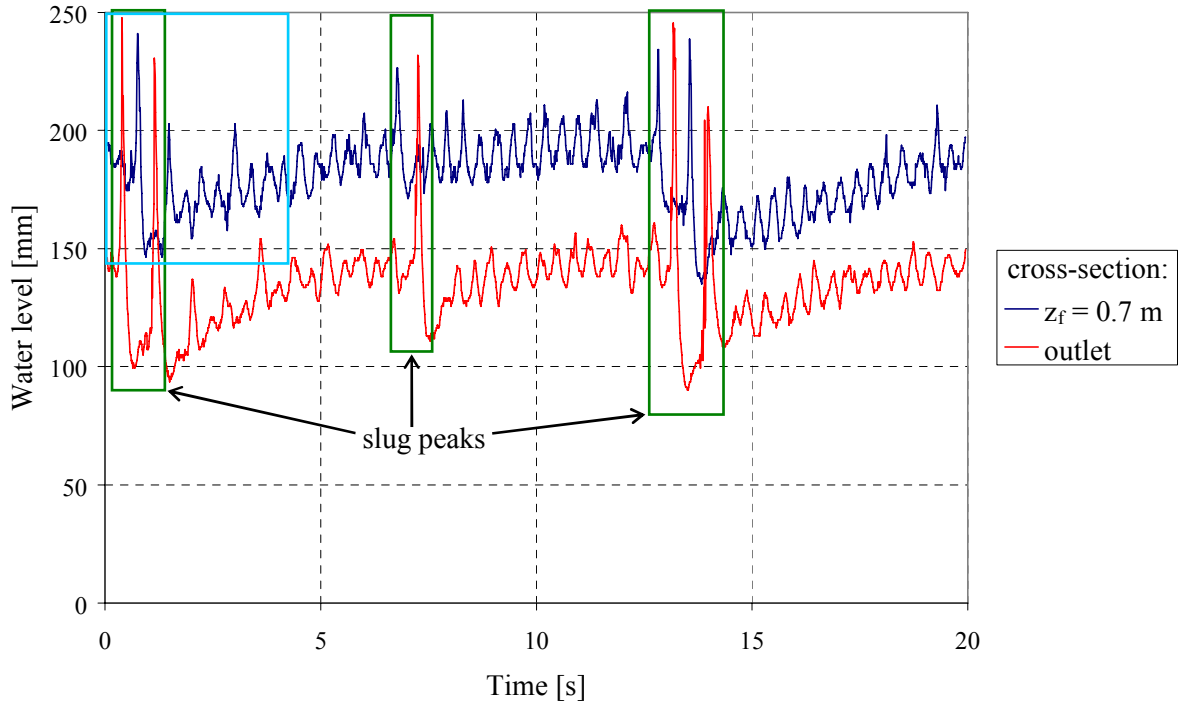


Fig. 2: Time-dependent water level during slug flow in the test-section (100 Hz measurement)

5. Results

The image sequence (see Fig. 3) compares the flow observed during the experiment with the corresponding CFD calculation. In both cases, a slug is developing. In the CFD calculation, the slug develops approximately at $t = 0.90$ s due to a high peak of the experimental water level at the inlet cross-section. The tail of the calculated slug and the flow behind it is in good agreement with the experiment. The entrainment of droplets in front of the slug could not be observed in the calculation. However, the rolling over and breaking of the wave, characteristic of a slug, are clearly to be seen in Fig. 3. These are created by the high air velocity.

In contrast to the measurement, the slug length is increasing in time in the calculation. This could be a result of the different amount of water in the channel at the beginning of the experiment and the simulation. While in the simulation, the liquid phase covered 78% of the channel, it represented about 70% at the beginning of the experiment. Furthermore, in the experiment, this value was also reduced by a first slug which carries a significant amount of water out of the channel. This first slug could not be simulated. This is probably an effect of the simplified initial conditions assumed in the calculation. Because of the constant initial water level, it took quite a long simulation time to establish a wavy flow along the channel, which is necessary for slug formation. Whereas at the beginning of the measurements, the test channel was already in a fully established intermittent slugging regime.

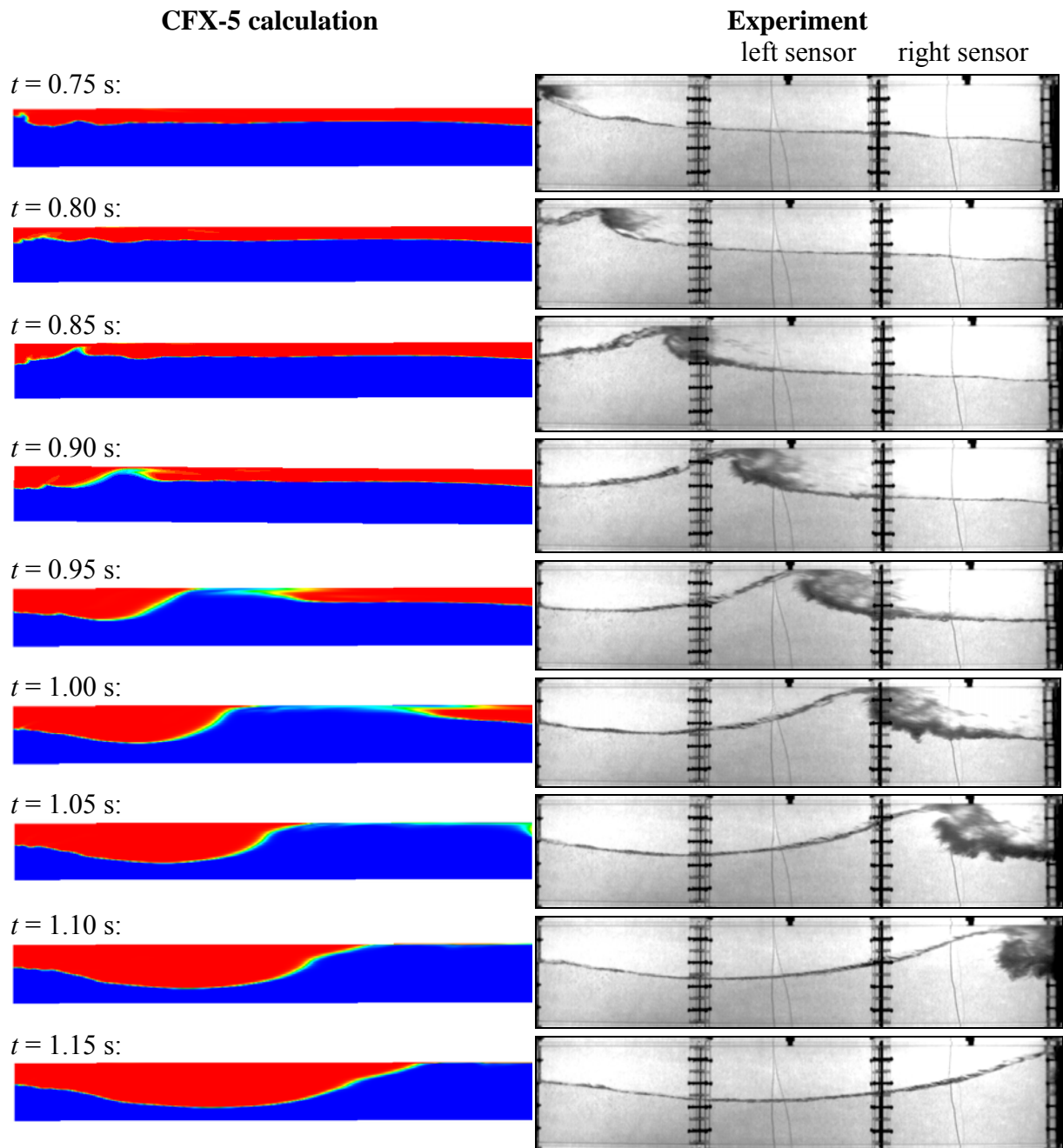


Fig. 3: Measured and calculated image sequences at slug flow conditions

The slug position extracted from the camera images is compared with the calculation result in Fig. 4. In the experiment, the slug moves along the duct with constant velocity. The velocity of the slug selected for the post-test calculation was 3.7 m/s. In contrast to this, the calculated slug propagation is characterized by an acceleration phase between 0.75 and 0.90 s when the slug is still in the process of formation. In a second phase, starting from $t = 0.90$ s when the wave blocks the whole cross-section of the channel, the velocity of the calculated slug stays nearly constant at 4.4 m/s on average. This is 18% higher than the experimental value.

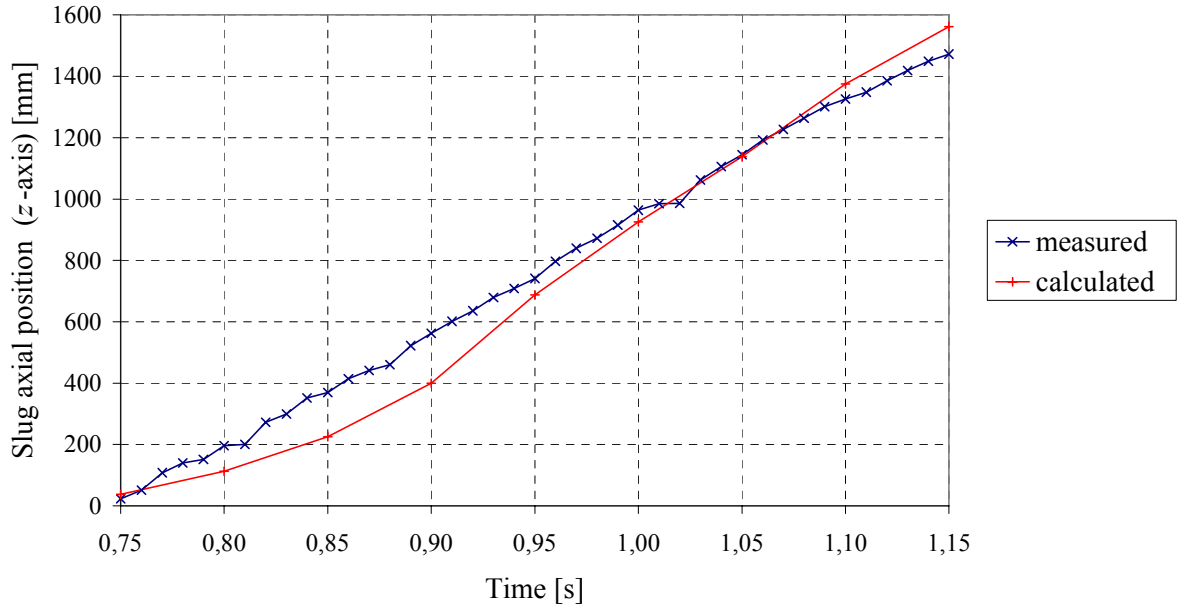


Fig. 4: Propagation of a slug - comparison between measurement and calculation

Fig. 5 shows the pressure field created by the slug in the CFD calculation. Due to the fact that the slug is driven by the gas pressure, a steep pressure gradient is observed at the slug front. This leads to the typical pressure history recorded by the transducers on top of the channel, which indicate a sudden pressure increase when the slug passes by (Fig. 6). Typical rise times were measured from 2 to 10 ms. An analysis of the camera pictures taken during the pressure measurements could explain the large spectrum of rise times. They are in fact an indicator of the slug length: the longer the slug, the longer the rise time. The pressure decreases simultaneously on both sensor positions, when the slug reaches the outlet separator.

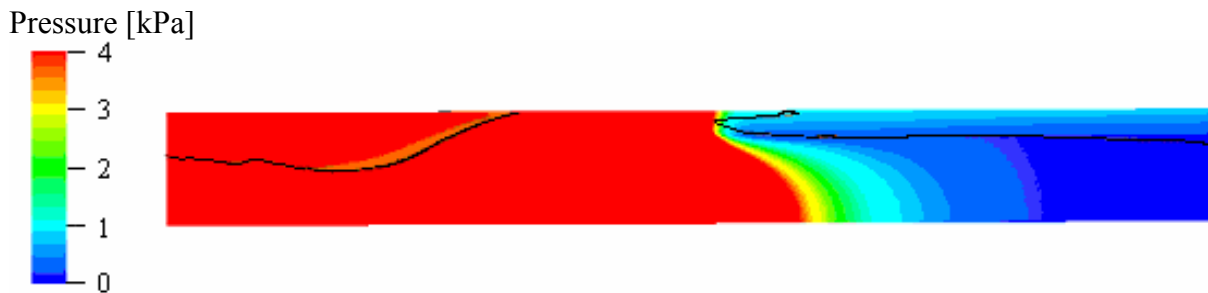


Fig. 5: Calculated pressure field at $t = 0.95$ s

The comparison of the time-dependent pressure at both sensor positions for the experiment and the calculation also shows that the first slug observed in the test was not simulated. Therefore, only the second pressure increase can be compared with the calculation. In the simulation, the pressure at the first sensor position increases later than in the experiment. At the second sensor position the increase happens simultaneously. Then the pressure decreases earlier in the calculation than in the experiment. All this is a consequence of the differences in the slug propagation (see Fig. 4).

Furthermore, the calculation overestimated the peak pressure (4.4 kPa) in comparison to the experiment (2.3 kPa). This is due to the different size of the experimental slugs. Since, in the experiment, the first slug removed a certain amount of water from the channel, the second

slug is much smaller than the first one. That is why the peak pressure of the first slug reaches values between 3.6 and 5.0 kPa (respectively at the first and second sensor positions), which is the order of magnitude of the calculated pressure peak.

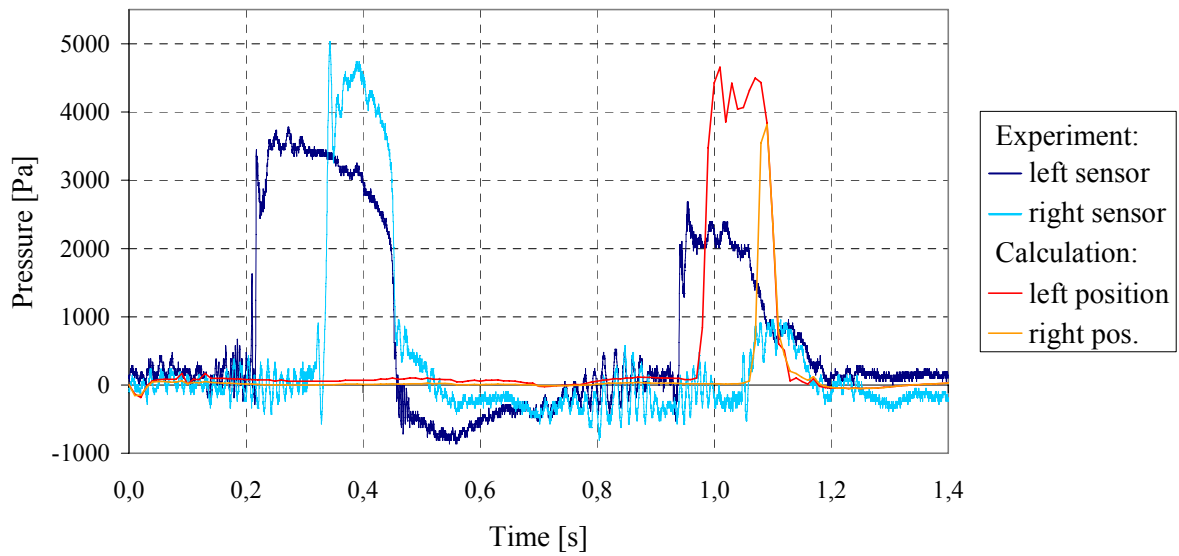


Fig. 6: Transient pressure at both sensor positions for experiment and CFX calculation

6. Particle Image Velocimetry (PIV) of a slug

A PIV-system was used to show the velocity field inside the slug. The laser-light sheet was focused in the middle of the test section. The PIV camera was directed to the upper part of the duct, in the region of the first pressure sensor.

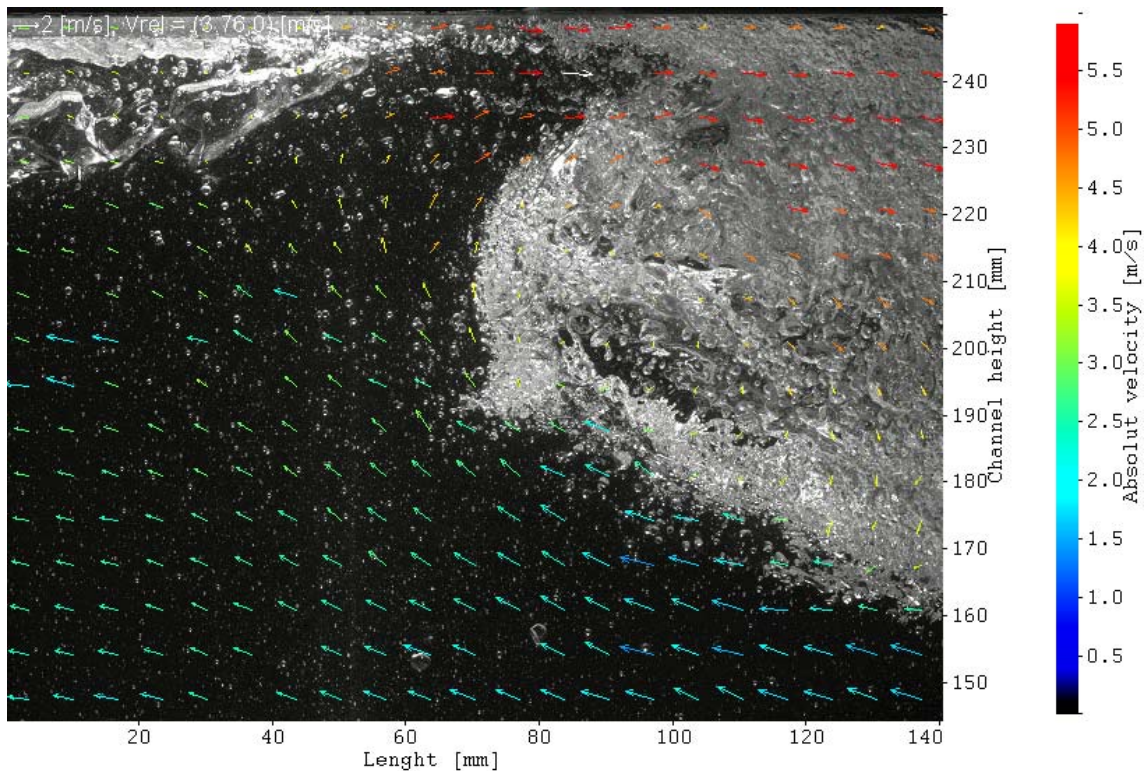


Fig. 7: Velocity field inside a slug (the vector colour shows the absolute velocity, its length and direction show the relative velocity compared to the propagation velocity of the slug)

A PIV picture of a slug with the measured velocity field is shown in Fig. 7. The slug propagation velocity is approximately 3.8 m/s, which is close to the velocity of the slug analysed in section 5. The vector colour shows that the small leak air flow on top of the slug entrains the water at local absolute velocities of about 6 m/s. The lengths and directions of the vectors show the velocities in a coordinate system that moves with the slug propagation velocity. It reveals the structure of the flow circulation inside the slug.

7. Summary and conclusions

For the investigation of an air/water slug flow, a horizontal channel with rectangular cross-section was built at Forschungszentrum Rossendorf. Optical measurements were performed with a high-speed video camera and were complemented by simultaneous dynamic pressure measurements. By an interface capture method, the water level history can be extracted from the image sequences. The pressure measurements show that the order of magnitude of the pressure level behind the slug is about a few kPa. The pressure increase is fast (2 to 10 ms) and linked to the slug length. Furthermore, the velocity field of a slug was measured using Particle Image Velocimetry (PIV). It reveals the inner flow circulation of the slug, around the point there the slug is rolling over.

A CFD simulation of the stratified co-current flow was performed using the code CFX-5 applying the two-fluid model with the free surface option. The slug flow was successfully simulated with a transient simulation in the horizontal channel, using time-dependent inlet boundary conditions from the experimental data. The behaviour of slug propagation at the experimental setup was qualitatively reproduced, while quantitative deviations require a continuation of the work.

References

- [1] T. Frank (2003), Numerical simulations of multiphase flows using CFX-5. CFX Users conference, Garmisch-Partenkirchen, Germany
- [2] T. Sühnel (2003), Aufbau und Inbetriebnahme eines horizontalen Luft-Wasser-Strömungskanals. Diplomarbeit, Hochschule Zittau/Görlitz (FH)
- [3] C. Vallée, T. Höhne, H.-M. Prasser, T. Sühnel (2005), Experimental modelling and CFD simulation of air/water flow in a horizontal channel. International topical meeting NURETH-11, Avignon, France, log# 479

Acknowledgements

This work is carried out in the frame of a current research project funded by the German Federal Ministry of Economics and Labour, project number 150 1265.

CFD SIMULATIONS OF SINGLE AND TWO-PHASE MIXING PROCESSES IN STIRRED TANK REACTORS

Hristo Vesselinov Hristov, Stephan Boden, Günther Hessel, Holger Kryk, Horst-Michael Prasser, and Wilfried Schmitt

1. Introduction

Mixing in stirred tanks is a widely used operation aiming to decrease the degree of non-uniformity of any system to which it is applied. Its engineering arrangement and realisation always depends on the system properties. The mixing can be employed to improve the mass transfer along with the heat transfer if needed. When a chemical reaction is designed to occur in a stirred vessel, reactants would require to be successively well mixed for reaction to proceed. If the reaction is relatively fast, the selectivity and the rate and yield will also be determined by the mixer performance.

Modelling a stirred tank using computational fluid dynamics (CFD) requires consideration of many aspects of the process [1]. First of all, the geometry of the stirred tank, even in the case it is very complex, needs to be described by a computational grid, required by the computational model. Second, the motion of the impeller should be treated in a special way, especially when the tank contains baffles or other stationary internals.

In the modelling of the stirred tank reactor two major advance steps have been completed: passive tracer and two-phase gas-liquid mixing. Although, in the case of the passive tracer, the numerical predictions of the liquid phase mixing were the primary task, the system was treated as two-phase flow in order to study the free surface deformation and its impact on the flow. A visualisation technique was applied to obtain an experimental observation of the process to be compared with the numerical predictions obtained using CFX 5.7 CFD software. The two-phase mixing in the stirred tank was studied under the mechanical agitation of a gas-inducing turbine. An X-Ray cone-beam tomography was applied to experimentally assess the process. The numerical predictions for the gas-phase distribution were validated against the experimental observations. The theoretical assessment of the two-phase flow was performed using CFX 10.

2. Experimental set-up

A laboratory scale Büchi Ecoclave 1.6 litre tank, schematically presented in Figure 1, was used to perform the mixing experiments and the numerical simulations. The tank with a diameter of 82 mm was mechanically agitated by a Pfaudler impeller, employed for the passive mixing, and by a gas-inducing turbine stirrer for two-phase flow mixing. The Pfaudler impeller with a diameter of 58 mm and the gas-inducing turbine with a diameter of 45 mm were both mounted at a clearance of 27 mm. In the case of the passive tracer mixing, the liquid level height was chosen to be equal to the tank diameter and in the case of the two-phase flow mixing it was 232 mm.

A video technique was applied to experimentally study the passive tracer mixing process. The initially stratified lighter (alcohol) coloured component and the heavier (water) transparent one were brought into motion by the rotating impeller. The mixing process was recorded on a digital camcorder and subsequently the images were digitally processed. To obtain the colour-calibration curve, the procedure was repeated for a number of different initial concentrations

of the lighter liquid. Different points, at which the optical distortions were minimal, were chosen to acquire the mixing curves of the concentration change in time. The comparison points were located close to the impeller shaft and the tank wall.

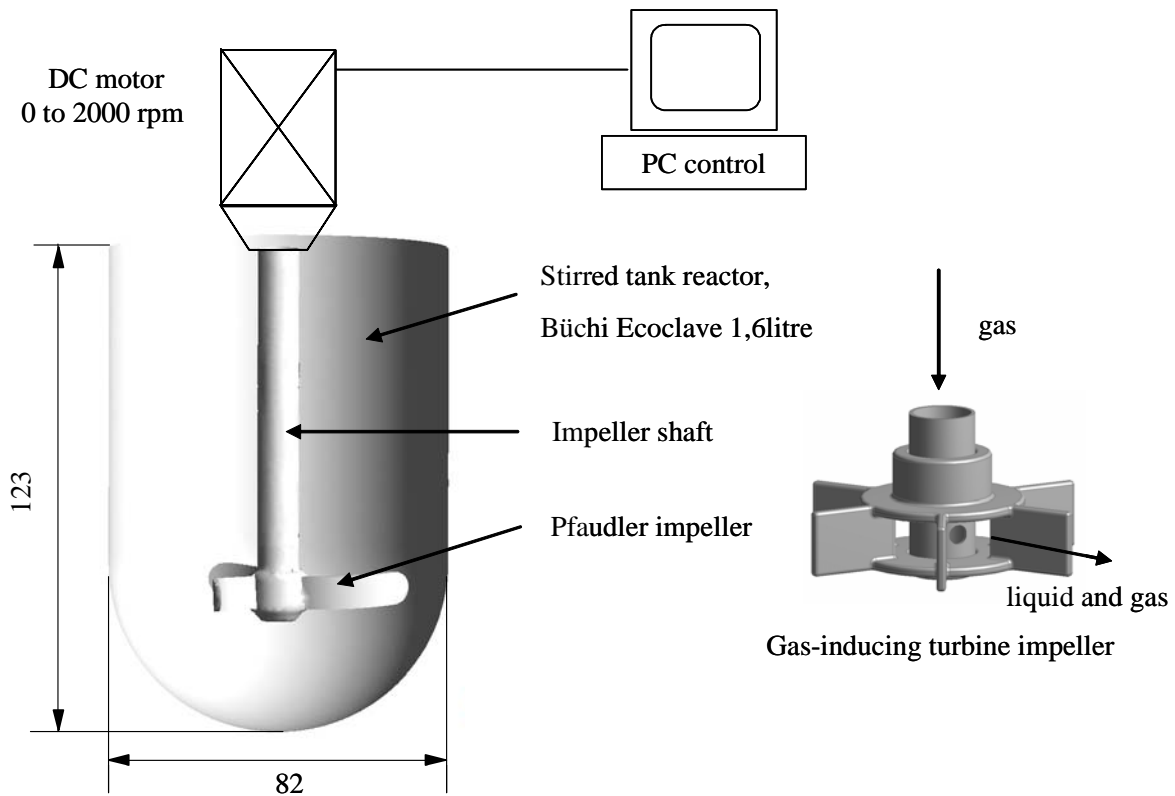


Fig. 1: Schematic view of the experimental rig and the gas-inducing turbine

The system under investigation comprises air as gas phase and isopropanol as liquid phase at room temperature. Both isopropanol and air, which were initially stationary, were brought into motion by the rotating impeller. Measurements carried out with the X-Ray cone beam tomography, were taken at five different stirrer speeds with thresholds of 50 rpm starting from 1000 rpm at which the gas inducement occurs for the given operating conditions. The final stirrer speed was 1200 rpm at which the central vortex virtually reaches the impeller. Additionally, video observations, performed with a digital camcorder, were taken to study the unsteady behaviour of the central vortex.

The X-Ray cone-beam tomography is a potential method to measure the phase distributions in stirred vessels. Three-dimensional information can be gathered within only one tomographic scan [2]. The reconstruction of a rotationally symmetric distribution field is even possible from a single radiographic image. Such an experimental approach was carefully examined and applied to obtain the quantitative measurements of gas-fraction profiles in a stirred tank reactor. Additionally, a moving slit technique was adapted to estimate the inherent scattered radiation offset, which emerges while uncollimated X-Rays penetrate the fluid-filled tank. An additional reference measurement was introduced and used to remove beam-hardening artefacts. An absolute quantification was possible due to the knowledge of the ratio of the fluids and the reference-materials X-Ray absorption coefficients. Phantom measurements inside the vessel were conducted for performance evaluation. A systematic measurement error

of less than 1.5% absolute gas fraction for local gas fractions up to 30% was achieved while maintaining a spatial resolution of better than 1 mm.

3. Theoretical assessment of the mixing process in the stirred tank reactor

3.1 Passive tracer mixing

The passive tracer mixing simulations were carried out to numerically assess the mixing behaviour of different density liquids. Such a process is a common operation in the process industry and occurs when a higher density liquid is injected into a tank filled with a lighter density one or in the case of impeller malfunctioning when the different density liquids can get stratified. The process might prove to be of significant importance, particularly in the case of reacting liquids for large-scale reactors operating in the industry.

The CFD analyses were performed with the CFX 5.7 numerical package. Although the non-baffled vessel exhibits an axi-symmetric behaviour on a macro-mixing scale, the process was regarded as three-dimensional in order to demonstrate the local instabilities associated with the blade passage. The dynamic mixing behaviour of two miscible liquids with different densities was numerically predicted from initially stratified conditions to complete mixing. Time steps of 0.01 seconds were found to satisfy the convergence criteria for the transient run. The gas phase was involved in the simulations to investigate the effect of the free surface deformation on the mixing process, which was modelled using the free surface model [3]. A single velocity field was assumed for the two-phase flow, imposed by the homogeneous two-phase flow model [3]. The multicomponent model [3] was applied to the liquid phase in which the two different density liquids were present. The suitability of the different turbulence models was also addressed but the $k-\epsilon$ turbulence model was finally employed. In order to obtain grid independent results, the numerical simulations were performed on different size grids. However, the grid elements size, in total just above 400 000 for the whole tank, was kept relatively low because of the dynamic behaviour of the liquid surface central vortex. Two domains, one stationary and one rotating with Transient Rotor interaction scheme [3], were used to represent the tank with the rotating impeller. Additionally, the impeller acceleration from stationary to 200 rpm was modelled.

A comparison between the experimentally observed and theoretically predicted integral mixing curves at four different locations is presented in Figure 2. Since the video visualisation technique provides integral mixing curves at the chosen locations, the predicted concentration values were exported and averaged along lines going through the tank and corresponding to these locations. The points located in the initially stratified isopropanol layer are not presented here since the colour change in time is strongly influenced by the liquid phase surface deformation. It is visible from Figure 2 that the CFD predictions qualitatively reproduce the visual observations. In all of the mixing curves, the mixing rate of the different density liquids is a bit over predicted, which indicates that the density layer is more rapidly destroyed when compared to the visual observations. Closer match between the experiment and the simulations is demonstrated for the lower part of the tank beneath the impeller (Figure 2(b)), which might be due to the radial pumping characteristics of the impeller. In this case, relatively stagnant zone, regarded as low mixing rate one, is present below the impeller because of the lack of baffles. This property of the non-baffled tank is captured by both the experiment and the numerical prediction. The complete mixing is predicted to happen at 13 seconds after the impeller start up, close to the experimentally measured value of 15 seconds.

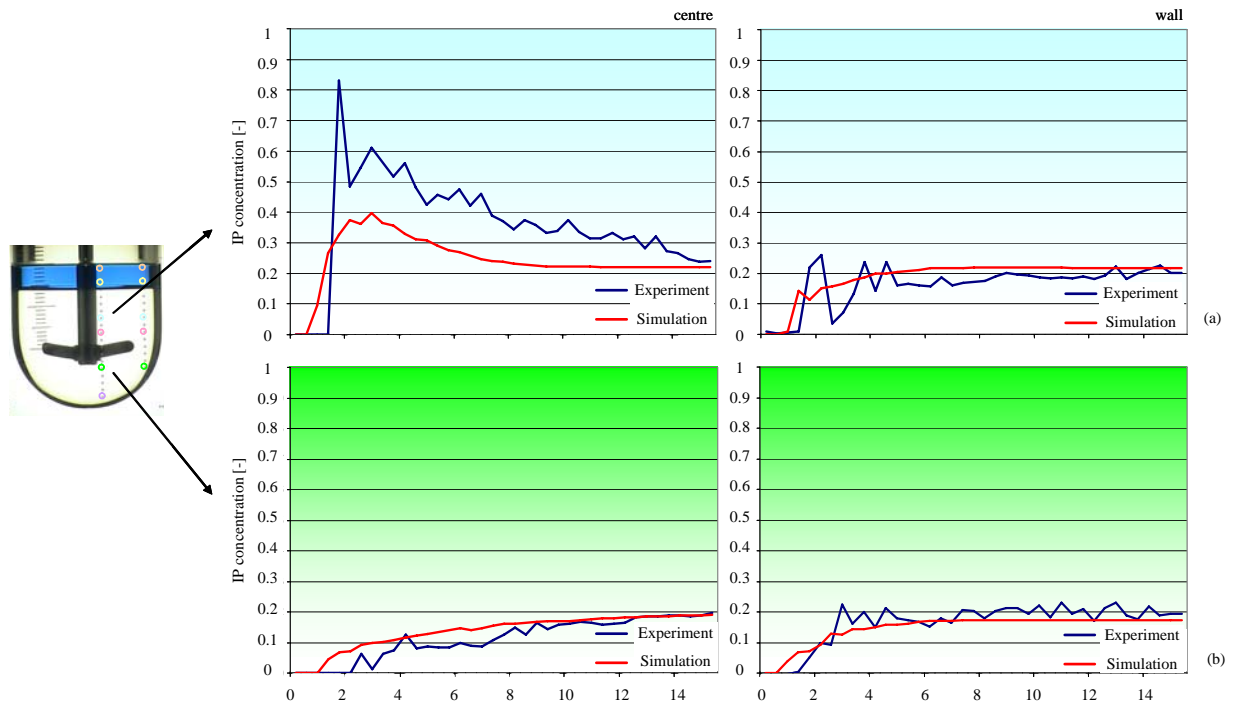


Fig. 2: Integral mixing curves at different locations

3.2 Two-phase flow in the stirred tank reactor

Gas-liquid mixing in stirred tank reactors is a common process in the industry. It is regarded as one of the most difficult to tackle because of its complexities in terms of flow regimes and multiphase operations. Traditionally the gas-liquid stirred tank reactor is equipped with an impeller responsible for dispersing the gas phase, which is usually supplied via a single dip pipe or a ring sparger mounted beneath the impeller. The gas-inducing impellers provide an alternative gas injection, in which case the gas is sucked via a hollow shaft and fed directly into the stirrer region. More gas bubbles are broken up into small bubbles when such a configuration is applied, which consequently provides higher mass transfer.

The computational fluid dynamics analyses of the stirred tank reactor were performed with CFX 10.0 numerical software. A full three dimensional approach was adopted in order to capture the spatial behaviour of the central vortex. Four steady state simulations at stirrer speed from 200 to 800 rpm were conducted to obtain an initial guess of the flow field and the phase distribution for the simulation at 1000 rpm. The numerical predictions above 1000 rpm used the previous simulation results as an initial guess. Starting from 1000rpm, five simulations were performed at stirrer speed thresholds of 50 rpm to be compared with X-Ray cone-beam tomography measurements. The tetrahedral mesh with above 1500000 elements was globally refined since a detailed view in the whole geometry is required. The stirred tank was broken down into four domains, three rotating and one stationary. A Frozen Rotor interaction scheme was used in the simulations to bond the multiple frames of references domains. The inhomogeneous two-phase flow model with the particle transport model was applied to the system with momentum transfer described by the drag force and turbulence transfer modelled by Sato enhanced eddy viscosity model [4]. The gas phase was modelled as dispersed fluid with a mean diameter of 1 mm and the liquid phase as continuous fluid. Different turbulence models and their suitability were considered for the liquid phase. The

gas-phase turbulence was modelled using the dispersed phase zero equation. The flow was regarded as buoyant and implemented using the density difference model.

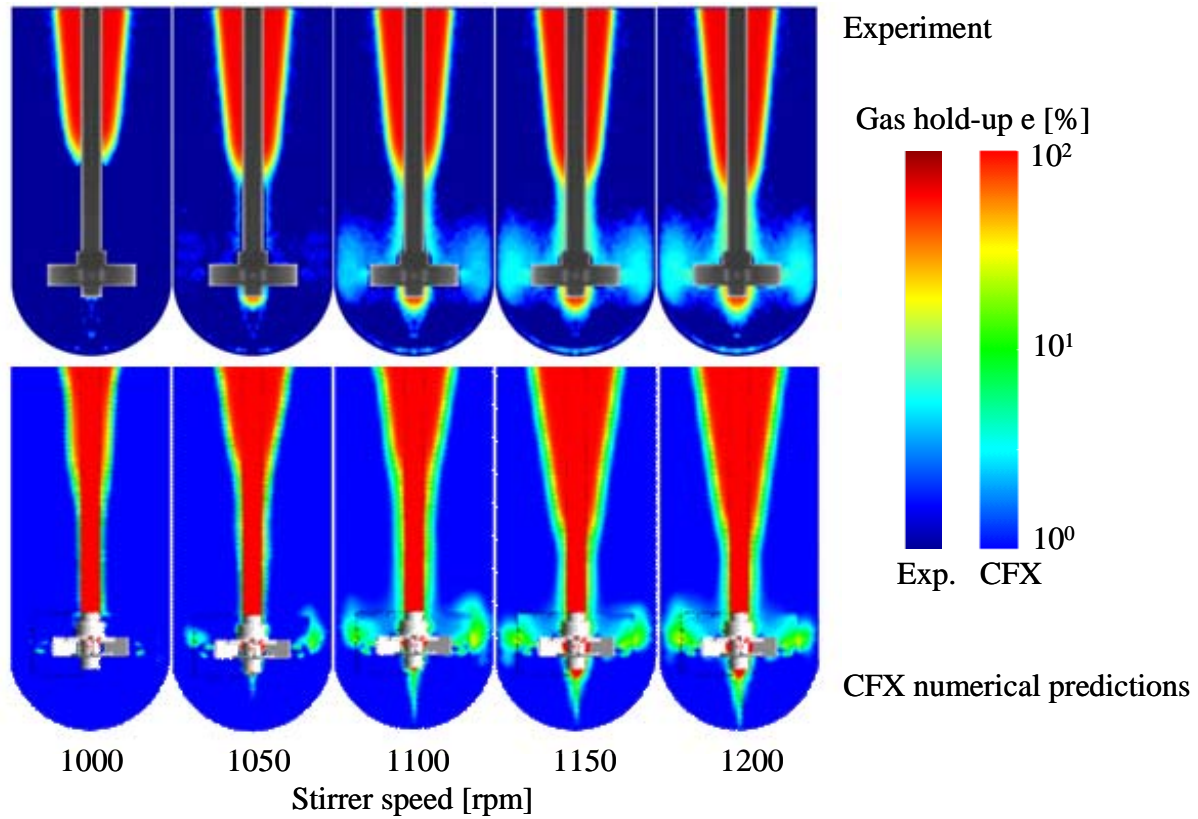


Fig. 3: Gas hold-up in stirred tank reactor at different impeller speeds

A comparison between the experimentally measured and numerically predicted gas hold-up distribution at different stirrer speed is presented in Figure 3. It is clearly visible that the CFD predictions closely mimic the experimental observations. The central vortex depths as well as its spread out closely correspond to the ones experimentally observed except for the lower stirrer speeds of 1000 and 1050 rpm, for which the dept is slightly under predicted. For impeller speed above 1050 rpm, the predicted central vortex depth and shape boundaries match exactly the experimentally measured ones. At stirrer speed of 1050 rpm and above, gas is captured beneath the impeller shaft as indicated in both the experimental and numerical results. It is clearly indicated in Figure 3 that the gas hold-up significantly increases with the stirrer speed as more gas gets induced by the rotating impeller. A slightly higher gas hold-up beneath the impeller shaft is experimentally measured. This might be associated with the time-spatial averaging procedure applied in the experiment.

4. Conclusions

The hydrodynamics of the different density liquids system is of particular importance for many chemical and biochemical reactions engineered to take place in stirred tank reactors. Although the initial conditions were to some extent idealised in order to avoid some complications raised by the presence of an injection, the studies showed strong influence of the density difference on the homogenisation. Such so called idealised conditions, however, also might occur in the stirred vessel, especially in the case of impeller malfunctioning. In case of impeller stoppage, i.e. breakdown, different density liquids present in the vessel might

get stratified. The CFD is also capable of capturing the two-phase flow in detail, which can provide valuable information for the industry. In particular, the spatial gas phase distribution, which can also have time-dependent behaviour, can have a crucial impact on the reactor performance. Different local gas hold-up in the vessel would determine different local mass transfer, which consequently would affect reaction rates and/or selectivity. The above described results demonstrate the potential of the CFD to assess in detail the fluid flow phenomena in the stirred tank reactor. The CFD based software in that sense can prove to be an essential tool for the reactor design, optimization and scale-up as well as for hazard analyses.

References

- [1] E. Marden Marshall and A. Bakker (2002), Computational Fluid Mixing, Fluent Inc., Lebanon, New Hampshire, USA
- [2] S. Boden, U. Hampel, M. Speck (2005), Quantitative Measurement of Gas Distribution in a Stirred Chemical Reactor with Cone-Beam X-ray Computed Tomography, Proceedings of the 4th World Congress on Industrial Process Tomography (05.-08.09.2005), Aizu, Japan), p. 813-818
- [3] ANSYS CFX User Manual (2005), ANSYS Inc.
- [4] Y. Sato and K. Sekoguchi (1975), Liquid velocity distribution in two-phase bubbly flow, Int. J. Multiphase Flow, 2, p79

BUOYANCY DRIVEN MIXING STUDIES OF NATURAL CIRCULATION FLOWS AT THE ROCOM FACILITY USING THE ANSYS CFX CODE

Thomas Höhne, Sören Kliem, Ulrich Rohde, and Frank-Peter Weiss

1. Introduction

A small break loss of coolant accident (SBLOCA) can lead to the interruption of one-phase flow natural circulation in the loops of a pressurized water reactor (PWR). This could happen when the high pressure safety injection (HPSI) should be partly unavailable. In such cases, a part of the decay heat is removed from the core in the reflux-condenser mode. This can lead to the production and accumulation of low borated coolant in the primary circuit. The primary system will be filled up again and one-phase natural circulation re-establishes. The one phase natural circulation forwards the under-borated condensate towards the core.

By theoretical analyses using the thermal-hydraulic system code ATHLET, the Gesellschaft für Reaktorsicherheit (GRS) revealed a special scenario which could possibly occur after a SBLOCA in the hot leg and safety injection into two hot legs [1]. This scenario was taken for CFD validation.

In addition, for a better understanding of the basic phenomena of boron dilution in pressurized water reactors (PWR) experimental investigations were performed in two test facilities. These are the Primärkreislauf (PKL) facility, operated by Framatome ANP [2] and the Rossendorf Coolant Mixing Model (ROCOM), operated by Forschungszentrum Rossendorf e.V. A detailed description of the ROCOM experiments is given in [3]. The PKL-system test on the scenario described in [1] showed a considerably different behaviour of the condensate transport towards the RPV: in that PKL test, the restart of natural circulation was slower and the slugs were transported at lower velocities and - important - at different times towards the RPV. The PKL and ROCOM experiments revealed, that the scenario calculated with ATHLET is conservative with respect to mixing.

For the ANSYS CFX code validation a ROCOM test case with density driven coolant mixing was selected from the test matrix (see Table 1). The experiment and the CFD-calculation described in this paper were performed to investigate the coolant mixing in the reactor pressure vessel (RPV). Similar analyses using the CFD-Code FLUENT were performed by Schaffrath et al. [4].

2. Rossendorf Coolant Mixing Model (ROCOM)

The Rossendorf Coolant Mixing Model (ROCOM) was constructed at the Forschungszentrum Rossendorf e.V. (FZR) for the investigation of coolant mixing in PWR [5,6]. The ROCOM facility has four loops each with an individually controlled pump (see Fig. 1). This allows to perform tests in a wide range of PWR flow conditions from natural convection flow up to forced convection flow at nominal flow rates including flow ramps (e.g. due to pump start up). ROCOM is operated with water at ambient temperatures because the RPV mock-up and its internals are made of perspex. Special attention was given to the scaling of all components that significantly influence the velocity fields. These are the core barrel with the lower support plate and the core simulator, the perforated drum in the lower plenum and the inlet and outlet nozzles of the main coolant lines with diffuser elements.

During inherent boron dilution in the scenario described in the introduction, the slug that accumulate in the loop could have a higher temperature and a lower density. Additionally the boron content influences the fluid density. In ROCOM this density difference is adjusted by the addition of ethyl alcohol. Additionally, the fluid is traced by adding minimum elements of salt, which do not affect the density.

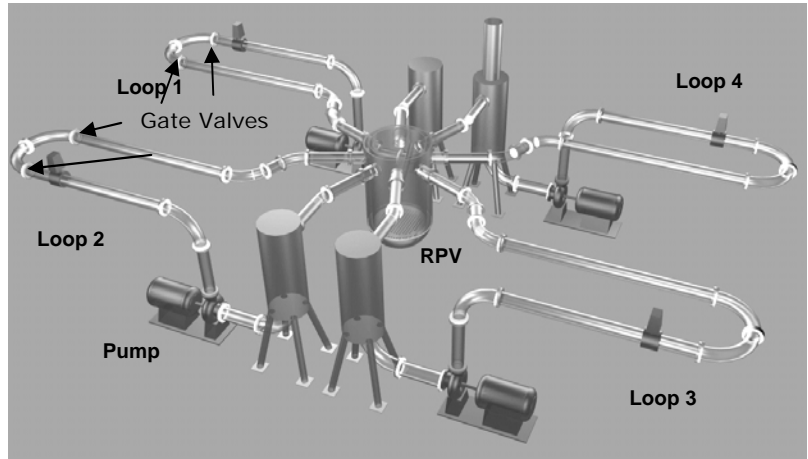


Fig. 1: Scheme of the ROCOM test facility

The acquisition of the concentration fields is performed with high spatial and temporal resolution measurements of the tracer concentration. For that purpose FZR applies self developed wire mesh sensors which measure the electrical conductivity between two orthogonal electrode grids [7].

Beside the measurements in the cold legs, two further wire-mesh sensors with 4 radial and 64 azimuthal measuring positions in the lower and upper downcomer and with 193 conductivity measurements at the core inlet were applied to the test facility. All sensors provide 200 images per second. Because a measuring frequency of 20 Hz is sufficient, ten successive images are averaged into one conductivity distribution. The measured conductivity values are transformed into a dimensionless mixing scalar $\Theta_{x,y,z}(t)$. It is calculated by relating the local instantaneous conductivity $\sigma_{x,y,z}(t)$ to the amplitude of the conductivity change in the cold leg of the loops with the slugs.

$$\Theta_{x,y,z}(t) = \frac{\sigma_{x,y,z}(t) - \sigma_0}{\sigma_1 - \sigma_0} \quad (1)$$

Θ represents the contribution of the coolant from the initial slugs to the mixture at the given position x,y,z . The upper reference value σ_1 in (1) is the conductivity in the initial slugs between the gate valves. The lower reference value σ_0 is the initial conductivity of the water in the test facility before the valves are opened. More details about the facility, the measurement devices, and the experiments performed earlier can be found in [5].

3. The experiments

Based on ATHLET-calculations in [1], the following boundary conditions were defined for the experiments: Two loops are working at a stationary level of 5 % of the nominal flow rate. A slug of de-borated water is located in both of the resting loops between the gate valves. The volume of these de-borated slugs corresponds to the volume of the whole loop seal and a part of the steam generator outlet chamber. This is 7.2 m^3 in each loop. In these loops, the circulation starts simultaneously and reaches a value of 6 % of the nominal flow rate. Three different flow ramps were considered (see table 1). Further, according to the thermo-hydraulic

calculations, a density difference exists between the de-borated slugs and the ambient coolant. This is due to the higher temperature of the slug in comparison to the ambient coolant.

The concentration difference between borated and de-borated coolant creates an additional density difference. To investigate the influence of the density difference, it was decided to vary this difference between 0 and 2 %. On that basis the following experimental matrix was created:

Table 1: Matrix of the experiments

	Density difference [%]	0	0.25	0.5	1.0	2.0
N°	ramp period [s]					
1	25	x	x	x	x	X*
2	50	x	-	-	-	x
3	75	x	-	-	-	x

*The boundary conditions of this experiment were used for code validation.

4. CFD Code and sensitivity analysis according to Best Practice Guidelines

The CFD code for simulating the mixing studies was ANSYS CFX [8]. ANSYS CFX is an element-based finite-volume method with second-order discretisation schemes in space and time. It uses a coupled algebraic multigrid algorithm to solve the linear systems arising from discretisation. The discretisation schemes and the multigrid solver are scalably parallelized. ANSYS CFX works with unstructured hybrid grids consisting of tet, hex, prism and pyramid elements.

4.1 Numerical diffusion, nodalisation, time step size and turbulence modelling

In the calculations, the High-Resolution (HR) discretisation scheme of ANSYS CFX was used to discretise the convective terms in the model equations. A second-order implicit scheme was used to approximate the transient terms. The time step size used was 0.1 s. The ethyl alcohol water mixture, which had a lower density, was taken as a tracer. It was modelled with the multi-component model of ANSYS CFX.

In a multi-component flow, the components share the same velocity, pressure and temperature fields. The properties of multi-component fluids are calculated on the assumption that the constituent components form an ideal mixture. The ethyl alcohol water mixture is modelled as a component with different density and viscosity compared to pure water. The mass fraction of the ethyl alcohol water mixture can be directly related to the mixing scalar described in Eq. (1). The Reynolds stress model proposed by Launder et al. [9] was used in combination with an ω -based length scale equation (BSL model) to model the effects of turbulence on the mean flow. Buoyancy production terms were included in the Reynolds stress equations and in the length-scale equation.

A transient time of 150 s was simulated. The calculations on 8 processors took 2 weeks of a 100-processor RedHat LINUX cluster (dual CPU compute nodes XEON, 3.2 GHz, ~1.3 Gflops, each containing 2 GBytes RAM).

4.2 Grid Generation

The mesh was generated with the ICEM CFD software. It consisted of 3.6 million nodes and 6.5 million hybrid elements (Fig 2). The mesh was refined at the perforated drum, in the lower support plate and at the wall regions of the cold legs. The downcomer and nozzle region was discretized with hexahedral cells (Figures 3 and 4).; tetrahedral elements were used for the lower plenum (Figures 3 and 5).

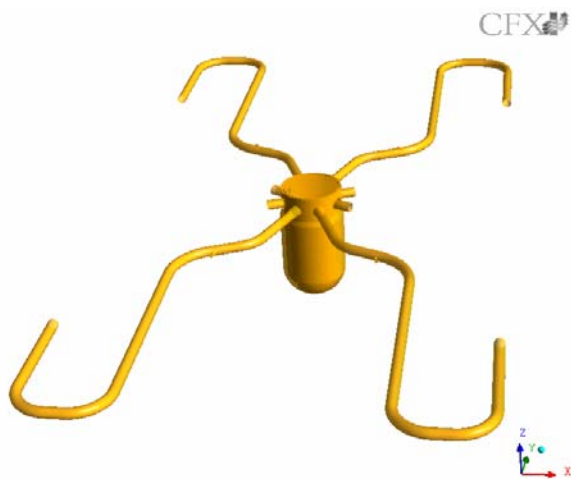


Fig. 2: Total flow domain

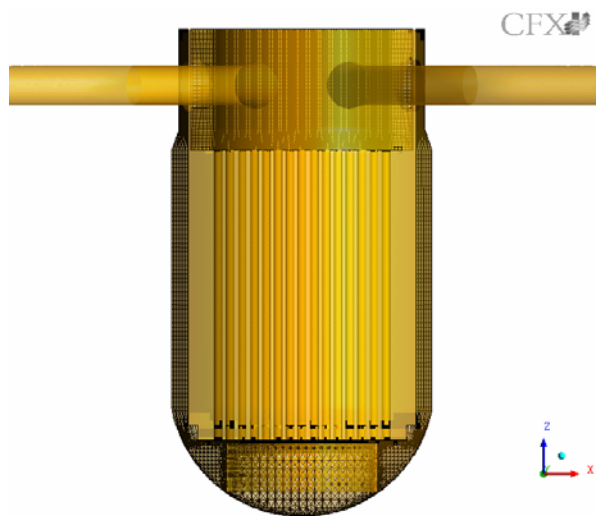


Fig. 3: Hybrid mesh, vertical cut

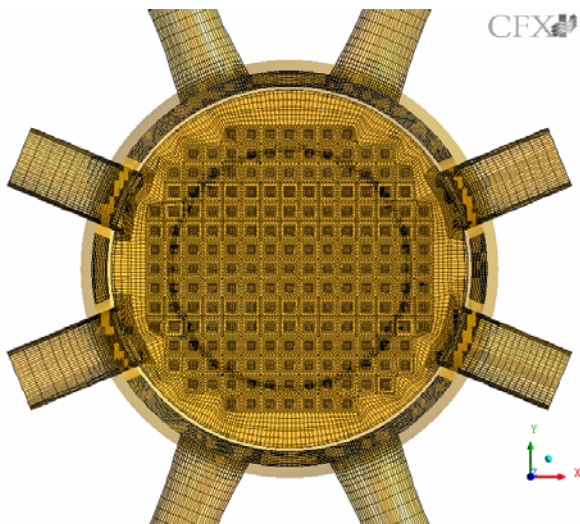


Fig. 4: Horizontal cut, inlet nozzle plane (hexa)

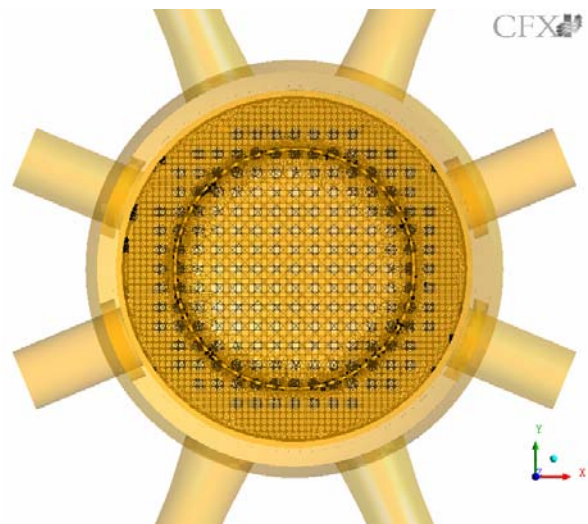


Fig. 5: Horizontal cut, lower plenum (tetra)

4.3 Boundary Conditions

For CFD validation a test from the matrix (Table 1) was taken, which is characterized by flow rates which are typical for natural convection conditions, quite large density differences between the two fluids and a steep flow ramp in the test run.

The test was performed under the following initial and boundary conditions which were also adjusted in the ANSYS CFX calculation: the loops 3 and 4 are operated with 5% of the nominal flow rate (9.25 m³/h), slugs of water with a 2% lower density are introduced in the bends between the gate valves in loop 1 and 2 and the flow rate in loop 1 and 2 is increased from 0 to 6% of the nominal flow in 18 s.

5. Results

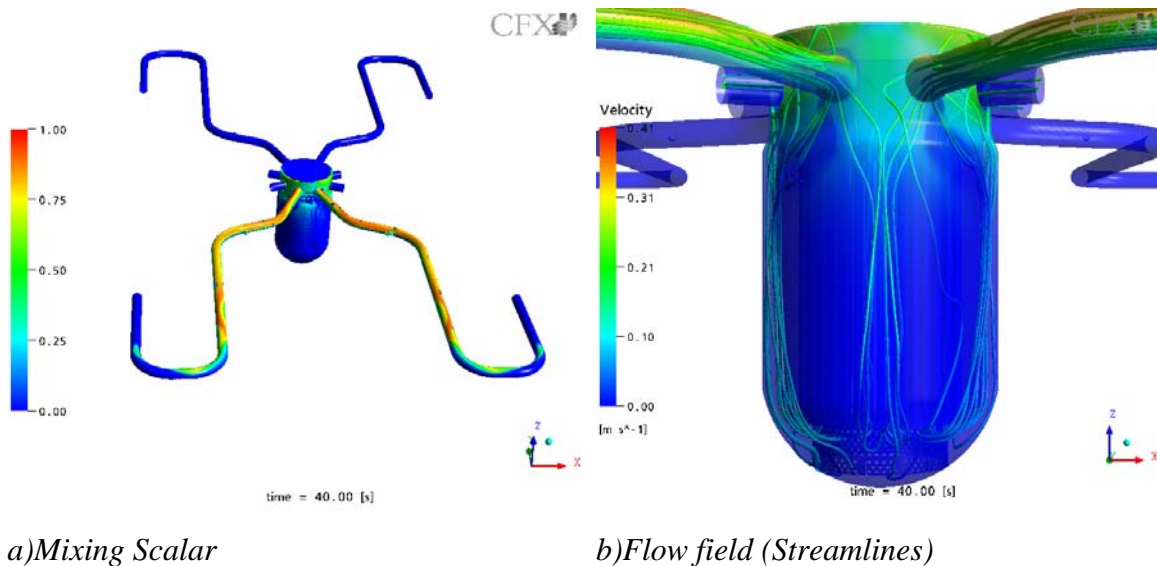
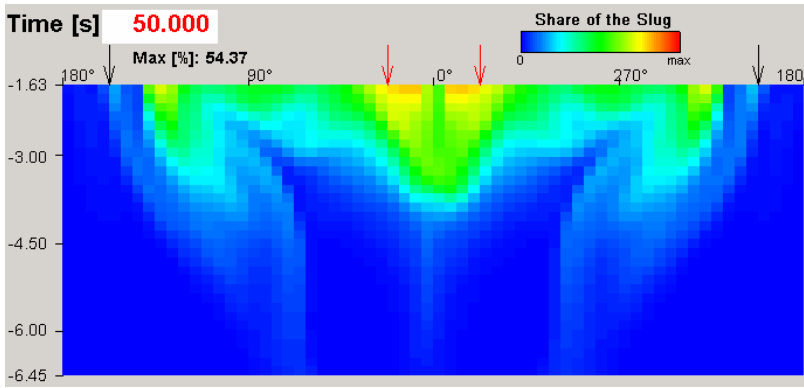


Fig. 6: Instantaneous mixing scalar distributions and streamlines representing the velocity field at $t=40s$

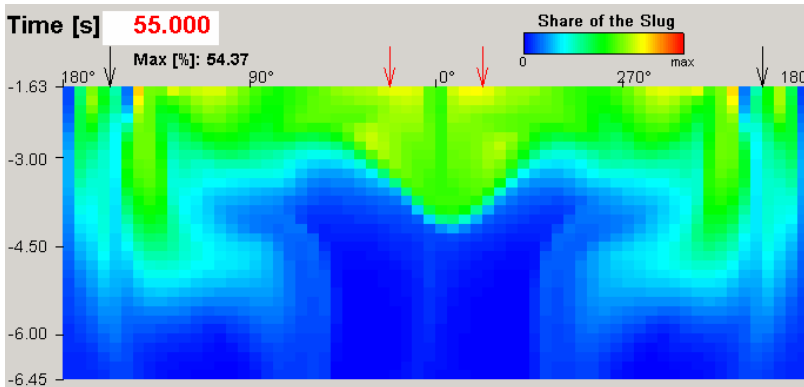
Fig. 6 shows the ANSYS CFX simulation of the transport of the slug with a density difference of 2% in the cold leg and the RPV mock-up at $t=40s$ after the start of the simulation, Fig. 7 shows the mixing scalar distribution in the unwrapped downcomer at $t=50, 55$ and 62 s.

The slugs with the lower density are transported through the cold legs towards the downcomer. The flow stratifies on the way to the RPV mock-up inlet. The lower density coolant flows in the upper part of the pipe cross section area and the higher density coolant in its lower part. After 50 s the slug has reached the upper measuring level of the downcomer. Already at this level, nearly the whole cross section of the downcomer is filled with lower density coolant. After 60 s the lower density coolant reaches the lower measuring level of the downcomer. The lower density coolant is detected first at the opposite side to the inlet nozzles of loop 1 and 2 (Fig. 7).

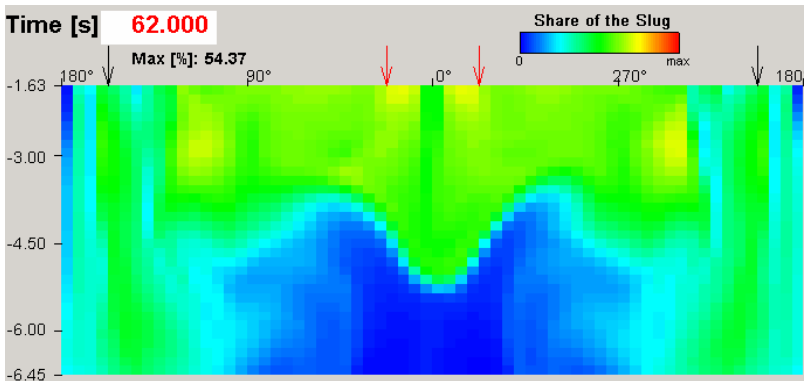
This phenomenon can be explained as follows: the low density coolant rises after introduction into the RPV mock-up above the inlet nozzle level. Then it flows in circumferential direction to the inlet nozzles of the loops 3 and 4. Here the lower density coolant mixes with the higher density coolant of the loops 3 and 4 and flows downwards. At the lower measurement level of the downcomer the maximum of the mixing scalar has decreased approx. by a factor of 2.5. With ongoing time the mixing scalar in the lower level downcomer measuring level does not increase significantly.



Mixing scalar ($t=50s$)



Mixing scalar ($t=55s$)



Mixing scalar ($t=62s$)

Fig. 7: Mixing scalar distribution in the unwrapped downcomer

part). The arriving time of the slug is well predicted. The calculation shows already in the cold leg a more intense mixing behaviour than it is observed in the experiment (smaller maximum values of the mixing scalar at $t=50s$).

Fig. 9 shows the circumferential distribution of the mixing scalar at the outer wall of the cold leg sensor at $t=40s$. The 0° -position is at the bottom of the cold leg. In this graph the calculations reflect the observed stratification of lighter water (tracer) on top of the heavier water of the experiment.

Two circumferential sensor positions in the middle of the upper and lower downcomer sensor plane were selected for comparison of data and predictions (Fig. 10). The circumferential distribution of the mixing scalar at the upper downcomer sensor at 40s shows the arrival of

A quantitative comparison of experiments and calculations is usually difficult, because turbulent, natural convection flows are characterised by hydraulically instable conditions and small driving forces, what obviously yield in non-stationary flow fields. The general agreement of the courses of the dominant quantities is thus the only way to assess a calculation. Local discrepancies in the transient courses are inevitably present in such comparisons due to statistical turbulent mixing effects.

In general, the code ANSYS CFX represents correctly the instantaneous azimuthal distribution of the mixing scalar in the downcomer. Discrepancies can not only be addressed to code and modelling differences but also to the instationary and stochastic character of turbulent flow.

Fig. 8 shows the mixing scalar at one local measurement point (position 0312 at the upper

the slug in the upper downcomer below the inlet nozzles of the loops 1 and 2. The shape of the perturbations of the experiment and simulation is almost identical. The distributions of the mixing scalar (experiment, calculation) at the lower downcomer sensor are plotted at $t=70s$ and show a maximum of the tracer at the opposite side of the two starting loops, which indicates, that the tracer transport is enhanced by fluid entrainment from the running loops 3 and 4.

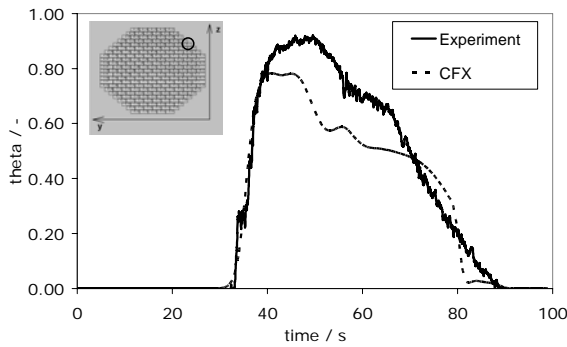


Fig. 8: Time dependent local mixing scalar at pos. 0312 of the cold leg inlet nozzle sensor

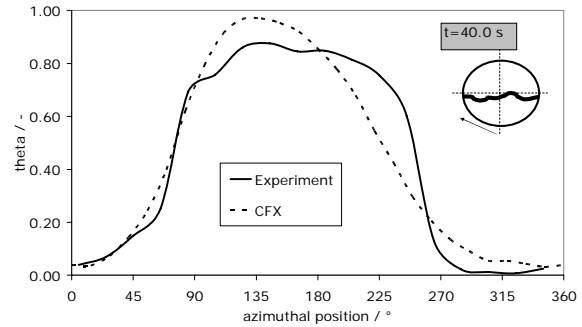
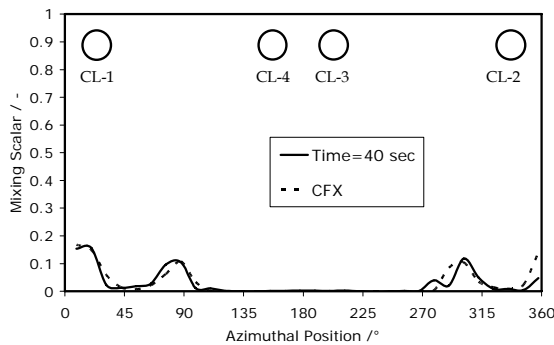
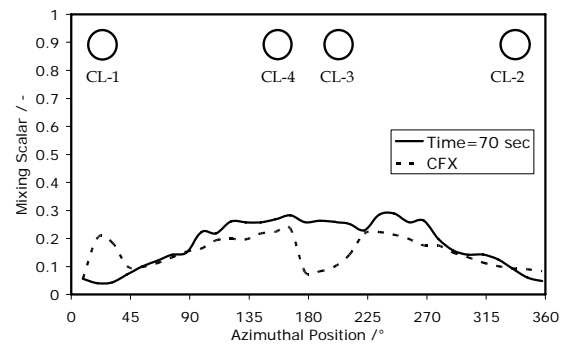


Fig. 9: Azimuthal mixing scalar distribution at $t=40s$ at the outer radius of cold leg inlet nozzle sensor



a) Mixing scalar at upper downcomer sensor at $t=40s$



b) Mixing scalar at lower downcomer sensor at $t=70s$

Fig. 10: Instantaneous azimuthal mixing scalar distributions for 32 positions of the upper and lower downcomer sensor

6. Summary

Mixing after injection of de-borated slugs into the RPV was investigated under simulated natural circulation conditions at the four loop 1:5 scaled test facility ROCOM. The corresponding boundary conditions were derived from calculations with the system code ATHLET for a postulated hypothetical SB LOCA scenario.

In the experiments, the period of time of the flow ramp and the initial density difference between the slugs and the ambient coolant was varied. An experiment with 2% density difference between the de-borated slugs and the ambient coolant was used to validate the CFD software ANSYS CFX. A Reynolds stress turbulence model was employed to model the effects of turbulence on the mean flow. A hybrid mesh consisting of 3.6 million nodes and 6.4 million elements was applied. The experiment and CFD calculation show a stratification in the downcomer. The less dense slugs flow around the core barrel at the top of the downcomer.

On the opposite side the lower borated coolant is entrained by the colder safety injection water and transported to the core.

The ANSYS CFX calculations show a good qualitative agreement with the experimental data. Differences between the predicted and measured concentration fields occur at some local positions. The obtained experimental and numerical results can be used for further studies of the core behaviour using coupled thermal-hydraulic and neutron-kinetic code systems.

References

- [1] Pointner, W. and Wohlstein, R. Initiating events and scenarios of boron dilution transients (in German). Annual meeting on Nuclear Technology 2003.; Proc. Of the Topical session: Experimental and theoretical investigations on boron dilution transients in PWRs. pp. 5-22. 2003.
- [2] Hertlein, R., Umminger, K., Kliem, S., Prasser, H.-M., Höhne, T. and Weiss, F.-P. Experimental and numerical investigation of boron dilution transients in pressurized water reactors. Nuclear Technology 141, 88 - 106. 2003.
- [3] Kliem S., Höhne, T., Prasser, H.-M., Rohde, U. Weiss, F.-P. Experimental investigation of coolant mixing in the RPV of a PWR during natural circulation conditions. Proceedings of ICONE12, 12th International Conference on Nuclear Engineering, Washington D.C., USA, April 25-29 2004. paper 49424. 2004.
- [4] Schaffrath A., Fischer, K.-C., Hahm, T., Wussow, S. Validation of the CFD Code Fluent by Post Test Calculation of the ROCOM Experiment T6655_21. The 11th International Topical Meeting on Nuclear Reactor Thermal-Hydraulics (NURETH-11), Popes' Palace Conference Center, Avignon, France. Paper: 141. 2005.
- [5] Grunwald, G., Höhne, T., Kliem, S., Prasser, Richter, K.-H., H.-M., Rohde, U., Weiss, F.-P. Versuchsanlage ROCOM zur Untersuchung der Kühlmittelvermischung in Druckwasserreaktoren - Ergebnisse quasistationärer Vermischungsexperimente. FZR Report 348. 2002.
- [6] Höhne, T., Kliem, Prasser, H.-M., Rohde, U. Experimental and numerical studies inside a reactor pressure vessel. 4th ASME/JSME Joint Fluids Engineering Conference, Hawaii, USA. CD-ROM. 2003.
- [7] Prasser, H.-M., Böttger, A., Zschau, J. A new electrode-mesh tomograph for gas liquid flows. Flow Measurement and Instrumentation 9, 111 ff., 1998.
- [8] ANSYS CFX User Manual. ANSYS-CFX. 2005.
- [9] Launder, B.E. - Reece, G.J. - Rodi, W. Progress in the Development of a Reynolds-Stress Turbulence Closure. J. Fluid Mech. 68(3):537-566. 1975.

Acknowledgments

The project this paper is based on was funded by the Nuclear Special Committee "Plant engineering" of VGB PowerTech (Germany).

GAS-LIQUID FLOW AROUND AN OBSTACLE IN A VERTICAL PIPE - EXPERIMENT AND COMPUTATIONAL FLUID DYNAMICS SIMULATION

Horst-Michael Prasser, Thomas Frank¹, Mathias Beyer, Helmar Carl, Suleiman Al-Issa, Heiko Pietruske, and Peter Schütz

1. Introduction

In the frame of the TOPFLOW project, vertical pipe flow is experimentally studied in order to develop and validate models for bubble forces as well as for bubble coalescence and fragmentation in a gas-liquid two-phase flow. After a large number of experiments in plain vertical pipes [1, 2], which are the basis of the development for a multi-bubble size model for ANSYS CFX 10.0, the large test section with a nominal diameter of DN200 (Fig. 1) was used to study the flow field around an asymmetric obstacle (Fig. 2). This is an ideal test case for the Computational fluid dynamics (CFD) code validation,

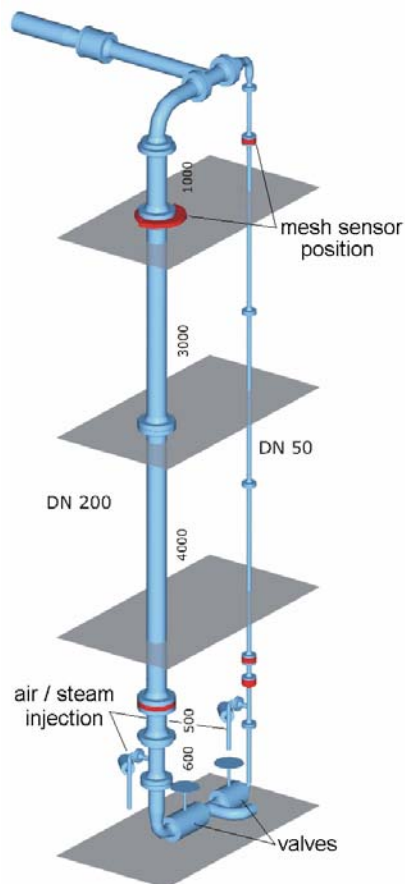


Fig. 1: Vertical test section DN200 of TOPFLOW

since the obstacle creates a pronounced three-dimensional two-phase flow field. Curved stream lines, which form significant angles with the gravity vector, a recirculation zone in the wake and a flow separation at the edge of the obstacle are phenomena widespread in real industrial components and installations, like bends, T-junctions, valves and safety valves. It has to be shown that the CFD-code predicts these phenomena well, after it has been equipped by new models, developed in simpler experimental geometries.

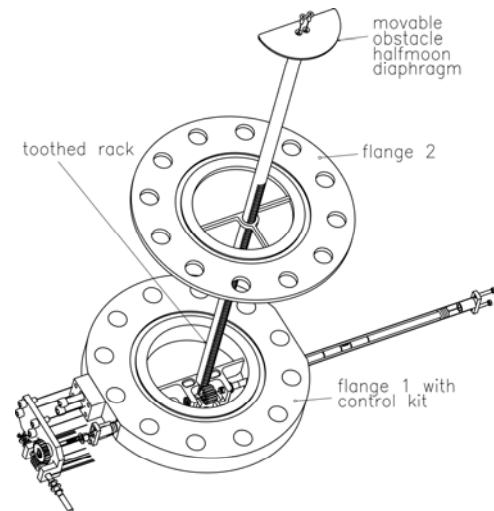


Fig. 2: Movable obstacle with drive support for TOPFLOW

Recently, test series were performed with an air-water flow at ambient conditions as well as with a steam-water mixture at a saturation pressure of 6.5 MPa [3]. Before the experiments were commissioned, an ANSYS CFX 10.0 pre-test calculation was carried out for one of the experimental tests.

¹ ANSYS Germany, Staudenfeldweg 12, 83624 Otterfing

2. Test arrangement

The test pipe has an inner diameter of 195.3 mm and a total height of 9 m. Water and gas are supplied from the bottom of the test section. The diaphragm (Fig. 2) is a half-moon shaped disk, the straight edge of which is arranged along the diameter of the pipe, while the circular edge is in a distance of 10 mm from the inner wall of the pipe. The disk is mounted on top of a toothed rod connected to a translation mechanism to change the axial position of the diaphragm.

Both obstacle and moving mechanism can be inverted and mounted either upstream or downstream of the wire-mesh sensor. The sensor was located 6.17 m downstream of the gas injection, when the obstacle was put upstream of the sensor. When the obstacle was put downstream of the sensor, the distance was 5.11 m. The arrangement allows to acquire local instantaneous void fractions from the full cross-section of the pipe with a spatial resolution of 3 mm and a rate of 2.5 kHz [4, 5] within the three-dimensional flow field around the diaphragm. The distance between sensor and diaphragm can be varied from 10 mm to a maximum distance of 520 mm without moving the sensor position, which is essential to perform high-pressure experiments in an efficient way, i.e. without dismantling and rearranging the test facility each time the measuring position has to be changed.

3. Test parameters

Measurements were carried out with an air-water flow at ambient pressure and a temperature of approximately 25 °C as well as with a steam-water mixture under saturation conditions at 6.5 MPa for the superficial velocities shown in Fig. 3. The following distances between diaphragm and mesh sensors were realized: $\Delta z = \pm 520, \pm 250, \pm 160, \pm 80, \pm 40, \pm 20, \pm 15, \pm 10$ mm. Wire-mesh sensor signals were recorded after achieving a steady state for a measuring period of 10 s for each combination of boundary conditions. For each realized combination of superficial velocities data from both air and steam tests are available.

		superficial gas velocity							
		m/s	0.0368	0.0574	0.0898	0.14	0.219	0.342	0.534
superficial water velocity	1.611	075	086	097	108	119	130	141	152
	1.017	074	085	096	107	118	129	140	151
	0.405	072	083	094	105	116	127	138	149
	0.102	069	080	091	102	113	124	135	146

Fig. 3: Test matrix (grey: test points)

4. CFX pre-test calculations

Before the experiments were carry out a pre-test calculation was set-up for the boundary conditions of the air-water test 074 (see test matrix, Fig. 3), which was performed at the superficial velocities $J_L = 1.0$ m/s and $J_G = 0.037$ m/s. Flow conditions correspond to the bubbly flow regime. For the CFD simulation with ANSYS CFX 10.0 the Eulerian two-phase flow model was used [6, 7], assuming that the gaseous phase consists of monodisperse bubbles with a pipe elevation dependent equivalent diameter of 4.8-5.2 mm in order to account for the hydrostatic bubble expansion. Both phases were treated as non-compressible. Bubble drag in accordance to Grace drag law, Tomiyama lift force, Frank's generalized wall lubrication force and the turbulent dispersion force (with Favre Averaged Drag Model) have been taken into account [8]. Bubble coalescence and fragmentation were neglected for this first pre-test simulation, although it can be assumed that bubble fragmentation will take place at the edges of the obstacle and coalescence might become of importance in regions of bubble accumulation i.e. in the wake behind the obstacle.

Steady state simulations with ANSYS CFX 10.0 were performed on two numerical meshes created with ICEM CFD Hexa and consisting of about 119.000 and 473.000 hexahedral mesh ele-

ments. Meshes were generated for half of the TOPFLOW geometry assuming axial symmetry. The flow domain for the CFD simulation consisted of 1.5 m pipe sections up- and downstream of the obstacle. Inlet boundary conditions were set to fully developed two-phase pipe flow profiles for air and water velocities, radial gas volume fraction distribution, turbulent kinetic energy and turbulent eddy frequency. At the outlet cross section of the 3.0 m long pipe section an averaged static pressure outlet boundary condition was used.

5. Experimental results

5.1 Void fraction distribution

The sensor data was used to calculate two-dimensional time-averaged void fraction distributions in the measuring plane. By combining the information from measurements with different distances between sensor and diaphragm, full three-dimensional void distributions around the obstacle were obtained. A centre cut along the axis of the test pipe in a vertical plane perpendicular to the straight edge of the half-moon diaphragm is a very illustrative way to visualize the void fraction field. This was done in Fig. 4 for the field up- and downstream of the diaphragm.

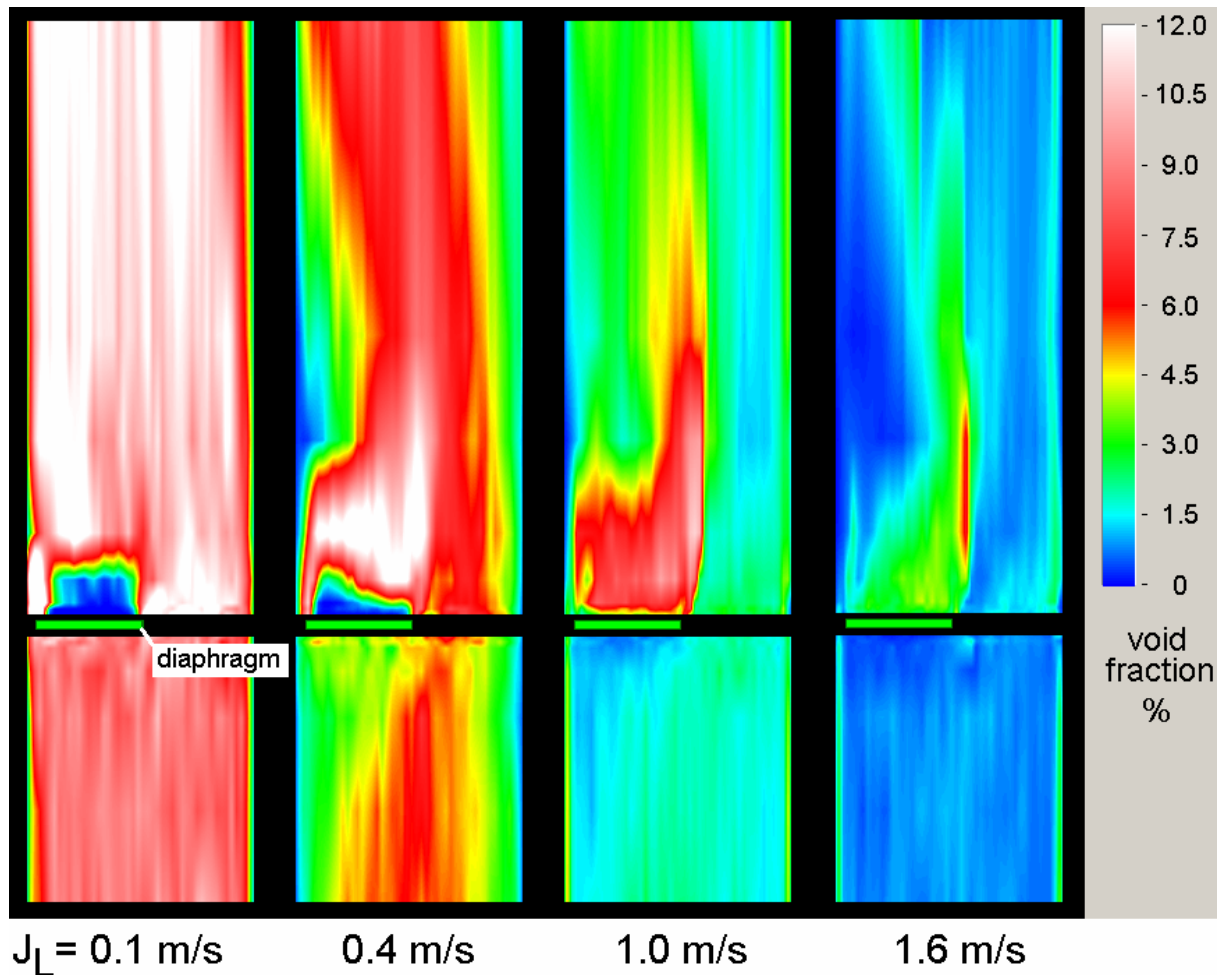


Fig. 4: Change of void fraction profiles up- and downstream of the diaphragm at $J_G = 0.037 \text{ m/s}$ with a variation of the superficial liquid velocity J_L

At small superficial water velocities, there is a region free of bubbles directly behind the obstacle, which vanishes with growing water velocity. The wake, i.e. the zone where a distortion of the

void field is found, grows in downstream direction with increasing liquid velocity, while the overall void fractions naturally decrease.

5.2 Horizontal bubble velocities

In the close vicinity of the eccentric diaphragm, bubbles were found to perform a sideward movement during their passage through the measuring plane of the sensor. This is caused by the bending of the streamlines. An estimation of the horizontal velocity component of the gaseous phase can be made by tracking the center of mass of the projection of each bubble onto the horizontal measuring plane during its passage. First, the coordinates of the centre of mass are calculated for each instant of the passage, followed by a linear regression of the coordinates as a function of time. The slope of the linear fit is interpreted as velocity components in x and y directions. An averaging of the velocity components is made in every measuring point of the sensor for all bubbles passing that point (normalized by void fraction).

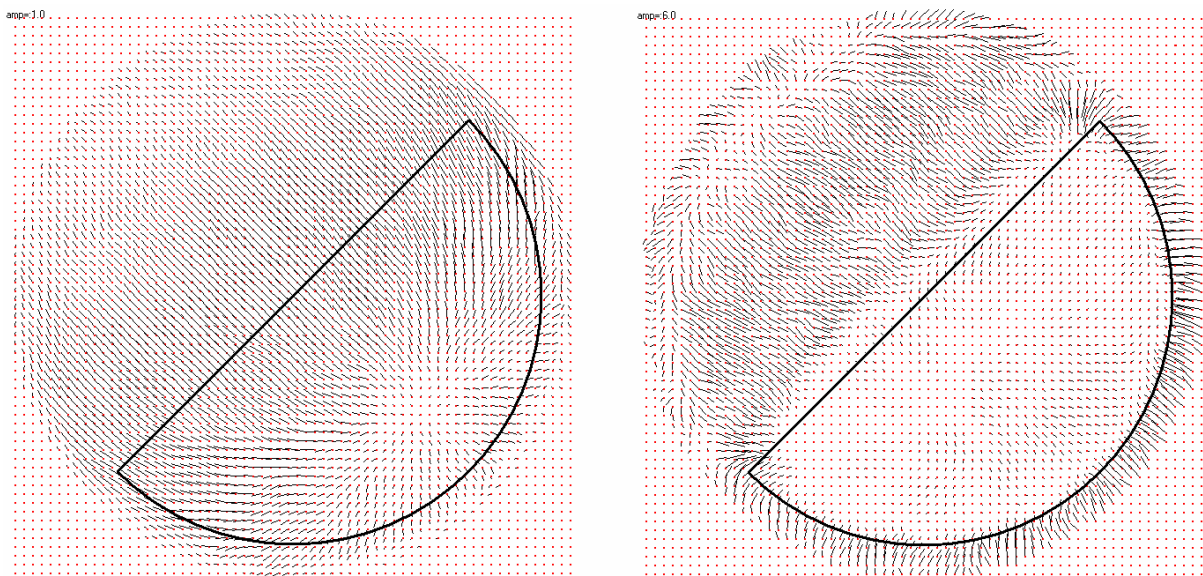


Fig. 5: Assessment of the horizontal velocity components by evaluation of the lateral movement of the center of mass of the bubble images during their passage through the sensor measuring plane, left: 40 mm upstream of the diaphragm, right: 40 mm downstream of the diaphragm, air-water test at $J_L=1$ m/s and $J_G=0.037$ m/s

As a result the two time-averaged velocity components v_x and v_y are obtained on the 64x64 measuring matrix. Vector plots are shown in Fig. 5 for both 40 mm upstream and, respectively, downstream of the diaphragm. These preliminary results show, that upstream of the diaphragm the velocity components in the x-y plane point away from the stagnation point. Downstream of the diaphragm, the tendency is inverted and vectors point back towards the recirculation zone that is found behind the diaphragm. This illustrates the large variety of information contained in the high-resolution mesh sensor data. The evaluation of the data will be continued.

5.3 Axial water velocities

There is a way to assess time-averaged local liquid velocities by evaluating the transit time of bubbles of a certain range of diameters. Due to the spatial resolution, the sensor data can be used to determine the lateral extension of each individual bubble by measuring the maximum area occupied by the bubble within the measuring plane during its passage [2, 5]. If a spherical bubble shape can be assumed, the diameter of a circle with an equivalent area divided by the time of the passage reveals the bubble velocity. A local instantaneous value of the liquid velocity is available after subtracting the bubble rise velocity. Time-averaged profiles of the axial liquid velocity are calculated by averaging individual values from a manifold of analysed bubbles.

Bubble deformation causes a systematic error that has to be eliminated by a calibration procedure. In order to keep the bubble deformation and the bubble rise velocity in a narrow band, velocities are calculated only from bubbles of a certain bubble size interval, which was set to 4-5 mm, so-called "marker bubbles". It was assumed that the bubble deformation can be accounted for by a calibration factor of the individual bubble velocity. This factor is determined by integrating the velocity profile found under the assumption of spherical bubbles over the cross-section and comparing the result with the known liquid superficial velocity.

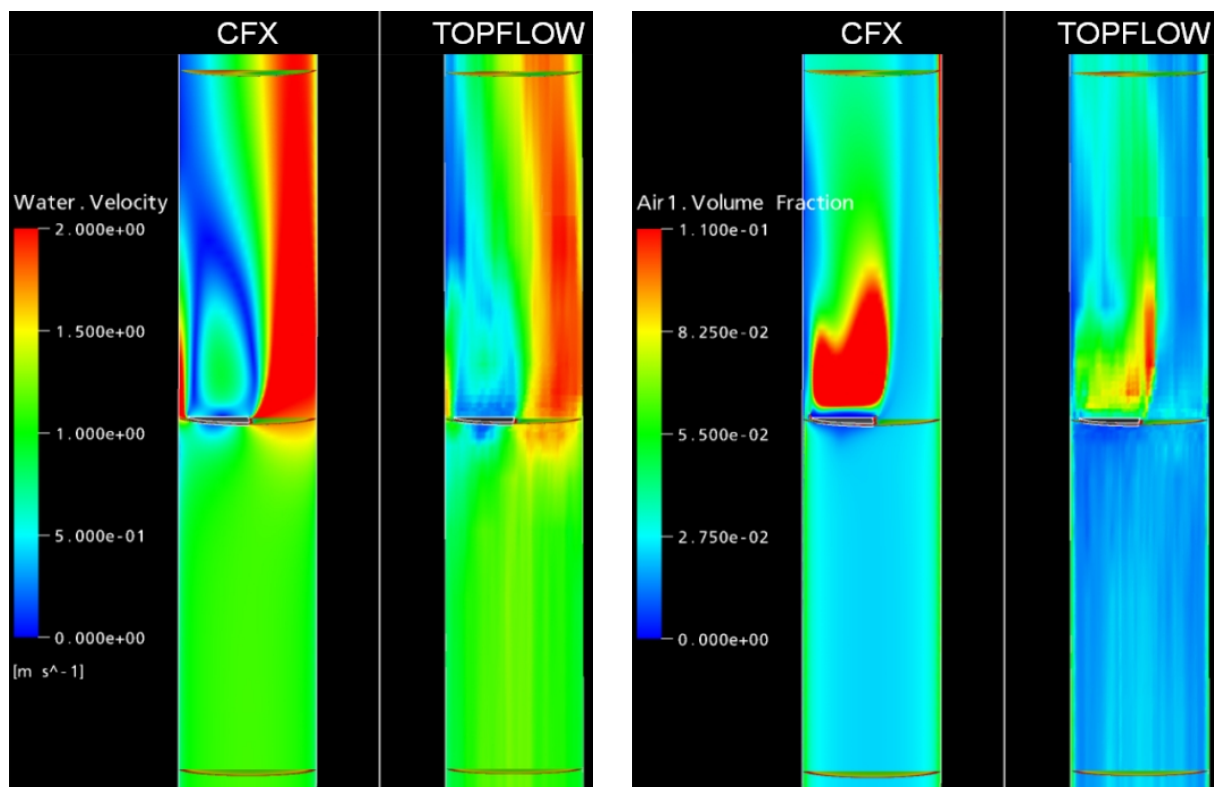


Fig. 6: Comparison between experiment and CFX pre-test calculation for the absolute water velocities (left) and the gas volume fraction distribution (right) for the region from 0.5 m upstream to 0.5 m downstream the obstacle; air-water test at $J_L=1$ m/s and $J_G=0.037$ m/s

The velocity distribution obtained in this way for the air-water test at $J_L = 1$ m/s and $J_G = 0.037$ m/s reports a recirculation zone behind the obstacle. It has to be kept in mind that the marker bubble method cannot supply information on the sign of the axial liquid velocity. Negative values expected in the centre of the recirculation zone can therefore not be reproduced and a local maximum is found instead (compare in Fig. 6, water velocities, the green zone above the obstacle).

By the estimation of liquid velocity profiles it becomes clear that the high gas fractions in the wake of the obstacle are caused by entrapping bubbles in the recirculation zone. Otherwise, upstream of the diaphragm the expected stagnation point is nicely reproduced and the concentration of the gaseous phase is decreased. Furthermore, the water velocity shows a maximum in the free cross-section area aside of the obstacle.

6. Comparison between the ANSYS CFX pre-test calculation and the experimental data

In preparation for the direct comparison of the CFD results and the experiments the 3-dimensional dataset from wire-mesh sensor measurements has been imported into the CFX graphical postprocessor. It makes it possible to use identical data processing and color schemes for visualization. Since experimental data have a fine (64×64) planar resolution in the x-y-plane but a limited coarser resolution in z-direction with respect to measuring planes, a pre-interpolation of the experimental data in z-direction has been applied with an axial resolution of the interpolated data with $\Delta z=1\text{ mm}$.

Results for absolute water velocity and gas volume fraction distributions are shown in Fig. 6. The velocity field shows the same location and intensity both of the recirculation zone above and the stagnation regions under the obstacle surface. Smaller details, like the velocity and void fraction values above the gap between the circular edge of the obstacle and the inner wall of the pipe are also found in a good agreement. The reattachment length of the flow to the pipe wall downstream the obstacle is slightly increased in the CFD simulation, which is probably linked to the higher amount of entrained gas void fraction in the vortex behind the obstacle. Furthermore, the present simulation tends to overpredict the void fractions in the wake. This is a result of the assumption of a mono-disperse bubbly flow with a bubble size differing from reality and neglecting bubble coalescence with formation of larger bubbles in the wake of the obstacle. The agreement can be improved by using measured bubble-size distributions from the region upstream of the obstacle as a boundary condition for post-test calculations or by application of the inhomogeneous MUSIG model for the prediction of bubble size distributions from local flow conditions.

7. Conclusions

A novel technique to study the two-phase flow field around an asymmetric diaphragm in a vertical pipe is presented, that allows to produce data for CFD code validation in complex geometries. Main feature is a translocation of the diaphragm to scan the 3D void field with a stationary wire-mesh sensor. Besides time-averaged void fraction fields, a novel data evaluation method, was developed to extract estimated liquid velocity profiles from the wire-mesh sensor data. Furthermore, a new method for the estimation of horizontal velocity components of the gaseous phase is introduced.

A pre-test calculation done by ANSYS CFX 10.0 resulted in a good agreement with the experiment in terms of all significant qualitative details of the void fraction and velocity distributions. The structure and the geometry of the entire flow field in general as well as the dimensions of recirculation and stagnation zones in particular were predicted in good accordance with experimental data. The fact that for the time being a simple monodispers bubbly flow was assumed, led to an overestimation of void fractions especially in the wake of the obstacle, while the velocity profiles are matching better. It is planned to continue with post-test calculations in order to achieve a better quantitative agreement by using measured bubble-size distributions from the region upstream of the obstacle as inlet boundary condition and in a further step by applying the inhomogeneous MUSIG model for the prediction of bubble size distribution and bubble coales-

cence. The experimental data will be used to validate this recently developed and implemented model against detailed bubble size and bubble scale resolved void fraction measurements.

References

- [1] Prasser, H.-M., Beyer, M., Böttger, A., Carl, H., Lucas, D., Schaffrath, A., Schütz, P., Weiss, F.-P., Zschau, J.: Influence of the pipe diameter on the structure of the gas-liquid interface in a vertical two-phase pipe flow, *Nuclear Technology* 152 (2005) 10. pp. 3-22.
- [2] H.-M. Prasser, Influence of the Gas Injection on the Void Fraction Profiles and Bubble Size Distributions of a Air-Water Flow in Vertical Pipes, 5th ICMF'04, Yokohama, Japan, May 30–June 4, 2004, paper No.: 187.
- [3] H.-M. Prasser, M. Beyer, H. Carl, H. Pietruske, P. Schütz: Steam-water experiments at high pressure to study the structure of the gas-liquid interface in a large vertical pipe, Annual Meeting on Nuclear Technology, Nuremberg, May 10-12, 2005, paper 215.
- [4] H.-M. Prasser, D. Scholz, C. Zippe, 2001, Bubble size measurement using wire-mesh sensors, *Flow Measurement and Instrumentation*, 12/4, pp.299-312, 2001.
- [5] H. Pietruske, H.-M. Prasser: Wire-mesh sensors for high-resolving two-phase flow studies at high pressures and temperatures, NURETH-11, Avignon, France, Oct. 2-6, 2005, paper No.: 533.
- [6] ANSYS CFX 10.0 Users Manual, ANSYS Inc., July 2005.
- [7] Th. Frank, J. Shi, A.D. Burns: “Validation of Eulerian multiphase flow models for nuclear reactor safety applications”, 3rd TPFMI, Pisa, 22.-24. Sept. 2004, pp. 1-8.
- [8] Th. Frank: Abschlussbericht zum Forschungsvorhaben 150 1271 “Entwicklung von CFD-Software zur Simulation mehrdimensionaler Strömungen im Reaktor-kühlsystem”, ANSYS Germany, Technical Report TR-06-01, Januar 2006, pp. 1-72.

Acknowledgements

The work is carried out as a part of current research projects funded by the German Federal Ministry of Economics and Labour, project numbers 150 1265 and 150 1271. Electronic equipment for wire-mesh sensors was developed in co-operation with TELETRONIC GmbH (www.tz-rotech.de/teletronic/). The authors express their gratitude to the technical TOPFLOW team.

NUMERICAL INVESTIGATIONS FOR INSULATION PARTICLE TRANSPORT PHENOMENA IN WATER FLOW

Eckhard Krepper, Alexander Grahn,
Sören Alt¹, Wolfgang Kästner¹, Alexander Kratzsch¹, and Andre Seeliger¹

1. Introduction

In 1992 a steam line safety relief valve inadvertently opened in the Barsebäck-2 nuclear power plant in Sweden. The steam jet stripped fibrous insulation from the adjacent piping system. Insulation debris was transported to the wetwell pool and about one hour after the start of the LOCA incident, the intact strainers of the drywell spray system became clogged. Although the incident in itself was not very serious, it revealed a weakness in the defense-in-depth concept which under other circumstances could have led to the emergency core cooling system (ECCS) failing to provide recirculation water to the core.

Research and development efforts of varying degree of intensity were launched in many countries. The corresponding knowledge bases were updated several times and several workshops were performed (see e.g. [1 to 4]). These activities reflect in most cases the view of regulators and utilities. This article intends to report the efforts to investigate the problem more in detail, with the aim of local hydrodynamic model development.

2. Joint Research Project

A joint research project performed in cooperation by the IPM-Zittau and Forschungszentrum Rossendorf is an experimental investigation of insulation debris transport and the development of CFD models for the description of particle transport phenomena in coolant flow. While experiments are performed at the IPM-Zittau, theoretical work is examined at Forschungszentrum Rossendorf.

The main topics of the project are

- Primary particle constitution: Experiments are performed to blast original samples of insulation material by steam under the thermal hydraulic conditions to be expected at a LOCA incident (i.e. at pressures up to 11 MPa). The material obtained by this method is then used as raw material for further experiments.
- Transport behaviour of fibres: The transport behaviour of the gained material is investigated in a water column by optical high-speed video techniques. The sinking velocity of the fibres is used to derive the drag coefficients and other physical properties of the modelled fibre phase, which are necessary for an adequate CFD simulation.
- Deposition and re-suspension of fibres: A flat channel with defined boundary conditions was used to examine the deposition and re-suspension behaviour at low velocities. The experiments are designed to work with laser PIV measurement and high-speed video. CFD approaches consider the influence of the fibre material viscosity.
- Effect of strainers: A test rig was used to study the influence the insulation material loading on the pressure difference observed in the region of the strainers. A CFD model was developed that uses the approach of a porous body. Correlations from the filter theory

¹ University of Applied Sciences Zittau/Görlitz, Institute of Process Technology, Process Automation, and Measuring Technology, Theodor Körner Allee 16, D-02763 Zittau, Germany

known in chemical engineering are adapted to the experiments and are used to model the flow resistance depending on the particle load. This concept enabled the simulation also of a partially blocked strainer.

3. Modelling of the fibre transport in water

3.1 The experiments

The particles obtained by blast experiments are inserted into a Plexiglas column having a height of 3 m, a width of 0.5 m and a depth of 0.1 m. Using high-speed video, a numerical evaluation of the distribution of sinking velocities was determined (see Fig. 1).

The distribution of sinking velocities is found (see Fig. 1 right side). The particles consist of an agglomeration of smaller particles of different sizes, densities and shape. Larger objects are disintegrated under the influence of the shear stresses and turbulence from the surrounding liquid. The turbulent wake of the larger particle agglomerations causes breakage of the following agglomerations that result in the generation of a fine fraction. Extensive tests have shown, that the sinking behaviour not only depends on the insulation material but also on the wettability of the fibres influenced by the age, the kind of drying and the hydrophobic properties of the material.

At the IPM-Zittau different methods of the Fuzzy Logic were applied to establish a classification of the particles.

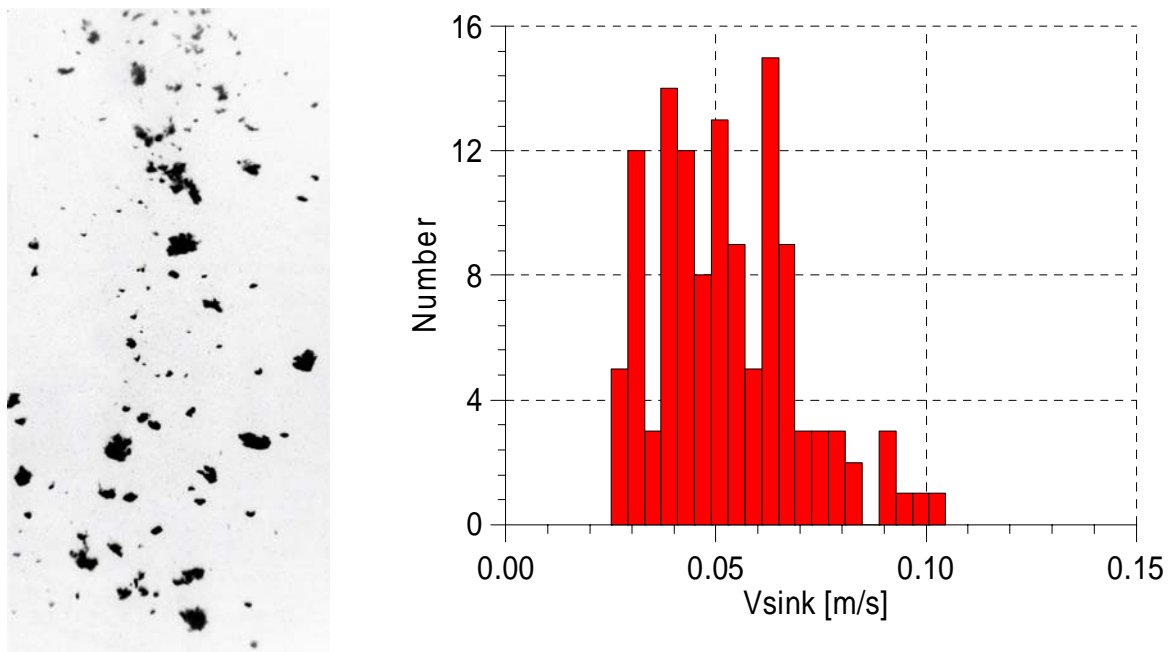


Fig. 1: Photography of sinking fibres (left side) and assessed distribution of sinking velocities measured in the test rig “column” investigating the material MD2

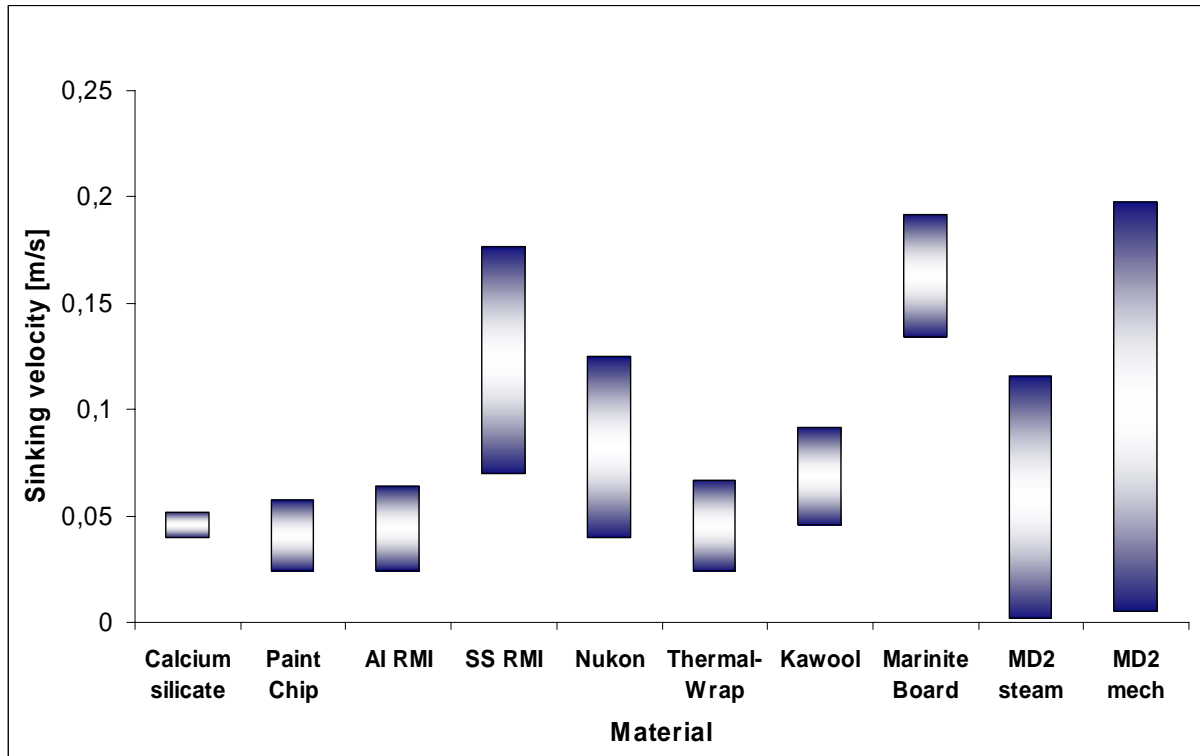


Fig. 2: Comparison of measured sinking velocities of the material MD-2 (last two columns) to published values of other insulation materials [2]

Figure 2 shows the sinking velocities of different insulation fibre materials. The MD-2 values measured in the facility in Zittau were compared with other materials. The Figure shows the dependency of the sinking velocity on the fragmentation procedure. The fragmentation by steam performed in the facility in Zittau results in sinking velocities of 0.005...0.12 m/s while fragmentation “by hand”, results in larger particles and larger sinking velocities in the order of 0.01-0.2 m/s.

3.2 CFD concept modelling the particle transport

The general question to be answered by a numerical simulation is to determine how the fibre material mass is deposited in a certain geometry (i.e. the reactor sump) and the mass of fibre entrained by the water flow. Since the momentum transport in the liquid flow plays an important role, the problem is clearly a three-dimensional problem that can be solved applying computational fluid dynamic (CFD) methods.

3D computational fluid dynamics (CFD) codes describe a fluid flow based on the solution of the conservation equations for mass, momentum and energy. CFD methods are distinguished by different solution strategies of the basic equations and physical models for the closure laws. For the problem examined here, two different approaches are known: The application of an Eulerian-Lagrangian or an Eulerian-Eulerian approach.

The first approach relies on the solution of the Navier Stokes equations for the continuous fluid phase and on the solution of the Lagrangian equations for single particles. The single particles are assumed to have a certain mass. The flow field acts on each particle and influences the particle path. The particles in turn affect the turbulence quantities of the fluid. A particle spectrum can be easily given as an inlet condition. Models describing the particle reflection, the erosion and the sedimentation at walls are known.

The Eulerian-Eulerian approach assumes that at least two fluids are continuously penetrating each other. The volume fraction of the fluids in each cell sums to unity. For each fluid, the full set of conservation equations is resolved. Therefore, each fluid has a different velocity field; however, the absolute pressure field is assumed to be the same for all fluids and particles. The mechanisms of interaction of the fluids are the flow resistance modelled by momentum transfer, phase change modelled by mass transfer and heat conduction modelled by energy transfer. Whereas the two latter interactions in the present problem are not relevant, the flow resistance is essential for the description of debris transport.

The long-term experience applying the Eulerian-Eulerian approach for the simulation of bubbly flow in the FZ-Rosendorf might be a further argument, to start using this technique.

3.3 Modelling the particle transport applying the Euler/Euler approach

The particle transport in the Eulerian-Eulerian approach is described by the momentum exchange between the two phases. In the case of dispersed spherical gas bubbles or spherical particles moving in a continuous fluid, the interacting forces between the two phases in principle have the form:

$$F_{Drag} = \frac{1}{2} n \rho A C_D |V|V \quad (1)$$

with the particle number density n , the liquid density ρ , the cross sectional area of the particle in flow direction A , the relative velocity between the phases V and the drag coefficient C_D . The drag coefficient depends on the Reynolds Number, which is defined as

$$Re = \frac{\rho |V| d}{\mu} \quad (2)$$

with μ as the dynamic liquid viscosity and d as the particle diameter.

For low velocities and Reynolds Numbers $\ll 1$ the viscous effects dominate the inertial effect and the regime is designated as Stokes flow and we find

$$C_D = 24 / Re \quad (3)$$

For higher velocities ($1000 < Re < 1.2 \cdot 10^5$) the inertial effects dominate the viscous effects resulting in turbulent motion where

$$C_D = 0.44 \quad (4)$$

In the transition region ($0.1 < Re < 1000$), where both effects are of the same order of magnitude, we find

$$C_D = \max \left[\frac{24}{Re} (1 + 0.15 Re^{0.687}), 0.44 \right] \quad (5)$$

The last equation is known as the Schiller/Naumann correlation.

In the actual case a “virtual particle” is defined as a small ball of wool fibres consisting mostly of water. This is correct as the water in the wool ball moves with the “particle velocity”. This is due to entrapment of the water and local forces binding the water to the particles. Therefore, the virtual particle density $\rho_{particle}$ found here is close to that of water (i.e. 1000 kg m^{-3}), whereas the density of real dry fibres ρ_P amounts to about $2800 \cdot 10^3 \text{ kg m}^{-3}$. The density difference of water and fibres in the gravity field results in the buoyancy force:

$$F_{buoyancy} = ngV_{particle} (\rho_{particle} - \rho_{water}) \quad (6)$$

The equality of buoyancy and drag forces yields the sinking velocity:

$$V_s = \sqrt{\frac{4}{3} g \frac{\rho_{particle} - \rho_{water}}{\rho_{water}} d \frac{1}{C_D}} \quad (7)$$

Equation (7) has to be solved iteratively since the drag coefficient C_D is Reynolds Number dependent. The share of fibres, r_P , in the virtual particle can be calculated by

$$r_P = \frac{\rho_{Vparticle} - \rho_{wasser}}{\rho_P - \rho_{wasser}} \quad (8)$$

Evaluating equation (5) and (7) for different combinations of virtual particle diameter and virtual particle density yields the sinking velocity shown in Fig. 3. The investigated material shown in Fig. 1 (right side) has an average sinking velocity of 0.05 m s^{-1} , which is found for a virtual density of 1030 kg m^{-3} and a virtual particle diameter of 5 mm . With a dry fibre density of 2800 kg/m^3 the dry fibre share in the virtual particle amounts to 0.0167 .

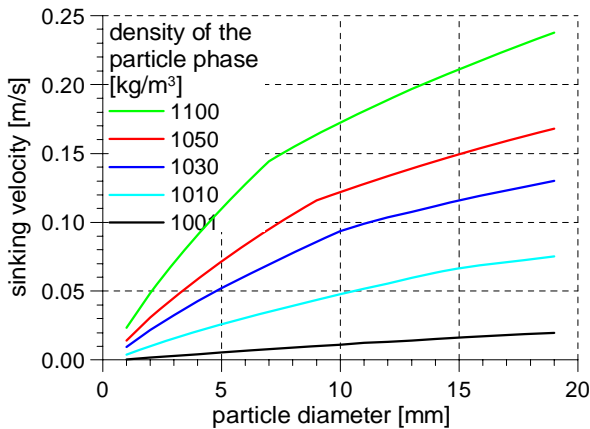


Fig. 3: Dependence of the sinking velocity on the virtual particle density and the virtual particle diameter

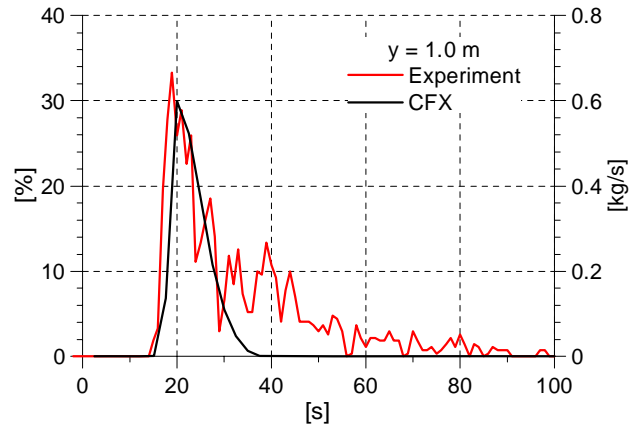


Fig. 4: Mass flow through a plane at a height of 1 m

The phenomena observed in the column were simulated by CFX. The transient started with an amount of fibres placed in the upper part of the column. The mass flow through a virtual horizontal plane at the height of 1.0 m was calculated and compared to measurements. This type of mass flow is hard to measure. Area fractions of the vertical observation plane occupied by the particles, which are obtained from video observations, were taken for comparison. Motion in the extension across the depth of the column is neglected. The

calculated maximum mass flow rate corresponds to the observation, since the average sinking velocity of 0.1 m/s was adjusted by simulated particle diameter of 5 mm and a particle density of 1080 kg/m³. The observed width of the maximum is caused by the scattering of sinking velocities and by the interaction with the liquid flow field in the column. Good agreement between the simulations at the assumed width and the observations was observed for the peak fraction; however, this changed as the effect of wake induced turbulence on particle motion and breakage reduced the sink rate resulting in the differences in the mass flow rates 40 seconds after the start of the test (see Fig. 4).

The demonstration given in this chapter shows that the Eulerian-Eulerian approach applied here is limited to the description of a certain particle size and density, whereas in the experiments, a particle spectrum is observed (see Fig. 1b). In principle the Eulerian-Eulerian approach enables the simulation of different dispersed phases representing different particle sizes and densities. Furthermore in the Eulerian-Lagrangian approach from its principle the definition of a spectrum of particle sizes and densities is possible. All these measures increase the numerical effort and reduce the numeric stability, which can limit the applicability of the models for the solution of practical problems. The required accuracy of the practical question to be answered has to decide on the preferred method.

4. Modelling of the sedimentation and re-suspension of fibres

4.1 Experiments

The sedimentation and re-suspension properties of fibres were investigated in a flat race track type channel with a width of 0.1 m, a depth of 1.2 m and straight sections with a length of 5 m (see Fig. 5). The bends had a radius of 0.5 m. The water flow is driven by two slow moving pumps driving the liquid at velocities between 0.01 and 1.0 m/s. Obstacles are placed in the straight sections to disturb the motion of the liquid and promote deposition of the particles. The deposition and re-suspension behaviour of the fibres was observed by using high-speed video and by Laser based PIV.

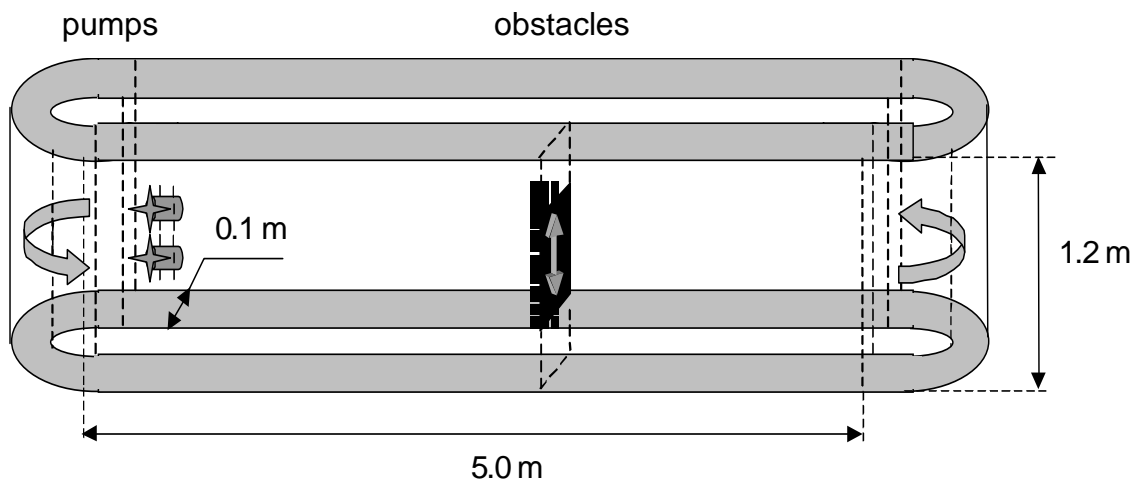


Fig. 5: Channel for investigation of the deposition and re-suspension properties

This revealed that the fibres agglomerate at a critical fibre volume fraction, which is manifested by a strong increase of viscosity. In addition, the fibres are deposited at the bottom of the channel below a critical water velocity of about 0.1 m/s, particularly at

locations downstream of the obstacles. Increasing the water velocity beyond 0.1 m/s causes the fibres to be mobilized again.

4.2 Simulation of sedimentation and re-suspension

Applying the Eulerian-Eulerian approach, the sedimentation and re-suspension behaviour of the fibres was simulated by a variable viscosity. The original concept proposed the simulation as a Non-Newtonian fluid, which is based on the simulation of a shear stress dependent viscosity. The observations of the fibrous flow in the channel have shown a volume fraction dependent behaviour of the fibres. Therefore during this step a dependency on the virtual particle volume fraction was simulated.

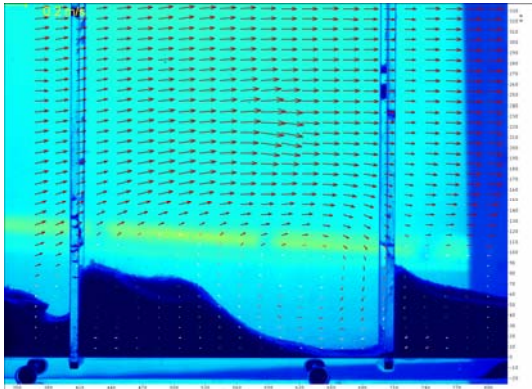


Fig. 6: Laser PIV measurements of the velocity field and the fibre distribution between two dams

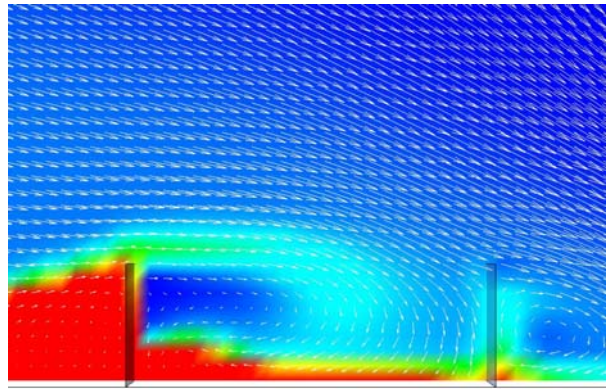


Fig. 7: Calculated water velocity field and fibre distribution applying the Euler/Euler approach using the CFD code CFX

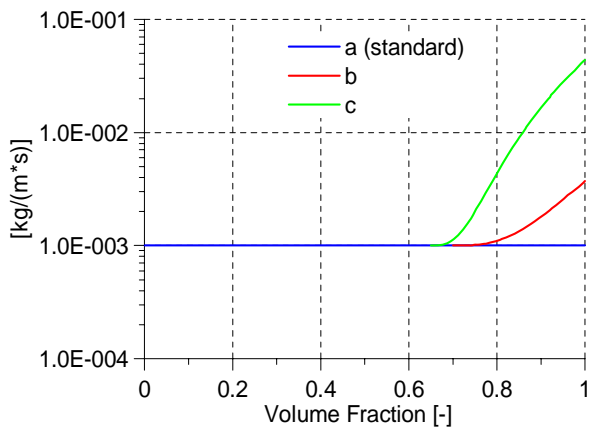


Fig. 8: Simulated dependencies of the dynamic fibre viscosity on the fibre volume fraction

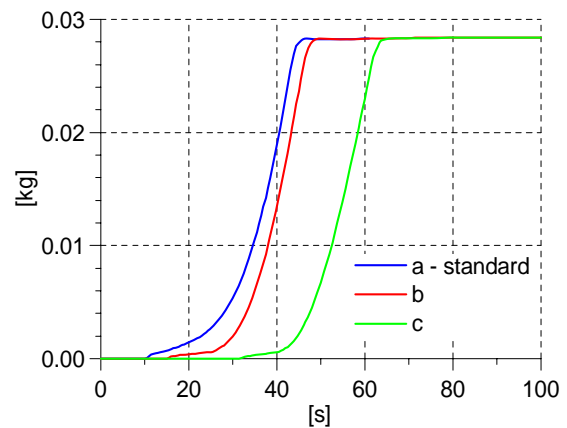


Fig. 9: Fibre mass accumulated between the dams

A feasibility study of the accumulation of fibres between two dams arranged at a distance of 0.3 m and having a height of 0.1 m was calculated by a transient CFX calculation and investigated in the experiment (see Fig. 6 and 7). The fibre mass accumulated between the dams in the simulations is presented in Fig. 9. The effect of the particle phase viscosity used is shown in Figs. 8 and 9 where the viscosity depend on the solids fraction. The results show that the CFD code at least is able to simulate the qualitative behaviour of the fibrous flow. Further investigations are underway to provide a deeper analysis of these experiments. The

evaluation of area fractions of the vertical observation plane occupied by the particles, which are gained from video observations of the fibrous volume fraction can be interpreted as a measure for the accumulated fibre mass. Neglecting the extension in the channel depth, these measurements will yield the necessary information in order to improve the physical representation of the solid phase with regards to the solid build-up observed in the experiments.

5. Modelling of strainers

5.1 Determination of the difference pressure as a function of fibre load and superficial velocity

Fibre layers are characterised by high volume porosity and easy compressibility. Due to the cumulative effect of frictional drag forces, acting on the individual fibres, the fibrous layer displays a porosity distribution with a maximum upstream of the strainer and a minimum at the strainer surface. While the porosity depends on the local compaction pressure, it determines the local differential pressure drop. This context can be described by

$$\frac{dp}{dx} = f(U, U^2, \varepsilon(p)) \quad (9)$$

with the liquid velocity U in x-direction and the porosity ε (s. Fig. 10.)

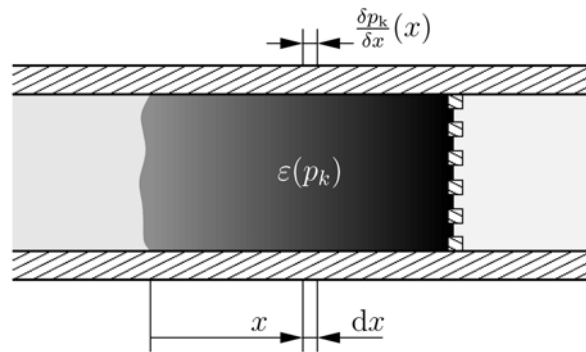


Fig. 10: Porosity in a fibre layer

The dependency of the porosity on the compaction pressure may be described by

$$\varepsilon(p) = \varepsilon_{\min} + (\varepsilon_0 - \varepsilon_{\min})e^{-Cp^D} \quad (10)$$

The empirical coefficients ε_0 , ε_{\min} , C and D are determined from compaction experiments (see Fig.12). These results enable the determination of the pressure difference on a strainer depending on the particle load.

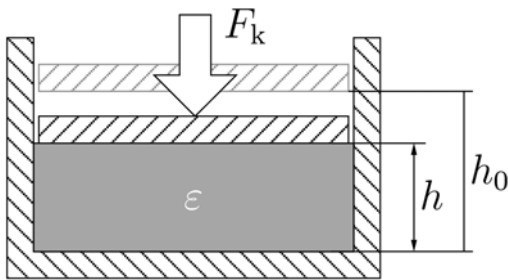


Fig. 11: Measuring principle of the compactness test

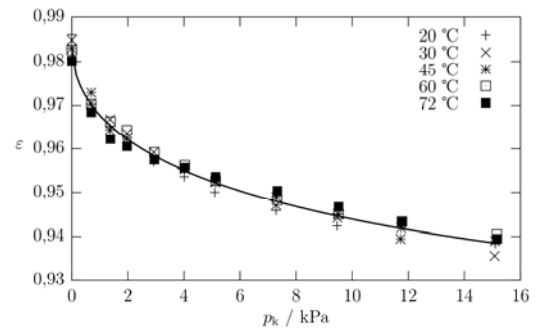


Fig. 12: Results of the compactness test for different temperatures

5.2 Implementation in a CFD code

The implementation of the derived correlations in a CFD code also enables the simulation of partially blocked strainers and the corresponding influence that this has on the flow field. The porous body approach used in CFD was applied in defining the region upstream of the strainer. This approach enables the simulation of a local flow resistance depending on the location:

$$-\frac{\partial p}{\partial x_i} = K_{loss}(y, z, t)\rho|U|U_i \quad (11)$$

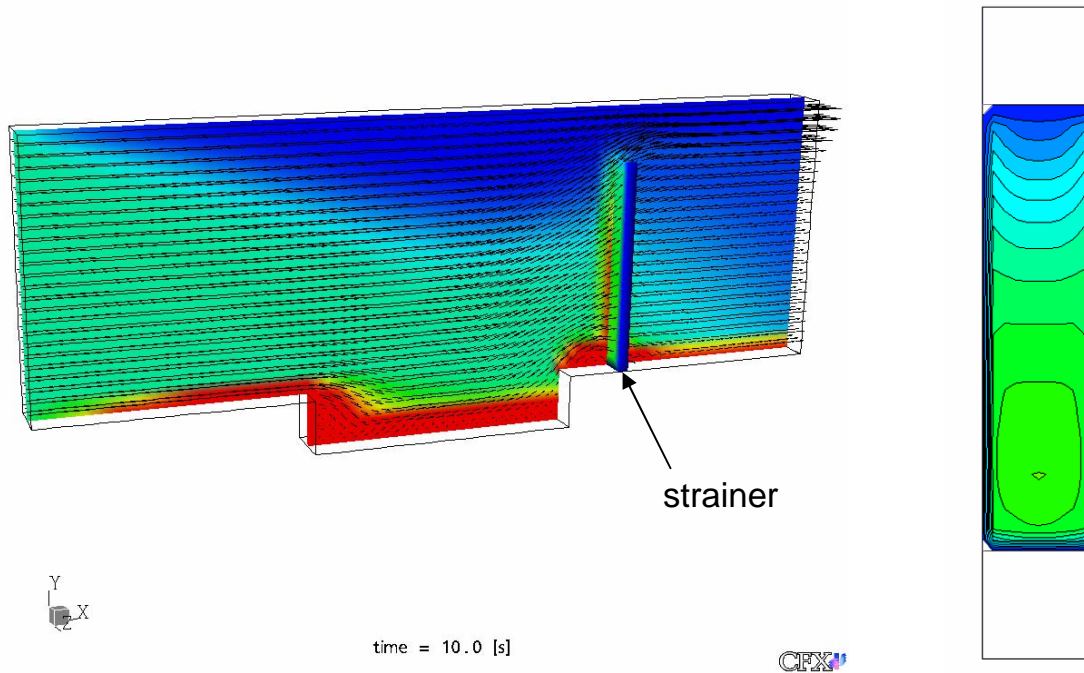


Fig. 13: Feasibility study of the described strainer model in a transient CFX calculation: The colour represents the volume fraction of the virtual particles (left side). On the right side the flow resistance of a gradual blocked strainer is shown

As an approximation, the flow resistance can be calculated from the integral particle mass flow:

$$K_{loss}(y, z, t) = F\left(\int_0^t \dot{m}_{fibres}(y, z, t) dt\right) \quad (12)$$

The function for the flow resistance K_{loss} in equation (11) can be derived by the relations found for equation (9) in chapter 5.1. Fig. 13 shows the result of a feasibility study of this concept in a transient CFX calculation. The application of the derived strainer difference pressure correlation adjusted to experiments in a CFD codes enables the simulation of a partially blocked strainer (see Fig. 13 right side).

6. Outlook

The project work is still underway. The presented results show, that the intended model approaches are feasible for the simulation of the interested phenomena. A more detailed

analysis of the experiments, particularly in the channel, will yield the information necessary for a physical derived sedimentation and resuspension model.

The observations of the experiments show that at higher circulation velocities (ca. > 0.5 m/s) the fibre sinking is replaced by a horizontal floating of the fibres. This phenomenon can be explained by the turbulence dispersion force.

A further subject of interest is the investigation of a plunging jet on the fibre distribution in a water pool.

References

- [1] Knowledge Base for Emergency Core Cooling System Recirculation Reliability, NEA/CSNI/R(95)11
- [2] Knowledge Base for the Effect of Debris on Pressurized Water Reactor Emergency Core Cooling Sump Performance, NUREG/CR-6808; LA-UR-03-0880
- [3] Knowledge Base for Strainer Clogging -- Modifications Performed in Different Countries Since 1992, NEA/CSNI/R(2002)6
- [4] Debris impact on Emergency coolant recirculation, Workshop Albuquerque, NM, USA February 2004, Proceedings OECD 2004 NEA No. 5468

Acknowledgements

The reported investigations are funded by the German Federal Ministry of Economy and Labour under contract No. 1501270

FIRST RESULTS WITH THE NEW HIGH-RESOLUTION GAMMA RAY TOMOGRAPH

André Bieberle, Uwe Hampel, Dietrich Hoppe, Eckhard Schleicher, Horst-Michael Prasser, Tobias Sühnel, and Cornelius Zippe

1. Introduction

For gamma ray tomography measurements of void fraction distributions in fuel rod bundles of boiling water reactors a new high resolution tomography system has been designed and built. Particular objectives of this application are the measurement of sub-channel void distribution and the investigation of dry-out effects in electrically heated fuel rod bundles. The application requires a robust tomography system that works in an industrial environment. In particular it was necessary to develop a high-resolution gamma radiation detector that is unsusceptible to strong magnetic fields, ambient temperature changes, and vibration forces. The developed detector is made of avalanche photodiodes (APD) coupled to small lutetium yttrium orthosilicate scintillation crystals (LYSO). Together with a special data processing unit and either a Cs¹³⁷ or a Co⁶⁰ source it can be operated as a tomography device for diverse diagnostic problems in science and engineering.

2. System design

2.1 Detector

The gamma radiation detector consists of LYSO scintillator crystals with an active area of 2 mm by 8 mm and 22 mm depth coupled to avalanche photo diodes. The shape of the scintillator crystal has been optimised with respect to detection efficiency and energy resolution [1]. Since most applications deal with thick metal vessels we gave priority to detection efficiency. Figure 1 shows the detector. The crystals have a long and tapered shape and are arranged in blocks of eight pieces. Each of these crystal blocks faces the avalanche photo diodes of a 2 x 8 APD array (S8550, Hamamatsu Inc.). Along with the APD chip, specified by [2], a set of eight charge sensitive amplifiers is gathered on a PCB board directly behind the crystal block. The amplifiers produce charge proportional voltage pulses of approximately 35 mV for the Cs¹³⁷ photo peak signal. Energy resolution is approximately 23%. The gamma radiation detector comprises 40 of these detector modules arranged as an arc of 40° angle and 744 mm arc length. In addition to crystals, APD, and amplifier electronics the detector includes power supply circuitry, a temperature regulated high voltage module for the APD bias voltage supply, and a thermoelectric cooling system for improved temperature stability. Pulse processing and counting is done by a separate electronic unit (Figure 2) containing 10 PCB boards with pulse processing and counting circuitry together with a controller board. The scheme of pulse processing is explained by the principle sketch in Figure 3. First, a pulse shaping stage takes the pulses of the charge sensitive preamplifier and shapes them to Gaussian pulses of 0.5 μs half width. This stage is followed by a gain adjustable amplifier that serves for pulse height adjustment. After that, a digitally controlled window comparator discriminates the pulses to exclude non photo peak pulses from counting. A following digital counter stage, which is fully realised in FPGA technology, contains a 24 bit counter, latch and multiplexing read-out electronics. Control and read out of the counters, digital threshold setting and communication with the PC is done by a micro controller. The PC is connected via USB interface.



Fig. 1: Views of the detector arc.



Fig. 2: Signal processing electronics (left) and view of one of the 10 pulse shaping and counting boards (right).

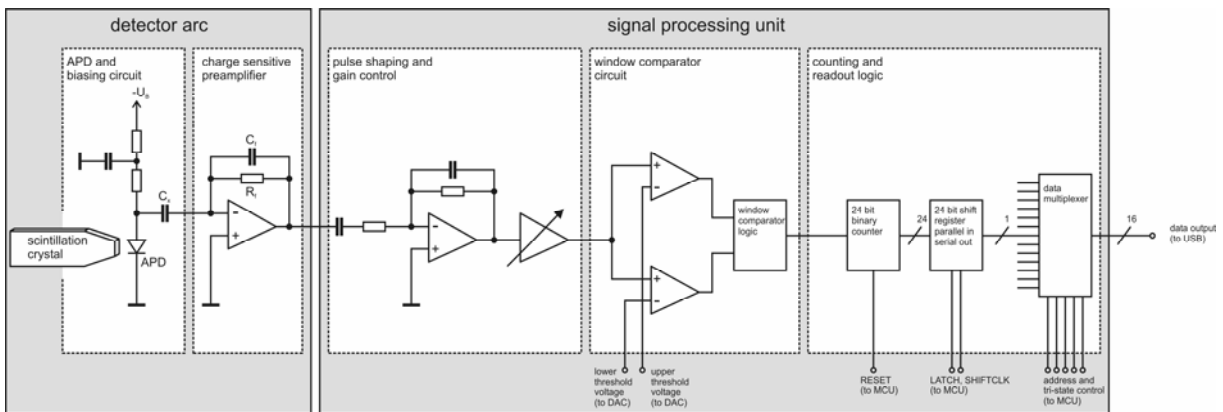


Fig. 3: Signal processing scheme of the radiation detector.

2.2 Isotopic source

We currently employ a Cs^{137} isotopic source with an activity of 165 GBq. The source capsule is of 5.6 mm diameter and 13 mm length. It is contained in a “Gammamat TIFF” shielding container. For the formation of a suitable radiation fan we devised a special tungsten collimator that is shown in Figure 4. The shielding container is placed on top of the collimator and fixed by a screw. By means of a Bowden cable the source can be moved through a metal guiding tube towards its working position in the lower central part of the collimator. There, a 1 cm high and 45° wide slit provides the radiation cone that is tightly fit to the active area of the detector. A laser positioning system is mounted on the collimator in order to precisely adjust the radiation fan orientation.

2.3 Tomograph gantry

For external measurement campaigns we built a special tomograph gantry (Figure 5). It comprises a four column spindle drive for vertical movement and a rotational table both driven by geared servo motors. The vertical driving range is about 2200 mm and rotation can be performed continuously. The gantry is made divisible to mount it about fixed objects of investigation. The rotational table carries the detector, the source and collimator, detector electronics, and a measurement PC. The source-detector separation is 970 mm. Electrical power is delivered through a slip line and data transfer and communication with the measurement PC is realised by W-LAN connection. The rotational table further comprises incremental angular sensors for projection and zero angle signal generation. In tomography scanning mode, data acquisition is synchronised with the projection sensor signal. The projection sensor gives 1000 signals per revolution. After each signal pulse, all detector counters are read out and data is transferred to the PC. In the PC, data is stored along with the time in microseconds between two successive projection angle sensor signals. In this way we obtain the count rates for 1000 projections of 0.36° angular step each.



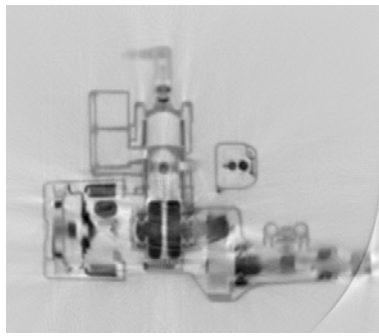
Fig. 4: View of the collimator with shielding container and Bowden cable.



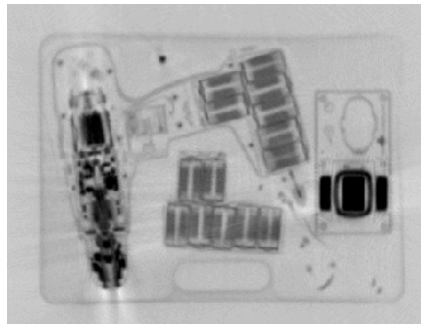
Fig. 5: View of tomograph gantry.

3. First results

Figure 6 shows a gallery of cross-sectional images of different technical and biological objects scanned with the new high resolution gamma ray tomograph. These images serve to demonstrate the imaging capabilities of the system. All objects have been scanned within approximately 10 minutes time. Inside a chamber of the hydrodynamic coupling wheel we have placed a plastic object with drilled holes in order to determine spatial resolution. It contains holes of diameters 6 mm to 1 mm in steps of 0.5 mm. From the cross-sectional image we obtained a spatial resolution of 3.5 mm. This value can be further improved if the effective source diameter would be made smaller. This will be possible in the future by using a Co^{60} source.



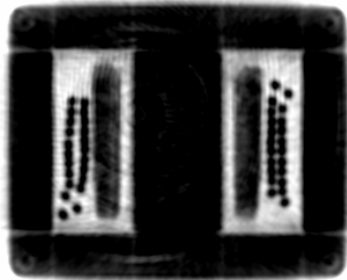
boat motor



screw driver set



pump



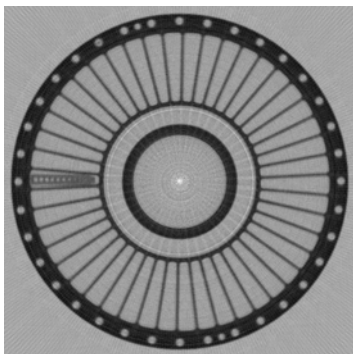
transformer



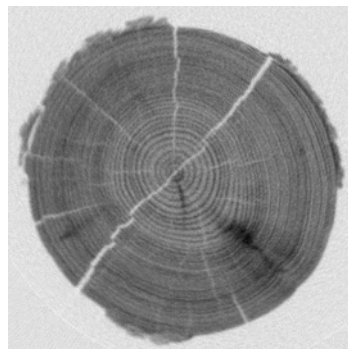
PC monitor



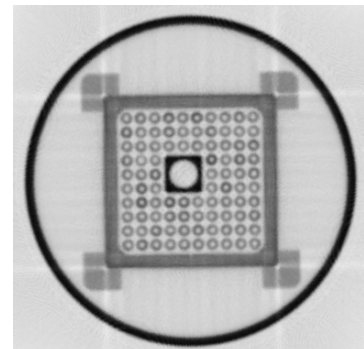
valve



turbo coupling wheel, \varnothing 33 cm



tree trunk (pine), \varnothing 33 cm



fuel element bundle, \varnothing 33 cm

Fig. 6: Examples for reconstructed cross-sectional images from gamma ray tomography.

References

- [1] A. Bieberle, E. Schleicher, U. Hampel, „New concepts for gamma tomography detectors”, FZR-407, 2004.
- [2] M. Kapusta, P. Crespo, D. Wolski, M. Moszynski, W. Enghardt, “Hamamatsu S8550 APD arrays for high-resolution scintillator matrices readout”, Nucl. Instruments and Methods in Physics Research A504, pp. 139-142, 2003.

Acknowledgements

We would like to thank AREVA ANP GmbH Germany for their support of the project.

NEW DEVELOPMENTS IN FAST NEEDLE PROBE SENSORS FOR MULTIPHASE FLOW MEASUREMENTS

Eckhard Schleicher, Marco Jose da Silva, and Uwe Hampel

1. Introduction

Measurement with local needle probes is a well-established method for the investigation of multiphase flows. Different measuring techniques have been employed for the needle probes in the past. The most known techniques are based on: conductivity, capacitance, optical and/or temperature measurements [1-3]. Based on the detection of single phases, these probes can provide information about void fraction, bubble size, frequency, and velocity, among others. The existing needle probe systems have limitations regarding the range of substances they are able to measure, the environmental conditions they can be applied to as well as their time resolution [3,4]. In this paper we describe two new developed needle probe sensors, which will enhance their application field. On one hand we present the further development of ultra-fast thermo needle probes for the phase-resolved temperature measurement aiming at the investigation of interfacial areas in the multiphase flow. On the other hand we introduce a new complex admittance needle probe, which is able to measure either conducting or non-conducting fluids, thus enabling the investigation of multiphase flow problems (e. g. three-phase flow of oil, water and gas in the oil extraction).

2. Enhanced thermo needle probes

In the past advanced needle probes with integrated micro-thermocouples have been introduced by Prasser *et al.* [5], which made it possible to measure local temperature and void fraction at the same spatial position. This was realized by making the sheath of the micro-thermocouple a measuring electrode for conductivity measurement. With such a probe the temperatures of the two different phases (e. g. steam and water) can be in principle distinguished. However, the mineral-insulated sheathed thermocouples still have a comparatively long time constant (~20 ms) [5]. Measuring in high-transient two-phase flows is therefore limited due to the slow time response of the probe. Additionally, the two signals had to be sampled sequentially because of the influence of the rectangular excitation voltage on the small temperature voltage signal. To solve this problem we have developed a new combined temperature and conductivity needle probe measuring system, which is able to handle grounded or direct sheathed thermocouples, i.e. where the thermocouple wires are electrically-joined to the protective sheath, as well as open thermocouples.

The measuring system consists of a needle probe, a special electronic circuit and a measuring computer. A schematic overview is given in figure 1. The needle probe is built in a tri-axial structure of three stainless steel electrodes. The electrodes are isolated from each other by two aluminium oxide ceramic tubes. The centre electrode (the probe tip itself) consists of a direct sheath thermocouple with 0.15 mm diameter. The second electrode is a steel tube of 0.8 mm diameter. The reference electrode, a 3 mm steel tube, is connected to the outer probe construction, which gives the mechanical stability as well as the grounded reference point. The local void fraction measurement is based on the detection of the local instantaneous electrical conductivity of the surrounding medium (fluid). A sine wave signal is applied to the measuring electrode. If the probe tip is in contact with the fluid of certain conductivity, an electric current flows towards ground potential, i.e. towards the reference electrode. If the

probe tip is covered by a gas bubble the current is interrupted. To avoid a current flow through thin liquid films still covering the isolating ceramics, a shielding electrode is placed between the measuring electrode and the metallic body of the probe. At the shielding electrode the same sinusoidal signal is applied resulting in an active shielding [6]. The positive input of a transimpedance amplifier is connected to a direct digital synthesizer (DDS 1), which generates the 200 kHz AC excitation signal. This signal is also applied to the shielding electrode, as mentioned above, for active shielding. The measuring electrode (micro-thermocouples sheath) is connected to the negative input. Due to the virtual short circuit between the negative and positive inputs of the operational amplifier, the excitation signal is also applied to the measuring electrode. The output signal of the transimpedance amplifier is thereby superimposed by a permanent signal, which has to be removed. Thus the signal corresponding to the current flow at the probe tip is obtained by subtracting a constant sine wave signal from the transimpedance amplifiers output signal by means of a difference amplifier. This constant sine wave signal is generated by a second DDS with the same frequency but with an adjustable phase for correcting of delay time differences. Both DDS generators work in synchronisation since they share the same reference clock. Eventually, a logarithmic amplitude detector detects the resulting sine wave signal of the conductivity path.

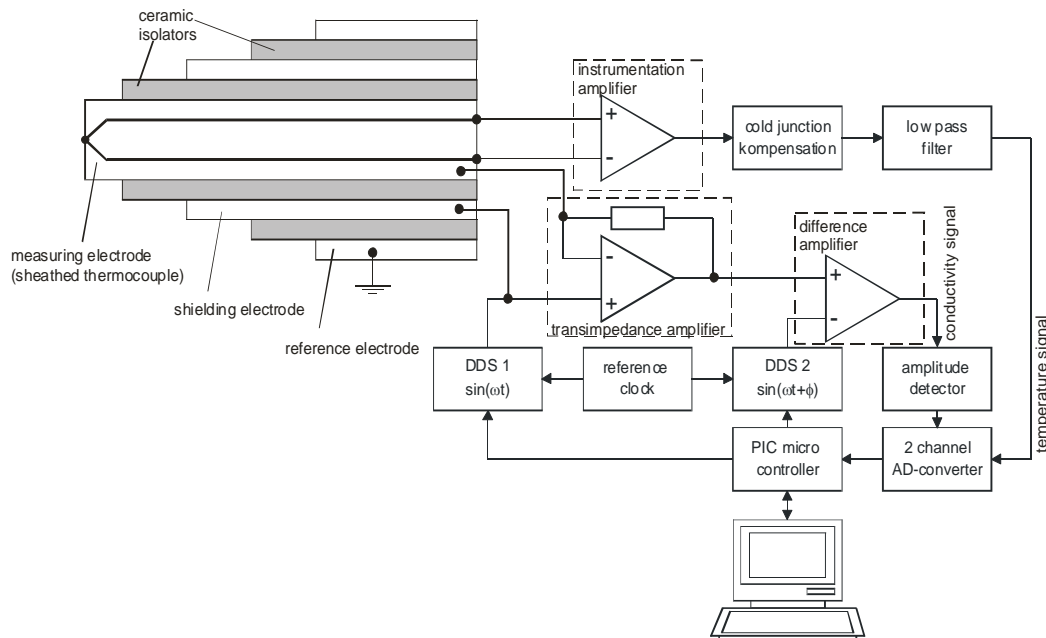


Fig. 1: Combined temperature and conductivity measurement system, consisting of the thermo needle probe and a special measuring electronics.

A high gain instrumentation amplifier amplifies the low voltage signal generated by the thermocouple (Seebeck coefficient of $41 \mu\text{V/K}$ for K-type). In order to suppress the 200 kHz excitation signal a very high common mode rejection is required for this amplifier. After a cold junction compensation the temperature signal is low-pass filtered (cut-off frequency of 10 kHz). Eventually, the two analogue voltage signals (conductivity and temperature) are sampled simultaneously at a sampling rate of 10 kHz by means of a two channel 12 bit AD-converter. A microcontroller is used to control the two DDS generators and the AD-conversion. It also realizes the communication with the measuring computer.

3. Complex admittance needle probes

Existing pure conductivity and capacitance needle probes have limitations regarding the range of substances they are able to measure. Conductivity probes can only differentiate an electrical conducting phase from a non-conducting one. Capacitance probes encounter problems when permittivities of the two phases are similar. The same difficulty occurs with optical probes and low refractive index differences. Temperature measurements are only possible when temperature gradients are encountered in the flow. Therefore, the probes have been utilized almost exclusively in two-phase flow measurements. There is a lack of measuring techniques for three- or multiphase flow problems. Typical occurrence for multiphase flow can be found in chemical reactors and petrochemical industry. Combination of conductivity with capacitance measurements could be an answer to the above problem. That means, instead of measuring in just one axis (real or imaginary) of the complex plane of admittances, one may use the full complex plane to characterize the fluids. Complex admittance/permittivity measurements are a standard tool in analytical chemistry [7], in which measuring times in the order of seconds to hundred of seconds are used to investigate sometimes entirely unknown substances. In process diagnostic measuring times in the range of microseconds to milliseconds are required in order to visualize dynamic processes, e. g. mixing of substances, multiphase flow, etc. The substances involved (and consequently their electrical properties) are in most cases known a-priori.

For the purpose of investigating dynamic processes in multiphase flow, we have developed and constructed a high-speed complex admittance measuring system. The measuring system consists of a needle probe and proper electronic circuitry, responsible to generate and measure the signals involved in determining the complex impedance. The probe itself is built in a double coaxial geometry. Two stainless steel electrodes (excitation and measuring electrode) are isolated from the common ground electrode (stainless steel tube) by a ceramic shell. Both coaxial arrangements are soldered together. The electronic circuitry determines impedance values by measuring the amplitude and phase of a sine wave signal. A block diagram of the electronic circuitry can be seen in the figure 2.

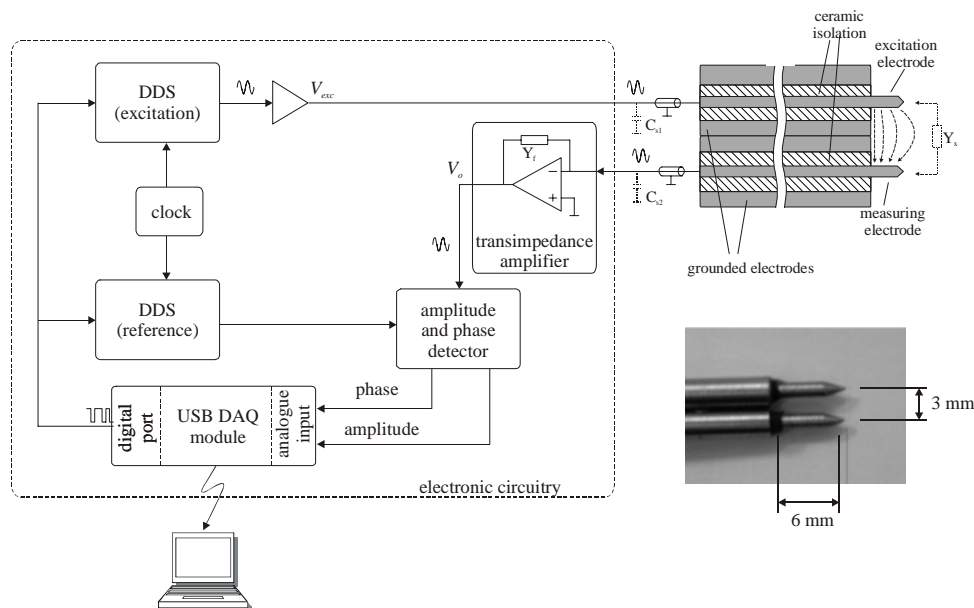


Fig. 2: Schematic diagram and picture of needle probe and block diagram of electronic circuitry.

Two direct digital synthesizers (DDS) ICs (AD9835, Analog Devices) generate the excitation and reference sine wave voltages. Frequencies up to 1 MHz can be generated and are user selectable. Both generators work phase-synchronized, since they share the same clock source. The excitation voltage V_i is supplied to the excitation electrode by means of a coaxial cable. The measuring electrode is connected to a transimpedance amplifier also by means of a coaxial cable. The output voltage of the transimpedance amplifier is directly proportional to the current I flowing from the excitation to the reference electrode $V_o = I / Y_f$, where Y_f is the admittance in the feedback loop of the operational amplifier. Since the unknown admittance of the fluid Y_x is grounded by the operational amplifier's virtual ground, the current I is the product of the input voltage V_i and this admittance, hence:

$$V_o = \frac{I}{Y_f} = V_i \cdot Y_x \cdot \frac{1}{Y_f} \quad (1)$$

Eventually, the output voltage V_o is input to an amplitude and phase detector block. The IC AD8302 (Analog Devices) realizes the function of measuring the amplitude and phase. This IC measures the amplitude ratio and the phase difference from V_o and the reference signal coming from the second DDS. The two DC outputs of the IC carrying the information on amplitude ratio and phase difference are fed into an A/D-converter (12 bit, 10,000 samples/s per channel) of the USB data acquisition (DAQ) module PMD-1208FS (Measurement and Computing). The USB DAQ module is connected to a PC through a USB 2.0 port. The digital port of the USB DAQ module is used to program the DDS sine generators. Furthermore, a program in the PC controls the frequency and phase lag of each DDS as well as the A/D-conversion sequence, and realizes the calculation of the admittance from the measured amplitude and phase values.

The complex admittance measured by the probe is directly proportional to the complex relative permittivity ϵ_r^* of the fluid under test according to [8]

$$Y = \epsilon_r^* \cdot \epsilon_0 \cdot j\omega \cdot k_g, \quad (2)$$

where ω denotes the angular frequency ($\omega = 2\pi f$), ϵ_0 the permittivity of vacuum (8.85 pF/m) and k_g the geometry factor of the probe. A calibration procedure can be carried out with a substance with known electrical properties (e.g. water or air) in order to determine the geometry factor of the probe. This way, the needle probe is also able to measure the complex permittivity of substances.

4. Results

4.1 Enhanced thermo needle probes

The system was calibrated with a conductivity meter Cond 330i (WTW, Germany) by measuring deionized water and dissolved sodium chloride in a conductivity range between 1 μ S/cm and 3000 μ S/cm. The temperature measurements have been calibrated by the thermo-calibrator Calisto 2250S (Klausmeier Kalibrier- & Messtechnik GmbH, Germany) in stirred water in a temperature range between 10 °C and 100 °C. The time constant of temperature measurement has been experimentally determined by dropping the probe from ambient air (25 °C) into water at 50 °C. The temperature response was assumed to be an exponential rise to a maximum, i.e. the response of a first order system [9]. The conductivity

signal was used as trigger for the start of the step response. We used the 63 % method to determine the time constant. That means the time constant is equal the time the temperature signal reaches 63 % of the end value. The experiment was repeated 10 times and a mean value of 3.6 ms was encountered. This value is approximately 5 times smaller than the previous system (17 ms) [5].

In order to show the capability of the system in investigating transient two-phase flows, it has been tested in the flowing experiment. A steam flow from boiling water was injected in a vessel containing tap water ($\kappa = 510 \mu\text{S}/\text{cm}$) at 32°C (fig. 3). The steam flow, at temperature of approximately 100°C , produced bubbles in the water. The thermo needle probe was placed directly on the output of the steam flow to detect the bubbles. The system was configured for a sampling frequency of 10 kHz per channel (conductivity and temperature).

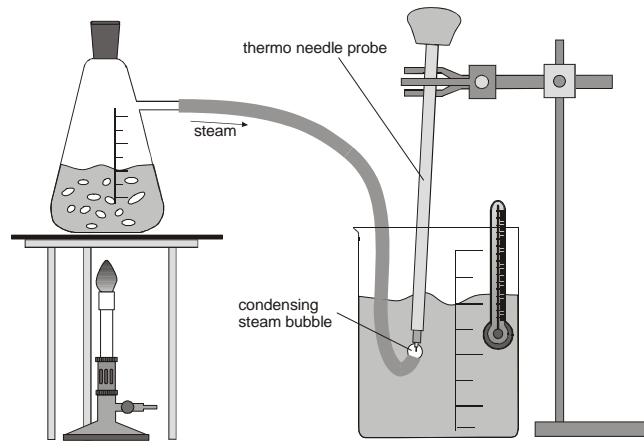


Fig. 3: Measuring setup for two-phase flows with different phase temperatures. The needle probe is placed directly to the outlet of a steam pipe in tap water, which was heated up during the experiment to 32°C .

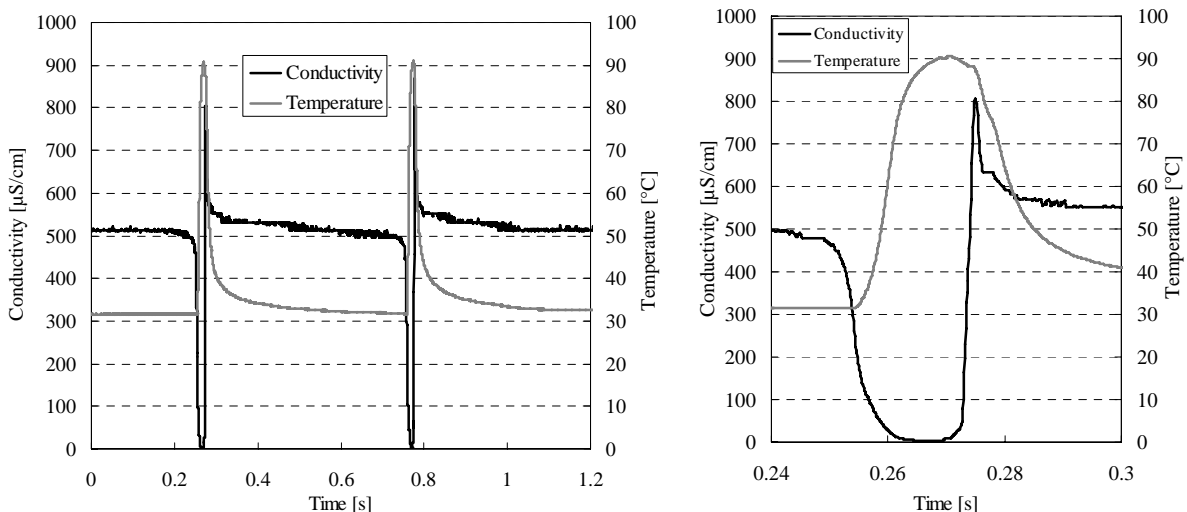


Fig. 4: Conductivity and temperature over the time in the water/steam two-phase-flow experiment. The diagrams show the measurements for two steam bubbles (left) and a zoom into the first one (right).

Figure 4 shows the results for the measurement of two bubbles and a detailed graphic for the first one. When the probe detected a steam bubble the temperature raised up to 90 °C and the conductivity dropped down to zero. Both signals return to their baseline values after the passage of the bubble. The combined analysis of both conductivity and temperature can reveal more details of the thermodynamic process.

4.2 Complex admittance needle probes

The system has been extensively tested by measuring different resistors, capacitors and parallel combinations thereof. Therefore a set of components were put in contact with the probe electrodes by the means of a connector. Resistors values in the range 100 k Ω - 1 M Ω and capacitors in the range 1.5 pF – 15 pF were used in this experiment. This value range is expected to be found in real fluid measurements. The values of each component had been firstly measured by an RLC meter (Fluke PM6304). The excitation frequency was set to 200 kHz. The values measured by the needle probe were then compared with the values from the RLC meter. Maximum relative errors of 5.11 % and 3.98 % have been obtained in the resistance and capacitance measurements, respectively.

The system has also been tested in measuring different liquids and air. The liquids were put in a metal cylinder 10 cm high and 10 cm in diameter and the probe was placed in the centre. Firstly, the system was calibrated by measuring air (empty probe) and deionized water. The excitation frequency was 200 kHz. Table 1 resumes the results of measured properties and compares it with reference data. Reference relative permittivity was taken from [10] and calculated for the ambient temperature of the samples. Reference conductivity was measured by the conductivity meter Cond 330i (WTW GmbH, Germany). For gasoline there exist no exact reference data, since this value is dependent on many parameters like e. g. hydrocarbons composition. Even so, the measured value is given on table 1 for comparison.

Table 1: Relative permittivity ϵ_r and conductivity κ measurements of different liquids and air

Substance	measured ϵ_r	reference ϵ_r	relative error [%]	measured κ [μ S/cm]	reference κ [μ S/cm]	relative Error [%]
Air	1.05	1.00	5.00	-0.01	0.00	-
Glycol	41.22	40.56	1.62	1.44	1.50	4.00
2-propanol	20.52	19.74	3.95	0.097	0.10	3.00
Deionized water	79.17	79.86	0.86	2.58	2.50	3.20
Water + salt	81.92	79.86	2.57	32.24	33.20	2.89
Diethyl Ether	4.33	4.27	1.41	-0.02	0.0	-
Gasoline	2.02	2.0 - 2.3	-	-0.01	0.0	-

In order to show the capability of the present system in measuring dynamic phenomena, it has been employed to measure air and water bubbles flowing in gasoline. The system was again calibrated by measuring air and deionized water. The excitation frequency was 200 kHz and sampling frequency was 5 kHz per channel. The needle probe was then located inside a plexiglas column. The flow of bubbles was also recorded with a high-speed video system (MotionPro HS Series, Redlake), aiming to compare this visualization technique with the needle probe system. Firstly, air bubbles were generated at the bottom of the column. Figure 5 shows the results for this experiment: pictures of an air bubble ascending in gasoline and the temporal evolution of relative permittivity and conductivity registered by the needle probe.

The relative permittivity value is lowered by the passage of the bubble, but the conductivity signal remains constant. As second experiment water bubbles ($\kappa = 1.4 \mu\text{S}/\text{cm}$) were dropped into the column. Figure 6 shows the results. The pictures show the water bubble descending in gasoline and the diagram provides again the temporal evolution of relative permittivity and conductivity. In this experiment, both signals increased since water is conductive and has a greater relative permittivity ($\epsilon_r \approx 80$) than gasoline ($\epsilon_r \approx 2$). In this way, it has been proved that the present system is able to detect the three different phases in a gasoline-air-water flow. From the best of our knowledge it is the first time that high-speed local complex permittivity measurements of three-phase flow have been carried out.

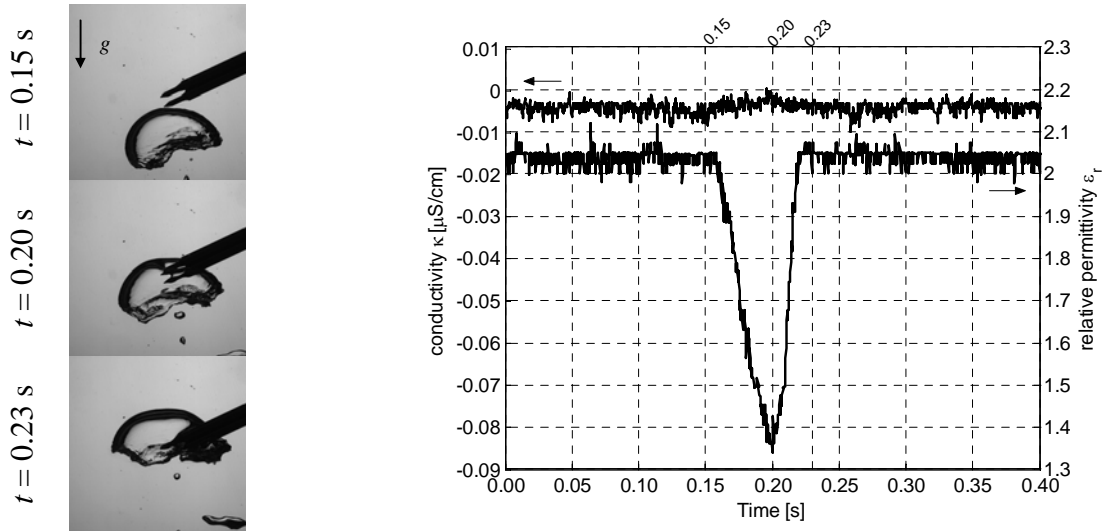


Fig. 5: Left: pictures of an air bubble ascending in gasoline, where t indicates the time of the picture and g the gravity acceleration vector. Right: temporal evolution of relative permittivity and conductivity signals.

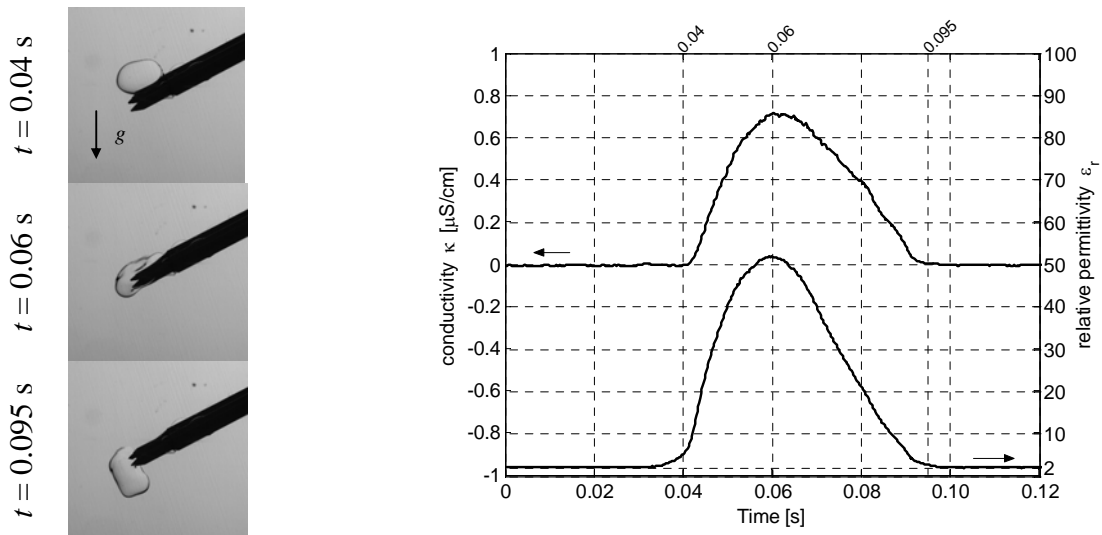


Fig. 6: Left: pictures of a water bubble descending in gasoline, where t indicates the time of the picture and g the gravity acceleration vector. Right: temporal evolution of relative permittivity and conductivity signals.

Conclusions

We have developed enhanced ultra-fast thermo needle probes with time constants of less than 4 ms with the capability of phase-resolved temperature measurement, aiming at the investigation of interfacial areas in multiphase flows (e.g. gas-steam-water flow). Furthermore, we have introduced a new complex admittance needle probe, which is able to measure conducting as well as non-conducting phase of a fluid flow, thus, enabling the investigation of multiphase flow problems with gas, water and organic fluid (e. g. crude oil). The new developed needle probe sensors have been tested in different multiphase laboratory experiments, showing a good performance. In the future, we will employ the new sensors in bigger scale experimental set-ups, for instance the TOPFLOW test facility at Rossendorf Research Centre and chemical reactors.

References

- [1] O.C. Jones, J.M. Delhaye, "Transient and statistical measurement techniques for two-phase flows" *International Journal of Multiphase Flow*, vol. 3, n. 2, pp. 89-116, 1976.
- [2] A. Cartellier, J.L. Achard, "Local phase detection probes in fluid/fluid two-phase flows", *Review of Scientific Instruments*, vol. 62, n. 2, pp. 279-303, 1990.
- [3] J. Werther, "Measurement techniques in fluidized beds", *Powder Technology*, vol. 102, n. 1, pp. 15-36, 1999.
- [4] C. Boyer, A.M. Duquenne, G. Wild, "Measuring techniques in gas-liquid and gas-liquid-solid reactors", *Chemical Engineering Science*, vol. 57, n. 16, pp. 3185-3215, 2002.
- [5] H. M. Prasser, A. Bottger, J. Zschau, T. Gocht, "Needle shaped conductivity probes with integrated micro-thermocouple and their application in rapid condensation experiments with non-condensable gases", *Kerntechnik*, vol. 68, n. 3, pp. 114-120, 2003.
- [6] B. Hage, J. Werther. "The guarded capacitance probe - a tool for the measurement of solids flow patterns in laboratory and industrial fluidized bed combustors", *Powder Technology*, vol. 93, n. 3, pp. 235-245, 1997.
- [7] J.R. Macdonald, W.B. Johnson, "Fundamentals of Impedance Spectroscopy," in: *Impedance Spectroscopy*, J.R. Macdonald, Ed. New York: John Wiley & Sons, 1987, pp. 1-26.
- [8] K. Asami, "Characterization of heterogeneous systems by dielectric spectroscopy", *Progress Polymer Science*, vol. 27, n. 8, pp. 1617-1659, 2002.
- [9] H. Turkoglu, B. Farouk, "Phase-resolved measurements in a gas-injected liquid bath" *International Journal of Heat and Mass Transfer*, vol. 39, n. 16, pp. 3401-3415, 1996.
- [10] D.R. Lide, *CRC Handbook of Chemistry and Physics*, 85th ed., Boca Raton, FL: CRC Press, 2005, pp. 6-155 - 6-177.

Acknowledgements

M. J. da Silva is supported by the "Coordenação de Aperfeiçoamento de Pessoal de Nível Superior" (CAPES), Brazil.

SOLIDIFICATION OF SN-PB ALLOYS WITH MAGNETIC FIELD CONTROL OF THE MELT FLOW

Sven Eckert and Bernd Willers

1. Introduction

The directional solidification of binary alloys is an example for self-organization and non-equilibrium pattern formation occurring dynamically at the solid-liquid interface. Natural or forced convection occurring in the liquid phase during solidification shows a distinct impact on the kinetics of the solidification process as well as on the resulting macro- and microstructures. The physical mechanism of the interaction between solidification and flow field is only insufficiently understood until now, however, the knowledge about that is of high technological importance.

The application of time varying magnetic fields can be considered as an effective tool to organize a well-defined flow structure in the liquid phase affecting the nucleation and solidification parameters. Once a flow occurs in the liquid melt during solidification, nucleation and grain growth are mainly governed by the convective transport of heat and solute. The consequences on the structure of solidified ingots are widely discussed in the literature. On the one hand it is known, that the application of mechanical or electromagnetic stirring promotes the formation of fine, equiaxed grains and promotes the columnar-to-equiaxed transition (CET) [1-5]. On the other hand, the occurrence of a forced flow during solidification may cause macrosegregation in cast alloys [6-8].

Numerical simulations of solidification processes have experienced a formidable growth during the last decades. As long as transport of heat and species during solidification is only controlled by diffusion the models to describe the distribution of temperature and solute concentration remain relatively tractable. Taking fluid flow into consideration makes theoretical predictions more difficult, because nonlinear terms appear in the conservation equations describing the coupling between velocity field, heat and mass transfer, and the solidification process. Serious predictions about the influence of the electromagnetic convection on the solidification require a detailed knowledge about the direction and intensity of the melt flow ahead of the solidification front. Three different flow regimes were recently identified by numerical simulations [9, 10], namely an initial adjustment phase, an inertial and an oscillatory phase. The latter is characterized by oscillations of toroidal vortices of the secondary flow and the appearance of Taylor-Görtler vortices along the lateral walls. These numerical predictions were confirmed by first velocity measurements during solidification using the ultrasound Doppler velocimetry (UDV) [11] revealing permanent modifications of the flow structure in the course of the solidification process.

2. Experimental procedure

The Sn-15wt%Pb alloy was prepared from 99.9%Pb and 99.9%Sn. The melt was solidified directionally from the bottom in a cylindrical stainless steel mould ($2R = 50$ mm, $H = 60$ mm) using the experimental set-up shown in Figure 1. By means of an electrical furnace the samples were melted and heated until a temperature of 300°C corresponding to a superheat of 90 K. The side walls of the mould were covered by thermal insulation to prevent heat losses in radial direction. The directional solidification was initialized by placing the mould on a water cooled copper chill. Mould and cooling chill were located concentrically inside a

magnetic inductor providing a rotating magnetic field (RMF). Magnetic intensities up to 25 mT were applied for a chosen frequency of 50 Hz.

During solidification the local temperatures were measured using an array of chromel-alumel thermocouples. Six thermocouples were positioned at different vertical positions along the axis of the sample and in the side walls of the mould, respectively. In order to monitor the heat removal from the sample two thermocouples were embedded in the bottom of the mould. The uncertainties of the temperature measurements in the considered range between 150°C and 350°C were estimated to be ≤ 1 K. Thermocouple voltages were recorded with scan rates up to 2 Hz by means of a multimeter DMM 2700 and a 20-channel differential multiplexer card 7700 (Keithley Instruments).

The solidified samples were sectioned longitudinally along its midplane. Milling was used to prepare the surface for metallographic treatment. The metallographic specimens were grinded on SiC-paper and subsequently polished in three steps. The etched specimens were examined by means of a metallographic microscope (Leitz Metallux 3).

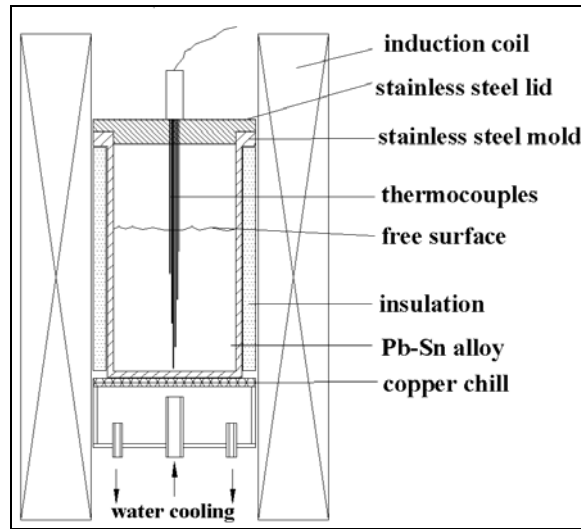


Fig. 1: Scheme of the experimental apparatus for directional solidification

3. Experimental results

A series of solidification experiments were conducted with variations of the magnetic field strength B . Simply spoken, the magnitude of the melt flow is represented by the corresponding Taylor number $Ta = \sigma \omega B^2 R^4 / 2 \rho \nu^2$ where ω stands for the frequency of the RMF and σ , ρ and ν denote the electrical conductivity, the density and the kinematic viscosity of the fluid, respectively. Other parameters such as cooling conditions were kept unchanged. Figure 2 shows cooling curves obtained at the thermocouple position $z = 24$ mm for different Taylor numbers Ta . This comparison reveals the acceleration of the cooling process in the liquid phase. The Liquidus temperature $T_L = 210^\circ\text{C}$ is reached earlier with growing Ta . However, the convection has no visible effect on the time when the solidification is completed at $T_S = 183^\circ\text{C}$. In this context we observe the development of a temperature plateau becoming obvious for $Ta > 10^7$. Consequently, a reinforcement of the convection in the bulk melt results in a prolongation of the local solidification time $\tau = t(T_S) - t(T_L)$ corresponding to a broadening of the mushy layer. The cooling rate $-dT/dt$ and the temperature gradient G_L were deduced from the cooling curves at the moment when the Liquidus temperature is registered at the respective position. The procedure described by Gandin [12] was used to roughly estimate the temperature gradient G_L ahead of the Liquidus isotherm. Results

representing the cooling rate and the temperature gradient are displayed in the Figures 3 and 4, respectively. The cooling rate increases with increasing Taylor number at the lowest thermocouple position indicating an increase of the heat transfer coefficient due to convection. In contrast to this finding a decrease of the cooling rate in the centre of the ingot can be detected. This phenomenon is related to the occurrence of the temperature plateau in the cooling curves displayed in Figure 2. The temperature gradients shown in Figure 4 are normalized with the value obtained for $Ta = 0$. A distinct reduction of the temperature gradient with growing Taylor number becomes visible indicating a thermal homogenisation of the melt. This tendency can be recognized for all thermocouple positions.

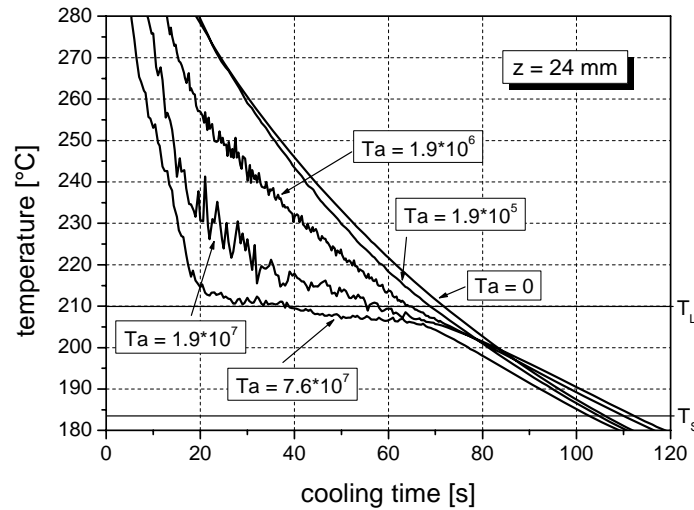


Fig. 2: Cooling curves measured during solidification for different Taylor numbers at the thermocouple position $z = 24 \text{ mm}$

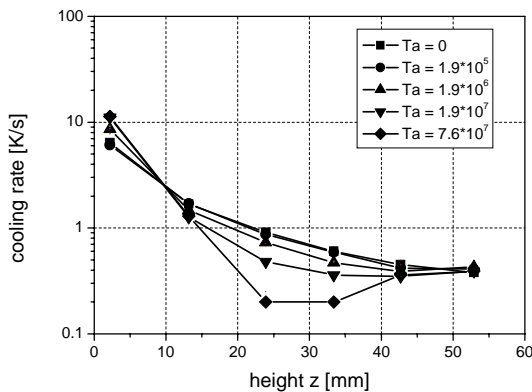


Fig. 3: Cooling rate obtained at various positions along the ingot axis for different Taylor numbers Ta

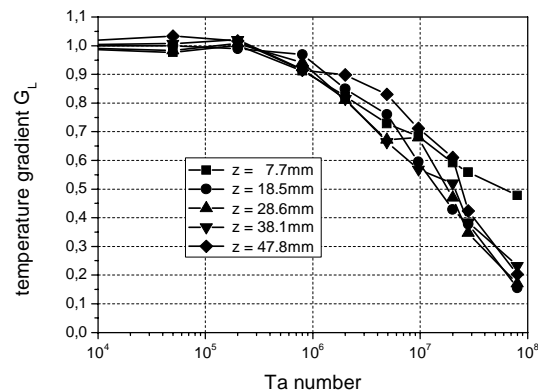


Fig. 4: Temperature gradient G_L ahead of the Liquidus isotherm as a function of the Taylor number Ta for different positions on the ingot axis (related to the value at $Ta = 0$)

The macrostructure was evaluated on the angular surface of the samples. In all experiments, where the solidification was carried out without RMF application, columnar grains expand over the entire height of the ingot parallel to the direction of the heat flux as displayed in Figure 5. A columnar-to equiaxed transition (CET) becomes visible if the melt is stirred

electromagnetically at Taylor numbers larger than $2 \cdot 10^5$. An enhancement of melt convection promotes the growth of equiaxed grains as shown by shifting the vertical position of the CET downwards with increasing Taylor number [5]. Moreover, the melt agitation obviously provokes a grain refinement which becomes more pronounced with increasing Taylor number. In the case of the lead-rich and the tin-rich alloys, respectively, the stirring of the melt causes an inclination of the columnar grains (see Figure 5). The melt was always rotating in clockwise direction, that means the grains grow towards the primary flow. The tilting of the columnar structure can be explained by the convective transport of solute rejected from the vicinity of the columnar front into the bulk region of the melt [13] leading to a steeper gradient of concentration at the upstream side as well as in the front of the dendrite tips. The corresponding enhancement of the constitutional undercooling triggers a growth of the dendritic structure towards the flow direction.



*Fig. 5: Macrostructures visualized on the angular surface of the solidified samples:
 $Ta = 0$ (left) and $Ta = 4.8 \cdot 10^6$ (right)*

A further experiment was performed starting the solidification at first without RMF. Then, the electromagnetic forcing was switched on with a certain delay. Figure 6 displays a detail of the microstructure obtained from the region where the solidification took place at that moment when the magnetic field was switched on. Dendrites with trunks growing vertically dominate the structure if the forced convection is absent. As soon as the flow comes up the secondary arms of the dendrites continue to grow towards the approaching flow instead of the primary trunks.

Moreover, the mechanism described above is also responsible for macrosegregation effects. Figure 7 shows a larger area of the same longitudinal section as already presented in Figure 6. Once the forced convection was initiated, an enrichment of eutectic alloy was found at the sample axis forming channel-like segregations. This phenomenon is attributed to the secondary flow inside the liquid phase. The vortex just above the mushy zone carries the excess of solute which is rejected ahead of the solidification front towards the middle of the liquid phase resulting in a depletion of tin in the region around the axis of rotation [14].

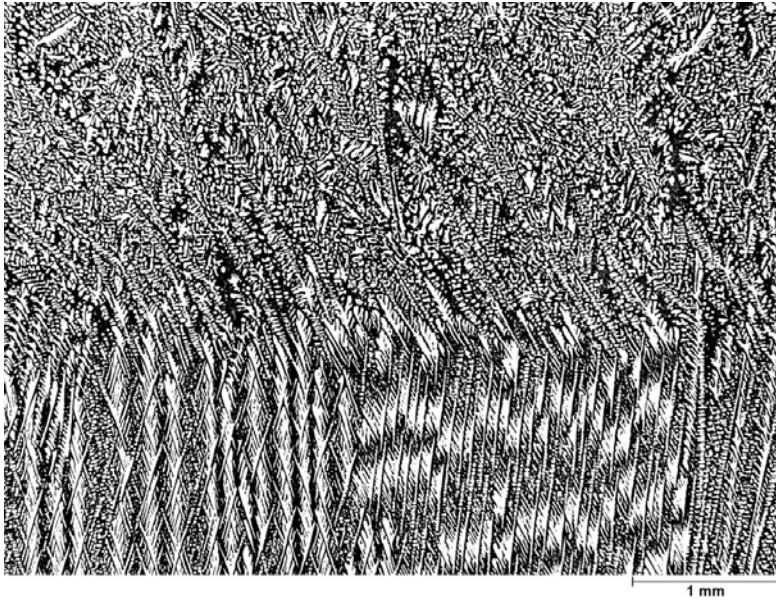


Figure 6: Micrograph showing the transition from parallel to inclined growth of the columnar dendrites caused by the initiation of the RMF-driven convection ($Ta = 2 \cdot 10^6$)



Figure 7: Channel-like segregation in the centre of a longitudinal section (same sample as Fig. 6)

4. Conclusions

The role of melt convection has been studied during directional solidification of Pb-Sn alloys. The melt was electromagnetically agitated using a rotating magnetic field (RMF). The following major conclusions can be drawn:

The forced convection influences significantly the concentration as well the temperature profile ahead of the solidification front. The convective transport of solute reduces the thickness of the solutal boundary layer. The electromagnetic stirring encourages a thermal homogenization of the liquid bulk zone. Therefore, the magnetic Taylor number Ta appears as a further, fundamental parameter like the cooling rate, the temperature gradient or the alloy composition controlling the level of undercooling and the length of the undercooled region ahead of the solidification front. The effect of the electromagnetic melt agitation can be verified both in the macro- and microstructure. The applied RMF provokes a distinct grain refinement for all considered alloy compositions. Equiaxed growth has shown to be encouraged by a forced convection in the melt. Therefore, a flow effect can be supposed both on the presence of nuclei in the melt and suitable conditions allowing them to grow in competition with the columnar front. The melt convection during solidification also results into characteristic segregation patterns. Therefore, an optimization of the flow structure is

required in order to achieve solidified ingots with an optimal microstructure, particularly composed of fine, equiaxed grains without macrosegregation.

References

- [1] G.S. Cole, G.F. Bolling: Enforced fluid motion and the control of grain structures in metal castings, *Trans. Met. Soc. AIME* 239 (1967) 1824-1835
- [2] D.B. Spencer, R. Mehrabian and M.C. Flemings, Rheological behavior of Sn-15 Pct Pb in the crystallization range, *Met. Trans.* 3 (1972) 1925-1932.
- [3] W.C. Johnston, G.R. Kofler, S. O'Hara, H.V. Ashcom, W.A. Tiller, Grain Refinement via Electromagnetic Stirring During Solidification, *Trans. Met. Soc. AIME* 233 (1965) 1856-1860
- [4] W.D. Griffiths and D.G. McCartney, The effect of electromagnetic stirring during solidification on the structure of Al-Si alloys, *Mater. Sci. Eng. A* 216 (1996) 47-60
- [5] B. Willers, S. Eckert, U. Michel, I. Haase, G. Zouhar, The columnar-to equiaxed transition in Pb-Sn alloys affected by electromagnetically driven convection, *Mater. Sci. Eng. A* 402 (2005) 55-65
- [6] C. Beckermann, Modelling of macrosegregation: applications and future needs, *Int. Mat. Rev.* 47 (2002) 243-261
- [7] P.J. Prescott, F.P. Incropera and D.R. Gaskell, Convective Transport Phenomena and Macrosegregation During Solidification of a Binary Metal Alloy: II-Experiments and Comparisons With Numerical Predictions, *Trans. ASME* 116 (1994) 742-749
- [8] J.K. Roplekar and J.A. Dantzig, A study of solidification with a rotating magnetic field, *Int. J. Cast Metals Research*, 14 (2001) 79-98
- [9] P.A. Nikrityuk, K. Eckert and R. Grundmann, A numerical study of unidirectional solidification of a binary metal alloy influenced by a rotating magnetic field, *Int. J. Heat Mass Transfer* (2006) article in press
- [10] P.A. Nikrityuk, K. Eckert and R. Grundmann, Numerical study of spin-up dynamics of a liquid metal stirred by rotating magnetic fields in a cylinder with the upper free surface, *Magnetohydrodynamics* 40 (2004) 127-146
- [11] S. Eckert, B. Willers, G. Gerbeth, Measurements of the Bulk Velocity during Solidification of Metallic Alloys, *Metall. Mater. Trans.* 36 A (2005) 267-270
- [12] Ch.-A. Gandin, *Acta Mater.* 48 (2000) 2483-2501
- [13] B. Chalmers, *Principles of Solidification*, John Wiley & Sons, New York, 1964
- [14] S. Eckert, B. Willers, P.A. Nikrityuk, K. Eckert, U. Michel, G. Zouhar, Application of a rotating magnetic field during directional solidification of Pb-Sn alloys: Consequences on the CET, *Mater. Sci. Eng. A* 413-414 (2005) 211-216

Acknowledgement

The research is supported by the Deutsche Forschungsgemeinschaft (DFG) in form of the SFB 609 "Electromagnetic Flow Control in Metallurgy, Crystal Growth and Electrochemistry" and under grant GE 682/10-1/2. This support is gratefully acknowledged.

A SIMPLE MODEL OF EARTH'S MAGNETIC FIELD REVERSALS

Frank Stefani, Gunter Gerbeth, and Uwe Günther

1. Introduction

There is ample paleomagnetic evidence that the Earth's magnetic field has reversed its polarity many times. The mean rate of reversals varies from nearly zero during the so-called superchrons to approximately 5 per Myr in the present. Many observations suggest a distinct asymmetry of reversals with the decay being much slower than the following recreation of the dipole with opposite polarity [1,2]. Observational data also indicate a possible correlation of the field intensity with the interval between subsequent reversals [2,3]. A third hypothesis concerns the bimodal distribution of the Earth's virtual axial dipole moment (VADM) with two peaks at approximately $4 \times 10^{22} \text{ Am}^2$ and at twice that value [4]. Although these reversal features are still controversially discussed, it is worthwhile to ask how they could be reflected by dynamo theory.

In a series of recent papers [5,6,7], we have analysed a simple mean-field dynamo model with a spherically symmetric helical turbulence parameter α with regard to the appearance of typical reversal features. Surprisingly, all of them turned out to be explainable by the peculiar magnetic field dynamics in the vicinity of an exceptional point of the spectrum of the non-selfadjoint dynamo operator where two real eigenvalues coalesce and continue as a pair of complex conjugate eigenvalues [8]. This exceptional point is typically associated with a nearby local maximum of the growth rate dependence on the magnetic Reynolds number. It is the negative slope of this curve between the local maximum and the exceptional point that makes stationary dynamos vulnerable to some prevailing noise. This way, the system can leave a (quasi-)stable state towards the exceptional point and beyond into the oscillatory branch where the polarity transition occurs. An apparent weakness of this reversal model, the necessity to fine-tune the magnetic Reynolds number and/or the radial profile $\alpha(r)$ in order to adjust the operator spectrum in an appropriate way, was overcome in [6]. For strongly supercritical dynamos we identified a general tendency of the exceptional point and the associated local maximum to move close to the zero growth rate line where the indicated reversal scenario can be actualised. In [7] we compared paleomagnetic data of five recent reversals with typical numerical time series resulting from our model. It was shown that it is again the strong super-criticality of the considered dynamo models that may explain the typical time scales of the observed asymmetric reversals.

In the present report we give an overview about our recent activities towards a better understanding of geomagnetic polarity reversals.

2. The model

We consider a simple mean-field dynamo model with a spherically symmetric, isotropic helical turbulence parameter α . The induction equation for the magnetic field \mathbf{B} reads

$$\frac{\partial \mathbf{B}}{\partial \tau} = \nabla \times (\alpha \mathbf{B}) + \frac{1}{\mu_0 \sigma} \Delta \mathbf{B} \quad , \quad (1)$$

with magnetic permeability μ_0 and electrical conductivity σ . For the Earth's outer core we will assume the magnetic diffusion time $\tau_{diff} = \mu_0 \sigma R^2$ to be ~ 200 kyr. The divergence-free magnetic field \mathbf{B} can be decomposed into a poloidal and a toroidal component, according to $\mathbf{B} = -\nabla \times (\mathbf{r} \times \nabla S) - \mathbf{r} \times \nabla T$. The defining scalars S and T are expanded in spherical harmonics of degree l and order m with expansion coefficients $s_{l,m}(r, \tau)$ and $t_{l,m}(r, \tau)$. For the envisioned spherically symmetric and isotropic α^2 dynamo model, Eq. (1) decouples for each degree l and order m into the following pair of equations:

$$\frac{\partial s_{l,m}}{\partial \tau} = \frac{1}{r} \frac{\partial^2}{\partial r^2} (r s_{l,m}) - \frac{l(l+1)}{r^2} s_{l,m} + \alpha(r, \tau) t_{l,m} \quad (2)$$

$$\frac{\partial t_{l,m}}{\partial \tau} = \frac{1}{r} \frac{\partial}{\partial r} \left[\frac{\partial}{\partial r} (r t_{l,m}) - \alpha(r, \tau) \frac{\partial}{\partial r} (r s_{l,m}) \right] - \frac{l(l+1)}{r^2} [t_{l,m} - \alpha(r, \tau) s_{l,m}] \quad (3)$$

The boundary conditions read $\partial s_{l,m} / \partial r |_{r=1} + (l+1) s_{l,m}(1) = t_{l,m}(1) = 0$. In the following we consider only the axial dipole field with $l=1$ and $m=0$ and will henceforth use the shorthand notation $s := s_{1,0}$ and $t := t_{1,0}$.

We will focus on a particular kinematic radial profile $\alpha_{kin}(r) = 1.916 \cdot C \cdot (1 - 6r^2 + 5r^4)$, which is characterized by a sign change along the radius.. Our main motivation for this choice is that quite similar profiles had been shown to exhibit oscillatory behaviour [9]. As was shown in [10], such sign changing α profiles seem indeed to be relevant for the Earth's outer core. Under the influence of the self-excited magnetic field the kinematic α profile must be reduced (or "quenched", which is the common notion in dynamo theory) in order to ensure saturation of the dynamo process. We assume here a special algebraic quenching by the magnetic field energy density, averaged over spherical angles, which can be expressed by $E_{mag}(r, \tau) = 2r^{-2} s^2(r, \tau) + r^{-2} (\partial(rs(r, \tau)) / \partial r)^2 + t(r, \tau)$. In addition to this quenching, the $\alpha(r)$ profiles are perturbed by radial profiles of noise which are considered constant within a certain correlation time τ_{corr} . Physically, such a noise term can be interpreted as a consequence of changing boundary conditions for the flow in the core, but also as a substitute for the omitted influence of higher multipole modes on the dominant axial dipole mode. In summary, the time dependent profile $\alpha(r, \tau)$ entering Eqs. (2,3) is written as

$$\alpha(r, \tau) = \frac{1.916 \cdot C \cdot (1 - 6r^2 + 5r^4)}{1 + E_{mag}(r, \tau) / E_0} + \xi_1(\tau) + \xi_2(\tau) r^2 + \xi_3(\tau) r^3 + \xi_4(\tau) r^4 \quad (4)$$

with the noise correlation given by $\langle \xi_i(\tau) \xi_k(\tau + \tau_1) \rangle = D^2 \cdot (1 - |\tau_1| / \tau_{corr}) \cdot \Theta(1 - |\tau_1| / \tau_{corr}) \delta_{ik}$. C is the magnetic Reynolds number, D is the noise strength, and E_0 measures the mean magnetic energy density. The equation system (2-4) is time-stepped by means of an Adams-Bashforth method.

3. Numerical results

In order to understand the asymmetry of reversals and the correlation of field strength with interval duration, we start with the noise-free case. Figure 1 shows the magnetic field

evolution according to the equation system (2-4) for $D=0$ and different dynamo numbers C . The critical value of C for the onset of dynamo action is 6.78. The nearly harmonic oscillation for $C=6.8$ becomes more and more saw-tooth shaped for increasing C , with a clear asymmetry between the slow field decay and the fast field recreation during the reversal. At $C=7.24$ a transition to a steady dynamo has occurred.

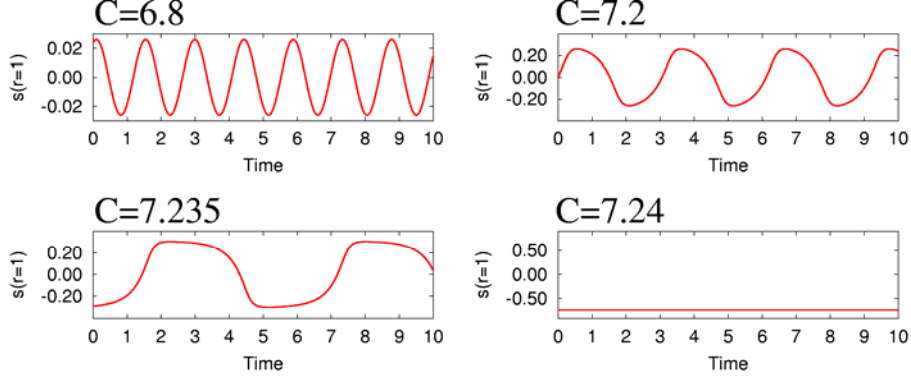


Fig. 1: Magnetic field evolution for the noise free case $D=0$.

In Fig. 2 we examine in detail the evolution of the magnetic field within approximately half a period of the anharmonic oscillation for the particular value $C=7.237$ that is only slightly below the transition from oscillatory to steady behaviour. Figure 2a shows the time dependence of the poloidal field component at the surface of the core, $s(r=1)$, during this half period, with the typical slow decay and the fast recreation of the field. This behaviour is analysed in detail at 9 selected instants τ_i ($i=1\dots 9$) for which the corresponding quenched profiles $\alpha(r, \tau_i)$ (Fig. 2c) and the instantaneous fields $s(r, \tau_i)$ (Fig. 2d) are depicted. We see in Fig. 2c that $\alpha(r)$ undergoes only slight changes during the anharmonic oscillation and that it comes very close to the unquenched, kinematic $\alpha_{kin}(r)$ (denoted by K) when the magnetic field is small in the middle of the reversal (approximately at instants 5 and 6).

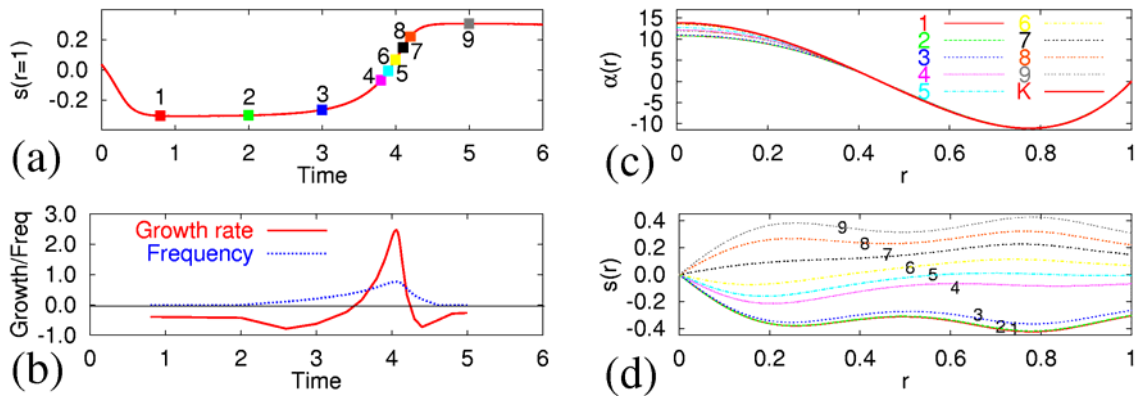


Fig. 2: Explanation of the field dynamics for $C=7.237$ and $D=0$.

To understand this sort of relaxation oscillation better, it is instructive to plug the instantaneous $\alpha(r, \tau_i)$ profiles into an eigenvalue solver (for which the time derivatives on the left hand sides of Eqs. (2) and (3) are replaced by $\lambda s(r)$ and $\lambda t(r)$, respectively, with $\lambda = p + 2\pi i f$). Figure 2b shows the resulting instantaneous growth rates p and the

instantaneous frequencies f during the half-oscillation. Evidently, the reversal starts with a very slow field decay (slightly negative p) which, however, accelerates itself and drives the system into an oscillatory behaviour (f becomes non-zero within $2.0 < \tau < 4.5$). Near $\tau = 4$, when the quenching of α is weak, the instantaneous growth rate reaches rather high values. Later we will see that for strongly supercritical dynamos these high growth rates result in a field dynamics that is much faster than what would be expected from the diffusion time-scale.

It is instructive to look not only on the time sequence of instantaneous eigenvalues as we did in Fig. 2b, but to identify the position of these eigenvalues relative to the exceptional point of the spectrum of the dynamo operator. For the considered $C=7.237$, we analyse in Fig. 3a the growth rates for the profiles $\alpha(r, \tau_i) = 1.916 \cdot C \cdot C^* \cdot (1 - 6r^2 + 5r^4) / (1 + E_{mag}(r, \tau_i) / E_0)$, where the additional scaling factor C^* has been introduced in order to identify the position of the eigenvalue (at the dashed vertical line $C^*=1$) relative to the exceptional points E_i . At the exceptional point E_k of the kinematic $\alpha_{kin}(r)$, the first eigenvalue branch K1 coalesces with the second branch K2 and both continue as a pair of complex conjugate eigenvalues. For all other curves ($i=1\dots 9$), only the exceptional points are indicated by E_i whereas the branches of the second eigenvalue have been omitted. In this framework, a reversal can be described as follows: At the instant 1, the slightly negative growth rate p is located close to the maximum of the non oscillatory branch. The resulting slow field decay accelerates itself, since the system moves down (instant 2) from the maximum of the real branch towards the exceptional point. Then the system enters the oscillatory branch (3-7). Finally the system moves back again (8,9) but with opposite polarity.

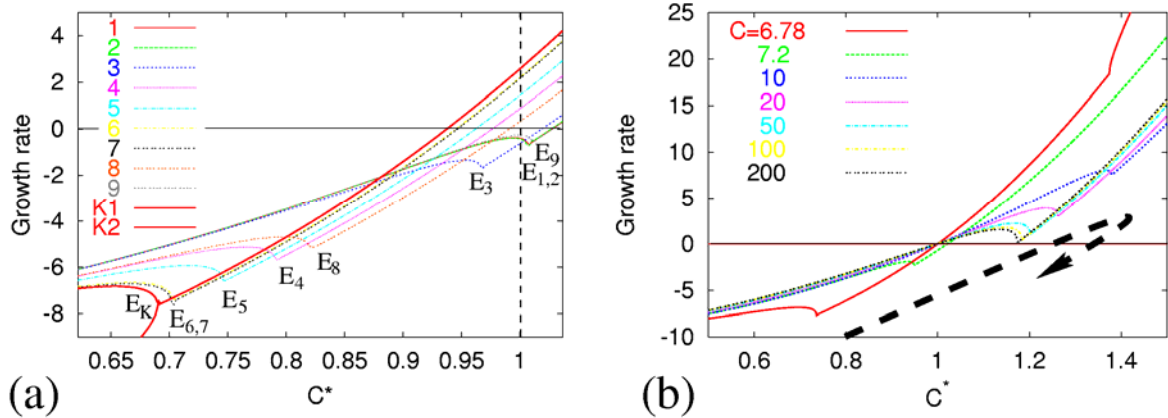


Fig. 3: The role of exceptional points for the understanding of reversals. (a) Growth rate dependence on C^* for the kinematic profile and for the quenched $\alpha(r, \tau_i)$ profiles. (b) Growth rates for the saturated α profiles with $C=6.78, 7.2, 10, 20, 50, 100, 200$.

The transition point between oscillatory and steady dynamos ($C=7.239$) is characterized by the fact that the maximum of the non-oscillatory branch crosses the zero growth rate line. Beyond this point, the field is growing rather than decaying, leading to a stable fixed point somewhere to the left of the maximum of the non-oscillatory branch, and hence to a non-oscillatory dynamo (cf. the case $C=7.24$ in Fig. 1). If noise comes into play it will soften the sharp border between oscillatory and steady dynamos. This means, in particular, that even above the transition point, the noise can trigger a jump to the right of the maximum from where the described reversal process can start (Fig. 2).

Having identified the exceptional point and the nearby local maximum as the spectral features that are responsible for both the slow decay before and the fast recreation of the field after the polarity transition, one may ask now why the operator of the actual geodynamo should possess just such a special spectrum. A possible answer to this question was given in [6] and is illustrated in Fig. 3b. Roughly speaking, highly supercritical dynamo (with $C \gg C_{\text{crit}}$) have a tendency to saturate in a state for which the exceptional point and its associated local maximum are situated close to the zero growth rate line. Interestingly, this happens independently on whether the exceptional point for the original $\alpha_{kin}(r)$ profile was above the zero growth rate line or below it. Our example belongs to the second type. Starting from the kinematic $\alpha_{kin}(r)$ ($C=6.78$), for which the exceptional point is well below the zero line, it rises rapidly above zero to a maximum value, but for even higher C it moves back towards the zero line.

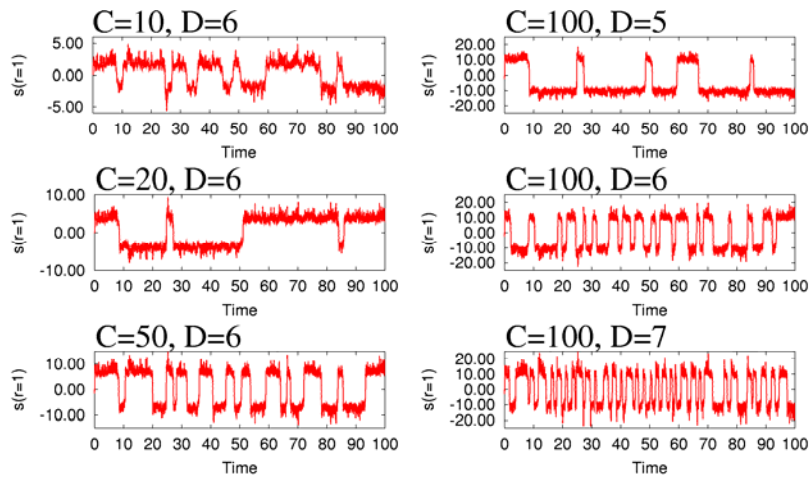


Fig. 4: Time series of the magnetic field for varying magnetic Reynolds numbers C and noise strengths D .

Without noise ($D=0$) and for $C > 7.239$, the position of the local maximum above the zero growth rate line leads to a steady dynamo. The presence of noise will sometimes bring the actual growth rate below zero, and then the indicated reversal process can start. A number of time series for different values of C and D is depicted in Fig. 4.

4. Comparison with paleomagnetic data

In this section we will validate if our model can explain real paleomagnetic data. For this purpose we have used recently published material about five reversals which occurred during the last two million years [3]. In Fig. 5a we show the virtual axial dipole moment (VADM) during the 80 kyr preceding and the 20 kyr following a polarity transition for five reversals from the last 2 million years, and their average. In all five individual curves, as well as in their averages, the asymmetry of the reversal process is clearly visible. The dominant features are a field decay over a period of 50-80 kyr and a rather sharp recreation of the field with opposite polarity within 5-10 kyr.

It has been an old-standing puzzle to explain in particular this fast recreation when a diffusive timescale of 200 kyr has to be taken into account. A possible solution of this problem is to assume a turbulent resistivity which is much larger than the molecular resistivity. However, this assumption which is hardly justified by physical arguments is by no means necessary to explain the asymmetry. Figure 5b exhibits the average curve of Fig. 5a together with four

average curves resulting from our numerical simulations. Apart from the only slightly supercritical case $C=8$, $D=1$, which provides a much too slow magnetic field evolution, the other examples with $C=20$, 50 , 100 and $D=6$ show very realistic time series with the typical slow decay and fast recreation. As noted above, the fast recreation results from the fact that in a small interval during the transition the dynamo operates with a nearly unquenched $\alpha(r)$ profile which yields, in case that the dynamo is strongly supercritical, rather high growth rates.

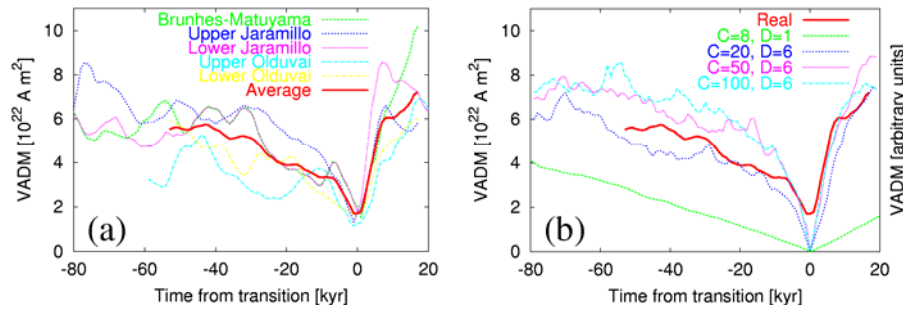


Fig. 5: Comparison of paleomagnetic reversal data (a) and numerically simulated ones (b).

5. Outlook

We have shown that a simple spherically symmetric α^2 dynamo model exhibits a number of features which are typical for Earth's magnetic field reversals, in particular an asymmetric shape. As it does not include the necessary North-South asymmetry of α we cannot claim that our model is an appropriate model of the geodynamo. Nevertheless, since the basic mechanism is not restricted to the particular mean-field model, it should be possible to identify it also in more realistic dynamo models.

References

- [1] J.-P. Valet, L. Meynadier (1993), Geomagnetic field intensity and reversals during the past 4 million years, *Nature*, 366, 238
- [2] J.-P. Valet, L. Meynadier (2005), Geomagnetic dipole strength and reversal rate over the past two million years, *Nature*, 435, 802
- [3] J. A. Tarduno, R. D. Cottrell, A. V. Smirnov (2001), High geomagnetic intensity during the mid-Cretaceous from Thellier analyses of single plagioclase crystals, *Science*, 291, 1779
- [4] R. Heller, R. T. Merrill, P. L. McFadden (2003), The two states of paleomagnetic field intensities for the past 320 million years, *Phys. Earth Planet. Inter.* 135, 211
- [5] F. Stefani, G. Gerbeth (2005), Asymmetric polarity reversals, bimodal field distribution, and coherence resonance in a spherically symmetric mean-field dynamo model, *Phys. Rev. Lett.* 94, Art. No.184506
- [6] F. Stefani, G. Gerbeth, U. Günther, M. Xu (2006), Why dynamos are prone to reversals, *Earth Planet. Sci. Lett.* 143, 828
- [7] F. Stefani, G. Gerbeth, U. Günther (2006), A paradigmatic model of Earth's magnetic field reversals (2006), *Magnetohydrodynamics*, in press
- [8] T. Kato, *Perturbation theory of linear operators*, Springer, Berlin, 1966
- [9] F. Stefani, G. Gerbeth (2003), Oscillatory mean field dynamos with a spherically symmetric, isotropic helical turbulence parameter α , *Phys. Rev. E* 67, Art. No. 027302
- [10] A. Giesecke, U. Ziegler, G. Rüdiger (2005), Geodynamo alpha-effect derived from box-simulations of rotating magnetoconvection, *Phys. Earth Planet. Int.* 152, 90

EVALUATION OF HOMOGENISATION ERROR IN TWO-GROUP NODAL DIFFUSION CALCULATION FOR VVER-1000 CORE

Petko Petkov¹ and Siegfried Mittag

1. Introduction

Two-group nodal (coarse mesh) neutron diffusion models are widely used in Light Water Reactor (LWR) core calculations. In these models, the reactor core is divided into coarse volume elements, i.e. the fuel assemblies are axially divided into layers to form (square or hexagonal) prisms that are called nodes. Node-homogenized two-group diffusion parameters (macroscopic cross sections and neutron diffusion coefficients), produced by transport-theory lattice codes, are input to the nodal reactor codes, such as DYN3D [1]. Applying nodal methods allows 3D full-core transient calculations in acceptable computing time.

In order to verify the accuracy of nodal codes, diffusion-theory benchmarks are applied. These mathematical benchmarks are usually defined by fine-mesh diffusion calculations, in which the assembly-size squares or hexagons are subdivided into much smaller sub-areas. In DYN3D verifications against this type of benchmark, the maximum relative deviation in the normalized assembly power distribution is about 1.5 %; k-eff differs not more than 30 pcm for VVER-1000 problems [1]. It should be borne in mind, however, that in such a benchmark reference solution, the same sets of node-homogenized two-group diffusion parameters, as applied in the nodal calculation, are used in all fine-mesh sub-areas of the respective nodes. Thus, errors arising from homogenization (and also from flux condensation and diffusion approximation) cannot be revealed by verification against these “homogeneous” diffusion-theory benchmarks.

Errors of such origin can be estimated by a comparison of nodal calculations to 2D heterogeneous multi-group transport-theory benchmarks, where the whole reactor core is divided into small regions according to the real material composition. Fuel pin cells are subdivided, applying the specific multi-group cross sections for the small material areas, thus taking into account full heterogeneity.

In a way, these benchmarks may be regarded as ideal experiments avoiding measurement errors. Obviously, they cannot replace real experiments. Errors in the basic nuclear cross sections and their pre-processing to be input to the transport codes, as well as errors due to approximations to solve the transport equation, make the difference between reality and the transport-theory benchmark solutions for a given core-reflector configuration.

2. Transport-theory calculations

The transport-theory code Mariko [2] has been applied for the definition of such benchmarks, because it is capable of solving two-dimensional heterogeneous full-core problems, including the radial reflector, with sufficient accuracy in an acceptable time. Mariko uses the method of characteristics for the solution of the neutron transport equation. The neutron source within each small region is not assumed to be spatially flat, but is approximated by a linear function. Moreover, the scattering anisotropy is explicitly treated (P1 scattering matrices). These two

¹ Institute for Nuclear Research and Nuclear Energy, Sofia (BG)

features allow the calculations to be accurate enough, namely in reactor regions with strong neutron flux gradients.

Reference transport-theory solutions have been computed by 23-group Mariko calculations. Mariko explicitly models the real 2D assembly and radial reflector geometry, thus ensuring adequate description of the spatial and energy interference effects. The lattice code Helios [3] was used to generate 23-group cross sections, needed for each material (fuel pin, cladding, coolant, absorber, reflector parts etc.). The same 23-group cross sections and the same Mariko transport solver have been applied to obtain homogenized two-group diffusion parameters for the fuel-assembly and reflector nodes. Single-assembly calculations are used for each fuel-assembly type according to the conventional calculation procedure [4]. Assembly discontinuity factors (ADFs), as defined by Smith [5], are determined from this solution. The B1 method [4] is applied for the calculation of the critical spectrum and corrected two-group diffusion coefficients.

3. Radial reflector treatment

Calculating accurate reaction rates near the radial edge of an LWR core poses a peculiar problem for nodal diffusion codes, owing to the strong gradients of the neutron flux in this region. The radial reflectors of Russian VVER are more complicated than those of Western PWR, due to the hexagonal shape of the VVER fuel assemblies. The detailed structure of a VVER-1000 reflector has been modeled in the Mariko calculations. Then, Koebke's equivalence theory (ET) [6] has been applied with the aim to get acceptable accuracy in the nodal method (DYN3D). Actually, for the radial reflector nodes, homogenized two-group diffusion parameters and reference discontinuity factors (RDFs), introduced by Smith [5], are calculated, using the reference Mariko transport-theory solution. Details of the 2D method applied to the hexagonal VVER core-reflector geometry are given in [7].

4. Benchmark definition for VVER-1000

The two-dimensional region of solution is a 60-degree sector (with 60-degree rotational symmetry) of the standard VVER-1000 reactor core, including also one ring of assembly-size radial reflector nodes. The assembly pitch is 23.72 cm. A hot-zero-power state at the moderator temperature of 302 °C and the boric acid concentration of 6.0 g/kg was chosen for the calculations. The benchmark represents a VVER-1000 first-cycle loading, at the beginning of cycle and all control rods withdrawn. The distribution of fuel assembly types is given in the figures below, the uppermost line in each hexagon meaning

- One-digit number: the year of presence in the core: first year (fresh fuel) in any case,
- Letter: fuel material type,
- Two-digit number: indicating the assembly numbering in the core sector.

The fuel material types are:

- A - 1.6 % enriched assembly without control rods,
- C - 3.0 % enriched assembly without control rods,
- E - profiled 4.4 % and 3.6 % enriched assembly with burnable absorber rods,
- F - 4.4 % enriched assembly with burnable absorber rods.

The radial reflector nodes are not shown in the figures. Owing to the complicated structure of the reflector, individual sets of homogenized two-group diffusion parameters and reference

discontinuity factors had to be generated for each of the 8 reflector nodes at the periphery of the 60-degree symmetry sector.

5. Results

The results calculated by DYN3D with assembly discontinuity factors (ADFs) for the fuel assemblies, but with unity discontinuity factors (UDFs) for the radial reflector nodes are given in Fig. 1. UDFs mean unity discontinuity factors, i.e. no correction of the reflector homogenization error is applied, simply by setting the discontinuity factors for the reflector-node boundaries to unity. The errors of the relative assembly-wise powers vary between -7.5 % and +7.8 %. The application of RDFs for the radial reflector nodes (Fig. 2) significantly decreases the errors to a range between -1.6 % and +1.1 %.

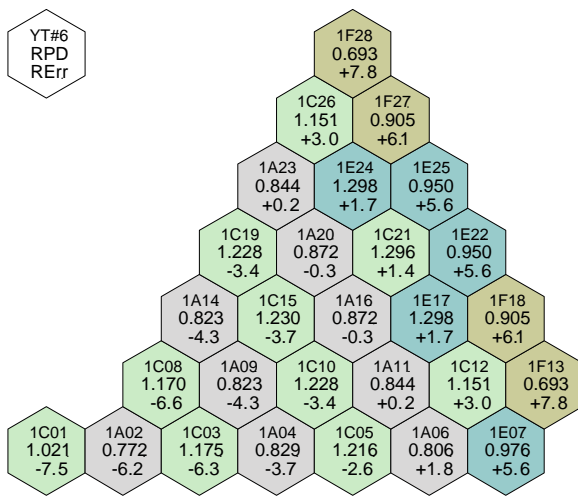


Fig. 1: Relative assembly-wise power distribution by DYN3D with assembly ADFs and reflector UDFs and relative deviations [%] from Mariko reference solution. k -eff error: +122 pcm.

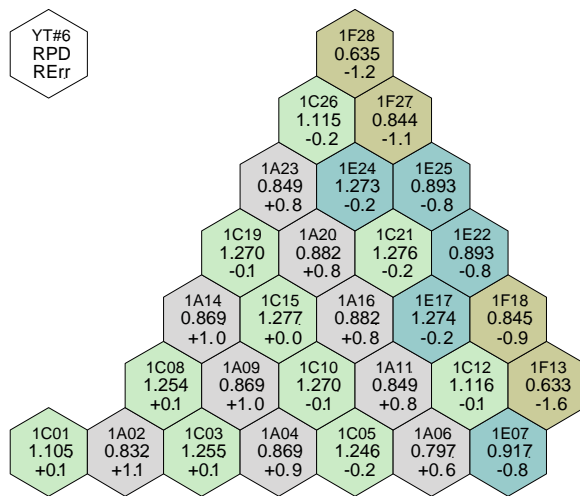


Fig. 2: Relative assembly-wise power distribution by DYN3D with assembly ADFs and reflector RDFs and relative deviations [%] from Mariko reference solution. k -eff error: -50 pcm.

If both the assembly and reflector discontinuity factors are set to unity, the agreement is still worse than in Fig. 1; the errors in the nodal power vary between -10.2 % and +12.6 %. The effect of the ADFs is mainly due the (more heterogeneous) E and F assemblies containing burnable absorber rods.

ADFs are easily calculated for the fuel assemblies by lattice codes producing the two-group diffusion parameters. Concerning the reflector nodes, it has been common practice in VVER calculations to use conventional core-reflector albedos instead. The albedos give the same good results as shown in Fig. 2, when calculated for the actual core loading. Using this set of albedos for a different core loading, however, namely if the enrichment and/or burnup at the radial core periphery is changed, can lead to additional errors above 2 % in the relative assembly power distribution. The reason for this behavior lies in the fact that the flux distribution near the reflector depends on the core, because a neutron can leave the core through a certain outer surface of a peripheral fuel assembly and re-enter the core through another one.

Additional benchmark tests have shown that reflector-node two-group diffusion parameters, including RDFs, are practically insensitive to the core loading, for which they have been calculated.

6. Conclusions

Errors arising from the radial-reflector-node homogenization in VVER-1000 core calculations can clearly surpass errors introduced by the coarse-mesh (nodal) method alone. For the VVER-1000 state studied in this paper, this homogenization error can be reduced to an appropriate level by applying either Koebke's equivalence theory (ET) to the reflector nodes or core-reflector (conventional) albedos. The ET method, using RDFs, is the better alternative, due to its insensitivity to the core loading.

References

- [1] U. Grundmann and F. Hollstein (1999), A Two-Dimensional Intranodal Flux Expansion Method for Hexagonal Geometry, *Nucl. Science and Engineering*, 133, 201.
- [2] P. T. Petkov (2002), Development of a Neutron Transport Code for Many-Group Two-Dimensional Heterogeneous Calculations by the Method of Characteristics, *Proc. X Symposium of AER* (p. 271), Moscow, Russia.
- [3] J. J. Casal et al. (1991), HELIOS: Geometric Capabilities of a New Fuel Assembly Program. *Proc. Int. Topical Meeting on Advances in Mathematics, Computations and Reactor Physics*, Vol. 2 (p. 10.2.1-1), Pittsburgh, USA.
- [4] R. J. J. Stamm'ler and M. J. Abbate (1983), *Methods of Steady-State Reactor Physics in Nuclear Design*. Academic Press, London 1983.
- [5] K. S. Smith (1986), Assembly Homogenization Techniques for Light Water Reactor Analysis. *Prog. Nucl. Energy* 17, 303.
- [6] K. Koebke (1981), Advances in Homogenization and Dehomogenization. *Proc. Int. Topical Meeting on Advances in Math. Methods for the solution of Nucl. Eng. Problems*, Vol. 2 (p. 59), Munich, Germany.
- [7] S. Mittag, P. T. Petkov, and U. Grundmann (2003), Discontinuity Factors for Non-Multiplying Material in Two-Dimensional Hexagonal Reactor Geometry, *Annals of Nuclear Energy*, 30, 1347.

CORE DESIGN AND TRANSIENT ANALYSES FOR WEAPONS PLUTONIUM BURNING IN VVER-1000 TYPE REACTORS

Ulrich Rohde, Ulrich Grundmann, Yaroslav Kozmenkov¹, Valery Pivovarov¹, and Yuri Matveev¹

1. Introduction

The presented core calculations are aimed at the demonstration of the feasibility of weapon-grade plutonium burning in VVER-1000 type reactors with emphasis on safety aspects of the problem. Particular objectives of weapon-grade Pu burning are the net burning of fissile Pu isotopes in general, but also the conversion of the Pu vector of the fuel from weapon-grade to reactor plutonium. While weapon-grade plutonium is almost pure fissile ²³⁹Pu, reactor plutonium is a mixture of the Pu isotopes 238, 239, 240, 241 and 242, which is not suitable for weapons. The even number isotopes are decaying spontaneously releasing neutrons, which would make a bomb un-controllable. Moreover, ²³⁸Pu decays with high heat release emitting alpha radiation. An amount of perhaps about 200 tons of weapon-grade plutonium has piled up world wide. Russia has declared to burn or convert about 34 tons of weapon-grade Pu [1].

The reactor physics analyses on Pu burning consist on the following steps:

- Fuel element design
- Core design
- Burn-up calculations to get the equilibrium cycle
- Analysis of reactivity initiated accidents (RIA)

The static design calculations are aimed at the proof that the design limits for the reactor core like maximum power peaking factors, maximum linear rod power or maximum coolant heat-up are met. The analysis of RIA has to demonstrate that no safety limits are exceeded during the transients. The background of the RIA analyses is the fact, that core loadings with MOX fuel are characterized by specific reactivity features, which are different from UOX fuel loadings:

- The Doppler coefficient of the reactivity is more negative, since plutonium isotopes have large resonance capture. A high Doppler feedback supports inherent safety.
- The higher total absorption cross sections for Pu-239 and Pu-241 than for U-235 lead to a harder spectrum in MOX fuels. MOX fuel disposes of a large negative moderator temperature feedback coefficient because of the stronger effect of the moderator in this harder spectrum.
- The lower level of thermal flux in MOX fuel reduces the efficiency of the absorbers. This leads to lower effectiveness of boron, burnable absorbers and control rods.
- The delayed neutron fraction and prompt neutron lifetime are smaller than those in UO₂ fuel. This leads to a smaller absolute reactivity margin to super-prompt criticality.

The work was performed within a research project on scientific-technical co-operation between Germany and Russia funded by BMWA². Reactor characteristics in the equilibrium cycle were calculated by using the three-dimensional diffusion code ACADEM developed in IPPE [2]. Transient analysis was performed with the 3D dynamics code DYN3D [3]. Genera-

¹ Institute of Physics and Power Engineering (IPPE), Obninsk (Russia)

² Bundesministerium für Wirtschaft und Arbeit

tion of neutronic data for the codes ACADEM and DYN3D was performed using the code WIMSD5 [4] connected to the nuclear data library developed in IPPE.

2. Core design and burn-up calculations

Two fuel compositions were studied: (a) standard uranium dioxide and (b) MOX-fuel utilizing weapon-grade plutonium. Three options of the core loading were considered:

- Option 1 – 100% loading with UO₂ fuel,
- Option 2 – 50% UO₂ + 50% MOX loading,
- Option 3 – 100% loading with MOX fuel.

Fuel elements with profiled enrichment and gadolinium burnable absorber were considered for all loading options. The outer fuel pins have a lower enrichment resp. plutonium content compared with the internally located pins. The fuel assemblies (FA) include 6 or 12 rods with gadolinium. The content of Gd₂O₃ in the special UO₂ fuel elements is 5 w/o. The uranium enrichment of Gd rods for all options is 3%. Control rods or burnable absorbers can be assigned to 18 water-filled positions per fuel assembly.

The equilibrium fuel cycle is characterized by the following features:

- loading of the same FA types (with respect to enrichment, MOX and Gd content) to the same positions in the core in each cycle,
- stabilized cycle duration,
- stabilized histories of boron concentration and peaking factors.

The equilibrium cycle is modeled by a cycling loading the same types of fuel elements and performing the same shuffling operations in each cycle. Each FA stays in the core three or four cycles. All fuel cycle calculations are based on the same operational history of the reactor during the cycle.

The main results of the analyses performed for the three defined options of core loading are presented in Table 1. As follows from the table, the equilibrium cycle length is between 284 and 288 effective full power days (EFPD). The critical boron concentration at the beginning of the cycle is between 1063 and 1775 ppm. For all considered loading options the radial power peaking factor (K_q) does not exceed the value of 1.35, representing the upper limit allowed by the Russian regulatory rules. In general, the absolute control group worth (in %) is higher at EOC than at BOC, because at EOC there is less absorber material in the core (boron, Gd). However, the control group worth in β_{eff} units is influenced by the change of β_{eff} with burn-up. For the UO₂ and the mixed loading, β_{eff} is decreased with increasing burn-up because of net Pu breeding. In the case of pure MOX loading, β_{eff} is increasing with burn-up, because there is less Pu in the core at EOC (net burning). The power peaking factors are lower at EOC because of the compensating effect of the burn-up.

Steady state core calculations have also been performed using the DYN3D code with the same cross section input data as for ACADEM. The differences in the radial power distributions are very small (average 1 – 2 %, maximum 4 %). A fine mesh diffusion calculation with 24 mesh points per fuel assembly in the horizontal plane was performed with ACADEM, while DYN3D is based on the nodal expansion method. Some differences of the calculated reactivity parameters occurred between DYN3D and ACADEM, as can be seen from table 1.

Looking at the total Pu balance for the three loading options it can be seen, that a net burning of Pu is performed only for the 100 % MOX loading. Even for the mixed loading with 50 % MOX, there is no net burning. However, the Pu vector is transformed from weapon grade to reactor plutonium.

Table 1: Main characteristics of fuel loadings in equilibrium cycle

Characteristics		Options		
		1	2	3
Initial concentration of boric acid under operating conditions, ppm	Xe=0 ACADEM (DYN3D) ³ Xe _{eq} ⁴	1430 1063(1100)	1649 1216(1269)	2363 1775(1779)
Fuel cycle length (days)		287	284	288
Value of radial power peaking factor K _q	BOC	1.31	1.33	1.35
	MAX	1.32	1.34	1.35
	EOC	1.27	1.31	1.28
Value of total power peaking factor K _V	BOC	1.61	1.60	1.62
	MAX	1.61	1.60	1.62
	EOC	1.49	1.50	1.39
Worth of working group of the control rods (%) at ACADEM (DYN3D)	BOC	0.74 (0.75)	0.59 (0.65)	0.59 (0.63)
	EOC	0.77 (0.77)	0.81 (0.83)	0.65 (0.68)
Reactivity coefficient of the moderator temperature dp/dγ _{H2O} ×10 ⁻⁴ /K	BOC	-2.17	-3.14	-3.36
	EOC	-6.11	-6.34	-6.63
Reactivity coefficient of the fuel temperature dp/dT _{fuel} ×10 ⁻⁵ /K	BOC	-2.63	-2.76	-2.90
	EOC	-2.92	-2.93	-2.96
Power reactivity coefficient caused by fuel temperature and moderator temperature, dp/dN×10 ⁻⁵ /MW	BOC	-0.58	-0.65	-0.70
	EOC	-0.83	-0.84	-0.86
Reactivity coefficient of the boron concentration, dp/dC _B ×10 ⁻⁵ /ppm	BOC	-7.33	-5.52	-3.82
	EOC	-8.54	-6.94	-5.00
Delayed neutron fraction, β _{eff} ×10 ⁻²	BOC	.635 (.622)	.509 (.494)	.370 (.371)
	EOC	.562 (.563)	.493 (.480)	.406 (.404)
Worth of working group of the control rods (β _{eff}) at ACADEM (DYN3D)	BOC	1.17 (1.21)	1.16 (1.32)	1.59 (1.70)
	EOC	1.37 (1.37)	1.64 (1.73)	1.60 (1.68)
Annual reactor loading, kg·year ⁻¹	²³⁵ U	789.4	434.0	61.2
	²³⁸ U	20345	19846	19784
	²³⁹ Pu		396.8	805.1
	²⁴⁰ Pu		25.5	51.7
	²⁴¹ Pu		0.44	0.89
	²⁴¹ Am		2.12	4.31
Annual reactor unloading, kg·year ⁻¹ :	²³⁵ U	194.3	110.9	26.5
	²³⁶ U	97.8	53.4	6.7
	²³⁸ U	19713	19237	19180
	²³⁸ Pu	3.94	2.68	1.27
	²³⁹ Pu	129.0	225.8	311.3
	²⁴⁰ Pu	54.5	110.8	169.1
	²⁴¹ Pu	34.6	66.2	99.9
	²⁴² Pu	13.4	18.9	26.3
	²⁴¹ Am	0.94	2.85	4.82
Total plutonium balance (unloading-loading), kg·year ⁻¹		235.5	1.6	-249.8

³ result obtained by ACADEM (result obtained by DYN3D)

⁴ xenon-free core and core with xenon at equilibrium

The changes of the reactivity coefficients of the moderator temperature, fuel temperature and boron acid concentration as well as the change of the β_{eff} value in the course of the fuel cycle are shown in figures 1 and 2. The curves designated on these figures as 1, 2 and 3 correspond to the first, second and the third core-loading options.

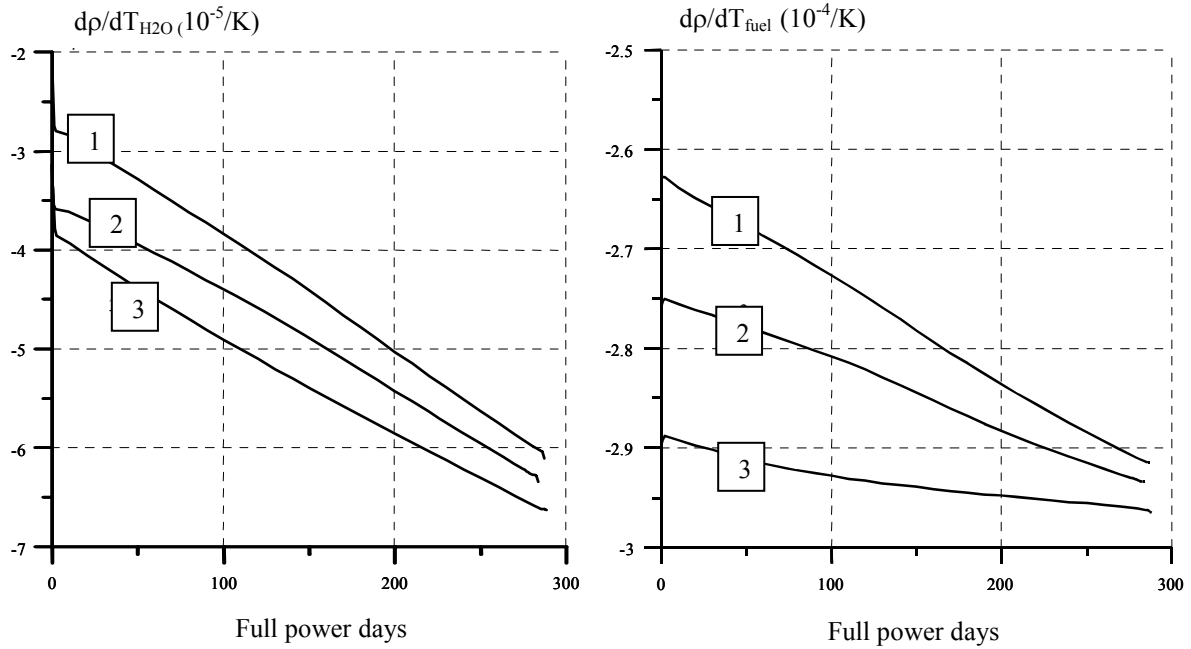


Fig. 1: Moderator temperature (left) and fuel temperature (right) reactivity coefficients versus effective power operation time

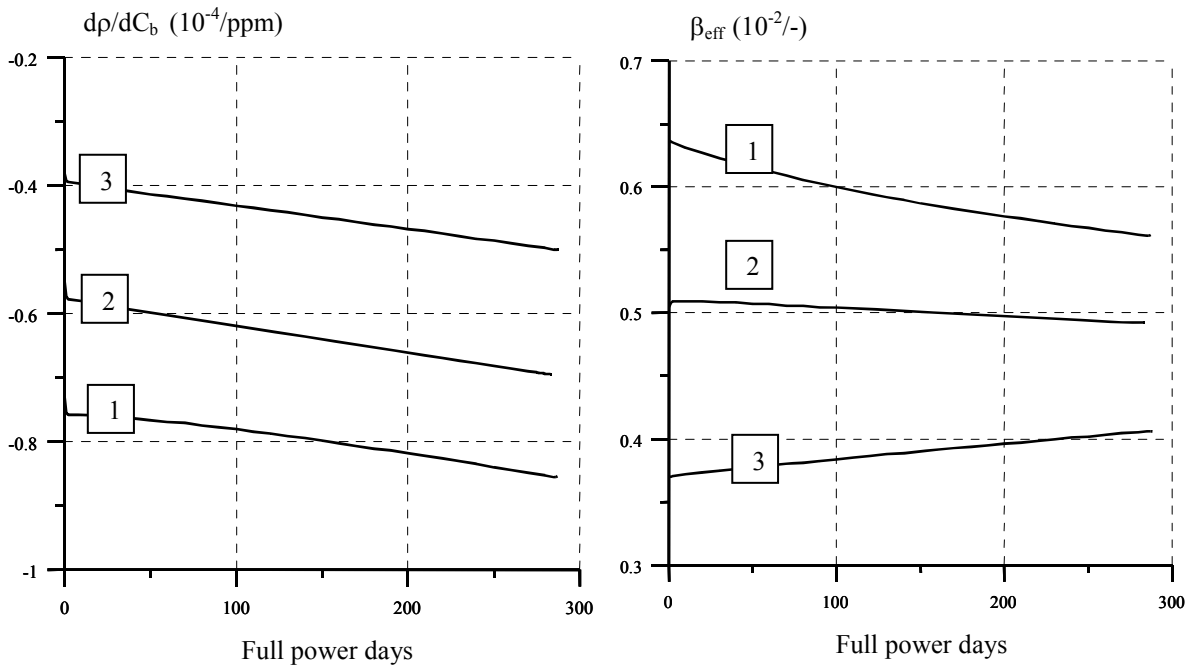


Fig.2: Boron concentration reactivity coefficients (left) and delayed neutron fractions (right) versus effective power operation time

As follows from figure 1, the moderator temperature reactivity coefficient and the fuel temperature reactivity coefficient for the MOX-fuel loading options 2 and 3 are more negative

than those for the standard uranium loading. Figure 2 shows that the absolute value of the boron concentration reactivity coefficients is about two times lower in the case of the 100 % MOX-fuel loading option than that for the 100 % UO₂ loading option. It is quite obvious that in the cases of the MOX-fuel loading options (2 and 3) the effective delayed neutron fraction is much lower than that for the UO₂ loading.

3. Transient analyses

Transient analyses were performed for the beginning and for the end (specified time point T = 280 days) of the equilibrium fuel cycle. The analyses of two reactivity-initiated accidents were performed for the three core loading options. The following initial events were considered:

- a) uniformly accelerated ejection of the 6th control rods group from the position 284 cm during 0.1 s,
- b) un-authorized withdrawal of the same group from the same position with a speed of 2 cm/s.

The initial state was nominal reactor power. A failure of the reactor scram was postulated for the both scenarios.

The main results of the analyses are presented in table 2. The evaluations show, that the maximum fuel temperatures reached during the accidents are well below the fuel melting point, and the departure from nucleate boiling ratio (DNBR) is much greater than 1. In general, the highest reactor peak powers are reached at the BOC states for all loading options. This corresponds to the fact, that the control rod worth is higher at EOC. The maximum reactor peak power is reached for the 2nd core-loading option (50% of MOX fuel) at T = 280 days. However, even in this case, it does not lead to an overheating of fuel rods. For all core-loading options, the highest fuel and cladding temperatures and the lowest DNBR value are observed at the beginning of the cycle. Their values are kept within permissible limits. Therefore, the nuclear safety against RIA was demonstrated for the MOX loadings, even for 100 % MOX (option 3).

In order to calculate the maximum fuel temperature, the "hot channel" model of DYN3D was used with a hot channel power factor of 1.41. The highest fuel temperature and the lowest DNBR occur in the case of maximum local power density during the transient. This does not necessarily correspond to the case with the highest total reactor peak power, because the local power density is determined by both the global reactor power and the local power peaking factor. Therefore, the maximum fuel temperature can be lower for EOC in comparison with BOC, even if the reactor peak power is higher, because the power peaking factors at EOC are lower. Moreover, the power peaking factors change in time during the control group ejection due to the deformation of the neutron flux field. The discussion shows, that space-dependent effects are important, which can be described only in 3D kinetics.

Figures 3 shows the time behavior of the reactor power for the ejection of the control rod group, fig. 4 shows the maximum fuel temperature and the critical power or DNB ratio. The critical power ratio is the factor, by which the rod power could be increased until heat transfer crisis (DNB) would occur leading to a rapid increase of the fuel rod cladding temperature.

Table 2: Estimated maximum values of the key safety parameters

Parameter	Initial state	Option 1	Option 2		Option 3
			MOX	UO ₂	
<i>Ejection of control rod group</i>					
Maximum reactor peak power (rel. to nominal)	BOC	1.23	1.26		1.33
	280 d	1.55	1.79		1.58
Max fuel temperature, °C	BOC	1668	1662	1581	1680
	280 d	1594	1488	1610	1514
Max cladding temperature, °C	BOC	350.9	351.0	350.8	351.0
	280 d	350.6	350.6	350.8	350.7
DNBR	BOC	1.19	1.21	1.29	1.18
	280 d	1.20	1.28	1.16	1.23
<i>Unauthorized withdrawal of control rod group</i>					
Maximum reactor peak power (rel. to nominal)	BOC	1.09	1.08		1.06
	280 d	1.10	1.10		1.07
Max fuel temperature, °C	BOC	1667	1658	1579	1674
	280 d	1595	1422	1612	1513
Max cladding temperature, °C	BOC	351.0	351.0	350.9	351.0
	280 d	350.6	350.5	350.7	350.6
DNBR	BOC	1.19	1.21	1.28	1.18
	280 d	1.20	1.29	1.16	1.23

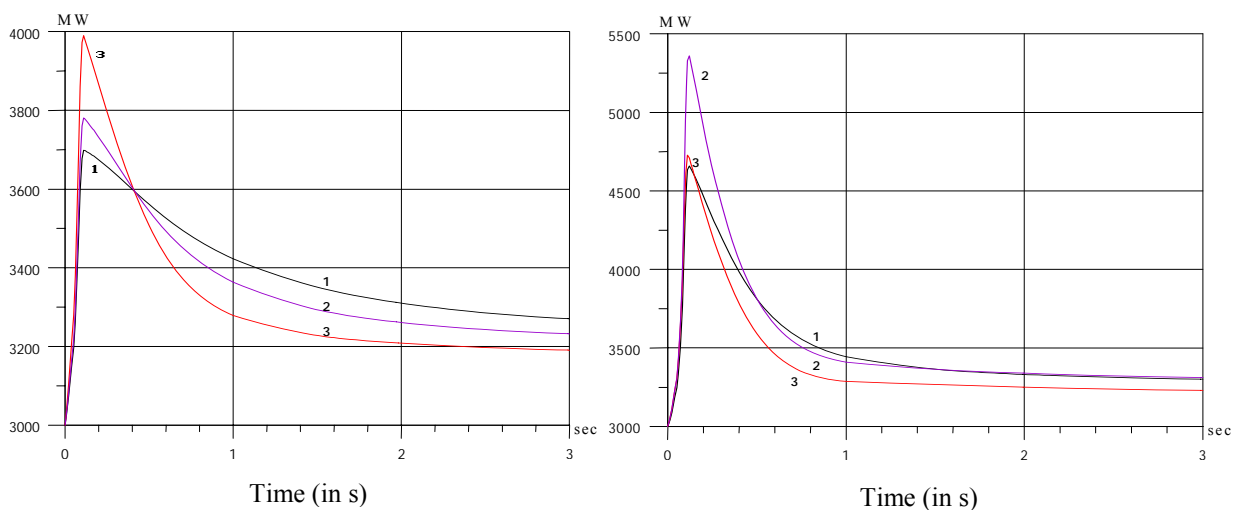


Fig. 3: Time behaviour of the reactor power during control rod group ejection at BOC (left) and EOC (right)

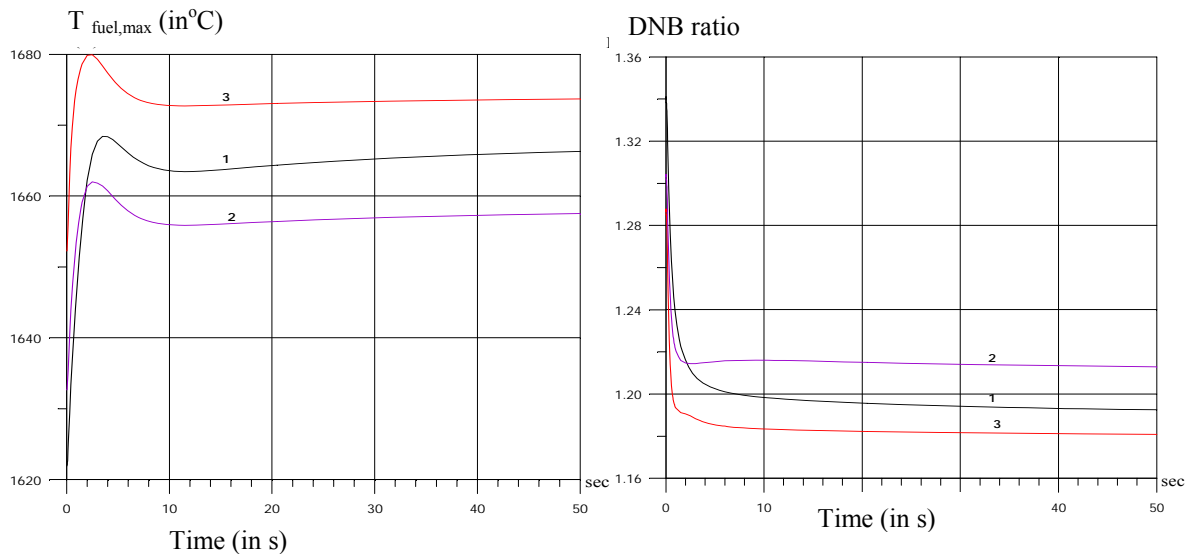


Fig. 4: Maximum fuel temperature (left) and minimum critical power ratio (right) for the control group ejection at BOC

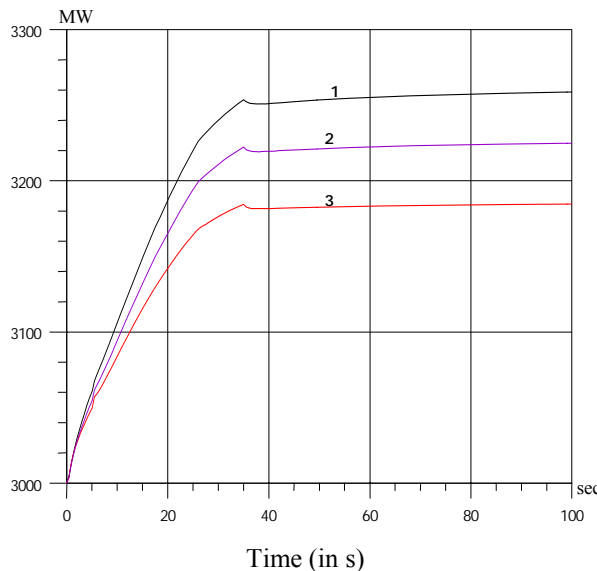


Fig. 5 shows the reactor power history for the inadvertent control group withdrawal. The asymptotic power level is about the same as in the case of control rod group ejection, as it should be expected. However, because the withdrawal is slowly, the inserted reactivity is almost promptly compensated by the feedback. Therefore, only a very small power peak occurs. The maximum fuel temperatures and minimum critical power ratios are about the same as for the ejection. For the ejection case, the maximum fuel temperatures are a little bit higher due to the first peak (see fig. 4)

Fig. 5: Reactor power time history for control rod group un-authorized withdrawal at BOC

4. Conclusions

The feasibility of the VVER-1000 type reactor for burning weapon-grade Pu and changing its isotopic composition has been shown.

The performed simulations demonstrated that the code DYN3D can be used for analyses of reactivity-initiated accidents in VVER type reactors with various fuel designs. Three different fuel-loading options have been considered (100%UO₂; 50%UO₂ + 50%MOX; 100% MOX). All considered cases meet the requirements on nuclear safety and design limits related to both normal operation conditions and during rod ejection accidents. Two reactivity related accidents have been analyzed, caused by a uniformly accelerated ejection of the operational control rod group during 0.1 s and unauthorized withdrawal of the same control rod group with

speed of $2 \text{ cm}\cdot\text{s}^{-1}$. The analyses have been performed for the beginning and the end of the fuel cycle. The maximum reactor power peak of 1.79 of the nominal reactor power was observed for the 2nd fuel-loading option (mixed loading). However, it does not cause an overheating of fuel rods.

References

- [1] Wingender, H.-J.: „Kann Atomwaffenmaterial für friedliche Zwecke genutzt werden?“, Oktober 2001, www.energie-fakten.de/html/schwerter-zu-pfugscharen
- [2] Bondarenko A., O. Komissarov, Y. Kozmenkov, Y. Matveev, Y. Orekhov, V. Pivovarov, V. Sharapov: „Reactor Physics and Safety Aspects of Various Design Options of a Russian Light Water Reactor With Rock-like Fuels“, Journal of Nuclear Materials, 319 (2003), p. 159-165
- [3] Grundmann U., U. Rohde: „DYN3D – A 3-dimensional Core Model for Steady State and Transient Analysis in Thermal Reactors“, Proceedings of the International Conference on the Physics of Reactors (PHYSOR'96), Mito (Japan), 16-20 September 1996
- [4] NEA-1507/04: „WIMSD A Neutronics Code for Standard Lattice Physics Analysis“, Distributed by the NEA Databank, 1997

Acknowledgement

The work reported about in this paper was funded by the German Federal Ministry of Economics and Labor under research contract number 150 1260.

MODELLING OF IN-VESSEL RETENTION AFTER RELOCATION OF CORIUM INTO THE LOWER PLENUM: EVALUATION OF THE THERMOSHOCK STRESSES DUE TO OUTSIDE VESSEL COOLING

Martin Abendroth, Hans-Georg Willschütz, and Eberhard Altstadt

1. Introduction

The hypothetical scenario of a severe accident with core meltdown and formation of a melt pool in the lower plenum of the reactor pressure vessel (RPV) in a light water reactor (LWR) can result in the failure of the RPV and the discharging of the melt to the containment. One accident management strategy could be the stabilization of the RPV by cooling the outside vessel wall with water.

The external water cooling leads to a sudden temperature drop (thermal shock) of the hot RPV wall and high temperature gradients resulting in inhomogeneous thermal strains and mechanical stresses.

An axis symmetric finite element (FE) model was developed to analyze spatial distribution and magnitude of these stresses. The model is based on the relevant physical phenomena as there are heat conduction, heat radiation, thermal expansion, and the elastic-plastic stress-strain relations of the material.

2. Model

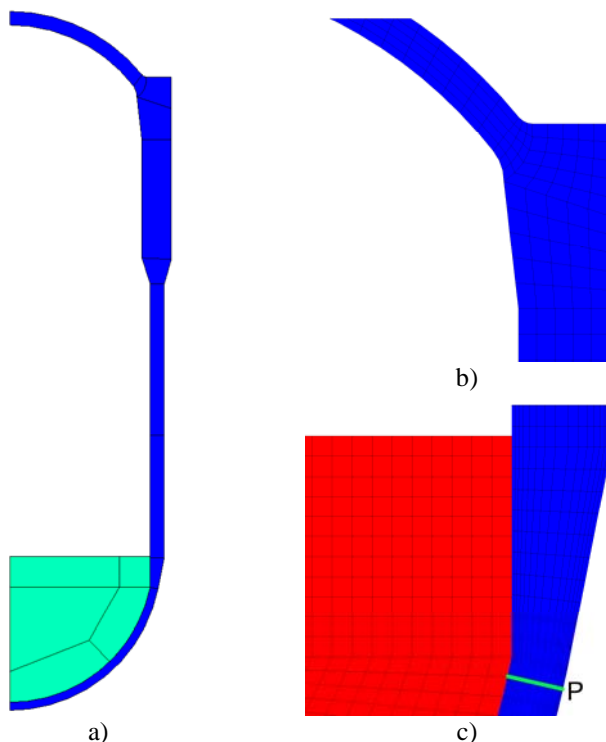


Fig. 1: FE model of the RPV: a) Area model, green – melt pool, blue – RPV; b) Detail of the upper head region; c) Detail of melt surface zone, the line and point P indicate the region of interest for the post processing

Fig. 1 shows the FE-model of a LWR pressure vessel (KONVOI type).

The study is focused on the bottom head of the vessel where the core melt is located. Therefore, the coolant in- and outlet nozzles, the holes for the control rods and all screw connections are not included in the model. This has the main advantage that an axis symmetric model can be established. The elements used for modeling the RPV are 4-node structural elements (solid185). The element size is constant in tangential direction of the lower head but varies in radial direction to the wall to be capable of reproducing the high temperature and stress gradients, which are to be expected in these zones. Since the lower part of the vessel is in the focus of this study it is modeled

with finer elements than the upper part of the RPV.

Additionally, special radiation elements are used to model the heat radiation inside and outside of the vessel. Contact elements between melt pool and inner vessel wall enable the interaction of the melt with the RPV wall.

The description of the heat transfer from the RPV to the surrounding water is an important part of the model. Here, we assume that the entire vessel is externally flooded. The Nukijama curve (see Fig. 2) characterizes the heat transfer from a heated horizontal plane to an upper water layer depending on the surface temperature. It covers different boiling regimes: 373 - 380 K – convective boiling, 380 - 403 K – stable nucleate boiling, 403 – 463 K – instable nucleate boiling, over 463 K film boiling). The temperature distribution and the resulting heat flux, plotted as vectors at the outer surface of the lower head region, are shown in Fig. 3.

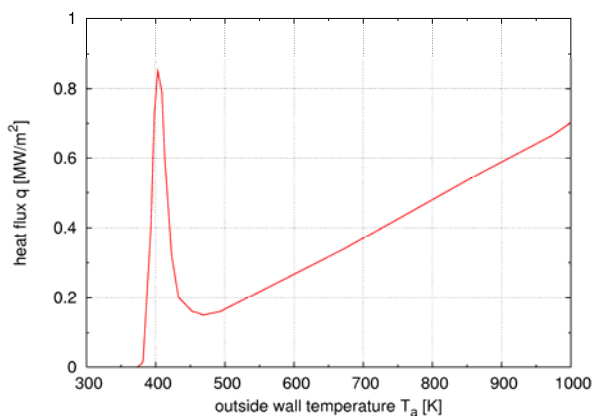


Fig. 2: Nukijama-curve (heat flux vs. surface temperature)

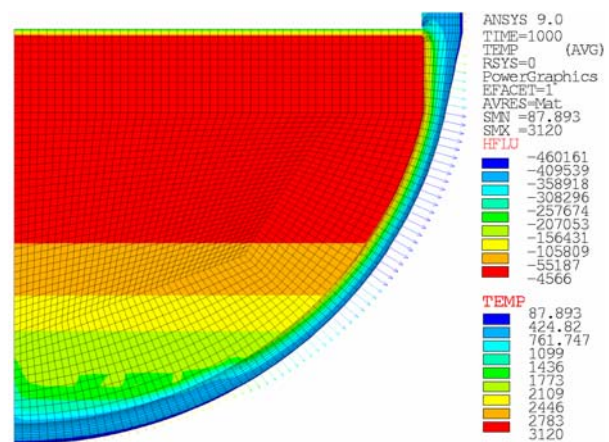


Fig. 3: Temperature distribution and heat flux boundary conditions in the lower head

3. Material Properties

The material properties of the RPV are chosen from the material data base for the French RPV steel 16MND5. This data base includes the thermal mechanical behavior of the material up to the melting temperature. For the core melt, an effective conduction convection model (ECCM) is used. It describes the heat transport in a core melt pool by anisotropic and inhomogeneous heat conduction. Details for both models can be found in [1-3].

4. Coupled Thermal Mechanical Problem

A coupled thermal mechanical problem has to be solved. Since the elements (solid185) do not allow for direct thermal mechanical coupling, a sequentially coupled simulation is necessary. The simulation is split into predefined time steps. For each time step a transient thermal solution is obtained. The subsequent mechanical simulation uses the spatial temperature field as a body load to calculate the thermal strain and the resulting stress field. The next time step starts with another thermal solution with the state at the end of the former time step as starting conditions. The time splitting of the simulation is necessary to account for phase changes, which occur in the melt. These phase changes are solved by switching between different

material models [1-3]. In Table 1, the boundary and starting conditions for the simulation are given.

Table 1: Initial and boundary conditions

Initial conditions for the thermal solution	
Constant wall temperature	$T_{wall}^0 = 600\text{K}$
Constant melt temperature	$T_{melt}^0 = 3000\text{K}$
Boundary conditions for the thermal solution	
Heat generation in the melt	$\dot{q}_{gen}^0 = 1 \text{ MW/m}^3$
Heat radiation emission coefficient inside	$\varepsilon = 0.75$
Heat radiation emission coefficient outside	$\varepsilon = 0.75$
Heat flux to the external water	Nukijama curve $\dot{q}(T)$
Loads for the mechanical solution	
Internal pressure	$p_0 = 25 \text{ bar}$
Acceleration of gravity	$g = 9.81 \text{ m/s}^2$
Temperature field at the beginning of a time step	$T_{mech}(x, t^{begstep}) = T_{therm}(x, t^{begstep})$
Temperature field at the end of a time step	$T_{mech}(x, t^{endstep}) = T_{therm}(x, t^{endstep})$

5. Results

First, we compare between the scenarios, where the RPV is cooled from outside versus a non cooled RPV. In the non cooled case the RPV loses thermal energy only due to heat radiation and free convection of the surrounding air. The resulting heat flow through the external surface is less than the generated volumetric heat rate in the melt for wall temperatures below the melting point of the RPV material. Therefore, after a certain time vessel failure must be expected as has been shown in [4, 5]. For the cooled scenario, a heat flow to the surrounding water can be established, which is larger than the generated heat rate. This results in a continuous cool down of the RPV and prevents its failure due to creep and ductile rupture.

Figure 4 shows the temperature distribution in the remaining vessel wall, left cooled, right non cooled, two hours after the beginning of the simulation. In both cases a part of the vessel wall melts off, since it exceeds temperatures above the melting point. After two hours, in the non cooled case, the remaining wall thickness is less than 25% of the original one and the temperatures are at a level where material loses its strength. The vessel material starts creeping and later ductile rupture failure of the vessel occurs. In the cooled case 65% of vessel wall remain solid at this time and the temperatures at the outside of the vessel are below the range where creep phenomena occur. This leads to the conclusion that an external vessel cooling can stabilize the vessel and prevent hazardous vessel failure.

Next, the phenomena regarding the thermo shock are discussed. Fig. 5 shows the stresses in the course of ten hours that occur at the outside of the vessel at the transition point from the spherical to the cylindrical region of the vessel which is the point, where the highest stresses occur (see Fig. 1). At the beginning of the simulation the whole vessel is at constant temperature $T_{wall}^0 = 600\text{K}$ and therefore no thermal stresses exist. The equivalent stress of 100 MPa is due to the internal pressure $p_0 = 25 \text{ bar}$ only. Later a thermal gradient and thermal

stresses are caused by the rapid temperature drop of the outer wall surface due to the cooling. The stresses rise rapidly into a range where plastic deformation occurs. The maximum of the equivalent stress is almost 500 MPa, which is 75% of the ultimate tensile strength of the material. This maximum is reached after 1000 seconds. After that time the temperature gradient through the vessel wall turns to be linear on a moderate level resulting in thermal stresses in the elastic range of the material.

Fig. 6 shows the stress component σ_z along a radial path through the vessel wall. The path is located at the transition from the spherical lower head to the cylindrical part of the vessel. It becomes clear that the highest stress are located on the outer (cooled) vessel wall. It is a biaxial tensile stress state. Inside the wall, a compression stress state dominates.

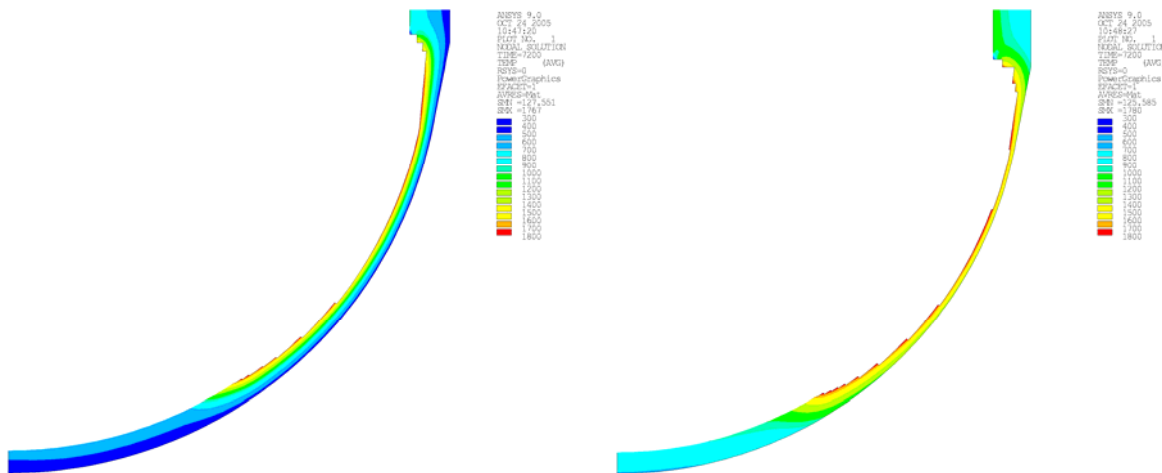


Fig. 4: Temperature field in the remaining vessel wall after two hours (left cooled, right non cooled)

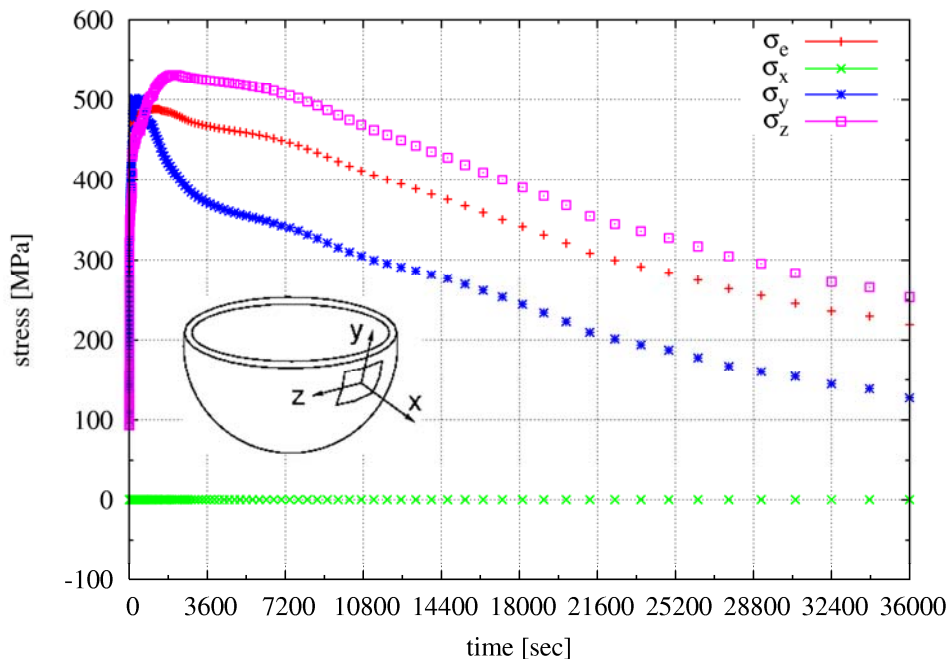


Fig. 5: Stresses at point P plotted over time (x – radial, y – tangential along circumference, z – tangential along meridian, σ_e – equivalent stress)

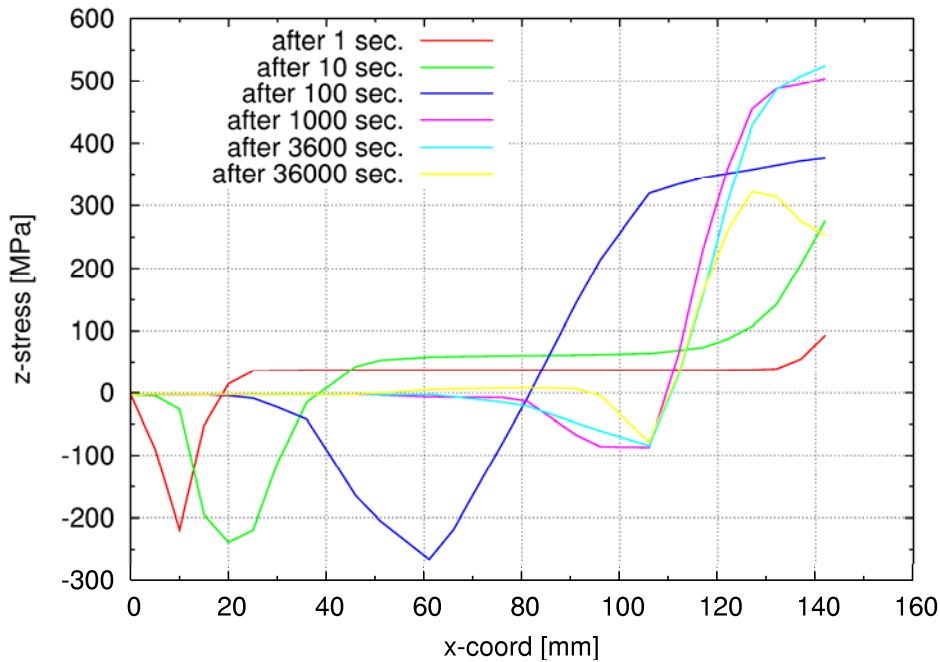


Fig. 6: Stress σ_z across the vessel wall (zero x-coordinate denotes the inside of the vessel))

6. Conclusion

The cooling of the RPV after a severe accident with a core melt down is an effective method to stabilize the vessel and prevent vessel failure. The cooling should begin as early as possible to minimize the amount of molten vessel material. The strains and stresses due to the thermo shock reach magnitudes where plastic deformation of the material occurs. The most stressed location is the transition region from the lower head to the cylindrical part of the vessel. At this region a weld zone exists, which is a potential location for cracks. Therefore, further studies should be performed regarding the vessel stability considering a surface crack in that transition region.

References

- [1] Willschütz, H.-G.; Altstadt, E.; Sehgal, B. R.; Weiss, F.-P.: Simulation of creep tests with French or German RPV-steel and investigation of a RPV-support against failure. *Annals of Nuclear Energy* 30(2005)10, 1033-1063
- [2] Willschütz, H.-G.; Altstadt, E.: Generation of a high temperature material data base and its application to creep tests with french and german RPV-steel. *Wissenschaftlich Technische Berichte FZR-353*, August 2002
- [3] Altstadt, E.; Willschütz, H.-G.; Sehgal, B.R.; Weiß, F.-P.: Modelling of in-vessel retention after relocation of corium into the lower plenum. *Wissenschaftlich Technische Berichte FZR-437*, Oktober 2005
- [4] Willschütz, H.-G.; Altstadt, E.; Sehgal, B.R.; Weiss, F.-P.: Recursively coupled thermal and mechanical FEM-analysis of lower plenum creep failure experiments; *Annals of Nuclear Energy* 33(2006)2, 126-148
- [5] Willschütz, H.-G.: Thermomechanische Modellierung eines Reaktordruckbehälters in der Spätphase eines Kernschmelzunfalls. *Wissenschaftlich-Technische Berichte FZR-447*, Januar 2006, von der Fak. Maschinenwesen der TU Dresden genehmigte Dissertation

THERMAL DISSOLUTION KINETICS OF IRRADIATION INDUCED CLUSTERS IN RPV STEELS

Frank Bergner and Andreas Ulbricht

1. Introduction

Neutron irradiation induces an increase of the brittle-to-ductile transition temperature of reactor pressure vessel (RPV) steels. It is now generally accepted that for low levels of phosphorus this increase is essentially caused by the formation and evolution of nm-sized copper enriched solute clusters [1] and/or (depending on composition) additional features specified as matrix damage [2] or vacancy solute complexes [3]. During a post-irradiation thermal annealing treatment clusters can either dissolve or coarsen. The aim of the work reported here was to contribute to the understanding of the annealing behaviour by means of small-angle neutron scattering (SANS) analyses performed after isochronal post-irradiation annealing treatments (annealing time: 10 h) at stepwise increasing levels of temperature.

2. Experiments

The chemical composition of the materials investigated is given in Table 1. The basic compositions correspond to the specification of the ASTM A533B cl.1 RPV steel. The materials M1 and M2 provided within the framework of international research programs are also known as JRQ and JPA, respectively. Mechanical properties, product specifications and final heat treatment are summarized in [4]. Notched bars of both materials of dimensions $10 \times 10 \times 55 \text{ mm}^3$ were irradiated in the prototype VVER-2 reactor at a temperature of 255°C up to three different neutron fluences. The irradiation conditions are summarized in Table 2.

From the irradiated specimens M1-I3 and M2-I2, slices of about 1 mm thickness were cut in order to perform isochronal annealings. The annealing time was 10 h for each slice followed by furnace cooling. The annealing temperatures applied to the individual slices are given in Table 3.

Table 1: Composition of the materials (analysis) in wt.-% (balance Fe)

Code	C	Mn	Si	Cr	Ni	Mo	V	S	P	Cu
M1	0.20	1.42	0.23	0.13	0.80	0.52	0.008	0.005	0.020	0.15
M2	0.18	1.33	0.26	0.16	0.73	0.55	0.006	0.004	0.020	0.29

Table 2: Irradiation conditions (irradiation temperature: 255°C)

Material code	Neutron fluence / 10^{18} cm^{-2} ($E > 0.5 \text{ MeV}$)	Flux density / $10^{12} \text{ cm}^{-2} \text{ s}^{-1}$ ($E > 0.5 \text{ MeV}$)
M1-I1	10	0.15
M1-I2	77	3.0
M1-I3	139	5.4
M2-I1	10	0.15
M2-I2	80	3.1
M2-I3	143	5.5

SANS measurements were performed at the spectrometers V4 of HMI-BENSCH Berlin [5] and D11 of ILL Grenoble [6]. In order to separate magnetic and nuclear scattering contributions, the specimens were placed in a saturation magnetic field of $B = 1.4$ T perpendicular to the incident neutron beam. The magnitude of the scattering vector, $Q = (4\pi/\lambda)\sin(\theta/2)$, where λ is the neutron wavelength and θ is the scattering angle, covered the range from 0.2 to 3.0 nm⁻¹. The volume distribution of scatterers was calculated from the magnetic scattering contribution using the indirect transformation method. A two-phase model of uniformly dispersed spherical scatterers of vanishing magnetic moment in the homogeneous matrix of ferromagnetic bcc iron was assumed. Data analysis is described in more detail in [4].

3. Results

Volume related size distributions of the unirradiated conditions, the as-irradiated conditions, and the irradiated and annealed conditions are presented in Fig. 1 for materials M1 and M2. The annealing behaviour of the two materials is generally similar. There is no indication for the measured volume distributions to consist of more than one component (i.e. to be bimodal or multi-modal) for each of the conditions investigated and for the covered size range. The microstructural parameters obtained from the SANS experiments are compiled in Table 3. The total volume fraction, c , of scatterers was calculated by integrating the volume distribution, $c_R = f(R)$. The radius, R_p , is defined as the peak abscissa of the function, $c_R = f(R)$. Additional information on the composition of the scatterers is obtained on the basis of the A-ratio (Table 3) defined as ratio of total SANS cross-section and the nuclear component.

We have observed that the total volume fraction of irradiation-induced clusters left after 10-hour annealing is a decreasing function of the annealing temperature (Fig. 1 and Table 3). The relative reduction of the total volume fraction of irradiation-induced scatterers, $(c_i - c_a)/c_i$, where c_i and c_a are the total volume fractions in the as-irradiated and annealed condition, respectively, is presented as a function of the inverse absolute annealing temperature in Fig. 2. With the exception of the highest annealing temperature, the observed dependence can be described by straight lines, the slopes of which are (1.22 ± 0.05) eV for material M1-I3 and (1.12 ± 0.11) eV for material M2-I2.

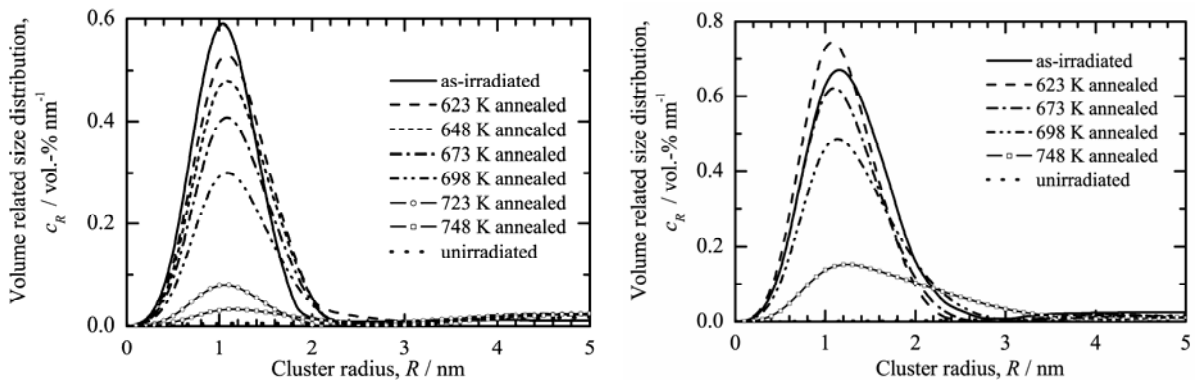


Fig. 1: Volume fraction of scatterers per radius interval, c_R , vs. cluster radius, R , for the unirradiated condition, M1, the as-irradiated condition, M1-I3, and six irradiated and annealed conditions (left) and for the unirradiated condition, M2, the as-irradiated condition, M2-I2, and four irradiated and annealed conditions (right).

Table 3: Microstructural parameters characterizing the irradiation-induced clusters and effect of annealing

Material / condition	Annealing temperature, T / K ($T / ^\circ\text{C}$)	Volume fraction, $c / \%$	Peak radius, R_p / nm	A-ratio
M1-I1	as-irradiated	0.21 ± 0.01	1.04 ± 0.05	2.1 ± 0.2
M1-I2	as-irradiated	0.34 ± 0.01	1.00 ± 0.05	2.4 ± 0.2
M1-I3	as-irradiated	0.50 ± 0.02	1.04 ± 0.05	2.6 ± 0.2
M1-I3-A1	623 (350)	0.48 ± 0.02	1.08 ± 0.05	2.4 ± 0.2
M1-I3-A2	648 (375)	0.46 ± 0.02	1.08 ± 0.05	2.4 ± 0.2
M1-I3-A3	673 (400)	0.39 ± 0.02	1.10 ± 0.05	2.4 ± 0.2
M1-I3-A4	698 (425)	0.29 ± 0.02	1.10 ± 0.05	2.2 ± 0.2
M1-I3-A5	723 (450)	0.06 ± 0.01	1.06 ± 0.05	2.0 ± 0.2
M1-I3-A6	748 (475)	0.02 ± 0.01	1.1 ± 0.1	2.0 ± 0.2
M2-I1	as-irradiated	0.62 ± 0.03	1.04 ± 0.05	2.7 ± 0.2
M2-I2	as-irradiated	0.75 ± 0.03	1.16 ± 0.05	2.5 ± 0.1
M2-I2-A1	623 (350)	0.73 ± 0.03	1.08 ± 0.05	2.5 ± 0.1
M2-I2-A3	673 (400)	0.64 ± 0.03	1.10 ± 0.05	2.5 ± 0.1
M2-I2-A4	698 (425)	0.57 ± 0.02	1.14 ± 0.05	2.5 ± 0.1
M2-I2-A6	748 (475)	0.24 ± 0.02	1.25 ± 0.1	4.0 ± 0.2
M2-I3	as-irradiated	0.83 ± 0.04	1.10 ± 0.05	2.7 ± 0.2

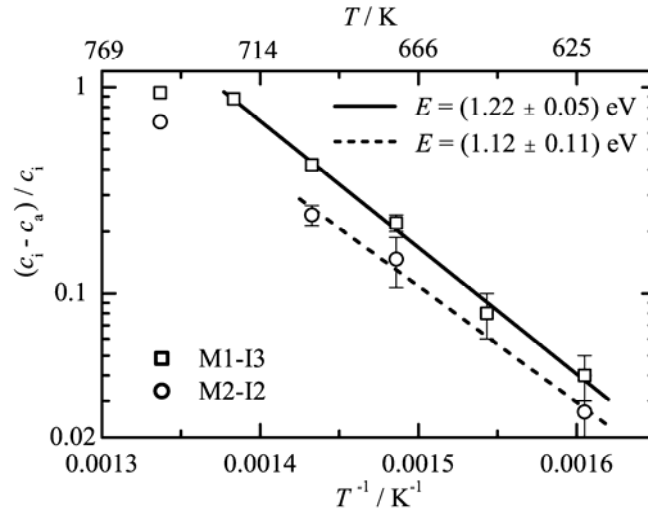


Fig. 2: Arrhenius plot of the dissolved fraction of irradiation-induced clusters as a function of the annealing temperature starting from the as-irradiated conditions M1-I3 and M2-I2.

4. Discussion

The most striking effect of post-irradiation annealing documented in Table 3 is the reduction of the total volume fraction of irradiation-induced clusters with increasing annealing temperature at approximately constant peak radius of the volume distribution (with the exception of the 475°C annealing of material M2-I2, i.e. condition M2-I2-A6). This observation immediately suggests that a certain number of irradiation-induced clusters essentially dissolve. Furthermore, the characteristic dissolution time of a single cluster must be much less than the annealing time of 10 hours. Otherwise, i.e. if the characteristic dissolution time were of the same order of magnitude as the annealing time (or even greater than that), the volume distribution would exhibit a shift to lower radii, which is contradictory to observation (Fig. 1).

Pareige et al. [7] have drawn a similar conclusion on the basis of a combined investigation by means of SANS and Atom probe field ion microscopy (APFIM) of a neutron-irradiated French RPV steel (0.07% Cu) annealed at 450°C for 2 h, 20 h, and 100 h. These authors estimated the characteristic dissolution time of a single cluster to be less than 2 h at 450 °C. From the present investigation it can be concluded that any remainder of the clusters after “dissolution” must be smaller than the detection limit of SANS, i.e. less than 0.5 nm. This conclusion holds analogously for any of the annealing temperatures applied.

According to Pareige et al. [7] the entire process of successive dissolution events of clusters at an annealing temperature of 450°C is not finished after 20 h of annealing. It is assumed that the same situation applies to the present annealing treatments. Therefore, the measured volume distributions represent an intermediate stage (not a final stage or saturation). Nevertheless, the observed Arrhenius behaviour documented in Fig. 2 strongly suggests that

- the process that controls the frequency of successive dissolution events is a thermally-activated process,
- the dissolution is controlled by one and the same process over the entire range of annealing temperatures, and
- the activation energy of the rate-controlling step is about 1.2 eV (Fig. 2).

The calculated ranges of the activation energy overlap for materials M1 and M2 (Fig. 2). It is therefore reasonable to assume one and the same process to control the dissolution rate for both materials.

It is not possible to give a conclusive interpretation of the mechanism of the dissolution process on the basis of the present measurements alone. However, it is worth noticing that a similar value of about 1.3 eV is reported for the vacancy migration energy in iron [8]. The essential role of vacancies in the dissolution sequence is supported by the fact that cluster atoms can move away from the cluster site only via a vacancy-assisted diffusion mechanism in the annealing temperature range.

The A-ratio of pure vacancy clusters and pure bcc Cu clusters in an iron matrix assumes values of about 1.4 and 12, respectively. The dependence on annealing temperature of the average A-ratio measured in this work has to be rated as comparatively weak, if any (with the exception of condition M2-I2-A6 to be discussed later). A small increase of the A-ratio with neutron fluence (from 2.1 to 2.6, Table 3) and a reversion of this increase due to annealing (from 2.6 to 2.0) is observed for material M1. The observed A-ratio for material M2 (with the mentioned exception) is about constant, $A = 2.5$.

The above observations, i.e. (1) a monomodal volume distribution of irradiation-induced clusters for each irradiation or annealing condition, (2) the general Arrhenius behaviour, and (3) the low variability of the A-ratio, suggest a single type of clusters present after neutron irradiation and post-irradiation annealing with a more or less uniform composition stable up to initiation of the dissolution process. The annealing condition M2-I2-A6 (i.e. the highest annealing temperature applied, 475°C) exhibits the only significant deviation from the behaviour discussed so far in a number of items:

- The peak radius, R_p , of the volume distribution is slightly shifted to higher values. This shift is even more pronounced, if the large-radius tail of the size distribution in Fig. 1 is considered.
- The measured A-ratio assumes a significantly higher value of 4.0 (Table 3) indicating higher Cu fractions in the clusters.
- The 475°C data point in Fig. 2 deviates from the general Arrhenius behaviour.

The conclusion is that, unlike the behaviour discussed so far, coarsening of Cu-rich precipitates takes place for material M2-I2 at an annealing temperature of 475°C. The lowest temperature at which coarsening takes place under the present conditions is between 425 and 475°C. It cannot be decided, whether this coarsening starts from remaining Cu clusters below the detection limit of SANS (<0.5 nm, i.e. <10 atoms) or from solute Cu after complete dissolution of the irradiation-induced clusters, but the first option seems to be more reasonable [7]. The occurrence of coarsening prior to complete dissolution in material M2 is attributed to the excess Cu of 0.29% as compared to 0.15% for material M1.

5. Conclusion

Depending on the Cu level of the RPV steel investigated, either “complete” (as seen by SANS) dissolution of the irradiation-induced clusters or onset of coarsening after incomplete dissolution is observed. One and the same thermally activated process characterized by an energy of activation of 1.2 eV controls the frequency of successive dissolution events for the materials and conditions investigated. The duration of a single dissolution event is much shorter than the applied annealing time of 10 h.

References

- [1] G. R. Odette, On the dominant mechanism of irradiation embrittlement of reactor pressure vessel steels, *Scripta Metall.* 17 (1983) 1183-1188.
- [2] R. G. Carter, N. Soneda, K. Dohi, J. M. Hyde, C. A. English, W. L. Server, Microstructural characterization of irradiation-induced Cu-enriched clusters in reactor pressure vessel steels, *J. Nucl. Mater.* 298 (2001) 211-224.
- [3] B. D. Wirth, P. Asoka-Kumar, R. H. Howell, G. R. Odette, P. A. Sterne, Positron annihilation spectroscopy and small angle neutron scattering characterization of nanostructural features in irradiated Fe-Cu-Mn alloys, *MRS Symp. Proc.* 650 (2001) R6.5.1-R6.5.6.
- [4] A. Ulbricht, J. Böhmert, H.-W. Viehrig, Microstructural and mechanical characterization of radiation effects in model reactor pressure vessel steels, *J. ASTM International* 2 (2005) ID JAI12385.
- [5] U. Keiderling, A. Wiedenmann, New SANS instrument at the BERII reactor in Berlin, Germany, *Physica B* 213&214 (1995) 895-897.
- [6] P. Lindner, R. P. May, P. A. Timmins, Upgrading of the SANS instrument D11 at ILL, *Physica B* 180&181 (1992) 967-972.
- [7] P. Pareige, P. Auger, S. Welzel, J.-C. Van Duysen, S. Miloudi, Annealing of a low-copper steel: hardness, SANS, atome probe, and thermoelectric power investigations, in: *Effects of radiation on materials: 19th Int. Symp.*, ASTM STP 1366, M. L. Hamilton, A. S. Kumar, S. T. Rosinski, M. L. Grossbeck, Eds., American Society for Testing and Materials, West Conshohocken, 2000, pp. 435-447.
- [8] A. Hardouin Duparc, C. Moingeon, N. Smetniansky-de-Grande, A. Barbu, Microstructure modelling of ferritic alloys under high flux 1 MeV electron irradiations, *J. Nucl. Mater.* 302 (2002) 143-155.

Acknowledgement

This work was supported within the PERFECT European Integrated Project under Contract No. F6O-CT-2003-508840 and by the Bundesministerium für Wirtschaft und Arbeit under Contract No. 1501260.

THE SOLUTION BEHAVIOUR OF PYRITE IN FOUR COLUMNS OF DIFFERENT POROUS SAND MATERIAL

Roland Kuechler and Klaus Noack

1. Introduction

The unsaturated transport of water and pollutants in a dump is a significant topic of environmental research. Rainwater penetrating into a dump on its flow path dissolves various minerals and can transport reacting species through the dump down to the ground water. Although not representing the full complexity of a natural system, modelled batch and column experiments play an important role. Not only with regards to according research, but especially, with respect to code verification. Moreover, with the help of suitably designed experiments which are combined with appropriate numerical modelling the investigations may be focussed on certain single phenomena among a complex system of interacting effects. With our experiments and calculations we generally follow this line and are presently studying the mineral dissolution under unsaturated conditions. There is an undisputed need for research in this field [1]. In recent years we developed a system of numerical codes called POLLUTRANS which calculates water and pollutant transports through the unsaturated zone [2]. It is based on diverse appropriate models describing the complex physical and chemical phenomena, being involved in the transports. The dissolution of minerals, however, is one of the most important processes. It decisively affects the amount of pollutants emitted to the ground water.

2. Batch and column experiments

The pyrite used in batch and column experiments, was a compound of the natural mineral from Elba. For both experiment types the minerals had to be prepared as follows. After crushing and dry sieving the grains came up to the desired size of about 200-300 μm , which is adequate to the grain size of the sand matrix. The powder has been washed with MilliQ-water and has been dried at a temperature of 50 $^{\circ}\text{C}$ in order to remove small particles from the grain surface.

In batch experiments defined masses of 5 g and 10 g pyrite were solved into 1 L MilliQ-water. The flasks had to be moved permanently by a rotation shaker to keep the mineral particles in suspension. In this case the mineral particles are completely moistened and the entire surface area of the mineral is in contact with the liquid. Twice test samples of the batch solution were filtered through a 0.2 μm filter and chemically analysed.

In the column experiments quartz sand from Provodin (4716, Provodin, Czech Republic) of different particle size distribution was used as column material to form the wanted variable water saturation. The relevant material parameters are summarised in Table 1. To achieve appropriate inertness of the sand it had to be washed with sulphuric acid and MilliQ-water because the pyrite solution was expected to be in the acid pH-range of 2 to 4. The sand was repeatedly rinsed with de-ionised water until conductivity could stabilise at 1 $\mu\text{S}/\text{cm}$. For the column experiment 40 g pyrite were mixed with 1 kg quartz sand. Columns of a height of 1 m and an inside diameter of 0.1 m were used. These were filled with a homogeneous sand/pyrite mixture. A peristaltic pump at the head of the column had to control the feeding of the water. The infiltration of the water in the column was carried out through seven points optimally arranged in a cover plate.

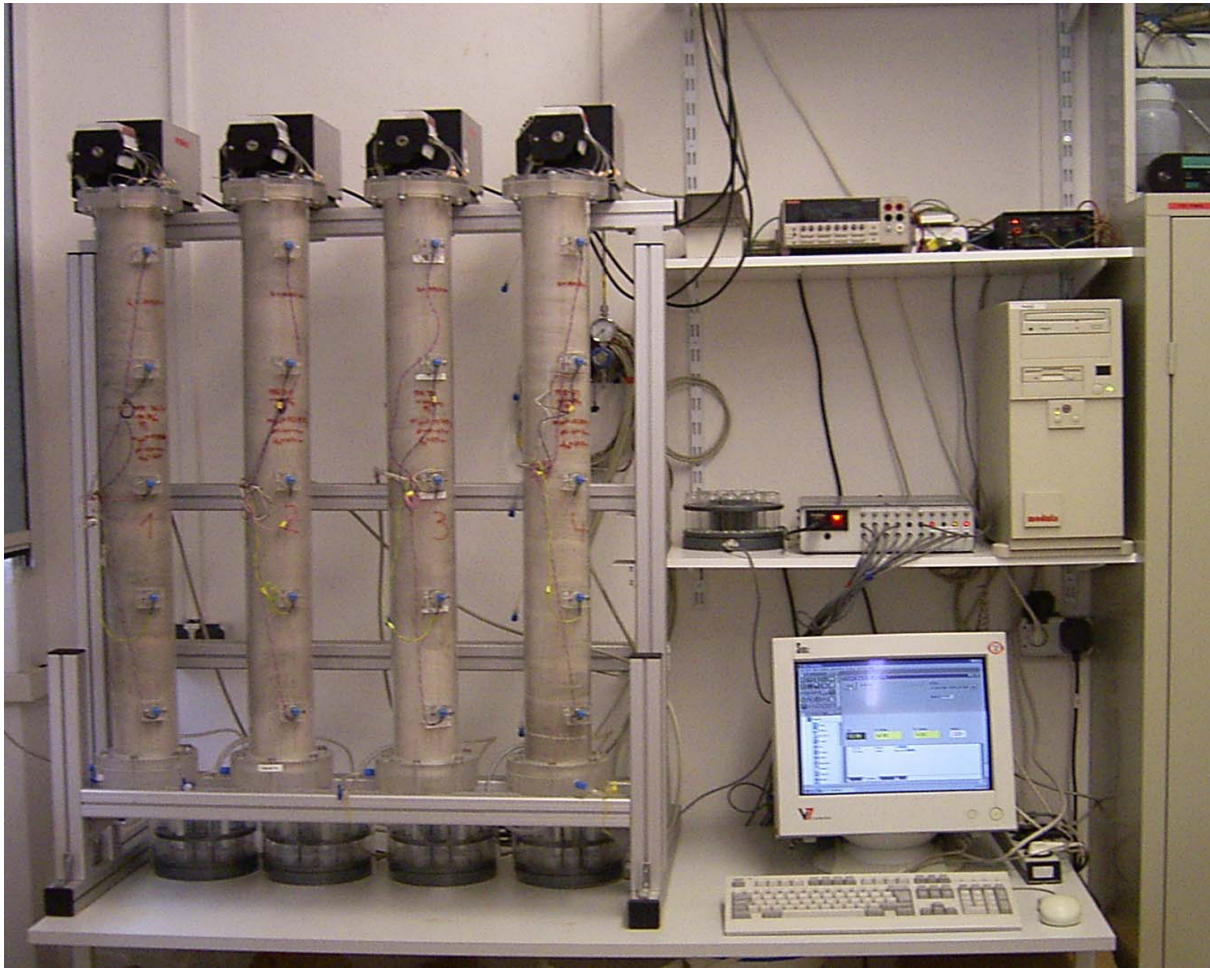


Fig. 1: Column experiment: Continuous measurement of the electrical conductivity with five electrodes. Sampling with suction cups at five points of column and with fraction collectors at the foot of the columns.

Table 1: Provodiner foundry sand (quartz sand)

sort	d_{50} (mm)	Grain size (mm)	Bulk density (g/cm^3)	Porosity n	Capillary rise (cm)	Range of constant saturation (cm)
PR 30/31	0.57	0.3-1.0	1.76	0.355	21	$0 < s=0.19 < 65$
PR 30	0.36	0.1-1.0	1.69	0.362	26	$0 < s=0.195 < 62$
PR 32	0.33	0.1-0.7	1.68	0.366	29	$0 < s=0.20 < 63$
PR 33	0.28	0.1-0.6	1.69	0.364	32.4	$0 < s=0.25 < 58$

A fraction collector at the column foot took samples from the leaking solution. The Darcy velocity through the column was monitored by measuring the water outflow into the fraction collector. The column was equipped with in-situ conductivity electrodes and with suction cups, which were equally distributed across the height. These measurements gave information about the pyrite dissolution dependent on column height. The foot of the columns was kept on saturated conditions so, that the water saturation s varied in the full range of $0 \leq s \leq 1$ dependent on height. At the end of the experiment, samples were taken at several measuring points. These are realised through lockable windows, which are evenly attached across the height of the column. Fig. 1 shows the laboratory column test device. Solutions, respectively solid portions of these samples were separated by centrifugation with the help of a $0.2 \mu\text{m}$ filter. The extracted solutions were chemically analysed and were used in order to measure

water saturation as well. Table 1 shows measured water saturations dependent on height for the four columns. The x coordinate is measured from top to bottom of the column. All measurement results such as the in-situ conductivity measurements, the chemical analysis of the leaking solution as well as the solutions in dependence on height were compared with results of numerical model calculations for pyrite dissolution in pure water. This comparison permits to estimate reductions of the reactive mineral surfaces caused by the unsaturated water flow. Any results of the column test are depicted in Fig. 3. The solutions were extracted by means of suction cups. The concentrations of cations were measured by means of ICP/MS. These measurement values are afflicted with an error of about 10%. The conductivity was measured with a four-electrode measuring cell from WTW GmbH Weilheim.

3. Description of the calculation model

In batch and column tests transport, storage, exchange and dissolution/precipitation processes may be investigated. We evaluated the experimental data on the basis of a complete one-dimensional migration model [3]: For pyrite dissolution our mixed kinetic-equilibrium system reads in detail

$$n \cdot s \frac{\partial c_i}{\partial t} + L(c_i) = \sum_p \eta \frac{A_p}{V} r_{i,p} + \sum W_{i,j}, \quad \text{with} \quad L(c_i) = v \frac{\partial c_i}{\partial x} - \alpha_L v \frac{\partial^2 c_i}{\partial x^2} \quad (1)$$

$$i = OH^-, HSO_4^-, H_2SO_4, FeSO_4, Fe(OH)_2^+, Fe(OH)_3$$

$$j = i \cup H^+, SO_4^{2-}, Fe^{2+}, Fe^{3+};$$

$$\begin{aligned} n \cdot s \frac{\partial c_{H^+}}{\partial t} + L(c_{H^+}) &= \eta \frac{A_{FeS_2}}{V} (2r_{H^+,FeS_2}^{(a)} + 16r_{H^+,FeS_2}^{(b)}) - r_{Fe^{2+} \rightarrow Fe^{3+}} + \sum W_{H^+,j}, \\ n \cdot s \frac{\partial c_{SO_4^{2-}}}{\partial t} + L(c_{SO_4^{2-}}) &= \eta \frac{A_{FeS_2}}{V} (2r_{SO_4^{2-},FeS_2}^{(a)} + 16r_{SO_4^{2-},FeS_2}^{(b)}) + \sum W_{SO_4^{2-},j}, \\ n \cdot s \frac{\partial c_{Fe^{2+}}}{\partial t} + L(c_{Fe^{2+}}) &= \eta \frac{A_{FeS_2}}{V} (r_{Fe^{2+},FeS_2}^{(a)} + 15r_{Fe^{2+},FeS_2}^{(b)}) - r_{Fe^{2+} \rightarrow Fe^{3+}} + \sum W_{Fe^{2+},j}, \\ n \cdot s \frac{\partial c_{Fe^{3+}}}{\partial t} + L(c_{Fe^{3+}}) &= r_{Fe^{2+} \rightarrow Fe^{3+}} - 14\eta \frac{A_{FeS_2}}{V} r_{Fe^{3+},FeS_2}^{(b)} + \sum W_{Fe^{3+},j}, \end{aligned}$$

where $W_{i,j} \neq 0$ are proportional to the appropriate mass action equations

$$\begin{aligned} W_{H^+,OH^-} &= W_{OH^-,H^+} && \approx K_W - \gamma_1^2 c_{H^+} c_{OH^-} \\ W_{H^+,SO_4^{2-}} &= W_{SO_4^{2-},H^+} = -W_{HSO_4^-,HSO_4^-} && \approx K_1 \cdot c_{HSO_4^-} - \gamma_2 c_{H^+} c_{SO_4^{2-}} \\ W_{H^+,HSO_4^-} &= W_{HSO_4^-,H^+} = -W_{H_2SO_4,H_2SO_4} && \approx K_2 \cdot c_{H_2SO_4} - \gamma_1^2 c_{H^+} c_{HSO_4^-} \\ W_{SO_4^{2-},Fe^{2+}} &= W_{Fe^{2+},SO_4^{2-}} = -W_{FeSO_4,FeSO_4} && \approx K_3 \cdot c_{FeSO_4} - \gamma_2^2 c_{Fe^{2+}} c_{SO_4^{2-}} \\ W_{Fe^{3+},OH^-} &= W_{OH^-,Fe^{3+}} = -W_{Fe(OH)_2^+,Fe(OH)_2^+} && \approx K_4 \cdot c_{Fe(OH)_2^+} - \gamma_1 \gamma_3 c_{Fe^{3+}} c_{OH^-}^2 \\ W_{Fe^{3+},OH^-} &= W_{OH^-,Fe^{3+}} = -W_{Fe(OH)_3,Fe(OH)_3} && \approx K_5 \cdot c_{Fe(OH)_3} - \gamma_1^3 \gamma_3 c_{Fe^{3+}} c_{OH^-}^3 \\ \text{if } \gamma_1^3 \gamma_3 c_{Fe^{3+}} c_{OH^-}^3 &\geq K_{Fe(OH)_3} && \text{then} \quad K_{Fe(OH)_3} = \gamma_1^3 \gamma_3 c_{Fe^{3+}} c_{OH^-}^3 \end{aligned}$$

In this equations are: c_i – the concentration of the ion species i , A_{FeS_2} - the total specific surface area of the pyrite particles. The coefficients are defined as: $n \cdot s$ - soil water content, n - porosity, s - water saturation of the pores, v - Darcy velocity, α_L - longitudinal dispersion length (dispersivity) of the medium, V - matrix volume, and $\gamma_1, \gamma_2, \gamma_3$ are the activity coefficients for single, double, and triple charged ions, respectively. They were calculated by using the Davies-Equation [4]. The $K_{1...5}$, describe mass action constants which are necessary to calculate the composition of solution, $K_{Fe(OH)_3}$ is the solubility constant for ferric hydroxide and K_W is the dissociation constant of water. The meaning of the individual terms in the weathering process is explained in the section 4.

Dissolution reactions will only occur at wetted mineral surfaces. In the batch test the entire grain surface is moistened. In any column, however, the possibility of soil moisture may be limited, and consequently, the reactive surface of the solid mineral phase may be less than the total grain surface. Therefore, it is necessary to consider whether or not the surface is in contact with the percolating water. Because of that, in the dissolution term of Equation (1) the factor

$$\eta = A_{column} / A \quad (A = A_{batch}) \quad (2)$$

is introduced to depict the relationship between the chemically effective surface in the sand column and the chemically effective surface in the batch. Sverdrup and Warffvinge [5] suppose this factor is given by $\eta = n \cdot s$. In the next section we compare our results with this hypothesis.

At the head of the column a third-type boundary condition was applied:

$$\left(v \cdot c_i - \alpha_L \cdot v \frac{\partial c_i}{\partial x} \right) \Big|_{x=0,t} = 0. \quad (3)$$

In the experiment this boundary condition is realised by means of peristaltic pumps leading to a homogeneous constant flow rate with a depth of few centimetres. The outflow at the bottom of the column into the volume simulating the groundwater was described by the boundary condition:

$$\frac{\partial c_i}{\partial x} \Big|_{x=L,t} = 0. \quad (4)$$

With $L(c_i) = 0$, $n \cdot s = 1$ and $\eta=1$, system (1) describes the batch test and for $\partial c_i / \partial t = 0$ the stationary column experiment. In the last case the solution algorithm for the system of partial differential equations (1) can be replaced by a system of ordinary differential equations.

In order to solve solute transport and chemical equilibrium equations we use a splitting approach where the calculation of one time step is split into a transport step and a chemical equilibrium calculation step. Both are carried out sequentially. The stationary boundary value system (1) is solved by means of a combination of the Runge-Kutta method and the shooting method. Both methods are described in the Numerical Recipes [6].

The results of differential equations describe the concentrations of ions in the pore water. The electrical conductivity of this solution is a function of all dissolved ions, type of ions, and

their potential to form charged or non-charged pairs or complexes. For low concentrations ($c < 10$ mmol/L) the conductivity can be computed with good approximation, also for strong electrolytes, as a linear combination of the ion concentrations:

$$\kappa = F \sum_i^{\text{all ion types}} b_i \cdot z_i \cdot c_i, \quad (5)$$

where the coefficients have the following meaning: F - Faraday constant, b_i - mobility of the ion type i and z_i is its charge. The good agreement between measurement and calculation results confirms that the solutions of our experiment are really diluted ones. The electrolytic conductivity is a sensitive integral parameter for dissolved, dissociated substances.

4. Dissolution reactions and rate laws

Weathering of pyrite contains an initiating reaction and a propagation cycle [7]. The initiating reaction involves the release of Fe^{2+} ions into the solution, either by oxidative dissolution of pyrite by O_2 or by Fe^{3+} . It is described as reactions a) and b), as follows:

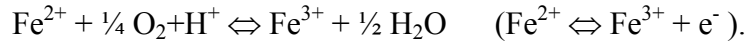


We used the relationship of Williamson and Rimstidt [8] as rate law for this process:

$$r_{\text{Fe}^{2+}, \text{FeS}_2}^{(a)} = \frac{1}{2} r_{\text{H}^+, \text{FeS}_2}^{(a)} = \frac{1}{2} r_{\text{SO}_4^{2-}, \text{FeS}_2}^{(a)} = k_{1p} \cdot a_{\text{H}^+}^{-0.11} \cdot \sqrt{c_{\text{O}_2}}. \quad (6)$$

The variables are referred to as a_i - activity of the i^{th} species defined by $a_i = \gamma_i \cdot c_i$, with γ_i - activity coefficient of the migrant i .

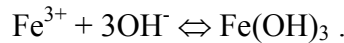
The next process of cycle is the oxidation of ferrous iron (Fe^{2+}) to ferric iron (Fe^{3+}):



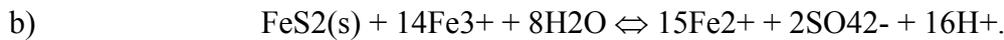
This reaction takes place in the water phase and is described by the following electron transfer rate [7]:

$$r_{\text{Fe}^{2+} \rightarrow \text{Fe}^{3+}} = k_{2p} \cdot c_{\text{Fe}^{2+}} \frac{c_{\text{O}_2}}{c_{\text{O}_2}^0} \begin{cases} 10^{-3.6} & \text{if } \text{pH} \leq 3 \\ 10^{-3.6 + (0.25(3-\text{pH}) - 0.46)(3-\text{pH})} & \text{otherwise} \end{cases}. \quad (7)$$

The concentration of Fe^{3+} ions at a pH value exceeding 3.5 is limited by the solubility of ferric hydroxide



Any ferric iron which remains in solution is subsequently reduced by pyrite, and consequently is generating an additional ferrous iron and acidity:

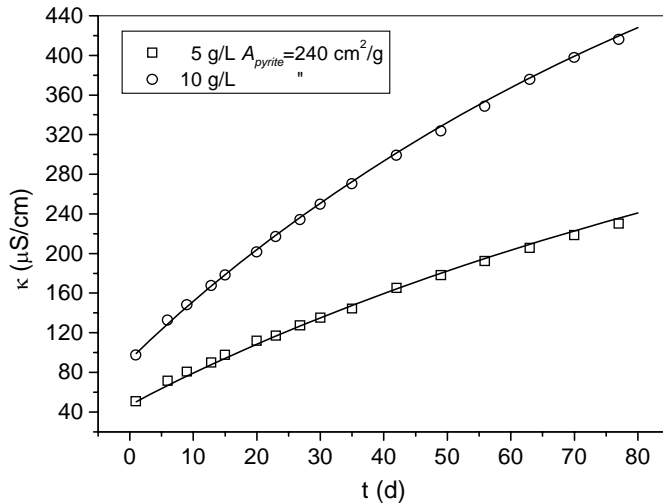


For this reaction again a rate law by Williamson and Rimstidt has been used

$$\frac{1}{15} r_{Fe^{2+}, FeS_2}^{(b)} = \frac{1}{16} r_{H^+, FeS_2}^{(b)} = \frac{1}{2} r_{SO_4^{2-}, FeS_2}^{(b)} = k_{1p} \frac{a_{Fe^{3+}}^{0.93}}{a_{Fe^{2+}}^{0.40}} \quad (8)$$

5. Discussion

The result of the batch test and of the corresponding calculation is shown in Fig. 2. The measurement showed a steep rise of conductivity during the first day. This is due to fine particles which dissolve very fast because of their relatively large surface. The curvature of the curves is caused by the change of pH value and by oxygen consumption. The calculation according to the system of equations (1) for the batch test was started with the initial concentrations after the first day. They were fitted to the measurements by means of varying the free parameter of the total surface of the pyrite grains A which resulted in $A=240 \text{ cm}^2/\text{g}$. The value of the pyrite surface obtained in this way is smaller than the value of $310 \text{ cm}^2/\text{g}$ as it is determined by the BET measurement. But, it is much larger than the value of $47 \text{ cm}^2/\text{g}$ resulting from the simple model of spherical grains. The BET method used for the estimation of the specific surface area of pyrite particles is based on the adsorption of a mono-layer of krypton.



In a column test, other parameters also influence the reactive surface as for instance: flow rate, porosity and dispersivity. These parameters were realized by the following values: flow rate or Darcy velocity $v= 0.65\pm 0.03 \text{ cm/d}$, porosity see Table 1, and dispersivity $\alpha_L \approx 1 \text{ cm}$ which was evaluated for the specific column length from a diagram [9]. Special attention was paid to keep constant the Darcy velocity.

Fig. 2: Electrolytic conductivity κ of pyrite solution in dependence on time measured in batch experiment.

The mean values of conductivities for the four columns are plotted in Fig. 3. In these figures, the solid curves are the results of stationary model calculations with the fitted values of the reactive pyrite surfaces as it is explained below. The extracted solution clearly shows an increasing conductivity going with the depth. This is caused by the release of Fe, H and SO_4 ions. Each ion is a solution product of the pyrite oxidation.

The fit to the individual measuring curves for the different sand samples result in clear differences for the effective surface areas.

PR30: $\eta A = 62 \text{ cm}^2 / \text{g} \rightarrow \eta = 0.26$, PR32: $\eta A = 81 \text{ cm}^2 / \text{g} \rightarrow \eta = 0.34$, PR33: $\eta A = 91 \text{ cm}^2 / \text{g} \rightarrow \eta = 0.38$
It is clear that only in this region with nearly constant water saturation this product could be assessed. With a transition into the region of higher water saturation also the oxygen content strongly decreases. In a depth of approximately 70 cm in the sand PR 33 the release of ions comes to an end. Here the transition to the saturation begins and a delivery of sufficient oxygen by diffusion is no longer possible and, therefore, the dissolution of pyrite is stopped..

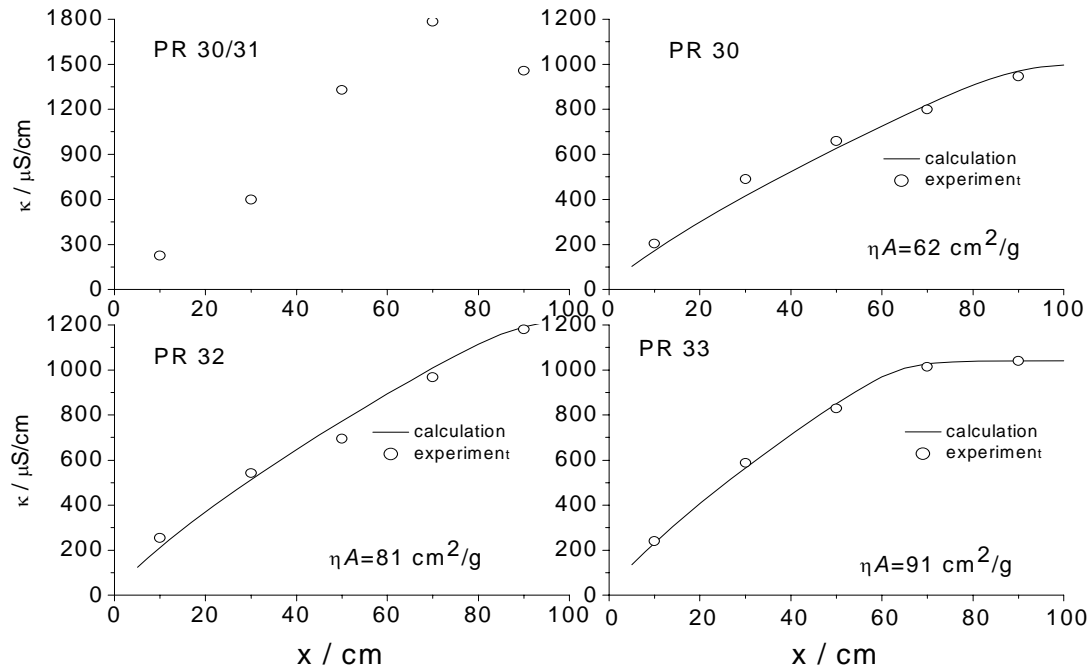


Fig. 3: Measured conductivity of the pyrite solution at the five test points for the four columns. The solid lines indicate the best fits for the reactive surface.

Although in the sands PR 30 and PR 33 the saturation s hardly distinguishes, we find great differences in the effective surface. Our assumption, that η essentially depends from the saturation is not confirmed by these tests. These experiments show clearly, that the storage parameters such as the solid-solid contact areas and the particle shape obviously have a greater influence on dissolution processes than assumed. Moreover, these values are very large in comparison with measurements of previous investigations, which gave results smaller or near to $n \cdot s$. That is, to find out the functional form of η further experiments are necessary.

References

- [1] J. I. Drever (1997), Geochemical processes, weathering and groundwater recharge in catchment. O. M. Saether & P. P. de Caritat (eds.) Balkema.
- [2] R. Kuechler and K. Noack (2002), Transport of reacting solutes through the unsaturated zone. *Transport in Porous Media* 49, pp. 361-375.
- [3] P. C. Lichtner (1996), Continuum Formulation of Multicomponent – Multiphase Reactive Transport, in P. C. Lichtner, C. I. Steefel and E. H. Oelkers (Eds.), *Reactive Transport in porous Media, Reviews in Mineralogy, Vol. 34*.
- [4] C. W. Davies (1962), Ion association. Butterworths; London, 190.
- [5] H. U. Sverdrup and P. Warfvinge (1991), On the geochemistry of chemical weathering. In K. Rosne'n (ed.); *Chemical weathering under field conditions. Rep. Forest Ec. Forest Soil* 63. Swedish Univ. Agri. Sci., 78-119.
- [6] W. H. Press, S.A. Teukolsky, W. T. Vetterling and B. P. Flannery (1992), *Numerical Recipes in Fortran*. Cambridge University Press.
- [7] P. C. Singer and W. Stumm (1970), The solubility of ferrous iron in carbonate-bearing waters. *J. Amer. Water Works Assoc.* 62, 198-202

- [8] M. A. Williamson and J. D. Rimstidt (1994), The kinetics and electrochemical rate determining step of aqueous pyrite oxidation. *Geochim. Cosmochim. Acta* 58, 5443-545
- [9] C. W. Fetter (1993), *Contaminant hydrogeology*. Prentice Hall, Upper Saddle River, NJ.

Summaries of research activities

Accident analysis of nuclear reactors

The research is aimed at the enhancement of the predictive capability of computer simulations of accident scenarios in nuclear reactors. This will be achieved by improvements of the neutron kinetics methods and e.g. by coupling of the reactor dynamics core model DYN3D to thermo-hydraulics system codes and computational fluid dynamics (CFD) simulations. In particular, it is the objective to promote the basic understanding of coolant mixing phenomena relevant for boron dilution and pre-stressed thermal shock scenarios and to better ascertain the capabilities of measures for in vessel retention of corium melt during severe LWR accidents.

*U. Grundmann
S. Kliem,
Y. Kozmenkov,
S. Mittag,
U. Rohde,
F. Schäfer,
A. Gommlich*

Development, validation and application of the code complex DYN3D - ATHLET

The Rossendorf reactor dynamics code DYN3D is undergoing a continuous development with respect to the improvement of physical models and numerical methods. A multi-group diffusion approach was implemented for an improved description of spectral effects, which are of increased importance in mixed-oxide (MOX) reactor core loadings. To validate this approach, an OECD benchmark on MOX cores was calculated. To enhance the accuracy of power density calculations, burn-up history effects are taken into account for the neutronics cross sections preparation. The extended DYN3D version is going to be integrated into the European code platform NURESIM.

The code DYN3D was used for core design and transient analyses in cooperation with the IPPE Obninsk aimed at studying the feasibility of weapons grade Plutonium burning in Russian VVER-1000 type reactors. The code complex DYN3D coupled with the thermo-hydraulic system codes ATHLET and RELAP5 is continuously validated against benchmark problems. Within an OECD/NEA benchmark on a pump trip transient in a VVER-1000 reactor, a comparison with results of the code system RELAP5/PARCS was performed. Based on the comprehensive expertise in simulation FZR contributed to analyses of complex NPP transients in NPP on request of the TÜV Hannover in the framework of the oversight procedure. Using the ATHLET code, analyses of the natural circulation stability features of advanced Boiling Water Reactors were performed for the General Electric company.

*Funded by: BMWA,
BMU, EC, TÜV
and industries*

*T. Höhne,
S. Kliem,
H.-M. Prasser,
U. Rohde,
T. Sühnel*

Analysis of deboration transients

After implementation of the semi-analytical mixing model SAPR into the coupled code complex DYN3D/ATHLET, transient analyses for various boron dilution accident scenarios have been performed. By applying SAPR, realistic boundary conditions for the boron concentration distribution at the core inlet can be provided. Therefore, conservative assumptions used in simplified modelling can be avoided. In this context, a diffusion-free numerical scheme for the description of the boron transport in the reactor core used in the code DYN3D was implemented into ATHLET, too. Besides of the start-up of the first main coolant pump after a loss-of-coolant accident, a further de-boration scenario with inadvertent injection of de-ionised water through the decay heat removal system was analysed.

Additional experiments simulating various boron dilution scenarios have

*Funded by industry
(VGB)*

*U. Grundman,
J. Krepel,
U. Rohde*

been performed at the Rossendorf coolant mixing test facility ROCOM. In these experiments, an innovative wire mesh sensor was used, which allows the detailed visualisation of the mixing phenomena in the reactor pressure vessel downcomer with high resolution in space and time.

Development of a DYN3D version for Molten Salt Reactors

The development of a version of the code DYN3D for dynamics studies of Molten Salt Reactors (MSR), which is one of the 'Generation IV' concepts, was completed. Modifications were made in the code to take into account the specifics of molten salt fuel. The model of delayed neutrons includes the convection of the precursor nuclei with the molten salt fuel. After completing the validation of the 1D neutron kinetics model within the European project MOST first 3D analyses of transients with relevant space-dependent effects (e.g. local coolant flow blockage) were performed.

Funded by the EC

*E. Krepper,
A. Grahn*

Simulation of sedimentation and re-suspension of insulating material in the reactor sump

Insulating material (mineral wool) may be released from pipes and components during loss-of-coolant accidents in NPP and will be transported with the coolant towards the reactor sump. There it might lead to blockage of the sieves separating the suction chambers of the safety injection pumps from the sump and would impede late phase safety injection.

The related project funded by BMWA aims at the simulation of sedimentation and re-suspension of the mineral wool particles in the sump pool flow. The work is done in co-operation with the University of Applied Sciences Zittau/Görlitz, where the experiments are done, while FZ Rossendorf is responsible for the CFD modelling. Based on sedimentation tests using original insulation materials, the sinking and transport behaviour of the mineral wool fibres in the water flow was simulated using the Euler/Euler continuum approach with an adjusted model of the interfacial drag. The sedimentation and the re-suspension of the fibres in the sump was modelled assuming dependence of the viscosity on the volume fraction of the insulation material. A physical model for the simulation of the blockage of the sump sieve was developed and tested. The follow-up project will focus on the modelling of the re-suspension of sedimented insulation material based on different CFD approaches (e.g. particle tracking, solidification models) as well as of an impinging water jet, which can re-mobilise sedimented material.

*H.-G. Willschütz,
E. Altstadt*

In-vessel corium melt retention in LWRs

An improved 2D thermo-mechanic finite element model has been developed for the evaluation of possible reactor vessel failure during a core melt down accident scenario. The thermal hydraulic and the mechanical calculations are recursively coupled. Using this model validated against data from the FOREVER experiment at KTH Stockholm, various scenarios with homogeneous melt configuration have been analysed. In these scenarios, an inner reactor vessel pressure of up to 163 bar was assumed. The simulations took into account the ablation of the inner wall in a simplified manner. The results have

*Funded by
BMW and
EC*

shown, that no RPV failure occurs, when the vessel is flooded from outside. The thermal stresses and strains occurring during the external flooding were calculated. It was concluded, that the mechanical loads induced by the thermal shock do not lead to RPV destruction if there is no initial crack.

Materials and components safety

The change in the toughness behaviour of reactor pressure vessel materials is investigated as it results from neutron and gamma irradiation. The consequences are evaluated with respect to the safety of light water reactors (LWRs). For this purpose, material and fracture mechanical parameters of irradiated specimens have to be measured under hot cell conditions. The interpretation of the experiments is supported by finite element calculations. The microstructural reasons and mechanisms of the neutron embrittlement are studied by small angle neutron scattering experiments and by nano-scaled modelling.

*U. Rindelhardt,
H.-W. Viehrig,
E. Altstadt,
C. Zurbuchen*

Investigation of reactor pressure vessel material of the dismantled Greifswald NPP

In co-operation with industry partners the drilling device was developed, built and tested for cutting out material from reactor pressure vessels. Then in total 5 trepans were cut from the RPV of unit 1 of the Greifswald NPP in November 2005. Three trepans were taken from the core weld material whereas the remaining two were cut from the base metal. For the investigation of this unique material, a research programme was elaborated in cooperation with partners in Finland and Russia. The manufacturing of fracture mechanical specimens has been started in the hot cell laboratories. The first testing results are expected for spring 2006.

*H.-W. Viehrig,
M. Abendroth,
M. Werner,
E. Altstadt,
C. Zurbuchen*

Application of the Master Curve Concept for irradiated material

In the FP6 of the EU FZR is involved in the Integrated Project PERFECT (Prediction of Irradiation Damage Effects in Reactor Components). FZR is leading a work package within the sub-project Mechanics Modelling. In this frame the VVER-440 RPV steel of the Greifswald NPP (unit 8) is analysed. The unirradiated material exhibits a large scattering of the fracture toughness and inter-granular cleavage fracture. It is therefore a suitable material for testing the applicability of the Master Curve Concept to inter-granular cleavage fracture and to inhomogeneous microstructure. An irradiation experiment was started in the LYRA facility of JRC Petten. More than 100 specimens (Charpy, tensile, CT) are irradiated. This experiment will be finished in February 2006.

In the frame of an industry co-operation with E.ON Kernkraft fracture mechanic tests were performed for an RPV material of the Brokdorf NPP (KBR). After machining of the specimens, tensile tests and Charpy impact tests were done. The reference temperature was determined according to the Master Curve Concept (ASTM E1921-02) using 1T-C(T) specimens. All the tests were supervised by the TÜV Süddeutschland.

The research project "Application of the Master Curve Concept for the toughness characterization of neutron irradiated reactor pressure vessel steels" was continued within the framework of the BMWi funded German nuclear reactor safety research programme. It is the aim of the project to apply the Master Curve Concept to highly irradiated RPV steels. The reference temperatures were evaluated of three different RPV materials and for four irradiation states (including the unirradiated state).

Funded by: EC,

*BMW and
E.ON Kernkraft*

To improve the data base, irradiated material from already tested specimens was re-used by means of reconstitution technique.

*F. Bergner,
A. Ulbricht*

Analysis of the irradiation induced micro-structural changes

At the GKSS in Geesthacht small angle neutron scattering (SANS), experiments were performed and evaluated with specimens of VVER-1000 RPV steels and low copper model alloys. These specimens were investigated in the frame of the EU project PERFECT. The results are used for the characterisation of irradiation defects in comparison with different experimental methods like PAS, APFIM and TEM applied by other project partners. In the case of the VVER-1000 steel a linear dependence of the volume fraction of the defects on the neutron fluence was observed. An extreme small effect of the irradiation was observed at the model alloys also for high Ni contents. This proves, that the embrittlement effect of Ni is tied to the presence of Cu.

Funded by EC

*F. Bergner,
A. Gokhman,
R. Kuchler*

Modelling of the irradiation induced embrittlement

Within the physics subproject of PERFECT a model has been developed for the simulation of irradiation-induced defects in RPV steels. It describes the evolution of vacancy clusters in pure bcc iron. The model is based on the rate theory considering the effect of lattice relaxation. The size distribution functions and the volume content were calculated and compared to those obtained by SANS measurements. The model was extended to the formation of pure Cu clusters and Cu-vacancy complexes like observed in Cu rich RPV steels. For a Cu rich model alloy, good agreement was achieved between the calculation results and the SANS measurement with respect to the fluence dependency of the volume fraction and cluster size.

Funded by EC

Particle and radiation transport

The research project aims at the development, verification and application of computational methods for particle and radiation transport. At present, the focus is on neutron/gamma/electron transport with applications in reactor physics, shielding and radiation physical experiments. The transport of radio-nuclides in water-unsaturated geological zones is a further topic of high relevance in the context of final disposal of radioactive waste and in the context of the left backs of uranium mining.

*J. Konheiser,
K. Noack*

Fluence calculations for the pressure vessel of reactor unit 1 of the decommissioned Greifswald NPP

In the framework of the German-Russian collaboration neutron and gamma fluences were calculated by means of the Monte Carlo Code TRAMO for several positions at the pressure vessel of unit 1. Especially, the fluence profiles along the depth of the pressure vessel wall at the trepan positions were computed.

The effective group cross sections used by TRAMO in the neutron/gamma-transport simulations were prepared with data from the latest release No. 8 of the evaluated nuclear data library ENDF/B-VI in the energy group structure of the BUGLE-96 data set. Energy spectra and several energy integrals of the fluences have been computed. To get the correct gamma fluences the neutron transport simulations had to be extended up to the range of thermal energies because high-energetic gammas can be emitted from captures of thermal neutrons.

In order to verify the TRAMO calculation an ex-vessel irradiation experiment was calculated, which was carried out during cycle 12. In this experiment, various fast neutron detector material samples were irradiated at the outer surface of the pressure vessel. The comparison between measured and calculated activities shows an agreement within 10 % with the only exception of the niobium detector where both results differ by to 40 %. The great deviation in case of niobium was finally attributed to the measurement technique used at that time which showed several shortcomings.

*Funded by
BMW A*

*J. Konheiser,
K. Noack*

Verification of TRAMO for fluence calculations in reactor dosimetry

The typical material conditions of the support construction are of special importance for safety assessments of PTS (pressurized thermal shock) accidents. In the framework of the German-Russian collaboration neutron fluence calculations were carried out for regions above the upper core edge of a VVER-1000 reactor for the first time inside and in the surrounding of the surveillance specimen container, and in the region of the pressure vessel support construction. The Russian cooperation partners made available results of activation measurements, which have been carried out at a running VVER-1000 reactor. The comparison between measured and calculated activations showed an unexpectedly good agreement within 10 % in most cases.

*Funded by
BMW A*

R. Koch

Transmutation of actinides in Molten Salt Reactors and in Pressurized Water Reactors

With the cell- and depletion code-system HELIOS-1.8 and with the code-combination of MCNP-4C2 and ORIGEN-2.1 the actinide and the fission product inventories for MSR- and PWR-benchmarks have been calculated up to high depletions of 80 MWd/kg. Our results to the Molten Salt Reactor are incorporated in the document collection of the Coordinated Research Project „Studies of Advanced Reactor Technology Options for Effective Incineration of Radioactive Waste“ of the IAEA. The calculations on the PWR were carried out in the framework of a benchmark problem initiated by the GRS. It was shown that even for an UOX-assembly, where the nuclear data are rather accurate known, the resulting nuclide inventories obtained by the institutions involved, may be rather different. The results of the Code-systems HELIOS and CASMO are in a relatively good agreement: up to the specific burnup of 40 MWd/kg the relative deviations are less than 5 % (Exception: Pu-238) and remain below 15 % for the specific burnup up to 80 MWd/kg.

*R. Kuechler,
K. Noack*

Migration of radio-nuclides in the unsaturated zone

In order to study the weathering process of pyrite batch and column experiments were carried out in four sand columns with different particle size distributions. The goal consisted in investigating the influences of both the particle size distribution and the water saturation on the reactive surface of the pyrite grains. Generally, it is accepted that under the conditions of an unsaturated water flow the chemically reactive surface of the mineral grains is considerably reduced. However, the test results show very clearly that the effective reactive surface in these sands depends more strongly on the grain structure and on their size distribution than on the saturation. Thereby, the quoted assumption that the reduction of the effective reactive surface is in the first place a function of the saturation is challenged.

Pulsed Photo-Neutron Source at the radiation source ELBE

The Rossendorf LINAC ELBE provides electrons with energies up to 40MeV. The pulsed electron beam can be injected into several beam lines to generate other types of radiation like parametric X-rays, infrared light, and neutrons. The neutrons are generated by (γ,n) reactions when the high energy electrons hit a high Z-target (liquid Pb) producing Bremsstrahlung. With the envisaged design, neutron source intensities in the range between 10^{12} - $10^{13}s^{-1}$ will be achieved. The ELBE parameters allow to convert the picosecond electron pulses into nanosecond neutron pulses which will be used to measure energy resolved neutron cross sections in a time of flight (TOF) facility. Due to the very short neutron pulses, an energy resolution of better than 1% can be reached after a TOF distance of only 3.9m. The usable energies range from 50keV to approx. 10MeV with an electron beam repetition rate of 0.5MHz. This is an interesting energy interval to measure neutron cross sections needed e.g. in the context of minor actinide transmutation.

The work is performed in close cooperation with the physics department of TU Dresden and the Rossendorf Institute of Nuclear and Hadron Physics.

D. Legrady

Calculations for the photo-neutron source at the ELBE accelerator

The optimum structure of the collimator of the n_TOF experiment at ELBE has to be determined by Monte Carlo calculations with the MCNP code. For that the radial profiles of the neutron and photon fluxes perpendicular to the beam axis at the positions of target and detector have to be considered. To be able to efficiently calculate these functions for various possible collimator designs an efficient schema of the MCNP weight window (WW) technique has been developed and tested. For neutron-neutron calculations the optimized WW technique yielded converged results after a 10 hour's run in comparison with the former non-converged three day's run.

Plastic and Li-glass scintillators are planned for detecting neutrons in ELBE n-TOF experiments. As both have non-Boltzmann characteristics in the detector function, some modification of the MCNP code tallying was necessary. A Fortran program has been written for proper post-processing of the simulated particle tracks.

K. Noack

B. Boehmer

Inquiry on data need for transmutation

A further activity devoted to the n_TOF experiment was an inquiry of the actual state of measured cross sections relevant for the topic "Transmutation of nuclear waste" in the energy range covered by the photo-neutron-source at ELBE. The inspection considered both the uncertainties of measured data and their impact on the design of a transmutation device either as reactor or as an accelerator driven system. From this investigation specific recommendations for the first series of cross section measurements have been drawn.

Safety and effectiveness of chemical processes

The objectives of the research activities include the increase of the safety, efficiency and environmental sustainability of processes and plants in the field of chemical engineering. Therefore, detailed analyses of chemical engineering processes are carried out using advanced online measuring algorithms and sensors. The results provide the basis for the numerical and experimental process simulation at normal operating conditions as well as at safety relevant fault scenarios, i.e. local hot spots and exothermic runaways. Numerical simulations of reactive flows in multiphase/ multicomponent systems are handled using constantly developed CFD codes. Additionally, MHD-based techniques are used to optimise the energy efficiency as well as the space-time yield of electrochemical processes.

*G. Hessel,
H. V. Hristov,
H. Kryk,
H.-M. Prasser,
W. Schmitt,
S. Boden,
U. Hampel,
D. Lucas,
A. Manera*

CFD simulation of chemical engineering processes

Gas-liquid mixing and reactive liquid mixing processes in laboratory-scale stirred tank reactors were modelled using the CFD software CFX. In terms of the local gas holdup, the simulation results exhibit a good agreement with experimental ones taken by x-ray cone beam tomography. A neutralisation reaction has been used in order to numerically predict transient reactive mixing processes. The experimental validation of the simulation results has been carried out by videographic detection of the colour change of pH-sensitive tracer solutions. The results are important milestones towards the CFD simulation of complex chemical processes.

Bubble columns are widely used for heterogeneous chemical processes. Their effectiveness strongly depends on the flow structure. Especially the transition between homogeneous and heterogeneous regime has been the focus of investigations for many years. The models and criteria, which can be found in the literature, are not able to explain the process in a consistent way. Nowadays, the bubble size dependent lateral lift force was identified as a key to solve this problem. By means of a linear stability analysis, criteria for the local stability of a bubbly flow dependent on the bubble size distribution were derived. After publication these findings were confirmed experimentally by two groups (University of Montreal and University of Delft).

*U. Hampel,
M. Schubert*

X-ray radiography

Intermittent feeding is an innovative method to improve the operating performance of fixed bed reactors. X-ray radiography was used to observe the local liquid hold-up inside such a laboratory scale reactor. The precision measurements of time-dependent axial hold-up profiles have been carried out in co-operation with the TU Dresden.

*G. Hessel,
H. Kryk,
W. Schmitt,
U. Hampel*

Optical sensor for gas-liquid flow visualisation in vent lines

The optical sensor for the visualisation of multiphase flow within the vent lines of chemical reactors was tested at stationary and transient flow conditions using the ALR miniplant. The sensor is based on a videoendoscopic imaging technique and comprises a unique short pulse stroboscopic illumination feature that enables to acquire microscopic snap shot images of flows at up to 10 m/s velocity. The concept and the design of the sensor were proved.

*G. Hessel,
H. Kryk,
W. Schmitt*

Strongly exothermic chemical reactions

Grignard reactions comprise considerable hazard potentials due to their specific process behaviour. A matter of particular interest is the influences of impurities (esp. water) on the thermal process behaviour. By means of calorimetric experiments at adiabatic conditions, it was shown that the water concentration influences the induction time. However, in the case of a runaway, it was found that the water concentration does not influence the maximum reaction rate. As a result of isothermal experiments, a significant impact of the water content in the solvent on the enthalpy of the initiation reaction due to exothermic side reactions was observed. By calorimetric studies of the reaction between the Grignard mixture and the water, a dependency of the reaction enthalpy on the amount of water due to a complex reaction network was shown. The results are of vital importance for safety-related assessment of the industrial process.

*T. Weier,
C. Cierpka,
J. Hueller,
G. Gerbeth*

Application of MHD to optimise electrochemical processes

The flow field in electrolyses cells of various geometries have been measured with Particle Image Velocimetry for copper electrolytes of different composition. When electrolysis takes place under the influence of a magnetic field, flow structures evolve due to the interplay of Lorentz forces and buoyancy. Even if the magnetic and the electric field are almost parallel, a significant Lorentz force effect could be demonstrated, which is of special interest with respect to the present debate regarding the influence of paramagnetic forces on electrochemical processes. It has been shown for cylindrical cells that the direction of the radial flow can be changed just by altering the electrode diameter. The reason for this effect is the modification of the electric field by the change of the electrode geometry.

Liquid metal magnetohydrodynamics

Magnetohydrodynamics investigates the interaction of electrically conducting liquids (liquid metals and semiconductors, electrolytes) with magnetic fields. On the one hand, in various applications, the use of magnetic fields provides a comfortable contact-less possibility to control the transport processes in such melts. On the other hand, problems as MHD turbulence or the homogeneous dynamo are the subject of intensive basic research.

*A. Cramer,
S. Eckert,
I. Grants,
R. Lantzsch,
J. Pal,
A. Pedchenko,
J. Priede,
Ch. Zhang,
G. Gerbeth*

Basics of MHD flows and MULTIMAG

Systematic experimental studies have been performed on the stability of metal flows under the combined influence of temperature gradients as well as steady and alternating magnetic fields. The complex set-up MULTIMAG provides best conditions for this kind of investigation. The theoretical predictions about the different transition to turbulence in rotating and travelling magnetic fields have been verified experimentally. In a travelling field this transition arises according to the linear instability, whereas in a rotating magnetic field turbulence occurs at a four times lower threshold than predicted by linear stability. For the stabilization of buoyant convection, the optimal combination of rotating and steady magnetic fields has been determined. In that way, the temperature fluctuations in the flow field could be reduced by about one order of magnitude. The performed stability studies lead, e.g., to the design of the travelling magnetic field meanwhile installed at the VGF crystal growth facility at TU Bergakademie Freiberg. In addition, systematic experimental studies were conducted on the influence of magnetic fields on liquid metal gas-bubble two-phase flows. For moderate steady field strengths, a destabilization of the metal flow has been found in contrast to the generally believed damping action of such magnetic fields.

*Funded by
DFG*

*B. Willers,
S. Eckert,
V. Galindo,
G. Gerbeth*

Magnetic field control of aluminum investment casting

Together with the industrial partner Aluminium Feinguss Soest (AFS) the magnetic field control of the aluminum pouring process has been analyzed under industrial conditions. The braking magnetic field action leads to a significant reduction of surface defects in the casting units. Reductions up to a factor of four in the defective rate of series of castings were obtained. Together with AFS, the developed casting control method has been submitted for a joint patent.

*Funded by
BMBF (DLR)*

*T. Weier,
Ch. Cierpka,
G. Mutschke,
V. Shatrov,
G. Gerbeth*

Boundary layer control in electrolytes

The experiments with variable wave forms of the electrode current confirmed that the unsteady excitation of the boundary layer is mainly determined by the amplitude of the Lorentz force rather than its duration. Numerical simulations have been performed about the energetic optimization of electromagnetic flow control taking into account for the first time the full coupling of flow and electromagnetic quantities. These simulations showed that most of the published results about the energetic breakthrough of the electromagnetic flow control are incorrect. Any hope for such an energetic breakthrough requires a load factor in the order of one, i.e. the flow induced electrical current must be

Funded by

DFG

of the same order as the externally applied one.

*S. Eckert,
B. Willers*

Magnetic control of solidification processes

In order to influence the microstructure of solidified metals, basic studies on the role of convection during the solidification process have been performed. Various compositions of Pb-Sn- as well as Al-Si-alloys have been solidified under the influence of a rotating magnetic field. The microstructure changed, from a columnar-dendritic one without magnetic field to an equiaxed one in case of an additional stirring of the liquid phase due to the magnetic field action. The in-situ measurement of the velocity field by the ultrasonic Doppler velocimetry during the solidification process provided an important access to understand the underlying complex phenomena in more detail.

*Funded by
DFG*

*S. Eckert,
G. Gerbeth*

Steel casting model CONCAST-LMM

Preliminary studies have been performed about the design of a liquid metal model of the continuous casting of steel. With the desirable flexibility of the flow control, such a facility comes into the order of about one million Euro. This project was submitted to DFG and was approved at the end of the year.

*Th. Gundrum,
F. Stefani,
G. Gerbeth*

Velocity reconstruction by magnetic tomography

The magnetic tomography of flows allows a fast measuring of three-dimensional, mean velocity fields in a fully contact-less way. An externally applied steady magnetic field is disturbed by the flow, and this field disturbance can be measured outside of the fluid volume by an array of magnetic field sensors. The mean flow field is then reconstructed by means of an inverse solver using a regularization technique. Applications are expected in the flow control of metal casting processes or in the measurement of melt velocities in crystal growth cases. Together with academic and industrial partners, a European project has been developed coordinated by FZR. The project was selected for funding at the end of the year.

*Funded by
DFG*

*D. Buchenau,
J. Priede,
W. Witke,
G. Gerbeth*

Electromagnetic flow rate measurements

The development of a contact-less flow rate measurement is an important but open topic. Based on the flow induced phase shift between emitting and receiving sensors, a new measuring principle has been developed. Test measurements showed that this solution is much less sensitive against small disturbances compared to the analysis of the corresponding field amplitudes.

Thermal fluid dynamics of multiphase systems

The work of the Institute in the field of thermal fluid-dynamics aims at the development of models for Computational Fluid Dynamics (CFD) codes that describe the transient evolution of gas-liquid two-phase flows along the flow path in pipes and in complex geometries. The models for dispersed bubbly flows have to describe as well bubble size dependent void fraction distributions as bubble coalescence and fragmentation. The theoretical work is based on sound experiments at the TOPFLOW test facility using advanced two-phase measuring instrumentation, which is developed in this framework.

*E. Krepper
D. Lucas,
J.-M. Shi*

Qualification of CFD models

The so-called inhomogeneous MUSIG model was developed at FZR and implemented into the CFD code CFX together with the code developer ANSYS-CFX[®]. It was used to simulate the evolution of a bubbly flow along a vertical pipe. The comparison with experimental data obtained at the TOPFLOW facility indicated a too fast migration of the bubbles from the pipe wall to the pipe centre in the simulations for some combinations of gas and liquid superficial velocities. This is caused by an over-prediction of the turbulent dispersion force. Beside bubble forces also bubble coalescence and break-up influence the evolution of the flow. Uncertainties exist as well regarding the suitability of the available models as regarding the input parameters. Both, bubble coalescence and bubble break-up strongly depend on turbulence, which can only unsatisfactorily be calculated accurately for two-phase flows with the present models. Nevertheless, the applicability of the inhomogeneous MUSIG model for poly-dispersed flows was shown by tuning the model constants for the coalescence and break-up.

Funded by BMWA

*H.-M. Prasser,
S. Alissa,
T. Höhne,
Ch. Valleé*

Validation of CFD codes for complex geometries

To test the new-implemented CFD models also for flows in complex geometries, experiments in a vertical pipe were done, in which one half of the pipe was blocked by a vertically moveable half-moon shaped obstacle. This allowed measuring complete 3D flow fields in the region influenced by the obstacle. By a new measuring method, not only fields of void fraction distribution, but also of the liquid velocity can be determined. Pre-test calculations for these experiments were done using ANSYS-CFX[®]. A good agreement was achieved for both, void fraction distributions and liquid velocity around the obstacle. The CFX code was also used to calculate the flow rate through a Leser[®] safety valve. The characteristic diagram for the flow rate showed an excellent agreement with given data from the manufacturer of the valve for air and water. For high initial pressure a systematic deviation of the air flow rate was observed, caused by the real gas properties in case of high Ma-number. A realistic increase of the volume fraction of the gas phase was observed in dependency on the pressure decrease in the CFX simulation.

*H.-M. Prasser,
M. Beyer,
S. Alissa*

Analysis of wire-mesh sensor data

A new evaluation method for wire-mesh sensor data was developed, which allows the measurement of the stationary field of the liquid velocity. It makes use of so-called marker-bubbles. For these bubbles,

the relative velocity to the liquid phase is constant and well known. Using the information on the known total liquid flow rate, the distribution of the liquid velocity can be obtained.

*U. Hampel,
E. Schleicher,
M. Bieberle,*

Development of a fast scanned electron beam computed tomography device

For an ultra fast X-ray computed tomography system with a scanned electron beam source, we developed a system concept and started manufacturing of major system components. The device comprises an electron beam X-ray source (max. 150 kV, max. 32 mA beam current) with a 10 kHz electron beam deflection unit and a semiconductor X-ray detector. The system will enable the generation of cross-sectional CT images at an imaging rate of up to 10 kHz.

Within the project „Ultra fast X-ray computed tomography for multi-phase flows“, funded by the Deutsche Forschungsgemeinschaft, we developed optimised image reconstruction algorithms for limited angle electron beam CT. Within this project, a two-phase flow loop was designed and constructed that will be operated inside a vacuum enclosure during tomographic experiments with our project partner IKE Stuttgart.

Funded by DFG

*U. Hampel,
A. Bieberle,
D. Hoppe*

Measurement of steam distributions in BWR fuel element bundles

For the measurement of the steam distribution in BWR fuel element bundles inside a highly absorbing pressure vessel we developed and constructed a gamma ray tomograph. The device consists of an isotopic source (Cs-137, 165 GBq), a high resolution detector arc with 320 scintillation detectors, made of avalanche photo diodes and LYSO crystals, a gantry and a control unit. The high resolution gamma ray tomograph was put into operation in August 2005 at the KATHY test loop facility of Framatome ANP GmbH in Karlstein. The project is co-financed by Framatome ANP GmbH.

*Funded by AREVA
NP*

*A. Zaruba,
D. Hoppe,
D. Lucas,
H.-M. Prasser*

High speed video analysis on bubble trajectories

Measurements on the bubble motion in gas-liquid flows were conducted as well in a flat rectangular bubble column as in vertical acrylic duct having a square cross-section using high-speed video analysis. By a statistical evaluation of bubble trajectories in the flat channel for stagnant liquid, the turbulent dispersion was determined. Drag, lift, and wall forces were investigated by the evaluation of the bubble trajectories in the vicinity of the wall. Other characteristic parameters of the bubbles as size distributions, velocity, shape and inclination angle were obtained by stereoscopic techniques and PIV. These data were used in cooperation with the Institute of Reactor Safety Research at the Research centre Karlsruhe for comparison with DNS simulations.

*E. Schleicher,
W. Zimmermann*

Measurement of gas distributions and bubble velocity fields in the model containment ThAI

Experiments were performed at the ThAI integral facility at Becker Technologies GmbH Eschborn to derive correlations between bubble size distribution in the reactor sump and aerosol concentration in the containment atmosphere. For these experiments, special double tip

coaxial conductivity needle probes and a set of data processing algorithms were developed. This equipment allowed the measurement of local void fraction, bubble rates, bubble size distributions, and mean rising velocities of bubbles at four locations close to the surface of the sump water level at different gas superficial velocities.

M. da Silva

Development of new measurement techniques for the study of multiphase flows with non-conducting liquids

On the basis of the existing needle probe and wire mesh sensor technology we developed new impedance sensors. These sensors measure the local electrical impedance instead of conductance at high data acquisition rates. The special challenge for impedance measurements is the comparatively low electrical signals which require a highly optimised measuring electronics. In the course of the work we developed a new impedance needle probe for measurement in multiphase flows, such as oil-water-gas mixtures in mineral oil processing or organic fluids in chemical engineering. Furthermore, a specially combined conductivity and temperature needle probe for rapid measurement of local conductivity and temperature in steam-water flows has been developed. This probe reaches time constants of a few milliseconds concerning the temperature signal. Two patents were filed for these sensors.

TOPFLOW thermohydraulic test facility

The acronym TOPFLOW stands for Transient Two Phase Flow Test Facility. This multipurpose thermal hydraulic facility is mainly used for the investigation of generic and applied steady state and transient two phase flow phenomena in either steam-water or air-water-mixtures. It has become the reference experimental facility of the German CFD (Computational Fluid Dynamic) Research Alliance. TOPFLOW has a maximum heating power of 4 MW and allows operation at pressures up to 7 MPa and temperature up to 285 °C in pipes and vessel geometries of industrial relevance. To support the theoretical model development and the CFD code validation, a series of experiments has been conducted at TOPFLOW at different test rigs in 2005.

*H.-M. Prasser,
H. Carl,
M. Beyer,
K. Lindner,
H. Pietruske,
P. Schütz*

Experiments in the vertical test sections DN50 and DN200 for the measurement of the dynamics of the gas-liquid interface

The executed test programme in the vertical test sections comprised experiments at 1, 2, 4 and 6.5 MPa pressures and the corresponding saturation temperatures. The superficial liquid velocity and the superficial steam velocity were varied as well as the inlet length for the measurement of the evolution of the two-phase flow structure along the flow path.

Preliminary studies were carried out on steam condensation in sub-cooled liquid due to interfacial heat transfer. The results obtained were used for the validation of the MUSIG-model in CFX-10 and for the simulation of condensation processes.

A dedicated series of air-water tests was executed to study the influence of the system pressure on the bubble size distribution. Wire-mesh data was recorded for 9 combinations of the superficial gas and liquid velocities. The pressure in the vertical test section DN200 was varied between 0,01 and 0,22 MPa in steps of 0.02 MPa. Furthermore, the matrix of superficial velocities was extended and special measurements were added with an increased time resolution of 10 kHz instead of 2.5 kHz.

Funded by BMWA

*H.-M. Prasser,
P. Schütz,
S. Al-Issa,
M. Beyer,
H. Carl,
H. Rußig*

Two-phase flow experiments in complex geometries

The three-dimensional void fraction distribution in the flow field around a half-moon shaped diaphragm placed in the large vertical test section (DN200) was measured with high spatial and time resolution using a wire-mesh sensor. The obstacle was mounted on top of a translation mechanism. In this way, it was possible to vary the measuring location without moving the sensor. The distance between sensor and obstacle was varied between 10 and 520 mm. Both the flow upstream and downstream of the diaphragm was studied, the tests were carried out with an air-water mixture at ambient conditions as well as with a saturated steam-water flow at 6.5 MPa and 280 °C.

Funded by BMWA

*H.-M. Prasser,
M. Beyer,
H. Carl,
P. Schütz,
M. Tamme,*

Hot leg model

The construction of the hot leg model is completed. During the commissioning tests, the design parameters were reached and the technical certificate was granted by TÜV. Initial problems with the air circulation fans in the cooling loop for the inner atmosphere of the

Ch. Vallee

pressure tank hosting the hot leg model were solved.

Problems with the thermal insulation of the test section inside the tank are still obstructing the launch of the experiments. It turned out that classical insulation materials, like glass wool with Al coating, mineral wool and foam glass are either not stable at 5 MPa and design temperature, or they lose the insulation capability with growing air pressure. The search for an appropriate insulation material is continued. A small dedicated autoclave which is equipped with an electrical heater was constructed and is now used for testing.

Funded by BMWA

H.-M. Prasser,

M. Beyer,

P. Schütz,

H. Carl,

H. Pietruske,

St. Weichelt

Thermal hydraulic experiments with the emergency condenser model

Heat up experiments at different experimental conditions were carried out. The characteristics for the heat removal by condensation in the tubes were measured on primary-side pressures up to 6.5 MPa. A further important result of these experiments was the visualisation of the temperature field of the spatially well resolved and instrumented secondary-side. The heat up process was recorded until boiling on the secondary-side occurred. The measured data enables the validation of CFD-codes. Additionally, the obtained results substantially contribute to the IAEA Coordinated Research Project: “Natural Circulation Phenomena, Modelling and Reliability of Passive Safety Systems that Utilize Natural Circulation”.

Funded by BMWA

Publications

Publications in journals

Abdrashitov, A.; Abdrashitov, G.; Anikeev, A.; Bagryansky, P.; Beklemishev, A.; Deichuli, P.; Ivanov, A.; Korepanov, S.; Maximov, V.; Murakhtin, S.; Lizunov, A.; Prikhodko, V.; Kapitonov, V.; Kolmogorov, V.; Khilchenko, A.; Mishagin, V.; Savkin, V.; Shoukajev, A.; Shulzhenko, G.; Solomakhin, A.; Sorokin, A.; Stepanov, D.; Stupishin, N.; Tsidulko, Yu.; Zouev, A.; Noack, K.; Fiksel, G.; Den Hartog, D.

Status of the GDT experiment and future plans

Fusion Science and Technology 47(2005)1T, 27-34

ISSN: 1536-1055

Aguirre, C.; Caruge, D.; Castrillo, F.; Dominicus, G.; Geutjes, A. J.; Saldo, V.; van der Hagen, T. H. J. J.; Hennig, D.; Huggenberger, M.; Ketelaar, K. C. J.; Manera, A.; Munoz-Cobo, J. L.; Prasser, H.-M.; Rohde, U.; Royer, E.; Yadigaroglu, G.

Natural circulation and stability performance of BWRs (NACUSP)

Nuclear Engineering and Design (2005)235, 401-409

Alsmeyer, H.; Albrecht, G.; Meyer, L.; Häfner, W.; Journeau, C.; Fischer, M.; Hellmann, S.; Eddi, M.; Allelein, H.-J.; Bürger, M.; Sehgal, B. R.; Koch, M. K.; Alkan, Z.; Petrov, J.; Gaune-Escard, M.; Altstadt, E.; Bandini, G.

Ex-vessel core melt stabilization research (ECOSTAR)

Nuclear Engineering and Design, Vol 235 (2-4), pp 271-284, February 2005

Anikeev, A. V.; Bagryansky, P. A.; Collatz, S.; Noack, K.

Plasma simulations of the SHIP experiment at GDT

Fusion Science and Technology 2005(2005)47 (1T), 212-214

Bagryansky, P. A.; Anikeev, A. V.; Ivanov, A. A.; Lizunov, A. A.; Maximov, V. V.; Murakhtin, S. V.; Stepanov, D. N.; Noack, K.; Prikhodko, V. V.; Solomakhin, A. L.

First results from SHIP experiment

Fusion Science and Technology (2005)47 (1T), 59-62

ISSN: 1536-1055

Bergner, F.

Scaling of self-similar long fatigue crack growth in aluminium alloys

Materials Science and Engineering A 400-401 (2005) 422-425

Bergner, F.; Müller, G.; Ulbricht, A.; van Ouytsel, K.; Blank, C.; Bras, W.; Dewhurst, C.

Deformation-induced small-angle scattering contrast in aluminium alloys

Nuclear Instruments and Methods in Physics Research B (Beam Interactions with Materials and Atoms) 238 (2005) 92-97

Dzugas, J.

Corrected procedure for crack lengths calculation by the unloading compliance technique for Charpy size specimens

Journal of Testing and Evaluation, Vol. 33, No. 6, Nov. 2005

Eckert, S.; Galindo, V.; Gerbeth, G.; Witke, W.; Buchenau, D.; Gerke-Cantow, R.; Nicolai, H.-P.; Steinrücken, U.

Strömungskontrolle bei Formfüllung mittels Magnetfeldern

Giesserei 92(05) (2005) 26-31

Eckert, S.; Willers, B.; Gerbeth, G.

Measurements of the bulk velocity during solidification of metallic alloys

Metallurgical and Materials Transactions, Vol. 36A, 2005, 267-270

Filip, O.; Hermann, R.; Gerbeth, G.; Priede, J.; Biswas, K.

Controlling melt convection - an innovation potential for concerted microstructure evolution of Nd-Fe-B alloys

Materials Science and Engineering A 413-414(2005), 302-305

Günther, U.; Stefani, F.

Third order spectral branch points in Krein space related setups: PT-symmetric matrix toy model, MHD α^2 -dynamo, and extended Squire equation

Czechoslovak Journal of Physics 55(2005)9, 1099-1106

ISSN: 0011-4626

DOI: 10.1007/s10582-005-0113-z

Günther, U.; Stefani, F.; Znojil, M.

MHD α^2 -dynamo, Squire equation and PT-symmetric interpolation between square well and harmonic oscillator

Journal of Mathematical Physics 46(2005), 063504-.

ISSN: 0022-2488

DOI: 10.1063/1.1915293

Günther, U.; Zhuk, A.; Bezerra, V.; Romero, C.

AdS and stabilized extra dimensions in multi-dimensional gravitational models with nonlinear scalar curvature terms R^{-1} and R^4

Classical and Quantum Gravity (2005)22, 3135-3167

Hammer, R.; Bergner, F.; Flade, T.; Jurisch, M.; Kleinwechter, A.; Schaper, M.

Material related fundamentals of cutting techniques for GaAs wafer manufacturing

Zeitschrift für Metallkunde 96(2005), 785-791

Hampel, U.; Hoppe, D.; Diele, K.-H.; Fietz, J.; Höller, H.; Kernchen, R.; Prasser, H.-M.; Zippe, C.

Application of gamma tomography to the measurement of fluid distributions in a hydrodynamic coupling

Flow Measurement and Instrumentation 16 (2005) 85-90, 2005

Hampel, U.; Speck, M.; Koch, D.; Menz, H.-J.; Mayer, H.-G.; Fietz, J.; Hoppe, D.; Schleicher, E.; Zippe, C.; Prasser, H.-M.

Ultrafast X-ray computed tomography with a linearly scanned electron beam source

Flow Measurement and Instrumentation 16 (2005), 65-72

Hermann, R.; Behr, G.; Gerbeth, G.; Priede, J.; Uhlemann, H.-J.; Fischer, F.; Schultz, L.

Magnetic field controlled FZ single crystal growth of intermetallic compounds

Journal of Crystal Growth, Vol. 275, e1533-e1538, 2005

Kolesnichenko, I.; Khripchenko, S.; Buchenau, D.; Gerbeth, G.
Electro-vortex flows in a square layer of liquid metal
Magnetohydrodynamics Vol. 41 (2005), No.1, pp. 39-51

Krepel, J.; Rohde, U.; Grundmann, U.; Weiss, F.-P.
DYN1D-MSR dynamics code for molten salt reactors
Annals of Nuclear Energy 32(2005)17, 1799-1824
DOI: 10.1016/j.anucene.2005.07.007

Krepper, E.; Lucas, D.; Prasser, H.-M.
On the modelling of bubbly flow in vertical pipes
Nuclear Engineering and Design 235 (2005) 597-611

Kryk, H.; Hessel, G.; Schmitt, W.; Tefera, N.
Gefahrenpotenziale bei Grignard-Reaktionen - Sichere Betriebsführung durch Online-Monitoring
Technische Überwachung 46(2005)7/8, 41-47

Kuna, M.; Abendroth, M.
Prüfung duktiler Werkstoffe mit dem Small Punch Test
Materialprüfung, Jahrg.47 (2005) 1-2, 45-54

Langenbuch, S.; Krzykacz-Hausmann, B.; Schmidt, K.-D.; Hegyi, G.; Kereszturi, A.; Kliem, S.; Hadek, J.; Danilin, S.; Nikonov, S.; Kuchin, A.
Comprehensive uncertainty and sensitivity analysis for coupled code calculations of VVER plant transients
Nuclear Engineering and Design, vol. 235, pp. 521-540 (2005)

Lucas, D.; Krepper, E.; Prasser, H.-M.
Development of co-current air-water flow in a vertical pipe
International Journal of Multiphase Flow 31(2005), 1304-1328

Lucas, D.; Prasser, H.-M.
Simulation of condensation in a sub-cooled bubbly steam-water flow along a large vertical pipe
Archives of Thermodynamics 26(2005)4, 49-59

Lucas, D.; Prasser, H.-M.; Manera, A.
Influence of the lift force on the stability of a bubble column
Chemical Engineering Science 60 (13): 3609-3619 Jul 2005

Manera, A.; Prasser, H.-M.; van der Hagen, Tim H. J. J.
Suitability of drift-flux models, void-fraction evolution and 3D flow pattern visualization during stationary and transient flashing flow in a vertical pipe
Nuclear Technology, 152 (1)2005: 38-53

Manera, A.; Rohde, U.; Prasser, H.-M.; van der Hagen, T. H. J. J.
Modeling of flashing-induced instabilities in the start-up phase of natural-circulation BWRs using the code FLOCAL
Nuclear Engineering and Design (2005), 235(14), pp. 1517-1535

Mittag, S.; Grundmann, U.; Weiß, F.-P.; Petkov, Petko T.; Kaloinen, E.; Keresztúri, A.; Panka, I.; Kuchin, A.; Ionov, V.; Powney, D.

Neutron-kinetic code validation against measurements in the Moscow V-1000 zero-power facility

Nuclear Engineering and Design 235 (2005) 485-506

Noack, K.; Pyka, N.; Rogov, A.; Steichele, E.

Shielding design of the PANDA spectrometer at the Munich high-flux reactor FRM-II

Radiation Protection Dosimetry 115(2005)1-4, 262-267

DOI: 10.1093/rpd/nci158

Plevachuk, Y.; Sklyachuk, V.; Yakymovych, A.; Willers, B.; Eckert, S.

Electronic properties and viscosity of liquid Pb-Sn alloys

Journal of Alloys and Compounds, Vol. 394 (2005), pp. 63-68

Prasser, H.-M.; Beyer, M.; Böttger, A.; Carl, H.; Lucas, D.; Schaffrath, A.; Schütz, P.; Weiß, F.-P.; Zschau, J.

Influence of the pipe diameter on the structure of the gas-liquid interface in a vertical two-phase pipe flow

Nuclear Technology 152(2005)Oct, 3-22

Prasser, H.-M.; Misawa, M.; Tiseanu, I.

Comparison between wire-mesh sensor and ultra-fast X-ray tomograph for an air-water flow in a vertical pipe

Flow Measurement and Instrumentation 16 (2005) 73-83

Priede, J.; Gerbeth, G.

A model of low-frequency rotating magnetic field with a weak axial gradient

Magnetohydrodynamics 41(2005)No.2, 189-198

Priede, J.; Gerbeth, G.

Breakdown of Burton-Prime-Slichter approach and lateral solute segregation in radially converging flows

Journal of Crystal Growth 285 (2005) 261-269

Priede, J.; Gerbeth, G.

Stability of an electromagnetically levitated spherical sample in a set of coaxial circular loops

IEEE Transactions on Magnetics, Vol. 41, Issue 6, pages 2089 - 2101 (June 2005)

Rohde, U.; Kliem, S.; Höhne, T.; Karlsson, R.; Hemström, B.; Lillington, J.; Toppila, T.; Elter, J.; Bezrukov, Y.

Fluid mixing and flow distribution in the reactor circuit - Part 1: Measurement data base

Nuclear Engineering and Design, 235 (2005) pp 421-443

Schaffrath, A.; Rohde, U.; Prasser, H.-M.; Scheuerer, M.

Sektionsberichte Jahrestagung Kerntechnik 2005 - Sektion 2: Thermo- und Fluidodynamik

atw - International Journal for Nuclear Power (2005)10, 594-606

ISSN: 1431-5254

Scheuerer, M.; Heitsch, M.; Menter, F.; Egorov, Y.; Toth, I.; Bestion, D.; Pigny, S.; Paillere, H.; Martin, A.; Boucker, M.; Krepper, E.; Willemsen, S.; Muhlbauer, P.; Andreani, M.; Smith, B.; Karlsson, R.; Henriksson, M.; Hemstrom, B.; Karppinen, I.; Kimber, G.
Evaluation of computational fluid dynamic methods for reactor safety analysis (ECORA)

Nuclear Engineering and Design 235(2005)2-4, 359-368

Schubert, M.;Boden, S.;Hampel, U.;Lange, R.
Untersuchung der Mehrphasenströmung in Trickle-bed-Reaktoren mittels Röntgenradiographie und Röntgentomographie

Chemie Ingenieur Technik 77 (2005) 1215

Shatrov, V.; Gerbeth, G.
Electromagnetic flow control leading to a strong drag reduction of a sphere

Fluid Dynamics Research 36 (2005) 153-173

Stefani, F.; Gerbeth, G.
Asymmetric polarity reversals, bimodal field distribution, and coherence resonance in a spherically symmetric mean-field dynamo model

Physical Review Letters 94(2005)18, 184506-1-184506-4

DOI: 10.1103/PhysRevLett.94.184506

Steinwarz, W.; Koller, W.; Dyllong, N.; Häfner, W.; Journeau, C.; Seiler, J. M.; Froment, K.; Cognet, G.; Goldstein, S.; Fischer, M.; Hellmann, S.; Nie, M.; Eddi, M.; Alsmeyer, H.; Allelein, H.-J.; Spengler, C.; Bürger, M.; Sehgal, B. R.; Koch, M. K.; Büscher, T.; Alkan, Z.; Petrov, J. B.; Gaune-Escard, M.; Weiss, F.-P.; Altstadt, E.; Bandini, G.

Ex-vessel core melt stabilization research (ECOSTAR)

Nuclear Engineering and Design 235(2005)2-4, 271-284

Ulbricht, A.; Boehmert, J.; Viehrig, H.-W.
Microstructural and Mechanical Characterization of the Radiation Effects in Model Reactor Pressure Vessel Steels

Journal of ASTM International 2(2005)10 Paper ID JAI12385

Ulbricht, A.; Böhmert, J.; Uhlemann, M.; Müller, G.
Small angle neutron scattering study on the effect of hydrogen in irradiated reactor pressure vessel steels

Journal of Nuclear Materials 336 (2005) 90-96

Vanttola, T.; Hämäläinen, A.; Kliem, S.; Kozmenkov, Y.; Weiß, F.-P.; Kereszturi, A.; Hadek, J.; Strmensky, C.; Stefanova, S.; Kuchin, A.

Validation of coupled codes using VVER plant measurements

Nuclear Engineering and Design, vol. 235, pp. 507-519 (2005)

Wangjiraniran, W.; Aritomi, M.; Kikura, H.; Motegi, Y.; Prasser, H.-M.

A study of non-symmetric air water flow using wire-mesh sensor

EXPERIMENTAL THERMAL AND FLUID SCIENCE 29(2005)3, 315-322.

Weier, T.; Hüller, J.; Gerbeth, G.; Weiss, F.-P.

Lorentz force influence on momentum and mass transfer in natural convection copper electrolysis

Chemical Engineering Science, Vol. 60, Nr. 1, 2005, S. 293-298

Willers, B.; Eckert, S.; Michel, U.; Haase, I.; Zouhar, G.
The columnar-to-equiaxed transition in Pb-Sn alloys affected by electromagnetically driven convection

Materials Science and Engineering A 402(2005), 55-65

DOI: 10.1016/j.msea.2005.03.108

Willers, B.; Eckert, S.; Nikritjuk, Petr A.; Eckert, K.; Michel, U.; Zouhar, G.
Application of a rotating magnetic field during directional solidification of Pb-Sn alloys: Consequences on the CET

Materials Science and Engineering A 413-414(2005), 211-216

Zaruba, A.; Krepper, E.; Prasser, H.-M.; Reddy Vanga, B. N.
Experimental study on bubble motion in a rectangular bubble column using high-speed video observations

Flow Measurement and Instrumentation 16(5)(2005), 277-287

Zaruba, A.; Krepper, E.; Prasser, H.-M.; Schleicher, E.
Measurement of bubble velocity profiles and turbulent diffusion coefficients of the gaseous phase in rectangular bubble column using image processing

Experimental Thermal and Fluid Science 29(2005), 851-860

Zhang, C.; Eckert, S.; Gerbeth, G.
Experimental study of a single bubble motion in a liquid metal column exposed to a DC magnetic field

Int. J. Multiphase Flow, Vol. 31 (2005), 824-842

Zippe, C.; Hoppe, D.; Fietz, J.; Hampel, U.; Hensel, F.; Mäding, P.; Prasser, H.-M.; Zippe, W.
Messung von Phasen- und Konzentrationsverteilungen in Blasensäulen mit Positronen-Emissions-Tomographie

Chemie Ingenieur Technik 77(2005)10, 1581-1587

DOI: 10.1002/cite.200507022

Conference contributions and other oral presentations

Adolphe, X.; Martemianov, S.; Piteau, A.; Weier, T.; Gerbeth, G.

Experimental investigation of the influence of Lorentz forces on local mass transfer and near wall turbulence by means of electrodiffusion probes

Joint 15th Riga and 6th pamir International Conference on MHD, 27.06.-01.07.2005, Riga, Latvia

Alt, S.; Hampel, R.; Kästner, W.; Lischke, W.; Seeliger, A.; Krepper, E.; Grahn, A.

Untersuchungen zum Verhalten von freigesetztem Isolationsmaterial in ruhender und horizontaler Kühlmittelströmung

Jahrestagung Kerntechnik 2005, 10.-12.05.2005, Nürnberg, Deutschland

Alt, S.; Seeliger, A.; Krepper, E.; Grahn, A.

Experimental and analytical investigations for debris transport phenomena in multidimensional water flow

The 11th International Topical Meeting on Nuclear Reactor Thermal-Hydraulics (NURETH-11), Paper 116, 02.-06.10.2005, Avignon, Frankreich

Altstadt, E.

Links of SARNET with the ISTC program - presentation of the contact expert group of severe accident management

SARNET - First Annual Review Meeting of Corium Topic, GRS Köln, 15.02.2004, Köln, Deutschland

Altstadt, E.; Beckert, C.; Galindo, V.; Naumann, B.; Weiss, F.-P.

Thermo-mechanical design of a photoneutron source for time-of-flight experiments

18th International Conference on Structural Mechanics in Reactor Technology, IASMIT, 07.-12.08.2005, Beijing, China

Altstadt, E.; Willschuetz, H.-G.

Possible consideration of METCOR experimental results in FE models for IVR

6th METCOR Project Meeting, Alexandrov Research Institute of Technology, 12.07.2005, Sankt Petersburg, Russia

Altstadt, E.; Willschütz, H.-G.; Sehgal, B. R.; Weiß, F.-P.

Vessel rupture: Synthesis of the FOREVER interpretation activity

ERMSAR 2005, IRSN, 14.-16.11.2005, Aix en Provence, France

Beckert, C.; Koch, R.

Reactor cell calculations with the codes HELIOS, MCNP and TransRay and comparison of the results

Annual Meeting on Nuclear Technology 2005, 10.-12.05.2005, Nürnberg, Deutschland

Bergner, F.

Validierung von Software-Komponenten zur Voraussage der strahleninduzierten Schädigung von RDB-Stahl

Sitzung des Projektkomitees Komponentenverhalten, Gesellschaft für Reaktorsicherheit, 21.02.2005, Dresden, BRD

Bergner, F.; Gokhman, A. R.; Altstadt, E.

Long term evolution of radiation induced damage - FZR contribution to rate theory
Second Plenary Meeting RPV & Internals - Physics Modelling, 17.-18.10.2005, Saclay, France

Bergner, F.; Gokhman, A. R.; Ulbricht, A.

Rate theory modelling of neutron irradiation induced cluster formation in RPV steels and iron based alloys
First Plenary Meeting RPV & Internals - Physics Modelling, 19.-21.01.2005, Manchester, UK

Bergner, F.; Gokhman, A. R.; Ulbricht, A.

Small-angle neutron scattering and rate theory applied to neutron-irradiation-induced clustering of defects and copper atoms in iron
Micromechanics and Microstructure Evolution: Modeling Simulation and Experiments, 12.-16.09.2005, Madrid, Spanien

Biswas, K.; Hermann, R.; Filip, O.; Acker, J.; Gerbeth, G.; Priede, J.

Influence of melt convection on microstructure evolution of Nd-Fe-B alloys using a forced crucible rotation technique
Magnetic and Superconducting Materials, 05.-09.09.2005, Agadir, Marokko

Biswas, K.; Hermann, R.; Filip, O.; Werner, J.; Gerbeth, G.; Priede, J.

Influence of melt convection on microstructure evolution of Nd-Fe-B alloys using forced crucible rotation technique
Tagung der Deutschen Physikalischen Gesellschaft, 09.03.2005, Berlin, Germany

Boehmer, B.; Konheiser, J.; Noack, K.; Rogov, A.; Stephan, I.; Hansen, W.; Hinke, D.; Unholzer, S.; Grantz, M.; Mehner, H.-C.

Measurements and Monte Carlo calculations of gamma and neutron flux spectra inside and behind iron/steel/water configurations
12th International Symposium on Reactor Dosimetry, 08.-13.05.2005, Gatlinburg, USA

Borodkin, G.; Khrennikov, N.; Böhmer, B.; Noack, K.; Konheiser, J.

Deterministic and Monte Carlo neutron transport calculation for Greifswald-1 and comparison with ex-vessel measurement data
12 th International Symposium on Reactor Dosimetry, 08.-13.05.2005, Gatlinburg, USA

Bousbia Salah, A.; Kliem, S.; Rohde, U.

Uncertainty and sensitivity analyses of the Kozloduy pump trip test by coupled RELAP5/PARCS code
Int. Top. Meeting on Mathematics and Computation, Supercomputing, Reactor Physics and Nuclear Appli., CEA France, 12.-15.09.2005, Avignon, Frankreich

Burtak, F.; Krepper, E.

Can we predict critical heat flux in fuel assemblies by CFD methods?
Annual Meeting on Nuclear Technology 2005, 10.-12.05.2005, Nürnberg, Germany

Cramer, A.; Eckert, S.; Galindo, V.; Gerbeth, G.; Witke, W.

Aluminum investment casting with magnetic field control of the mould filling process
International Symposium on Liquid Metal Processing and Casting, 18.-21.09.2005, Santa Fe, New Mexico, USA

Cramer, A.; Varshney, K.; Zhang, C.

Experimental results on the fluid flow in an electromagnetically driven metallic melt
Materials Science & Technology, 25.-28.09.2005, Pittsburgh, PA, USA

Eckert, S.; Cramer, A.; Galindo, V.; Gerbeth, G.; Willers, B.

Electromagnetic flow control for casting and metallurgical applications: Model experiments and measuring techniques
2nd Sino-German Workshop on EPM, 16.-19.10.2005, Dresden, Germany

Eckert, S.; Gerbeth, G.; Gundrum, T.; Stefani, F.

Velocity measurements in metallic melts

2005 ASME Fluids Engineering Division Summer Meeting, ASME, 19.-23.07.2005, Houston, TX, USA

Eckert, S.; Gerbeth, G.; Stefani, F.

Velocity measurements in metallic melts: New developments and applications

Annual meeting of JSPS, JSPS, 27.-28.01.2005, Nagoya, Japan

Eckert, S.; Willers, B.; Nikritjuk, Petr A.; Eckert, K.; Michel, U.; Zouhar, G.

Electromagnetically driven convection applied during solidification of Pb-Sn alloys

Material Science & Technology 2005, TMS, 25.-28.09.05, Pittsburgh, USA

Eckert, S.; Zhang, C.; Gerbeth, G.

The influence of an external DC magnetic field on the behaviour of bubble driven liquid metal flows

MULTIMET, Workshop on Multiphase Flows in Metallurgy, 28.-30.09.05, Prague, Czech Republik

Filip, O.; Hermann, R.; Gerbeth, G.; Priede, J.; Biswas, K.

Controlling melt convection - an innovation potential for concerted microstructure evolution of Nd-Fe-B alloys

International Conference on Advances in Solidification Processes, 07.-10.06.2005, Stockholm, Sweden

Frank, T.; Krepper, E.; Eickenbusch, H.

Practical calculation of bubble column flow with CFX-5

Workshop on Multi-Phase Flow: Simulation, Experiment and Application, ANSYS-CFX, Forschungszentrum Rossendorf e.V., 31.05.-03.06.2005, Rossendorf, Germany

Gailitis, A.; Lielausis, O.; Platacis, E.; Gerbeth, G.; Gundrum, T.; Stefani, F.

New measurements of magnetic fields, pressure and velocity at the Riga dynamo experiment

Perm Dynamo Days, 7-11 February, 2005

Gailitis, A.; Lielausis, O.; Platacis, E.; Gerbeth, G.; Gundrum, Th.; Stefani, F.

Magnetic field details of the Riga dynamo experiment

IAGA 2005 Scientific Assembly, 18.-29.07.2005, Toulouse, France

Gailitis, A.; Lielausis, O.; Platacis, E.; Gerbeth, G.; Stefani, F.

Riga dynamo experiments

Joint 15th Riga and 6th pamir International Conference on MHD, 27.06.-01.07.2005, Riga, Latvia

Galindo, V.; Grants, I.; Lantsch, R.; Gerbeth, G.; Pätzold, O.
Fluid flow analysis under the influence of a travelling magnetic field - simulation and experiment

DGKK-Arbeitskreis Angewandte Simulation in der Kristallzüchtung - 4. Workshop, 03.-04.11.2005, Heigenbrücken, Germany

Gerbeth, G.

A review of MHD activities at Forschungszentrum Rossendorf

JSPS Meeting, Nagoya University, 29.01.2005, Nagoya, Japan

Gerbeth, G.

Activities on applied MHD at Forschungszentrum Rossendorf

Materials Science & Technology, Symposium "Electromagnetics in materials Processing", 25.-28.09.2005, Pittsburgh, USA

Gerbeth, G.

MHD research activities at the Research Center Rossendorf

Meeting of COST Action P17, Working Group VI, 07.-08.12.2005, Hannover, Germany

Gerbeth, G.

Process control by tailored magnetic fields - examples from crystal growth, metal casting and solidification

JSPS Meeting, Nagoya University, 28.01.2005, Nagoya, Japan

Gerbeth, G.

Review of applied MHD research at Forschungszentrum Rossendorf

Central Iron & Steel Research Institute (CISRI), 26.05.2005, Peking, China

Gerbeth, G.; Eckert, S.; Galindo, V.; Willers, B.

Liquid metal flows in AC and DC magnetic fields and its application to casting processes

The 2nd Workshop on Electromagnetic Processing of Materials (Asian-EPM2005), 22.-25.05.2005, Shenyang, China

Gerbeth, G.; Stefani, F.

Proposal for a Taylor-Dean experiment to investigate the magnetorotational instability

Perm Dynamo Days, 7-11 February, 2005

Gokhman, A.; Bergner, F.; Ulbricht, A.

Modelling of the evolution of vacancy clusters in neutron-irradiated iron

Annual Meeting on Nuclear Technology 2005, German Atomic Forum and German Nuclear Society, 10.-12.05.2005, Nürnberg, BRD

Gokhman, A. R.; Bergner, F.; Ulbricht, A.

Iron matrix effects on cluster evolution in neutron irradiated reactor steels

9th Research Workshop Nucleation Theory and Applications, Joint Institute for Nuclear Research, 25.06.-03.07.2005, Dubna, Russia

Grahn, A.; Krepper, E.

Numerical investigations of insulation debris transport phenomena in water flow

Workshop on Multi-Phase Flow: Simulation, Experiment and Application, ANSYS/CFX, Forschungszentrum Rossendorf e.V., 31.05.-03.06.2005, Rossendorf, Germany

Grundmann, U.

Comparisons of DYN3D results with the reference solution of the AER-FCM-101 benchmark

IAEA Workshop on "Neutronic Analyses of BNPP-1 Reactor Core. Task 7.8 of IRA4035", IAEA Wien, 10.-14.10.2005, Wien, Österreich

Grundmann, U.

Description of 3D calculations of decay heat and thermal hydraulic equations

IAEA Workshop on "Neutronic Analyses of BNPP-1 Reactor Core. Task 7.8 of IRA4035", IAEA Wien, 10.-14.10.2005, Wien, Österreich

Grundmann, U.

Overview on space-time core calculations for VVER reactors

IAEA Workshop on "Neutronic Analyses of BNPP-1 Reactor Core. Task 7.8 of IRA4035", IAEA Wien, 10.-14.10.2005, Wien, Österreich

Grundmann, U.; Kliem, S.; Mittag, S.; Rohde, U.

The influence of the coolant flow fluctuations on the consequences of a hypothetical boron dilution event

Annual Meeting on Nuclear Technology 2005, Kerntechnische Gesellschaft e. V., Deutsches Atomforum e. V., 10.-12.05.2005, Nuremberg, Germany

Gundrum, T.; Gerbeth, G.; Kunadt, H.; Stefani, F.; Xu, M.

Contactless inductive flow tomography experiments with liquid metals

8th MHD-Days 2005, Astrophysikalisches Institut Potsdam, 28.-29.11.2005, Potsdam, Deutschland

Gundrum, Th.; Gerbeth, G.; Stefani, F.; Xu, M.

Experimental aspects of contactless inductive flow tomography

Joint 15th Riga and 6th PAMIR International Conference on Fundamental and Applied MHD, Institute of Physics, University of Latvia, Riga - Latvia, 27.06.-01.07.2005, Jurmala, Latvia

Günther, U.; Gerbeth, G.; Stefani, F.

The beauty of spherically symmetric α^2 -dynamos: Exceptional points, oscillations, and chaotic reversals

Perm Dynamo Days, 7-11 February, 2005

Günther, U.; Kirillov, O.

Perturbation theory for non-selfadjoint operator matrices and its application to the MHD α^2 -dynamo

4th International Workshop on Pseudo-Hermitian Hamiltonians in Quantum Physics, University of Stellenbosch, Western Cape, South Africa, 23.-25.11.2005, Stellenbosch, South Africa

Günther, U.; Kirillov, O.; Stefani, F.

Bundle stratification of PT-symmetric 4×4 matrix systems and fourth-order spectral branch points of MHD α^2 -dynamos

4th International Workshop on Pseudo-Hermitian Hamiltonians in Quantum Physics, University of Stellenbosch, Western Cape, South Africa, 23.-25.11.2005, Stellenbosch, South Africa

Günther, U.; Stefani, F.; Znojil, M.

Krein space related physics: PT-symmetric Quantum Mechanics, MHD α^2 -dynamios, planar Couette flows, ...

3rd International Workshop on Pseudo-Hermitian Hamiltonians in Quantum Physics, Koç University, Istanbul, Turkey and Nuclear Physics Institute, Rez near Prague, Czech Republic, 20.-22.06.2005, Istanbul, Turkey

Hampel, U.

Computertomografie für Mehrphasenströmungen

Ehrenkolloquium an der Hochschule Zittau/Görlitz, Fachbereich Elektro- und Informationstechnik, Hochschule Zittau/Görlitz, 15.04.2005, Zittau, BRD

Hampel, U.

X-ray tomography

DPI PO Day, Dutch Polymer Insitute, 10.02.2005, Enschede, Niederlande

Hermann, R.; Filip, O.; Biswas, K.; Gerbeth, G.; Priede, J.

Influence of melt convection on the microstructure of Nd-Fe-B- alloys

2nd Sino-German Workshop on EPM, 16.-19.10.2005, Dresden, Germany

Hessel, G.; Hristov, H. V.; Kryk, H.; Prasser, H.-M.; Schmitt, W.

A study on the mixing behaviour of different density liquids in a stirred tank reactor by passive and reactive tracers

GVC/DECHEMA Jahrestagung, 06.-08.09.2005, Wiesbaden, Deutschland

Hessel, G.; Hristov, H. V.; Kryk, H.; Prasser, H.-M.; Schmitt, W.

The influence of the density difference on the mixing process in mechanically agitated reactor

Conference on Computational Fluid Dynamics in Chemical Reaction Engineering IV, 19.-24.06.2005, Barga, Italy

Hessel, G.; Kryk, H.; Schmitt, W.; Tefera, N.

Untersuchungen zur sicheren Prozessführung von Grignard-Reaktionen

GVC/DECHEMA Jahrestagung 2005, 06.-08.09.2005, Wiesbaden, Deutschland

Höhne, T.

Application of Best Practice Guidelines for the use of computational fluid dynamics in the reactor safety analysis

Course Mathematical Modelling, West Bohemian University Pilsen, Czech Republic, 24.11.2005, Pilsen, Czech Republic

Höhne, T.

CFD-simulation of coolant transient benchmark v1000ct –1, exercise 3 using results of Dyn3d/Athlet coupled code calculation

OECD/DOE/CEA VVER-1000 Coolant Transient Benchmark - Third Workshop, Gesellschaft für Anlagen- und Reaktorsicherheit (GRS) mbH, Garching, Germany, 03.-07.04.2005, Garching, Deutschland

Höhne, T.

Experimental investigation and CFD simulation of an air/water flow in a horizontal channel

Multiphase Flows: Simulation, Experiment and Applications, ANSYS Germany-FZR, 31.05.-03.06.2005, FZR Dresden, Deutschland

Höhne, T.

Nachrechnung der Leistungsparameter des Vollhub-Feder –Sicherheitsventils Leser Type 441 mit CFX-10

DECHEMA/GVC-Arbeitsausschuß “Sicherheitsgerechtes Auslegen von Chemieapparaten“ 60. Sitzung am 30.11./01.12.2005 im DECHEMA-Haus, 30.11.2005, Frankfurt am Main, Deutschland

Höhne, T.

Numerical modelling of a transient slug mixing experiment of the ROCOM test facility using CFX-5

The 11th International Topical Meeting on Nuclear Reactor Thermal-Hydraulics (NURETH-11), NURETH, 3.10.2005, Avignon, France

Höhne, T.

Untersuchungen zur Kühlmittelvermischung: Ergebnisse numerischer Simulationen mit CFX-5 im Vergleich mit experimentellen Ergebnissen an der Vermischungsanlage ROCOM

Forschungszentrum Karlsruhe, Institut für Reaktorsicherheit, Seminarreihe 2004/2005, 13. Januar, 2005

Höhne, T.; Bezrukov, Y.

CFD calculation of a mixing experiment in the VVER-1000 reactor model

The 4-th International Conference SAFETY ASSURANCE OF NUCLEAR POWER PLANTS WITH WWER, FSUE EDO, 23.05.2005, Podolsk, Russian Federation

Höhne, T.; Bieder, U.; Kolev, N.

CFD-simulation of thermalhydraulic benchmark v1000ct –2

OECD/DOE/CEA VVER-1000 Coolant Transient Benchmark - Third Workshop, Gesellschaft für Anlagen- und Reaktorsicherheit (GRS) mbH, Garching, Germany, 03.-07.04.2005, Garching, Deutschland

Höhne, T.; Kliem, S.; Rohde, U.

CFD- analysis of the mixing pattern under various flow conditions at the ROCOM test facility using CFX-5

13th International Conference on Nuclear Engineering 2005, ASME, 16.05.2005, Beijing, China

Höhne, T.; Scheuerer, M.; Kliem, S.

Numerical modelling of a buoyancy driven flow in a reactor pressure vessel using CFX-5

The 11th International Topical Meeting on Nuclear Reactor Thermal-Hydraulics (NURETH-11), NURETH, 3.10.2005, Avignon, France

Hristov, V. H.; Prasser, H.-M.; Kryk, H.; Hessel, G.; Schmitt, W.

CFD analyses for stirred tank reactor: mixing behaviour of different density liquids

Workshop on Multi-Phase Flow: Simulation, Experiment and Application, ANSYS-CFX, Forschungszentrum Rossendorf e.V., 31.05.-03.06.2005, Rossendorf, Deutschland

Kenjeres, S.; Renaudier, S.; Hanjalic, K.; Stefani, F.

Computational study of flow and magnetic field interactions in Riga dynamo

Joint 15th Riga and 6th PAMIR International Conference on Fundamental and Applied MHD, Institute of Physics, University of Latvia, Riga - Latvia, 27.06.-01.07.2005, Jurmala, Latvia

Kliem, S.; Langenbuch, S.; Weiß, F.-P.

Uncertainty analyses of coupled thermal hydraulic/neutron kinetic code calculations

Jahrestagung Kerntechnik 2005; Fachsitzung: Neuere Methoden im Nachweisverfahren bei Störfallanalyse, 10.-12.05.2005, Nürnberg, Deutschland

Kliem, S.; Mittag, S.; Weiß, F.-P.; Langenbuch, S.

Uncertainty and sensitivity analysis for the modeling of a start-up experiment in a VVER-1000 reactor

4th International Conference: Safety Assurance of Nuclear Power Plants with WWER", FSUE EDO "Gidropress" Podolsk, 23.-26.05.2005, Podolsk, Russland

Kliem, S.; Mittag, S.; Weiß, F.-P.; Langenbuch, S.

Uncertainty and sensitivity analysis for the modeling of transients with interaction of thermal hydraulics and neutron kinetics

11th International Topical Meeting on Nuclear Reactor Thermal-Hydraulics (NURETH-11), CEA France, 02.-06.10.2005, Avignon, France

Klug, J.; Altstadt, E.; Beckert, C.; Beyer, R.; Freiesleben, H.; Greschner, M.; Grosse, E.; Junghans, A. R.; Naumann, B.; Noack, K.; Schneider, S.; Seidel, K.; Wagner, A.; Weiss, F.-P.

Development of a neutron time-of-flight source at the ELBE accelerator

New Trends in Nuclear Physics Applications and Technology, European Physical Society, 06.09.2005, Pavia, Italien

Konheiser, J.; Rindelhardt, U.; Viehrig, H.-W.

Post mortem investigations of Greifswald VVER 440 reactor pressure vessel: Recent progress in dosimetry and material investigations

4th International Conference on: Safety assurance of nuclear power plants with WWER, Podolsk (Russia), 23-25 May 2005

Kozmenkov, Y.; Grundmann, U.; Kliem, S.; Rohde, U.; Weiss, F.-P.

V1000CT-1 benchmark analyses with the DYN3D/RELAP5 and DYN3D/ATHLET coupled code systems

11th Int. Top. Meeting on Nuclear Reactor Thermal-Hydraulics NURETH11, 02.-06.10.2005, Avignon, France

Krepel, J.; Rohde, U.; Grundmann, U.

Simulation of molten salt reactor dynamics

Nuclear Energy for New Europe 2005, Nuclear Society of Slovenia, 05.-08.09.2005, Bled, Slovenia

Krepel, J.; Rohde, U.; Grundmann, U.; Weiss, F.-P.

Spatial dynamics of MSRE

in: ASME, JSME, CNS: Proceedings of 13th International Conference on Nuclear Engineering, Beijing: ASME, JSME, CNS, 2005

Krepper, E.; Egorov, Y.

CFD-modelling of subcooled boiling and application to simulate a hot channel of a fuel assembly

13th International Conference on Nuclear Engineering, ICONE-13, Chinese Nuclear Society, 16.-20.05.2005, Peking, China

Krepper, E.; Egorov, Y.

CFD-modelling of subcooled boiling and application to simulate a hot channel of a fuel assembly

Workshop on Multi-Phase Flow: Simulation, Experiment and Application, ANSYS Germany, Forschungszentrum Rossendorf e.V., 31.05.-03.06.2005, Rossendorf, Germany

Krepper, E.; Grahn, A.; Alt, S.; Kästner, W.; Kratzsch, A.; Seeliger, A.

Numerical investigations for insulation particle transport phenomena in water flow

23rd CADFEM Users Meeting 2005, 09.-11.11.2005, Bonn, Deutschland

Krepper, E.; Lucas, D.; Prasser, H.-M.; Shi, J.-M.; Rohde, U.

Two-phase flow simulations in the FZ Rossendorf using CFX-5

11th Workshop on Two Phase Flow Predictions, Martin-Luther-Universität Halle-Wittenberg, 05.-08.04.2005, Merseburg, Deutschland

Krepper, E.; Prasser, H.-M.; Frank, T.

Air-water flow in a vertical pipe with sudden changes of superficial water velocity

The 11th International Topical Meeting on Nuclear Reactor Thermal-Hydraulics (NURETH-11), 02.-06.10.2005, Avignon, Frankreich

Lantzsch, R.; Galindo, V.; Grants, I.; Pätzold, O.; Gerbeth, G.; Stelter, M.; Cröll, A.

Fluid flow analysis and vertical gradient freeze crystal growth in a traveling magnetic field

Joint 15th Riga and 6th PAMIR International Conference on Fundamental and Applied MHD, Institute of Physics, University of Latvia - Riga, 27.06.-01.07.2005, Jurmala, Latvia

Lucas, D.; Krepper, E.; Prasser, H.-M.

Modeling of the evolution of bubbly flow along a large vertical pipe

The 11th International Topical Meeting on Nuclear Reactor Thermal-Hydraulics, NURETH-11, 02.-06.10.2005, Avignon, France

Lucas, D.; Prasser, H.-M.

Simulation of bubble condensation with a multi-bubble size class model

Workshop on Multi-Phase Flow: Simulation, Experiment and Application, Rossendorf, 31 May - 3 June 20, ANSYS-CFX, Forschungszentrum Rossendorf e.V., 31.05.-03.06.2005, Rossendorf, Deutschland

Lucas, D.; Prasser, H.-M.

Simulation of phase transfer in case of bubbly steam-water flow along a large vertical pipe

4th International Conference on transport phenomena in multiphase systems, Gdańsk University of Technology, Institute of Fluid-Flow Machinery, Polish Academy of Sciences, 26.-30.06.2005, Gdansk, Poland

Lucas, D.; Prasser, H.-M.; Manera, A.

Linear stability analysis for the effect of the lift force in a bubble column

43rd European Two-Phase Flow Group Meeting, 11 - 13 May 2005, Prague, Czech Republic, 11.-13.05.2005, Prague, Czech Republic

Manera, A.

A startup procedure for natural circulation boiling Water Reactors

The 11th International Topical Meeting on Nuclear Reactor Thermal-Hydraulics (NURETH-11), 02.-06.10.2005, Avignon, France

Manera, A.

Strategies for the start-up procedure of natural circulation Boiling Water Reactors
Jahrestagung Kerntechnik 2005, 10.-12.05.2005, Nuremberg, Germany

Manera, A.; Prasser, H.-M.; Lucas, D.

Experimental investigations on bubble turbulent diffusion in a vertical large-diameter pipe by means of wire-mesh sensors and correlation techniques

The 11th International Topical Meeting on Nuclear Reactor Thermal-Hydraulics (NURETH-11), 02.-06.10.2005, Avignon, France

Nikritjuk, Petr A.; Eckert, K.; Eckert, S.; Willers, B.

Electromagnetically-driven convection during solidification: Heat and mass transfer in solidifying Pb-Sn melts

EUROMAT 2005, 05.-08.09.05, Prague, Czech Republik

Ošmera, B.; Boehmer, B.; Ballesteros, A.; Konheiser, J.; Kyncl, J.; Hordosy, G.; Keresztúri, A.; Belousov, S.; Ilieva, K.; Kirilova, D.; Mitev, M.; Smutný, V.; Polke, E.; Zaritsky, S.; Töre, C.; Ortego, P.

Accurate determination and benchmarking of radiation field parameters relevant for pressure vessel monitoring. A review of some REDOS project results

Twelfth International Symposium on Reactor Dosimetry, ASTM International, 08.-13.05.2005, Gatlinburg, Tennessee, USA

Petkov, T.; Mittag, S.

WWER radial reflector modeling by diffusion codes

15-th Symposium of AER, NPP Dukovany, 03.-07.10.05, Znojmo, Czech Republic

Pfingsten, W.; Mibus, J.; Küchler, R.

Reactive transport codes applied to gypsum dissolution in a laboratory column experiment with focus on sensitivity of model concepts and data uncertainty

Fifth International Conference on Calibration and Reliability in Groundwater Modelling, Netherlands Institute of Applied Geoscience and International Commission on Groundwater, 06.-09.06.2005, Scheveningen, The Netherlands

Pietruske, H.; Prasser, H.-M.

Wire-mesh sensors for high-resolving two-phase flow studies at high pressures and temperatures

The 11th International Topical Meeting on Nuclear Reactor Thermal-Hydraulics (NURETH-11), 02.-06.10.2005, Avignon, France

Prasser, H.-M.; Beyer, M.; Carl, H.; Gregor, S.; Lucas, D.; Pietruske, H.; Schütz, P.; Weiss, F.-P.

Evolution of the structure of a gas-liquid two-phase flow in a large vertical pipe

Eleventh International Topical Meeting on Nuclear Reactor Thermal Hydraulics, NURETH 11, October 2-6, 2005, Avignon, France

Prasser, H.-M.; Beyer, M.; Carl, H.; Gregor, S.; Manera, A.; Pietruske, H.; Schütz, P.; Weiss, F.-P.

The thermal hydraulic test facility TOPFLOW: Overview on experimental capabilities and instrumentation

11th Workshop on Two-Phase Flow Predictions, Martin Luther University Halle-Wittenberg, 05.-08.04.2005, Merseburg, Germany

Prasser, H.-M.; Gregor, S.

Evolution of interfacial area concentration in a vertical air-water flow measured by Wire-Mesh Sensors

Eleventh International Topical Meeting on Nuclear Reactor Thermal Hydraulics, NURETH 11, October 2-6, 2005, Avignon, France

Priede, J.; Gerbeth, G.; Hermann, R.; Behr, G.

Float-zone crystal growth with a novel melt flow control

Joint 15th Riga and 6th PAMIR International Conference on Fundamental and Applied MHD, Institute of Physics, University of Latvia, Riga - Latvia, 27.06.-01.07.2005, Jurmala, Latvia

Reddy Vanga, B.; Lopez de Bertodano, M.; Krepper, E.; Zaruba, A.; Prasser, H.-M.

Two fluid model LES of a bubble column

The 11th International Topical Meeting on Nuclear Reactor Thermal-Hydraulics (NURETH-11), 02.-06.10.2005, Avignon, Frankreich

Rindelhardt, U.; Konheiser, J.; Viehrig, H.-W.

Investigation of WWER RPV steel and cladding from Greifswald NPP

Workshop "Improved Reactor Pressure Vessels (RPV) Structural Integrity Assessment for NPPs", IAEA, 18.-21.10.2005, Madrid, Spain

Rohde, U.; Grundmann, U.

Mathematical models in the DYN3D-FLOCAL code – consequences on reactor analysis results

Course on Mathematical Modelling, West Bohemian University, 24.11.2005, Plzen, Czechia

Rohde, U.; Höhne, T.; Kliem, S.; Hemström, B.; Scheuerer, M.; Dury, T.; Remis, J.; Muhlbauer, P.; Toth, I.; Elter, J.; Bezrukov, Y.; Toppila, T.; Lillington, J.

Fluid mixing and flow distribution in the reactor circuit (FLOMIX-R)

The 4-th International Conference "SAFETY ASSURANCE OF NUCLEAR POWER PLANTS", FSUE EDO Gidropress, 23.-25.05.2005, Podolsk, Russian Federation

Rohde, U.; Kliem, S.; Höhne, T.; Prasser, H.-M.; Hemström, B.; Toppila, T.; Elter, J.; Bezrukov, Y.; Scheuerer, M.

Measurement data base on fluid mixing and flow distribution in the reactor circuit

The 11th International Topical Meeting on Nuclear Reactor Thermal-Hydraulics (NURETH-11), 02.-06.10.2005, Avignon, France

Shi, J.-M.; Zwart, P.; Frank, T.; Krepper, E.; Lucas, D.; Rohde, U.; Prasser, H.-M.

A multiple field multiple size group model for poly-dispersed gas-liquid flows, part 1. model concepts and equations

3rd Joint CFX & FZR Workshop on Multiphase Flows: Simulation, Experiments and Application, FZR, ANSYS CFX Germany, 31.05.-03.06.2005, Dresden, Germany

Stefani, F.; Gerbeth, G.; Gailitis, A.; Lielausis, O.; Platacis, E.

Have we understood the Riga dynamo?

Perm Dynamo Days, 7-11 February, 2005

Stefani, F.; Gerbeth, G.; Günther, U.

A paradigmatic model of Earth's magnetic field reversals

Joint 15th Riga and 6th PAMIR International Conference on Fundamental and Applied MHD, Institute of Physics, University of Latvia, Riga - Latvia, 27.06.-01.07.2005, Jurmala, Latvia

Stefani, F.; Gerbeth, G.; Günther, U.; Xu, M.

Reversals made simple

8th MHD - Days 2005, Astrophysikalisches Institut Potsdam, 28.-29.11.2005, Potsdam, Deutschland

Stefani, F.; Xu, M.; Gerbeth, G.

The role of lid layers on the performance of von Karman type dynamos

Seminarvortrag, Ecole Normale Supérieure de Lyon, Laboratoire de Physique, Ecole Normale Supérieure de Lyon, Laboratoire de Physique, 03.11.2005, Lyon, France

Thomas, H.; Sören, K.

Coolant mixing studies of natural circulation flows at the ROCOM test facility using CFX-10

23rd CADFEM Users' Meeting 2005, ANSYS CFX & ICEM, 11.11.2005, Bonn, Deutschland

Uhlemann, M.; Müller, G.; Ulbricht, A.; Böhmert, J.

Einfluss von Wasserstoff auf die Zähigkeit von bestrahlten Reaktordruckbehälterstählen

55. Sitzung des RSK-Ausschusses „Druckführende Komponenten und Werkstoffe“, Beratungsausschuss „Druckführende Komponenten und Werkstoffe“ der Reaktor-Sicherheitskommission, 05.-06.07.2005, Berlin, BRD

Ulbricht, A.; Bergner, F.

Detecting irradiation induced damage in RPV steels by SANS

First Plenary Meeting RPV & Internals - Physics Modelling, 19.-21.01.2005, Manchester, UK

Ulbricht, A.; Bergner, F.

Microstructural analysis by means of Small-angle neutron scattering

Second Plenary Meeting RPV & Internals - Physics Modelling, 17.-19.10.2005, Saclay, France

Ulbricht, A.; Bergner, F.

Microstructural analysis of WWER RPV materials with Small-angle neutron scattering

Perfect meeting on VVER materials, 13.-14.06.2005, Bratislava, Slovakia

Vallee, C.; Höhne, T.; Prasser, H.-M.; Sühnel, T.

Experimental modelling and CFD simulation of air/water flow in a horizontal channel

The 11th International Topical Meeting on Nuclear Reactor Thermal-Hydraulics (NURETH-11), NURETH, 3.10.2005, Avignon, France

Vallee, C.; Höhne, T.; Sühnel, T.

Experimente zur CFD-Validierung der Zweiphasen-Strömung im Heißstrang eines Druckwasser-Reaktors

Jahrestagung Kerntechnik 2005, Deutsches Atomforum e.V. / Kerntechnische Gesellschaft e.V., 10.-12.05.2005, Nürnberg, Deutschland

Vallee, C.; Sühnel, T.

Experimental investigation and CFD simulation of an air/water flow in a horizontal channel (Part 1: Measurements)

FZR & Ansys Multiphase flow workshop, FZR & Ansys Germany, 31.05.-03.06.2005, Dresden, Germany

Viehrig, H.-W.

Integritätsbewertung von Reaktordruckbehälter

124. Sitzung des Arbeitskreises Dresden der Gesellschaft für zerstörungsfreie Prüfung e.V., Gesellschaft für zerstörungsfreie Prüfung, 27.10.2005, Dresden, Deutschland

Viehrig, H.-W.; Wallin, K.

Anwendung des Master-Curve-Konzeptes zur Zähigkeitscharakterisierung inhomogener Reaktordruckbehälterstähle

37. Tagung des DVM-Arbeitskreises Bruchvorgänge, Deutscher Verband für Materialforschung und -prüfung, 22.02.2005, Hamburg-Harburg, Deutschland

Viehrig, H.-W.; Wallin, K.; Murasov, M.

Application of the Master Curve approach on WWER-440 reactor pressure vessel steel of the nuclear power plant Greifswald unit 8

The 4th International Conference "Safety Assurance of Nuclear Power Plants with WWER", GIDROPRESS, 22.05.2005, Podolsk, Russia

Weier, T.; Gerbeth, G.

Experimental results on the effect of wall-parallel Lorentz forces on lift and drag of hydrofoils

2nd International Symposium on Seawater Drag Reduction, 23.-26.05.2005, Busan, South Korea

Weier, T.; Hüller, J.; Gerbeth, G.; Weiss, F.-P.

Velocity measurements and concentration field visualizations in natural convection copper electrolysis under magnetic field influence

Joint 15th Riga and 6th PAMIR International Conference on Fundamental and Applied MHD, 27.06.-01.07.2005, Rigas Jurmala, Latvia

Weiß, F.-P.

Analysen zur Kühlmittelvermischung und zum Kernverhalten bei unterstellter Borverdünnung in Druckwasserreaktoren

IKET-Kolloquium, FZ Karlsruhe, 28.06.2005, Karlsruhe, D

Weiß, F.-P.

Bewertung der Nachhaltigkeit heutiger Technologien der Stromerzeugung - Aggregation der Indikatoren -

Internationaler ILK-Workshop, ILK, 23.02.2005, Frankfurt/Main, D

Weiss, F.-P.

Borverdünnungstransienten in DWR - ROCOM-Experimente zur Kühlmittelvermischung und reaktordynamische Analysen

IKET-Kolloquium, FZ Karlsruhe, 28.06.2005, Karlsruhe, D

Willers, B.; Eckert, S.; Dong, J.

Solidification of SnPb and AlSi alloys in a rotating magnetic field

2nd Sino-German Workshop on EPM, 16.-19.10.2005, Dresden, Germany

Willers, B.; Eckert, S.; Nikritjuk, Petr A.; Eckert, K.; Michel, U.; Zouhar, G.
Application of a rotating magnetic field during directional solidification of Pb-Sn alloys: Consequences on the CET
International Conference on Advances in Solidification Processes, 07.-10.06.05, Stockholm, Schweden

Willers, B.; Nikritjuk, Petr A.; Eckert, K.; Eckert, S.
Flow structures during solidification of metallic alloys affected by a rotating magnetic field
Joint 15th Riga and 6th PAMIR International Conference on Fundamental and Applied MHD, 27.06.-01.07.2005, Riga, Latvia

Willschuetz, H.-G.
Simulation of the FOREVER experiments: enhancement and approach to a prototypic scenario
Seminar at the chair of Nuclear Power Safety, Royal Institute of Technology, Professor Nam Dinh, Chair of Nuclear Power Safety, Royal Institute of Technology, 12.10.2005, Stockholm, Sverige

Willschuetz, H.-G.; Altstadt, E.
Thermo-mechanical FE-modelling of in-vessel retention
SARNET - First Annual Review Meeting, GRS Köln, 15.02.2005, Köln, Deutschland

Willschuetz, H.-G.; Altstadt, E.
Verhalten des Reaktordruckbehälters bei einem unterstellten Kernschmelzunfall
Seminar Energieverfahrenstechnik WS 2005/2006, TU Dresden, Fakultät Maschinenwesen, 20.10.2005-26.01.2006, Dresden, Deutschland

Willschuetz, H.-G.; Altstadt, E.; Weiss, F.-P.
Recursive coupling of thermal and mechanical FE-models of a creeping pressure vessel with a heated melt pool
ICAPP 2005, International Congress on Advances in Nuclear Power Plants, KNS, AESoJ, SNE, SFEN, ANS, IAEA, OECD-NEA, CNS, KTG, CNS, 15.-19.05.2005, Seoul, Korea

Xu, M.; Gerbeth, G.; Gundrum, T.; Stefani, F.
On the integral equation approach and some related inverse problems in MHD
Perm Dynamo Days, 7-11 February, 2005

Xu, M.; Stefani, F.; Gerbeth, G.
Integral equation approach to dynamo experiments and inverse problems
Kolloquium der Forschergruppe Magnetofluiddynamik, TU Ilmenau, Forschergruppe Magnetofluiddynamik, TU Ilmenau, 23.11.2005, Ilmenau, Deutschland

Zaruba, A.
Experimental investigation of the flow in a bubble column
Seminar, Institut für Reaktorsicherheit (IRS), Forschungszentrum Karlsruhe, 24.11.2005, Karlsruhe, Deutschland

Zaruba, A.; Krepper, E.; Prasser, H.-M.
Experiments on turbulent diffusion of the gaseous phase in rectangular bubble column using image processing
Eleventh International Topical Meeting on Nuclear Reactor Thermal Hydraulics, NURETH 11, October 2-6, 2005, Avignon, France

Zhang, C.; Eckert, S.; Gerbeth, G.

Experimental studies of bubble-driven liquid metal flows in a static magnetic field

2nd Sino-German Workshop on EPM, 16.-19.10.2005, Dresden, Germany

Zhang, C.; Eckert, S.; Gerbeth, G.

Experimental study about gas-liquid metal two-phase flows under the influence of a DC magnetic field

The 2nd Workshop on Electromagnetic Processing of Materials (Asian-EPM2005), 22.-25.05.2005, Shenyang, China

Contributions to proceedings and other collected editions

Abdrashitov, A.; Abdrashitov, G.; Anikeev, A.; Bagryansky, P.; Beklemishev, A.; Deichuli, P.; Ivanov, A.; Korepanov, S.; Maximov, V.; Murakhtin, S.; Lizunov, A.; Prikhodko, V.; Kapitonov, V.; Kolmogorov, V.; Khilchenko, A.; Mishagin, V.; Savkin, V.; Shoukajev, A.; Shulzhenko, G.; Solomakhin, A.; Sorokin, A.; Stepanov, D.; Stupishin, N.; Tsidulko, Yu.; Zouev, A.; Noack, K.; Fiksel, G.; Den Hartog, D.

Status of the GDT experiment and future plans

5th Int. Conf. on Open Magnetic Systems for Plasma Confinement,, Budker Institute of Nuclear Physics Novosibirsk, 05.-09.07.2004, Novosibirsk, Russia

Status of the GDT Experiment and Future Plans: Beljan Ltd., Dexter, Michigan 48130

Adolphe, X.; Martemianov, S.; Piteau, A.; Weier, T.; Gerbeth, G.

Experimental investigation of the influence of Lorentz forces on local mass transfer and near wall turbulence by means of electrodiffusion probes

Joint 15th Riga and 6th pamir International Conference on MHD, 27.06.-01.07.2005, Riga, Latvia, Vol. 2, 151-154

Albrecht, T.; Grundmann, R.; Mutschke, G.; Gerbeth, G.

Numerical investigation of transition control in low conductive fluids

Joint 15th Riga and 6th PAMIR International Conference on Fundamental and Applied MHD, 27.06.-01.07.2005, Riga, Latvia, Vol. 1, 145-148

Alt, S.; Hampel, R.; Kästner, W.; Lischke, W.; Seeliger, A.; Krepper, E.; Grahn, A.

Untersuchungen zum Verhalten von freigesetztem Isolationsmaterial in ruhender und horizontaler Kühlmittelströmung

Jahrestagung Kerntechnik 2005, 10.-12.05.2005, Nürnberg, Deutschland

Alt, S.; Seeliger, A.; Krepper, E.; Grahn, A.

Experimental and analytical investigations for debris transport phenomena in multidimensional water flow

The 11th International Topical Meeting on Nuclear Reactor Thermal-Hydraulics (NURETH-11), 02.-06.10.2005, Avignon, Frankreich

Altstadt, E.; Beckert, C.; Galindo, V.; Naumann, B.; Weiss, F.-P.

Thermo-mechanical design of a photoneutron source for time-of-flight experiments

18th International Conference on Structural Mechanics in Reactor Technology (SMiRT 18), IASMIRT, 07.-12.08.2005, Beijing, China

Thermo-mechanical design of a photoneutron source for time-of-flight experiments

Altstadt, E.; Willschütz, H.-G.; Sehgal, B. R.; Weiß, F.-P.

Vessel rupture: Synthesis of the FOREVER interpretation activity

ERMSAR 2005, IRSN, 14.-16.11.2005, Aix en Provence, France

Anikeev, A. V.; Bagryansky, P. A.; Collatz, S.; Noack, K.

Plasma simulations of the SHIP experiment at GDT

5th Int. Conf. on Open Magnetic Systems for Plasma Confinement,, Budker Institute of Nuclear Physics Novosibirsk, 05.-09.07.2004, Novosibirsk, Russia

Open Magnetic Systems for Plasma Confinement: Beljan Ltd., Dexter, Michigan 48130

Bagryansky, P. A.; Anikeev, A. V.; Ivanov, A. A.; Lizunov, A. A.; Maximov, V. V.; Murakhtin, S. V.; Stepanov, D. N.; Noack, K.; Prikhodko, V. V.; Solomakhin, A. L.

First results from SHIP experiment

5th Int. Conf. on Open Magnetic Systems for Plasma Confinement, Budker Institute of Nuclear Physics Novosibirsk, 05.-09.07.2004, Novosibirsk, Russia
Open Magnetic Systems for Plasma Confinement: Beljan Ltd., Dexter, Michigan 48130

Bechta, S. V.; Khabensky, V. B.; Granovsky, V. S.; Kroushinov, E. V.; Vitol, S. A.; Gusarov, V. V.; Almiashv², V. I.; Mezentseva², L. P.; Petrov, Yu. B.; Lopukh, D. B.; Fischer, M.; Bottomley, D.; Tromm, W.; Barrachin, M.; Altstadt, E.; Piluso, P.; Fichot, F.; Hellmann, S.; Defoort, F.

CORPHAD and METCOR ISTC projects

ERMSAR 2005, IRSN, 14.-16.11.2005, Aix en Provence, France

Becker, G.; Schiebelsberger, B.; Rindelhardt, U.; Weber, W.

Sonne in der Schule: Betriebsergebnisse aus den Programmen in Bayern, Sachsen und Norddeutschland

20. Symposium Photovoltaische Solarenergie, DGS, 09.-11.03.2005, Staffelstein, Deutschland

Beckert, C.; Koch, R.

Reactor cell calculations with the codes HELIOS, MCNP and TransRay and comparison of the results

Annual Meeting on Nuclear Technology 2005, 10.-12.05.2005, Nürnberg, Deutschland

Bieberle, A.; Hampel, U.; Schleicher, E.; Hoppe, D.; Prasser, H.-M.; Sühnel, T.; Zippe, C.

Design and performance of a high-resolution gamma tomography device

4th World Congress on Industrial Process Tomography, 05.09.-08.09.2005, Aizu, Japan

Boden, S.; Hampel, U.; Speck, M.

Quantitative measurement of gas distributions in a stirred chemical reactor with cone-beam X-ray computed tomography

4th World Congress on Industrial Process Tomography, 05.-08.09.2005, Aizu, Japan
Proceedings of 4th World Congress on Industrial Process Tomography, 0 85316 255 7, 813-818

Bousbia Salah, A.; Kliem, S.; Rohde, U.

Uncertainty and sensitivity analyses of the Kozloduy pump trip test by coupled RELAP5/PARCS code

Int. Top. Meeting on Mathematics and Computation, Supercomputing, Reactor Physics and Nuclear Appli., CEA France, 12.-15.09.2005, Avignon, Frankreich
Proc. of the Int. Top. Meeting on Mathematics and Computation, Supercomputing, Reactor Physics ...

Cramer, A.; Eckert, S.; Galindo, V.; Gerbeth, G.

Applications of AC and DC magnetic fields in metallurgical or crystal growth processes

International Workshop on Materials Analysis and Processing in Magnetic Fields, National High Magnetic Field Laboratory, 17.-19.03.2004, Tallahassee, FL, USA, p. 157-168 (2005)

Cramer, A.; Eckert, S.; Galindo, V.; Gerbeth, G.; Witke, W.

Aluminum investment casting with magnetic field control of the mould filling process

International Symposium on Liquid Metal Processing and Casting, 18.-21.09.2005, Santa Fe, New Mexico, USA, ISBN: 0-87170-827-2, 295-303

Cramer, A.; Eckert, S.; Galindo, V.; Priede, J.; Gerbeth, G.

Applications of AC and DC magnetic fields in metallurgical and crystal growth processes

in: H. Wada, H.J. Schneider-Muntau (Hrsg.): Materials Processing in Magnetic Fields, Singapore: World Scientific Publishing, 2005, 157-168

Cramer, A.; Gundrum, Th.; Varshney, K.; Gerbeth, G.

Experimental investigation of rotating magnetic field driven flow by highly sensitive potential probe measurements

Joint 15th Riga and 6th PAMIR Interantional Conference on Fundamental and Applied MHD, Institute of Physics, University of Latvia, Riga - Latvia, 27.06.-01.07.2005, Jurmala, Latvia

Da Silva, M. J.; Hampel, U.; Schleicher, E.

Neue Konzepte für die kombinierte Leitfähigkeits- und Impedanzmessung in hochtransienten Mehrphasenströmungen

7. Dresdner Sensor-Symposium, Forschungsgesellschaft Messtechnik Sensorik und Medizintechnik e.V. Dresden, 12.-14.12.2005, Dresden, Deutschland

Proceedings 7. Dresdner Sensor-Symposium - Neue Herausforderungen und Anwendung in der Sensortechnik: TUDpress, ISBN: 3-938863-29-3, 139-142

Eckert, S.; Gerbeth, G.; Gundrum, T.; Stefani, F.

Velocity measurements in metallic melts

2005 ASME Fluids Engineering Division Summer Meeting, ASME, 19.-23.07.2005, Houston, TX, USA

FEDSM2005-77089

Frank, T.; Zwart, P.; Shi, J.-M.; Krepper, E.; Lucas, D.; Rohde, U.

Inhomogeneous MUSIG model – a population balance approach for polydispersed bubbly flows

International Conference Nuclear Energy for New Europe 2005, 05.-08.09.2005, Bled, Slovenia

Gailitis, A.; Lielausis, O.; Platacis, E.; Gerbeth, G.; Stefani, F.

Riga dynamo experiments

Joint 15th Riga and 6th pamir International Conference on MHD, 27.06.-01.07.2005, Riga, Latvia, Vol. 1, 15-24

Gerbeth, G.; Eckert, S.; Galindo, V.; Willers, B.

Liquid metal flows in AC and DC magnetic fields and its application to casting processes

The 2nd Workshop on Electromagnetic Processing of Materials (Asian-EPM2005), 22.-25.05.2005, Shenyang, China, 42-44

Gokhman, A.; Bergner, F.; Ulbricht, A.

Modelling of the evolution of vacancy clusters in neutron-irradiated iron

Annual Meeting on Nuclear Technology 2005, German Atomic Forum and German Nuclear Society, 10.-12.05.2005, Nürnberg, BRD

Proceedings of the Annual Meeting on Nuclear Technology: INFORUM GmbH, 634-640

Grahn, A.; Prasser, H.-M.

Fluid-dynamic instabilities during mass transfer across the interface between to immiscible liquids

6th world conference on experimental heat transfer, fluid mechanics and thermodynamics, 17.-21. April 2005, Miyagi, Japan

Grundmann, U.; Kliem, S.; Mittag, S.; Rohde, U.

The influence of the coolant flow fluctuations on the consequences of a hypothetical boron dilution event

Annual Meeting on Nuclear Technology 2005, Kerntechnische Gesellschaft e. V., Deutsches Atomforum e. V., 10.-12.05.2005, Nuremberg, Germany
Jahrestagung Kerntechnik 2005: INFORUM GmbH

Gundrum, Th.; Gerbeth, G.; Stefani, F.; Xu, M.

Experimental aspects of contactless inductive flow tomography

Joint 15th Riga and 6th PAMIR International Conference on Fundamental and Applied MHD, Institute of Physics, University of Latvia, Riga - Latvia, 27.06.-01.07.2005, Jurmala, Latvia

Proceedings of the Joint 15th Riga and 6th PAMIR Conference on Fundamental and Applied MHD, Vol. 2, 319-322

Höhne, T.

Numerical modelling of a transient slug mixing experiment of the ROCOM test facility using CFX-5

The 11th International Topical Meeting on Nuclear Reactor Thermal-Hydraulics (NURETH-11), 02.-06.10.2005, Avignon, France
CD-ROM, paper 481

Höhne, T.; Bezrukov, Y.

CFD calculation of a mixing experiment in the VVER-1000 reactor model

The 4-th International Conference SAFETY ASSURANCE OF NUCLEAR POWER PLANTS WITH WWER, FSUE EDO, 23.-26.05.2005, Podolsk, Russian Federation

Höhne, T.; Kliem, S.; Rohde, U.

CFD- analysis of the mixing pattern under various flow conditions at the ROCOM test facility using CFX-5

13th International Conference on Nuclear Engineering, 16.-20.05.2005, Beijing, China
CD-ROM

Höhne, T.; Scheuerer, M.; Kliem, S.

Numerical modelling of a buoyancy driven flow in a reactor pressure vessel using CFX-5

The 11th International Topical Meeting on Nuclear Reactor Thermal-Hydraulics (NURETH-11), 02.-06.10.2005, Avignon, France
CD-ROM, paper 480

Kenjeres, S.; Renaudier, S.; Hanjalic, K.; Stefani, F.

Computational study of flow and magnetic field interactions in Riga dynamo

Joint 15th Riga and 6th PAMIR International Conference on Fundamental and Applied MHD, Institute of Physics, University of Latvia, Riga - Latvia, 27.06.-01.07.2005, Jurmala, Latvia

Proceedings of the Joint 15th Riga and 6th PAMIR Conference on Fundamental and Applied MHD, Vol. 1, 93-96

Kliem, S.; Langenbuch, S.; Weiß, F.-P.

Uncertainty analyses of coupled thermal hydraulic/neutron kinetic code calculations

Jahrestagung Kerntechnik 2005, 10.-12.05.2005, Nürnberg, Deutschland

Proceedings der Fachsitzung: Neuere Methoden im Nachweisverfahren bei Störfallanalysen, Berlin: INFORUM GmbH, 79-105

Kliem, S.; Mittag, S.; Weiß, F.-P.; Langenbuch, S.

Uncertainty and sensitivity analysis for the modeling of a start-up experiment in a VVER-1000 reactor

4th International Conference: Safety Assurance of Nuclear Power Plants with WWER", FSUE EDO "Gidropress" Podolsk, 23.-26.05.2005, Podolsk, Russland

Proc. of the 4th Int. Conference: Safety Assurance of Nuclear Power Plants with WWER" (CD-ROM)

Kliem, S.; Mittag, S.; Weiß, F.-P.; Langenbuch, S.

Uncertainty and sensitivity analysis for the modeling of transients with interaction of thermal hydraulics and neutron kinetics

11th International Topical Meeting on Nuclear Reactor Thermal-Hydraulics (NURETH-11), CEA France, 02.-06.10.2005, Avignon, France

Proceedings of the 11th Int. Top. Meeting on Nuclear Reactor Thermal-Hydraulics (CDROM paper 461)

Kolesnichenko, I.; Khripchenko, S.; Buchenau, D.; Gerbeth, G.

Electro-vortex flows in shallow liquid metal layers

Joint 15th Riga and 6th PAMIR International Conference on Fundamental and Applied MHD, Institute of Physics, University of Latvia, Riga - Latvia, 27.06.-01.07.2005, Jurmala, Latvia

Koncar, B.; Krepper, E.; Egorov, Y.

CFD modeling of subcooled flow boiling for nuclear engineering applications

International Conference "Nuclear Energy for New Europe 2005", 05.-08.09.2005, Bled, Slovenia

Konheiser, J.; Rindelhardt, U.; Viehrig, H.-W.

Post mortem investigations of Greifswald VVER 440 reactor pressure vessel: Recent progress in dosimetry and material investigations

4th International Conference on Safety Assurance of Nuclear Power Plants with WWER, OKB Gidropress, 23.-25.05.2005, Podolsk, Russian Federation

Conference CD, Podolsk

Konheiser, J.; Rindelhardt, U.; Viehrig, H.-W.

RPV investigations of Greifswald WWER-440 units: New dosimetry results and material testing concepts

Annual meeting on nuclear technology 2005, May 10-12, Nürnberg, Proc. p.641, Deutsches Atomforum, 10.-12.05.2005, Nürnberg, Deutschland

Proc. Annual Meeting on Nuclear Technology, 641

Kozmenkov, Y.; Grundmann, U.; Kliem, S.; Rohde, U.

Comparative assessment of coupled RELAP5/PARCS and DYN3D/RELAP5 codes against the Kozloduy-6 pump trip test

Int. Top. Meeting on Mathematics and Computation, Supercomputing, Reactor Physics and Nuclear Appli., CEA France, 12.-15.09.2005, Avignon, France

Proc. of the Int. Top. Meeting on Mathematics and Computation, Supercomputing, Reactor Physics ...

Kozmenkov, Y.; Grundmann, U.; Kliem, S.; Rohde, U.; Weiss, F.-P.

V1000CT-1 benchmark analyses with the DYN3D/RELAP5 and DYN3D/ATHLET coupled code systems

11th Int. Top. Meeting on Nuclear Reactor Thermal-Hydraulics (CDROM paper 254), American Nuclear Society, 02.-06.10.2005, Avignon, France

Proceedings of the 11th Int. Top. Meeting on Nuclear Reactor Thermal-Hydraulics (CDROM paper 254)

Krepel, J.; Grundmann, U.; Rohde, U.; Weiss, F.-P.

Dynamics of MSR

Structural mechanics in reactor technology, SmiRT18, International Association for Structural Mechanics in Reactor Technology (IASMiRT), 08.-12.08.2005, Beijing, China

Krepel, J.; Rohde, U.; Grundmann, U.

Simulation of molten salt reactor dynamics

Nuclear Energy for New Europe 2005, Nuclear Society of Slovenia, 05.-08.09.2005, Bled, Slovenia

Krepel, J.; Rohde, U.; Grundmann, U.; Weiss, F.-P.

Spatial dynamics of MSRE

in: ASME, JSME, CNS: Proceedings of 13th International Conference on Nuclear Engineering, Beijing: ASME, JSME, CNS, 2005

Krepper, E.; Egorov, Y.

CFD-modelling of subcooled boiling and application to simulate a hot channel of a fuel assembly

13th International Conference on Nuclear Engineering, Chinese Nuclear Society, 16.-20.05.2005, Peking, China

Krepper, E.; Grahn, A.; Alt, S.; Kästner, W.; Kratzsch, A.; Seeliger, A.

Numerical investigations for insulation particle transport phenomena in water flow

23rd CADFEM Users Meeting 2005, 09.-11.11.2005, Bonn, Deutschland

Krepper, E.; Lucas, D.; Prasser, H.-M.; Shi, J.-M.; Rohde, U.

Two-phase flow simulations in the FZ Rossendorf using CFX-5

11th Workshop on Two Phase Flow Predictions, Martin-Luther-Universität Halle-Wittenberg, 05.-08.04.2005, Merseburg, Deutschland

11th Workshop on Two Phase Flow Predictions

Krepper, E.; Prasser, H.-M.; Frank, T.

Air-water flow in a vertical pipe with sudden changes of superficial water velocity

The 11th International Topical Meeting on Nuclear Reactor Thermal-Hydraulics (NURETH-11), 02.-06.10.2005, Avignon, Frankreich

Lantzsch, R.; Galindo, V.; Grants, I.; Pätzold, O.; Gerbeth, G.; Stelter, M.; Cröll, A.
Fluid flow analysis and vertical gradient freeze crystal growth in a traveling magnetic field

Joint 15th Riga and 6th PAMIR International Conference on Fundamental and Applied MHD, Institute of Physics, University of Latvia, Riga - Latvia, 27.06.-01.07.2005, Jurmala, Latvia, Vol.2, 197-200

Lucas, D.; Krepper, E.; Prasser, H.-M.

Modeling of the evolution of bubbly flow along a large vertical pipe

*The 11th International Topical Meeting on Nuclear Reactor Thermal-Hydraulics (NURETH-11), NURETH, 02.-06.10.2005, Avignon, France
Paper 051*

Lucas, D.; Prasser, H.-M.

Simulation of phase transfer in case of bubbly steam-water flow along a large vertical pipe

*4th International Conference on transport phenomena in multiphase systems, Gdańsk University of Technology, Institute of Fluid-Flow Machinery, Polish Academy of Sciences, 26.-30.06.2005, Gdansk, Poland
Proceedings of the 4th International Conference on transport phenomena in multiphase systems, Gdansk, Poland: IFFM Publishers, 83-88237-90-X, 345-350*

Lycklama à Nijeholt, J.-A.; Höhne, T.

CFD modeling of the mixing of deborated with borated water in a reactor pressure vessel

*ENC 2005 European Nuclear Conference, ENS ANS CEA, 11.-14.12.2005, VERSAILLES, France
CD-ROM*

Manera, A.

A startup procedure for natural circulation boiling Water Reactors

The 11th International Topical Meeting on Nuclear Reactor Thermal-Hydraulics (NURETH-11), 02.-06.10.2005, Avignon, France

Manera, A.

Out-of-phase flashing-induced instabilities in a natural circulation two-phase system with parallel channels

*4th Int. Conf. on Transport Phenomena in Multiphase Systems, 26.-30.06.2005, Gdansk, Poland
Proc. of 4th Int. Conf. on Transport Phenomena in Multiphase Systems*

Manera, A.

Strategies for the start-up procedure of natural circulation Boiling Water Reactors

Jahrestagung Kerntechnik 2005, 10.-12.05.2005, Nuremberg, Germany

Manera, A.; Prasser, H.-M.; Lucas, D.

Experimental investigations on bubble turbulent diffusion in a vertical large-diameter pipe by means of wire-mesh sensors and correlation techniques

The 11th International Topical Meeting on Nuclear Reactor Thermal-Hydraulics (NURETH-11), 02.-06.10.2005, Avignon, France

Petkov, T.; Mittag, S.

WWER radial reflector modeling by diffusion codes

*15-th Symposium of AER, NPP Dukovany, 03.-07.10.05, Znojmo, Czech Republic
Proceedings of 15-th Symposium of AER, Budapest: Kiadja a KFKI Atomenergia Kutató
Intézet, 963-372-6328, 39-50*

Pfingsten, W.; Mibus, J.; Küchler, R.

Reactive transport codes applied to gypsum dissolution in a laboratory column experiment with focus on sensitivity of model concepts and data uncertainty

*Fifth International Conference on Calibration and Reliability in Groundwater Modelling,
Netherlands Institute of Applied Geoscience and International Commission on Groundwater,
06.-09.06.2005, Scheveningen, The Netherlands
Reactive transport codes applied to gypsum dissolution in a laboratory column experiment
with focus*

Pietruske, H.; Prasser, H.-M.

Wire-mesh sensors for high-resolving two-phase flow studies at high pressures and temperatures

*The 11th International Topical Meeting on Nuclear Reactor Thermal-Hydraulics (NURETH-11), 02.-06.10.2005, Avignon, France
CD-ROM, Paper 533*

Prasser, H.-M.; Beyer, M.; Carl, H.; Gregor, S.; Lucas, D.; Pietruske, H.; Schütz, P.; Weiss, F.-P.

Evolution of the structure of a gas-liquid two-phase flow in a large vertical pipe

Eleventh International Topical Meeting on Nuclear Reactor Thermal Hydraulics, NURETH 11, October 2-6, 2005, Avignon, France, paper 399.

Prasser, H.-M.; Beyer, M.; Carl, H.; Gregor, S.; Schütz, P.; Weiss, F.-P.

Flow structure during steam condensation in sub-cooled water in a large vertical pipe using wire-mesh sensors

*4th International Conference on transport phenomena in multiphase systems, Gdańsk
University of Technology, 26.-30.06.2005, Gdansk, Poland
Proceedings of HEAT-2005, 433-438*

Prasser, H.-M.; Beyer, M.; Carl, H.; Pietruske, H.; Schütz, P.; Weiß, F.-P.

Steam-water experiments at high pressure to study the structure of the gas-liquid interface in a large vertical pipe

Annual Meeting on Nuclear Technology, German Atomic Forum and German Nuclear Society, 10.-12.05.2005, Nürnberg, Deutschland, 98-101

Prasser, H.-M.; Gregor, S.

Evolution of Interfacial Area Concentration in a Vertical Air-Water Flow Measured by Wire-Mesh Sensors

Eleventh International Topical Meeting on Nuclear Reactor Thermal Hydraulics, NURETH 11, October 2-6, 2005, Avignon, France. paper 398.

Priede, J.; Gerbeth, G.; Hermann, R.; Behr, G.

Float-zone crystal growth with a novel melt flow control

Joint 15th Riga and 6th PAMIR International Conference on Fundamental and Applied MHD, Institute of Physics, Universtiy of Latvia, Riga - Latvia, 27.06.-01.07.2005, Jurmala, Latvia, Vol. 2, 189-192

Reddy Vanga, B.; Lopez de Bertodano, M.; Krepper, E.; Zaruba, A.; Prasser, H.-M.

Two fluid model LES of a bubble column

The 11th International Topical Meeting on Nuclear Reactor Thermal-Hydraulics (NURETH-11), 02.-06.10.2005, Avignon, Frankreich

Rindelhardt, U.; Fatterschneider, H.

Module efficiencies and performance measurements: Summary of a 10 years measuring program

20th European Photovoltaic Solar Energy Conference and Exhibition, 06.-10.06.2005, Barcelona, Spain

Rohde, U.; Höhne, T.; Kliem, S.; Hemström, B.; Scheuerer, M.; Dury, T.; Remis, J.; Muhlbauer, P.; Toth, I.; Elter, J.; Bezrukov, Y.; Toppila, T.; Lillington, J.

Fluid mixing and flow distribution in the reactor circuit (FLOMIX-R)

4th Scientific and Technical Conference "Safety Assurance of NPP with WWER", EDO Gidropress, 23.-26.05.2005, Podolsk, Russia

Rohde, U.; Kliem, S.; Höhne, T.; Prasser, H.-M.; Hemström, B.; Toppila, T.; Elter, J.; Bezrukov, Y.; Scheuerer, M.

Measurement data base on fluid mixing and flow distribution in the reactor circuit

11th International Topical Meeting on Nuclear Reactor Thermal Hydraulics, SFANS/SFEN, 02.-06.10.2005, Avignon, France, 2-9516195-0-2

Shatrov, V.; Gerbeth, G.

On MHD drag reduction and its efficiency

Joint 15th Riga and 6th PAMIR International Conference on Fundamental and Applied MHD, Institute of Physics, University of Latvia - Riga, 27.06.-01.07.2005, Jurmala, Latvia

Shi, J.-M.; Burns, A.; Prasser, H.-M.

Turbulent dispersion of bubbles in poly-dispersed gas-liquid flows in a vertical pipe

The 13th International Conference on Nuclear Engineering, Chinese Nuclear Society (CNS), ASME, JSME, 15.-20.05.2005, Beijing, P.R. China

Speck, M.; Hampel, U.; Koch, D.; Mayer, H.-G.; Menz, H.-J.; Prasser, H.-M.; Schleicher, E.
A limited-angle CT approach for a fast scanned electron-beam X-ray tomography with application to multi-phase flow measurements

Proceedings of the 4th World Congress on Industrial Process Tomography, Aizu, Japan, Sept. 2005

Stefani, F.; Gerbeth, G.; Günther, U.

A paradigmatic model of Earth's magnetic field reversals

Joint 15th Riga and 6th PAMIR International Conference on Fundamental and Applied MHD, Institute of Physics, University of Latvia, Riga - Latvia, 27.06.-01.07.2005, Jurmala, Latvia

Proceedings of the Joint 15th Riga and 6th PAMIR Conference on Fundamental and Applied MHD, Vol. 1, 97-100

Stefani, F.; Gerbeth, G.; Günther, U.; Gundrum, T.; Xu, M.
Inverse problems in magnetohydrodynamics: theoretical and experimental aspects
Inverse problems, design and optimization symposium, Florida International University, Miami, USA; Federal University of Rio de Janeiro, Brazil, 17.-19.03.2004, Rio de Janeiro, Brazil

Inverse problems, design and optimization, Vol. II, Rio de Janeiro: E-papers Publishing House Ltd, 85-7650-030-2, 151-158

Thomas, H.; Sören, K.

Coolant mixing studies of natural circulation flows at the ROCOM test facility using CFX-10

*23rd CADFEM Users' Meeting 2005, ANSYS CFX & ICEM, 09.-11.11.2005, Bonn, Deutschland
CD-ROM*

Ulbricht, A.; Keiderling, U.

Synergism effects between Ni and Cu on the radiation susceptibility of RPV model alloys
in: Y. Kirschbaum, A. Brandt, M. Tovar, D. Bischoff, R. Michaelsen: BENSC Experimental Reports 2004, Berlin: Hahn-Meitner-Institut, HMI - B 601, 2005, ISSN 0936 - 0891, 155

Vallee, C.; Höhne, T.; Prasser, H.-M.; Sühnel, T.

Experimental modelling and CFD simulation of air/water flow in a horizontal channel
*The 11th International Topical Meeting on Nuclear Reactor Thermal-Hydraulics (NURETH-11), 02.-06.10.2005, Avignon, France
CD-ROM, paper 479*

Vallee, C.; Sühnel, T.

Experimental investigation and CFD simulation of an air/water flow in a horizontal channel (Part 1: Measurements)

*FZR & Ansys Multiphase flow workshop, FZR & Ansys Germany, 31.05.-03.06.2005, Dresden, Germany
Workshop proceedings*

Weier, T.; Gerbeth, G.

Experimental results on the effect of wall-parallel Lorentz forces on lift and drag of hydrofoils

*2nd International Symposium on Seawater Drag Reduction, 23.-26.05.2005, Busan, South Korea
Proceedings of the 2nd International Symposium on Seawater Drag Reduction ISSDR 2005, Busan, 267-281*

Weier, T.; Hüller, J.; Gerbeth, G.; Weiss, F.-P.

Velocity measurements and concentration field visualizations in natural convection copper electrolysis under magnetic field influence

*Joint 15th Riga and 6th PAMIR International Conference Fundamental and Applied MHD, 27.06.-01.07.2005, Rigas Jurmala, Latvia
Proceedings of the Joint 15th and 6th PAMIR International Conference on Fundamental and Applied MHD, Riga, Vol. 2, 143-146*

Willers, B.; Nikritjuk, Petr A.; Eckert, K.; Eckert, S.

Flow structures during solidification of metallic alloys affected by a rotating magnetic field

Joint 15th Riga and 6th PAMIR International Conference on Fundamental and Applied MHD, 27.06.-01.07.2005, Riga, Latvia, Vol. 2, 269-272

Willschuetz, H.-G.; Altstadt, E.; Weiss, F.-P.

Recursive coupling of thermal and mechanical FE-models of a creeping pressure vessel with a heated melt pool

ICAPP 2005, International Congress on Advances in Nuclear Power Plants, KNS, AESoJ, SNE, SFEN, ANS, IAEA, OECD-NEA, CNS, KTG, CNS, 15.-19.05.2005, Seoul, Korea
ICAPP 2005, International Congress on Advances in Nuclear Power Plants, Seoul: Korean Nuclear Society

Willschütz, H.-G.; Altstadt, E.; Weiss, F.-P.

Recursively coupled FEM-analysis of pressure vessel creep failure experiments

Jahrestagung Kerntechnik 2005, Nürnberg

Zaruba, A.; Krepper, E.; Prasser, H.-M.

Experiments on turbulent diffusion of the gaseous phase in rectangular bubble column using image processing

Eleventh International Topical Meeting on Nuclear Reactor Thermal Hydraulics, NURETH 11, October 2-6, 2005, Avignon, France, proceedings CD-ROM, paper 388.

Zhang, C.; Eckert, S.; Gerbeth, G.

Experimental study about gas-liquid metal two-phase flows under the influence of a DC magnetic field

The 2nd Workshop on Electromagnetic Processing of Materials (Asian-EPM 2005), 22.-25.05.2005, Shenyang, China, 297-298

Zhang, C.; Eckert, S.; Gerbeth, G.

Motion of single gas bubbles rising in a liquid metal exposed to a DC magnetic field

Joint 15th Riga and 6th PAMIR International Conference on Fundamental and Applied MHD, 27.06.-01.07.2005, Riga, Latvia, Vol. 1, 195-198

FZR reports and other reports

Altstadt, E.; Beckert, C.; Beyer, R.; Freiesleben, H.; Galindo, V.; Greschner, M.; Grosse, E.; Junghans, A.; Klug, J.; Naumann, B.; Schneider, S.; Seidel, K.; Wagner, A.; Weiß, F.-P.
Energiedispersive Untersuchung der Wechselwirkung schneller Neutronen mit Materie - gemeinsamer Abschlussbericht der DFG Projekte GR 1674/2 und FR 575/5
Wissenschaftlich-Technische Berichte / Forschungszentrum Rossendorf; FZR-426 April 2005
104 Seiten

Altstadt, E.; Willschuetz, H.-G.; Sehgal, B. R.; Weiss, F.-P.
Modelling of in-vessel retention after relocation of corium into the lower plenum
Wissenschaftlich-Technische Berichte / Forschungszentrum Rossendorf; FZR-437 Oktober 2005
100 Seiten

Altstadt, E.; Willschütz, H.-G.
Beitrag zur Modellierung der Schmelzerückhaltung im RDB nach Verlagerung von Corium in das untere Plenum: Berechnung des Temperaturfeldes und der viskoplastischen Verformung der Behälterwand
Wissenschaftlich-Technische Berichte / Forschungszentrum Rossendorf; FZR-412 Januar 2005
101 Seiten

Beyer, M.; Carl, H.
Unterstützung der ukrainischen Aufsichtsbehörde beim Ausbau der verbesserten betrieblichen KKW-Überwachung (Teil 3)
Wissenschaftlich-Technische Berichte / Forschungszentrum Rossendorf; FZR-429 Mai 2005
39 Seiten

Bieder, U.; Höhne, T.
Inherent Dilution: Qualification of TRIO_U on a ROCOM experiment
Grenoble: CEA/DEN/GRE/DER/SSTH/LMDL-2004-029, 2005
29 Seiten

Burwell, M. J.; Höhne, T.; Scheuerer, M.
Nachrechnung des ROCOM Experiments T6655_Y1 mit dem CFD-Programm CFX-5
München: GRS - A - 2871, 2005
14 Seiten

Grahn, A.
Strömungsinstabilitäten bei Stoffübergang und chemischer Reaktion an der ebenen Grenzfläche zwischen zwei nicht mischbaren Flüssigkeiten
Wissenschaftlich-Technische Berichte / Forschungszentrum Rossendorf; FZR-417 Januar 2005
171 Seiten

Grundmann, U.; Rohde, U.; Mittag, S.; Kliem, S.
DYN3D version 3.2 - code for calculation of transients in light water reactors (LWR) with hexagonal or quadratic fuel elements - description of models and methods -
Wissenschaftlich-Technische Berichte / Forschungszentrum Rossendorf; FZR-434 August 2005
140 Seiten

Kliem, S.; Grundmann, U.; Rohde, U.

Methodenentwicklung zur Analyse von Störfallszenarien mit Frischdampfleck und Borverdünnung mit Hilfe des Codesystems ATHLET-DYN3D - Abschlussbericht Teil 2
Wissenschaftlich-Technische Berichte / Forschungszentrum Rossendorf; FZR-438 Oktober 2005

124 Seiten

Rohde, U.; Höhne, T.; Kliem, S.; Scheuerer, M.; Hemström, B.; Toppila, T.; Dury, T.; Klepac, J.; Remis, J.; Mühlbauer, P.; Vyskocil, L.; Farkas, I.; Aszodi, A.; Boros, I.; Lycklama a. Nijeholt, J.-A.

The European project FLOMIX-R: Fluid mixing and flow distribution in the reactor circuit - Final summary report

Wissenschaftlich-Technische Berichte / Forschungszentrum Rossendorf; FZR-432 August 2005

129 Seiten

Rohde, U.; Kliem, S.; Hemström, B.; Toppila, T.; Bezrukov, Y.

The European project FLOMIX-R: Description of the slug mixing and buoyancy related experiments at the different test facilities (Final report on WP 2)

Wissenschaftlich-Technische Berichte / Forschungszentrum Rossendorf; FZR-430 August 2005

214 Seiten

Toppila, T.; Höhne, T.; Kliem, S.; Elter, J.; Remis, J.; Klepac, J.; Farkas, I.; Aszodi, A.; Boros, I.

The European project FLOMIX-R: Description of the experimental and numerical studies of flow distribution in the reactor primary circuit (Final report on WP 3)

Wissenschaftlich-Technische Berichte / Forschungszentrum Rossendorf; FZR-431 August 2005

103 Seiten

Weiss, F. P.; Rindelhardt, U. (Editors)

Annual Report 2004 - Institute of Safety Research

Wissenschaftlich-Technische Berichte / Forschungszentrum Rossendorf; FZR-420 März 2005

171 Seiten

Patents

Hermann, R.; Gerbeth, G.; Filip, O.; Priede, J.

Verfahren zur schmelzmetallurgischen Herstellung von Magnetlegierungen auf Nd-Fe-B-Basis

WO 2005/003396 A1

Hermann, R.; Gerbeth, G.; Filip, O.; Priede, J.; Schultz, L.

Verfahren und Vorrichtung zur schmelzmetallurgischen Herstellung von Magnetlegierungen auf Nd-Fe-B-Basis

WO 2004/112993 A1

Hoppe, D.; Kernchen, R.

Hydromechanische Maschine

DE 10 2004 001 047 A1

Prasser, H.-M.; Hampel, U.

Anordnung zur Röntgentomographie mit einem elektronisch abgelenkten Elektronenstrahl

DE 103 56 601 A1

Priede, J.; Gerbeth, G.; Hermann, R.; Behr, G.; Schultz, L.; Uhlemann, H.-J.

Verfahren und Vorrichtung zum Ziehen von Einkristallen durch Zonenziehen

DE 103 28 859 A 1

PhD and diploma theses

PhD theses

Hans-Gorg Willschütz

Thermomechanische Modellierung eines Reaktordruckbehälters in der Spätphase eines Kernschmelzunfalls
TU Dresden, Fakultät Maschinenwesen

David Legrady

Improved Monte Carlo Methods with Application to Borehole Logging Simulations
Delft University of Technology

Diploma theses

Sabine Gregor

Thermohydraulische Modellierung der Kondensation von Dampf in einer unterkühlten Flüssigkeitsströmung
TU Dresden, Fakultät Maschinenwesen, Fachrichtung Energietechnik

Jana Seebecker

Meteorologische Grundlagen und Qualitätskriterien von Windindices
Universität Leipzig, Fakultät für Physik und Geowissenschaften

Falk Brückner

Impedanzmessung mehrphasiger Fluide mit Nadelsondenmesssystemen
HTW Dresden

Awards 2005

Jiří Krepel

Contest of Young Authors
Nuclear Energy for New Europe 2005, Bled (Slovenia)

Simulation of Molten Salt Reactor Dynamics

Date: 08 July 2005

Horst-Michael Prasser

Forschungspreis 2005 des FZR

Experimentelle Validierung von CFD-Codes

Date: 12 December 2005

Hans-Georg Willschütz

Förderpreis 2005 der Friedrich-und-Elisabeth-BOYSEN-Stiftung

Thermomechanische Modellierung eines Reaktordruckbehälters in der Spätphase eines Kernschmelzunfalls

Date of award: 29 April 2006

M. Speck, U. Hampel, D. Koch, H.-G. Mayer, H.-J. Menz, H.-M. Prasser, E. Schleicher

The Maurice Beck Prize
Best Paper at the 4th World Congress on Industrial Process Tomography, Aizu (Japan)

A Limited-Angle CT Approach for a Fast Scanned Electron-Beam X-ray Tomography with Application to Multi-Phase Measurements

Date: 08 September 2005

Guests

Borodkin, Gennadi

04.01.2005 – 03.03.2005

Gosatomnadzor Moskau/Russland

Pedcenko, Aleksandrs

09.01.2005 -15.02.2005

Institute of Physics Riga/Lettland

Dzukan, Jan Dr.

01.02.2005 – 28.02.2005

01.11.2005 – 30.11.2005

SKODA Research Plzen/Tschechien

Murasov, Mykhail

28.02.2005 – 27.05.2005

Polytechnisches Institut Kiew/Ukraine

Liu, Heping

09.03.2005 – 12.03.2005

Ben-Gurion University/China

Knaepen, Bernard

15.03.2005 – 17.03.2005

Univerity Brüssel /Belgien

Petkov, Petko Dr.

16.03.2005 – 15.05.2005

Bulgarische Akademie der Wissenschaften/Bulgarien

Borodin, Vladimir Dr.

22.03.2005 – 03.04.2005

14.04.2005 – 22.05.2005

28.05.2005 – 08.07.2005

RRC Kurchatov Institute Moskau/Russland

Priede, Janis Dr.

04.04.2005 – 30.04.2005

19.09.2005 – 22.10.2005

Institute of Physics Riga/Lettland

Gashenko, Ilya Vladimirovich

26.03.2005 – 20.05.2005

Elektrogorsk Research and Engineering Centre/Russland

Molokov, Sergei Prof.

30.03.2005 – 31.03.2005

Conventry University/Großbritannien

Mikhailovich, Boris Dr.
14.04.2005 – 22.04.2005
BGU University Beer-Sheva/Israel

Odenbach, Stefan Prof.
28.04.2005 – 30.04.2005
Universität Bremen/ZARM

Jie, Dong Dr.
16.05.2005 – 08.06.2005
Jiao Tong University Shanghai/China

Egorov, Grigory A.
30.05.2005 – 03.07.2005
Novgorod Technical University/Russland

Koncar, Bostjan Dr.
23.05.2005 – 24.06.2005
Jozef Stefan Institut Ljubljana/Slovenien

Melnikov, Vladimir V. Prof.
30.05.2005 – 12.06.2005
Novgorod Technical University/Russland

Kamnev, Mikhail
31.05.2005 – 27.08.2005
Novgorod Technical University/Russland

Anikeev, Andrey Dr.
05.06.2005 – 01.07.2005
Budker Institut Novosibirsk/Russland

Bousbia Salah, Anis Dr.
25.07.2005 – 11.09.2005
Universität Pisa/Italien

Kotsarev, Alexander
14.06.2005 . 18.06.2005
Kurchatov Institute Moskau/Russland

Nikonov, Sergey
14.06.2005 – 18.06.2005
Kurchatov Institute Moskau/Russland

Willemetz, Jean-Claude Dr.
19.06.2005 – 21.06.2005
Signal Processing Lausanne/Schweiz

Kirillov, Oleg Dr.

10.07.2005 – 12.07.2005

Universität Hannover

Plevachuk, Yuri Dr.

20.07.2005 – 30.07.2005

14.12.2005 – 17.12.2005

Staatliche Universität Liv/Ukraine

Gokhmann, Alexander Prof.

01.08.2005 – 31.10.2005

South Ukrainian Pedagogical University K.D.Ushinski Odessa/Ukraine

Petkov, Petko Dr.

15.08.2005 -14.12.2005

Bulgarische Akademie der Wissenschaften Sofia/Bulgarien

Cvachovec, Frantisek Prof.

19.09.2005 – 30.09.2005

UJV Rez/Tschechien

Khrennikov, Nikolay Dr.

18.10.2005 – 21.10.2005

Gosatomnadzor Moskau/Russland

Borodkin, Gennadi

16.10.2005 – 15.12.2005

Gosatomnadzor Moskau/Russland

Danitseva, Irina

18.10.2005 – 21.10.2005

Gosatomnadzor Moskau/Russland

Gelfgat, Yuri Prof.

19.10.2005 – 20.10.2005

Institute of Physics Riga/Lettland

Grants, Ilmars Dr.

19.10.2005 – 20.10.2005

Institute of Physics Riga/Lettland

Ivanov, Alexandre Prof.

23.11.2005 – 05.12.2005

Budker Institute Novosibirsk/Russland

Khalimonchuk, Volodymyr

04.12.2005 – 10.12.2005

Scientific Technical Centre for Nuclear and Radiation Safety of the Ukraine, Kiev/Ukraine

Ovdiyenko, Yuri

04.12.2005 – 10.12.2005

Scientific-Technical Centre for Nuclear and Radiation Safety of the Ukraine/Ukraine

Samsonov, Boris Prof.

12.12.2005 – 15.12.2005

Physics Department of Tomsk State University/Russland

Meetings und Workshops

International TOPFLOW PTS Meeting

Organizers: FZR, CEA, EdF
Rossendorf, 18-20 April 2005

Workshop zur Kühlmittelvermischung in DWR

Organizers: FZR, VGB, TÜV
Rossendorf, 21 April 2005

Multiphase Flow Simulation, Experiment and Application

Organizers: FZR and ANSYS Germany
Rossendorf, 31 May-01 June 2005

International Conference on Fundamental and Applied MHD

Organizers: University of Latvia, Riga (Latvia), LEGI Grenoble (France), FZR
Júrmala (Lettland), 27 June-01 July 2005

2nd Sino-German Workshop on Electromagnetic Processing of Materials

Organizers: FZR and Department of Material Engineering Shanghai/China
Supported by DFG and the Sino-German Science Center, Peking
Dresden, 16-19 October 2005

23. Hauptsitzung der Deutsch-Schweizerischen Kommission für die Sicherheit kerntechnischer Einrichtungen (DSK)

Dresden, 3-4 November 2005

Seminars of the Institute

Dr. M. Abendroth

Identifizierung von schädigungsmechanischen Materialparametern aus dem Small Punch Test mit Hilfe neuronaler Netze

06.01.2005

K. Aygozhiev, S. Kriger (RWTH Aachen)

Impact of Improved Fuel Elements on Reactivity Transients in LWR

20.01.2005

G. Laczko (PTB Braunschweig)

Messung von Ionenspuren mit einer hochauflösenden Zeitprojektionskammer und Vergleich mit MC-Simulationen

03.02.2005

Dr. D. Lucas, Dr. E. Krepper, Dr. J.-M. Shi

Modellentwicklung für die Simulation von Blasenströmungen in vertikalen Rohren

17.02.2005

Dr. R. Koch

Reaktorkonzepte zur Verbrennung von Plutonium und minoren Actiniden

03.03.2005

Dr. H. Liu (Ben-Gurion University, Israel)

Insight into Metallurgical Process and Transport Phenomena by Means of Development of Mathematical Models

10.03.2005

H.-J. Friedrich (VKTA Dresden)

Elektrochemische Aufbereitung von sauren Grubenwässern – Stand, Probleme und Perspektiven

17.03.2005

Prof. Dr. S. Molokov (University of Coventry)

MHD Problems in Fusion

31.03.2005

S. Kliem

Statistische Unsicherheitsanalysen zur Simulation von Transienten in LWR

28.04.2004

H.-G. Willschütz

Modellierung der Schmelzerückhaltung im RDB eines Leichtwasserreaktors

19.05.2005

J. Konheiser, Dr. K. Noack

Messungen und MC-Berechnungen von Gamma- und Neutronenflussspektren in und hinter Stahl-Wasser-Konfigurationen
26.05.2005

Dr. H.-M. Prasser

Heiße Versuche an der vertikalen Teststrecke DN200 von TOPFLOW
09.06.2005

Dr. J. Starflinger (FZ Karlsruhe)

Das „High Performance Light Water Reactor (HPLWR)“-Konzept
23.06.2005

Dr. A. Grahn, Dr. E. Krepper

Modellierung der Siebverstopfung durch Isolationsmaterial bei der Sumpfkühlung – Stand und Perspektiven der Modellierung des Partikeltransports
15.09.2005

Dr. T. Höhne, R. Vaibar

Experimente und CFD-Simulation zur auftriebsgetriebenen Vermischung
22.09.2005

H.-G. Willschütz, Dr. E. Altstadt

Modellierung der Schmelzerückhaltung im RDB eines Leichtwasserreaktors
06.10.2005

Prof. Mikielewicz (Universität Gdansk)

Hydrodynamics and heat transfer in bubble flow in the boundary layer
27.10.2005

Ch. Zhang, Dr. S. Eckert

Experimental studies on MHD two-phase flows
03.11.2005

Dr. M. Posselt (FWI)

Atomistische Simulation von Defekten in Festkörpern
17.11.2005

Dr. R. H. Mathiesen (SINTEF Materials and Chemistry, Trondheim/Norwegen)

Time-resolved x-ray imaging in studies of advanced alloy solidification processes
30.11.2005

S. Boden, H. Hristov

Measurements and CFD predictions of a two-phase flow in a stirred tank
15.12.2005

Lecture courses

Frank-Peter Weiß, Mathias Werner

Zuverlässigkeit und Sicherheit technischer Systeme
TU Dresden, Fakultät Maschinenwesen
SS 2005 und WS 2005

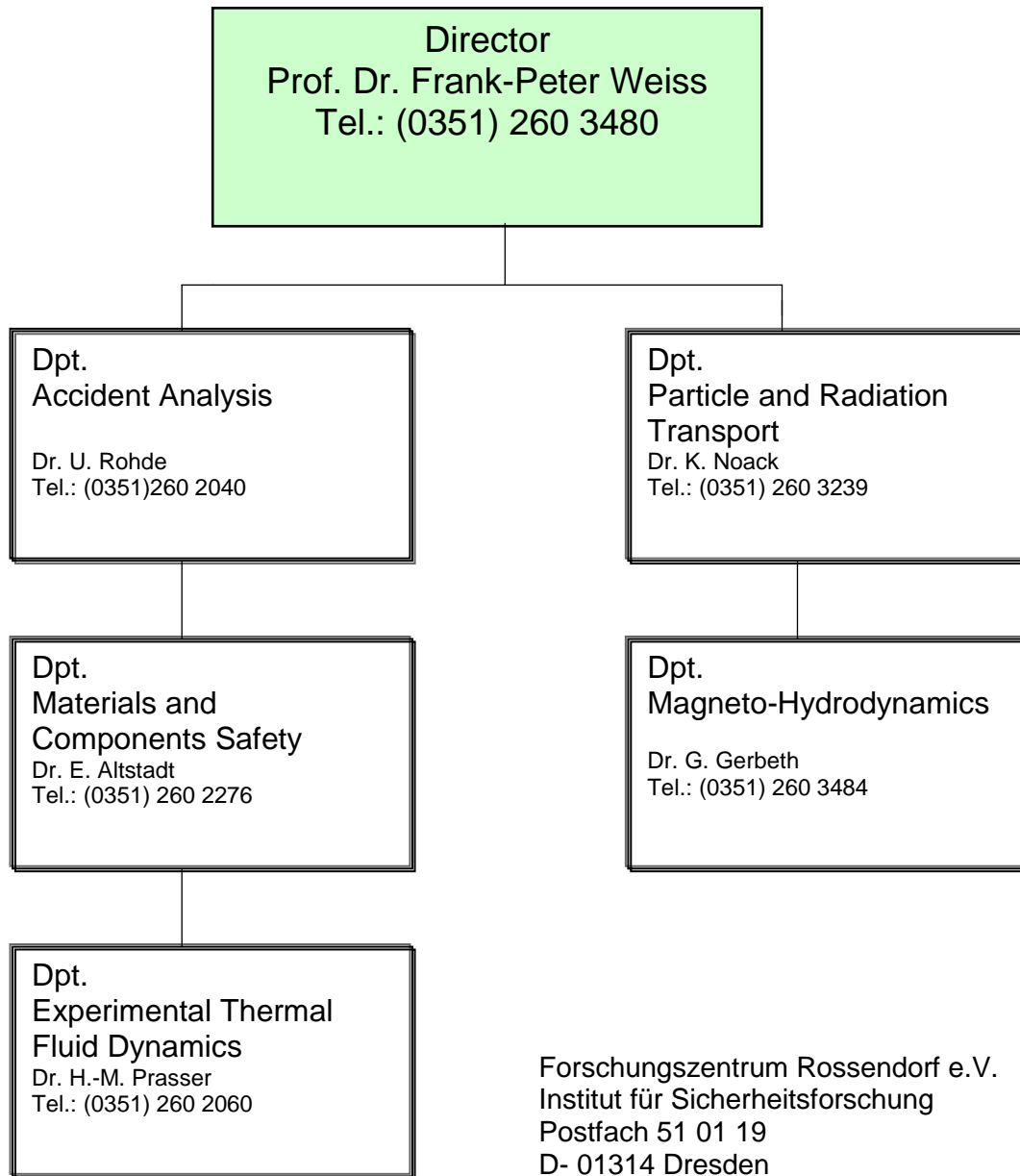
Udo Rindelhardt

Erneuerbare Energien I und II
Technische Universität Chemnitz, Fakultät Elektrotechnik/Informationstechnik
SS 2005 und WS 2005

Frank Bergner

Werkstofftechnik (Vorlesung und Seminar)
TU Dresden, Fakultät Maschinenwesen
SS 2005

Departments of the Institute



Personnel

Director: Prof. Dr. F.-P. Weiß

Scientific Staff

Abendroth, Martin Dr.
Altstadt, Eberhard Dr.
Avalos, Zuniga-Raul
Beckert, Carsten
Bergner, Frank Dr.
Beyer, Matthias
Bodele, Emmanuel
Carl, Helmar Dr.
Cartland-Glover, Gregory Dr.
Chatrov, Viktor Dr.
Cramer, Andreas Dr.
Eckert, Sven Dr.
Galindo, Vladimir Dr.
Gerbeth, Gunter Dr.
Grahn, Alexander Dr.
Grants, Ilmars Dr.
Grundmann, Ulrich Dr.
Gundrum, Thomas
Günther, Uwe Dr.
Hampel, Uwe Dr.
Hoppe, Dietrich Dr.
Höhne, Thomas Dr.
Hristov, Hristo Vesselin Dr.
Kliem, Sören
Koch, Reinhard Dr.
Konheiser, Jörg
Kozmenkov, Yaroslav
Krepel, Jiri
Krepper, Eckhard Dr.
Kryk, Holger Dr.
Küchler, Roland Dr.
Lucas, Dirk Dr.
Manera, Annalisa Dr.
Mittag, Siegfried Dr.
Müller, Gudrun Dr.
Mutschke, Gerd

Noack, Klaus Dr.
Pal, Josef
Prasser, Horst-Michael Dr.
Rindelhardt, Udo Prof. Dr.
Rohde, Ulrich Dr.
Schäfer, Frank Dr.
Schleicher, Eckhard
Shi- Jun-Mei Dr.
Stefani, Frank Dr.
Ulbricht, Andreas
Viehlig, Hans-Werner Dr.
Weier, Tom
Werner, Matthias Dr.
Willers, Bernd
Willschütz, Hans-Georg Dr.
Xu, Mingtian Dr.

PhD Students

Al Issa, Suleiman
Bieberle, André
Bieberle, Martina
Boden, Stephan
Buchenau, Dominique
Cirpka, Christian
Silva da, Marco
Vallee, Christophe
Zaruba, Aliaksandr
Zhang, Chaojie

Technical Staff

Behrens, Sieglinde
Berger, Torsten
Bobrov, Pavel Dr.
Bombis, Doris
Borchardt, Steffen
Erlebach, Stephan
Forker, Klaus
Futterschneider, Hein
Gommlich, André
Henke, Steffen
Hessel, Günther
Kunadt, Heiko
Leonhardt, Wolf-Dietrich
Lindner, Klaus
Losinski, Claudia
Nowak, Bernd
Pietzsch, Jens
Pietruske, Heiko
Richter, Annett
Richter, Henry
Richter, Joachim
Richter, Petra
Roßner, Michaela
Rott, Sonja
Rußig, Heiko
Schleißiger, Heike
Schmitt, Wilfried Dr.
Schneider, Gisela
Schütz, Peter
Schuhknecht, Jan
Skorupa, Ulrich
Spieler, Dagobert
Sühnel, Tobias
Tamme, Marko
Webersinke, Wolfgang
Weichelt, Steffen
Weiß, Rainer
Zimmermann, Wilfried
Zippe, Cornelius Dr.